Laboratório Nacional de Computação Científica

Programa de Pós-Graduação em Modelagem Computacional

Multiscale Modelling of Fibrous Materials: from the elastic regime to failure detection in soft tissues

Felipe Figueredo Rocha

Petrópolis, RJ - Brasil

5 de Abril de 2019

Felipe Figueredo Rocha

Multiscale Modelling of Fibrous Materials: from the elastic regime to failure detection in soft tissues

Tese submetida ao corpo docente do Laboratório Nacional de Computação Científica como parte dos requisitos necessários para a obtenção do grau de Doutor em Ciências em Modelagem Computacional.

Laboratório Nacional de Computação Científica

Programa de Pós-Graduação em Modelagem Computacional

Supervisor: Pablo Javier Blanco

Co-supervisor: Raúl Antonino Feijóo

Petrópolis, RJ - Brasil

5 de Abril de 2019

XXXX

Rocha, Felipe Figueredo

Multiscale Modelling of Fibrous Materials: from the elastic regime to failure detection in soft tissues / Felipe Figueredo Rocha. – Petrópolis, RJ - Brasil, 5 de Abril de 2019-

181 p. : il. ; 30 cm.

Orientador(es): Pablo Javier Blanco e Raúl Antonino Feijóo

Tese (D.Sc.) – Laboratório Nacional de Computação Científica
Programa de Pós-Graduação em Modelagem Computacional, 5 de Abril de 2019.

1. Palavra-chave1. 2. Palavra-chave2. 2. Palavra-chave3. I. Blanco, Pablo Javier. II. LNCC/MCTI. III. Título

CDD: XXX.XXX

Felipe Figueredo Rocha

Multiscale Modelling of Fibrous Materials: from the elastic regime to failure detection in soft tissues

Tese submetida ao corpo docente do Laboratório Nacional de Computação Científica como parte dos requisitos necessários para a obtenção do grau de Doutor em Ciências em Modelagem Computacional.

Aprovada por:

Prof. Pablo Javier Blanco, D.Sc.
(Presidente)

Prof. Rubens Sampaio Filho, Ph.D.

Prof. Fernando Alves Rochinha, D.Sc.

Prof. Eduardo Alberto Fancello, D.Sc.

Prof. Abimael Fernando Dourado Loula, D.Sc.

Prof. Regina Célia Cerqueira de Almeida, D.Sc.

Petrópolis, RJ - Brasil
5 de Abril de 2019

Dedication

To Mariluce (in memoriam)

Acknowledgements

If there is one thing that I cannot complain about my graduate period, it would be the lack of helpful people that I worked with. In fact, quite a number of helpful people have crossed my way during these 4 years of thesis. This thesis would not come to an end without them.

Of course, the top position of this list is for my supervisor prof. Pablo Blanco (hereafter just Pablo). I can say that he was more than just an excellent academic tutor, but someone that in many many times trusted on me, in my ideas, calculations, simulations, etc, even more than myself. Roughly, 99% of the times that I talked to him during these almost 6 years of work (Master included), I went out more confident than before talking. I think this a rare statistics, at least if I compare with most of my friends. I also believe that this is one of most valuable help that someone can offer in such a long and harsh journey, as the doctorate is. Finally, I would like to thank for the trust and freedom that you dispensed to me for conducting my research and for such a cutting-edge topic you proposed.

The second person of this list is my co-supervisor, prof. Raúl Feijóo. Even almost always collaborating by email, he was like a “human compiler”, pointing out very rapidly every single wrong or not well explained line of my texts. Such attitude took my research to a really higher level of formalisation that I could not had without his very wise observations. Moreover, he taught me, together with Pablo, the most important subject that I have learnt at LNCC, I am talking about variational formulations in mechanics. I am really glad to have learnt this topic in a such unique and passionating manner with them. Certainly, this good influence will persist quite a long time in my career. At last, but not the least, they both are the most hardworkers people that I ever met in academia, they were always available at the time that I needed, with replies faster than my capacity to process them. Such commitment has been inspiring.

Pursuing with the list, I was lucky to collaborate actively with more two great experts in solid mechanics, prof. Eduardo de Souza Neto and prof. Pablo Sánchez, they both were very influential in different periods of the thesis. Firstly, I am glad for the time I spent at the CIMEC (Santa Fé) learning damage and fracture theories from prof. Pablo Sánchez, prof. Alfredo Huespe and Sebastian Toro, other very supportive people that I met in this long path. Also in CIMEC, I am very happy to have met Carlos and prof. Victor Fachinotti, thank you for the ‘mates’, wine and ‘assados’. I am also pleased for my sandwich period in ZCCE (Swansea) and the supervision that I received of prof. Eduardo de Souza Neto. Thanks for all support you gave me and for every hour (yes, hours!) spent on the blackboard discussing lack of convergence issues. I cannot forget about Quang, my best friend in Swansea, but also my great collaborator, with whom I still share a lot of 'discrete multiscale ideas' and bugs via Skype, you can't imagine the whole importance that our discussions had to keep my motivation flying high during the time in Swansea. I cannot forget my other friends from Swansea, with whom I shared a couple of pints, jazz and walking, thank you Reza, Marcos, Débora, Alex, Chenna, Emilio, etc, the list is huge.

I also want to acknowledge prof. Anne Robertson (University of Pittsburgh) who gave me the opportunity to have a glimpse on real world experiments on arteries and look closely those beautiful images of microphoton microscopy. This contributed quite a lot to a pure computational mechanics guy as me. Thank you so much to Gade Piyusha and Chao Sang (her PhD students) to have conducted and explained me patiently all details of those experiments.

Coming back to Brazil, I want to acknowledge the evaluation board for accepting this duty and taking their time to read the manuscript. Thanks a lot to prof. Rubens Sampaio, prof. Fernando Rochinha, prof. Eduardo Fancello, prof. Abimael Loula and profa. Regina Almeida. I extend the acknowledge for all great professors who taught me at LNCC, this thesis has at least a tiny bit of every of their courses.

I really appreciated the working environment inside the HeMoLab team. Thank you so much Alonso, Carlos, Gonzalo Ares, Gonzalo Maso, Paulo, Lucas, Heloisa, Krishna and the visitors Sofia and Jorge, for really nice conversations, bash and SolverGP hints, dinners, 'mates', coffees, beers, pastas and 'limoncellos'. I wish you all the best for your scientific careers.

During my stay at LNCC, besides the official courses, I had the opportunity to learn a bit of several other subjects, different from my background, which I would never have imagined to have contact one day. I feel myself really lucky to be in a such interdisciplinary and helpful environment created here. Besides that, having spent the first 6 years of my adult age at LNCC, I have learnt a lot about life and about myself, situations that I had never passed before I experienced here. Certainly, everyone of my close friends here had taught me a lot without perceiving. For all these 'free' lessons and all the other unstressful moments of coffee, lunch, 'esfihas', pizzas, trails, going outs and so on, a big acknowledge goes to Aarito, Alan, Aline(s), Andrés(s), Bruno, Caio, Cauê, Diogo, Fortià, Gastão, Harão, Heber, Juanzito, Leonardo, Leandro, Lucas, Lucão, Luiza, Stephen, Nicolas, Nicolau, Paulinho, Pedro, Quinelato, Rodrigo, Secis, Thiagão, Tiene, Volpatto, Wellerson and Weslley (I hope to have not forgotten anyone).

I wish to say special thanks to all the staff of the LNCC, particularly to Ana Néri, Roberta, Marcelly, Ana Paula, Aline and Babi (now my yoga instructor). For their efficiency and kindness, you all help a lot to let the environment of research less harsh as possible. I also acknowledge the public agencies CNPq, Faperj, CAPES and the project

INCT-MACC for the financial support.

Finally, I wish to dedicate this work to my family, specially to my Mommy (In memorian) and my brothers Jakelúcio, Lúcio and Júnior and their families and also to 'tia Ana', Daniel and Wana. I would like to extend these compliments to Bruna, Isa, Maurício e Daniel, thanks for being for quite a while my second family (and what a family!).

ceiiinosssttuv = ut tensio sic vis

Robert Hooke (Lectiones Cutleriana, 1679)

Abstract

Fibrous materials are an important class of either biological and artificial materials and hence are essential to a wide spectrum of fields, ranging from medicine and biology to industrial applications. From the vast number of soft biological fibrous materials, this thesis found its inspiration from those tissues of the arterial walls. This is mainly motivated by the fact that cardiovascular diseases are one of the leading causes of death worldwide and consequently, to gain insight into the mechanisms underlying the progression of most of these diseases, a detailed characterisation of the mechanical behaviour of the arterial wall is required. This involves not only the simple phenomenological model for the material, but also the understanding of evolution processes such as damage, growth, remodelling and, eventually, failure. In this context, the multiscale constitutive modelling raises as a rational approach in which these complexities are naturally accounted for through micromechanical interactions between the basic unit blocks of the biological soft tissues, such as collagen fibres, pores, smooth muscle cells, etc. In particular, this thesis deals with the construction of a multiscale model to characterise the macroscale constitutive behaviour of a fibrous material featuring a discrete microstructure, i.e., a network of fibres. Both, the purely elastic and inelastic regimes in the finite strain setting are addressed, and in the latter case, until failure and strain localisation phenomena emerge. To reach this aim, the classical multiscale theory for continua had to be generalised to deal consistently with randomly distributed pores crossing the Representative Volume Element (RVE) boundary. Importantly, this theory provides a novel minimally constrained kinematically admissible set for the displacement fluctuations, consisting in the lower bound of the mechanical response and also is of utmost importance to analyse microscopic strain localisation phenomena. Finally, as the third and last contribution of the thesis, on the light of the discontinuous bifurcation analysis, we use the derived multiscale model for a network of fibres to study the macroscale manifestation of damage processes unfolding at the level of individual fibres. Hence, strain localisation is observed and is identified as the main cause of nucleation of macroscale cracks, characterising the critical point of failure in our context. Such point, in which the macroscale problem becomes ill-posed, is determined by the spectral analysis of the so-called acoustic tensor, which also provides information about the macroscale failure pattern (unit normal and crack opening vectors). In all these models, the Method of Multiscale Virtual Power (MMVP) has been employed, providing a systematic methodology based on variational formulations to characterise the microscale equilibrium problem, consistent boundary conditions, as well as the homogenisation formulae which define the associated first Piola-Kirchhoff stress tensor and the constitutive tangent tensor in the macroscopic continuum.. Numerical experiments showing the suitability of the present methodology are shown and discussed.

Keywords: Constitutive Multiscale Modelling; Network of fibres; Representative volume element; Strain localisation; Discontinuous Bifurcation Analysis.

Resumo

Materiais fibrosos são uma importante classe de dentre os que compõem tecidos biológicos e materiais artificiais, e por esta razão são fundamentais em um largo espectro de contextos desde medicina e biologia até aplicações industriais. Dentre o enorme número de tecidos fibrosos, essa tese foi inspirada naqueles encontrados nas paredes arteriais. Isso é principalmente motivado pelo fato que as doenças cardiovasculares são umas das principais causas de morte no mundo e que, para entender os mecanismos de evolução dessas enfermidades, se faz necessário uma caracterização detalhada do comportamento mecânico da parede arterial. Isto inclui não apenas um simples modelo constitutivo fenomenológico para o material, mas também o entendimento de processos evolutivos como o dano, crescimento, remodelamento e, eventualmente, falhas. Neste contexto, a modelagem constitutiva multiescala aparece como uma alternativa mais racional na qual estas complexidades são naturalmente levadas em consideração pelas interações micromecânicas dos componentes básicos que constituem os tecidos biológicos, isto é, fibras de colágeno, poros, células de músculo liso, etc. Em particular, esta tese trata da construção de um modelo para caracterizar o comportamento constitutivo macroscópico de um material fibroso constituído de uma microestrutura discreta, nesse caso uma rede de fibras. É analisado tanto o regime elástico quanto o inelástico em grandes deformações, e nesse último caso até o momento que ocorre a detecção de uma falha juntamente com a localização de deformação. Para se chegar neste objetivo, a teoria clássica multiescala para um meio contínuo poroso teve que ser generalizada para tratar de maneira mecanicamente consistente Elementos de Volumes Representativos (EVR) cujos vazios atingem a fronteira. É importante destacar que essa teoria estabelece um novo conjunto admissível de mínima restrição cinemática para o campo de flutuações de deslocamento, caracterizando a cota inferior teórica para a resposta mecânica, aspecto fundamental na análise do fenômeno de localização de deformação na microescala. Finalmente, baseado na análise de bifurcação descontínua, o modelo desenvolvido para a rede de fibras é usado para se estudar o efeito macroscópico dos processos de danificação que ocorrem no nível das fibras. Desta forma, a localização de deformação é observada e identificada como a principal causa da nucleação de macro-fissuras, caracterizando o ponto crítico de falha no nosso contexto. Tal ponto, no qual o problema mecânico na macroescala se torna mal-posto, é determinado pela análise espectral do tensor acústico, que também determina o padrão da fissura na macroescala (direção da normal e abertura da trinca). Em todos estes modelos, o Método da Potência Virtual Multiescala (MPVM) foi utilizado por se tratar de uma metodologia sistemática baseada em formulações variacionais que permite caracterizar o problema de equilíbrio na microescala, condições de contorno consistentes, bem como fórmulas de homogeinização que definem o primeiro tensor de Piola-Kirchhoff e o tensor constitutivo tangente do modelo no contínuo macroscópico. Por fim, experimentos numéricos mostrando o potencial da metodologia proposta são apresentados e discutidos.

Palavras-chave: Modelagem constitutiva multiescala; Redes de fibras; Elemento de volume representativo; Localização de deformação; Análise de bifurcação descontínua.

List of Figures

Figure 1 – Arterial wall structure. Asked for permission from (HOLZAPFEL; GASSER; OGDEN, 2000)). 27
Figure 2 – Overview of several spatial scales in the cardiovascular system. Images extracted from the Adan-Web (http://hemolab.lncc.br/adan-web/) and asked for permission from (ROBERTSON; WATTON, 2013). 28
Figure 3 – Arterial tissue rupture (asked for permission from (ROBERTSON; HILL; LI, 2012)). 28
Figure 4 – Duality diagram for the principle of virtual power in single scale. 41
Figure 5 – Diagram of kinematics: relation between spaces and operators found in (2.10), (2.11), (2.10), (2.19), (2.14) and also the generalised deformation operator at microscale ($\mathcal{D}_\mu$) defined analogously as in (2.2). 47
Figure 6 – Multiscale setting for the modelling in continuum solid mechanics. . . . 49
Figure 7 – Microscale domain with random distribution of circular voids. The integral of the normal vector over the solid part of the RVE boundary (in bold) is not zero. 62
Figure 8 – Multiscale setting for the modelling in continuum mechanics in random porous media. 63
Figure 9 – Scheme of the boundary partitioning for a generic porous RVE geometry. 64
Figure 10 – Different types of RVE domains with the corresponding denomination for the different parts of the boundaries. Case I: internal voids imply that the RVE is $\mathbf{n}_\mu$-balanced ($\bar{\mathbf{n}}_\mu = \mathbf{0}$). Case II: voids reach the boundary, but due to the structured arrangement of the voids the RVE is $\mathbf{n}_\mu$-balanced ($\bar{\mathbf{n}}_\mu = \mathbf{0}$). Case III: voids reach the boundary in a random manner, so the RVE is $\mathbf{n}_\mu$-unbalanced ($\bar{\mathbf{n}}_\mu \neq \mathbf{0}$). 67
Figure 11 – Macroscale continuum and discrete microscale RVE domains. 77
Figure 12 – Example of a porous RVE featuring connected slender structural components. 80
Figure 13 – Typical joints reaching the RVE boundary. 80
Figure 14 – Notation and basic ingredients in the geometrical/topological description of the *Network* of fibres. 84
Figure 15 – Concept of joint normal vector in different situations. Left inset: regular hexagonally-shaped joint with $A_{\alpha_1} = A_{\alpha_2} = A_{\alpha_3}$, yielding $\mathbf{m}_i = \mathbf{0}$. Middle inset: arbitrary joint with $A_{\alpha_1} \neq A_{\alpha_2} \neq A_{\alpha_3}$ and so $\mathbf{m}_i \neq \mathbf{0}$. Right inset: Joint at a corner. 86
Figure 16 – Affine kinematics and nonaffine kinematics due to the existence of fluctuations. 89

Figure 17 – Fibre in its material and spatial configurations, and interpretation of the generalised strain and stress vectors. 109
Figure 18 – Imaginary cylinder (truss) in different deformed configurations enclosing a bundle of collagen fibres. 111
Figure 19 – Example of homogeneous network. 128
Figure 20 – Reorientation of fibre families considering different fibre orientation angles due to three different node perturbations (realisations for a fixed random seed value). The angle distribution as a function of the macroscale stretch (top row) and the topology of fibres in the original (mid row) and the deformed network at the maximum level of stretch $\lambda = 2.0$ (bottom row). 130
Figure 21 – Homogenised constitutive response (left column) and non-affinity index (right column) considering fibre area variation (top row) and fibre orientation (bottom row). 131
Figure 22 – Histogram of the activation stretch following a Gamma-distribution for the different realisations defined in terms of the pair $(m, s)_{\lambda^a}$. 132
Figure 23 – Homogenised constitutive response for different distributions of the activation stretch parameter. 133
Figure 24 – λ^a-heterogeneity in the RVE for the different realisations: impact on the non-affinity and overall activation ratio. 133
Figure 25 – Network of fibres generation through the replication of a basic unit pattern (multiplication factor from 1 to 5, i.e. left to right panels). Perturbation level l_1 in top row, and perturbation level l_2 in the bottom row. Gray color stands for the fibre transversal area values (darker color indicates larger area). 135
Figure 26 – The impact of boundary conditions on the displacement fluctuation field. Networks warped with the displacement fluctuation for models $\widetilde{\mathscr{U}}_\mu^{\mathsf{L}}$ (red) and $\widetilde{\mathscr{U}}_\mu^{\mathsf{M}}$ (blue) at the last pseudo-time in the pure axial test. 136
Figure 27 – Total deformed configuration of the RVE along the pseudo-time showing activated fibres (in red) for the $\widetilde{\mathscr{U}}_\mu^{\mathsf{M}}$ model, at the perturbation level l_2, and for the pure axial test. 136
Figure 28 – Total deformed configuration of the RVE along the pseudo-time showing activated fibres (in red) for the $\widetilde{\mathscr{U}}_\mu^{\mathsf{M}}$ model, at the perturbation level l_1, and for the combined axial-shear test 136
Figure 29 – Convergence of the homogenised stress response with respect to the RVE size for the $\widetilde{\mathscr{U}}_\mu^{\mathsf{L}}$ (red dashed line) and $\widetilde{\mathscr{U}}_\mu^{\mathsf{M}}$ (blue solid line) models. 138
Figure 30 – Convergence analyses with respect to the RVE size for the $\widetilde{\mathscr{U}}_\mu^{\mathsf{L}}$ (red dashed line) and $\widetilde{\mathscr{U}}_\mu^{\mathsf{M}}$ (blue solid line) models. Heterogeneity levels l_1 (left) and l_2 (right). 139

Figure 31 – Homogenised stress for different boundary conditions. Stress components during pseudo-time for the $\widetilde{\mathscr{U}}_\mu^{\mathsf{L}}$ (dashed lines) and $\widetilde{\mathscr{U}}_\mu^{\mathsf{M}}$ (solid lines) models. 140
Figure 32 – Three-dimensional RVE from a piece of an adventitia layer and projections on the coordinate planes. 142
Figure 33 – Homogenised stress tensor components along the loading program for the different circumferential angles. 142
Figure 34 – Reference and deformed configurations of 3D networks. Colours represent fibre area at the begining of the loading program (first row) and the fluctuation magnitude for the last loading step (second row). 143
Figure 35 – Results of the study case Ex1-a. 148
Figure 36 – Results of the study case Ex1-b. 149
Figure 37 – Results of the study case Ex1-c. 150
Figure 38 – Deformed state of fibre networks at the last step of the loading program. From top to bottom, cases Ex2-a to Ex2-c, with LBS (left) and MCS (right) being used. 151
Figure 39 – Homogenised stress components throughout the loading program and critical points (vertical lines). From top to bottom: Ex2-a, Ex2-b and Ex2-c. 152
Figure 40 – Different snapshots of the network of fibres for cases Ex3A-a and Ex3A-b displaying distribution of fibre area (upper frame) and deformed configuration for different states of material deterioration. 156
Figure 41 – Homogenised stress components throughout the loading program and critical points for Ex3A-a (band) and Ex3A-b (balls). 156
Figure 42 – Different snapshots of the network of fibres for different realisations in the case Ex3R-a. 157
Figure 43 – Homogenised stress components throughout the loading program and critical points for different realisations of the case Ex3R-a. 157
Figure 44 – Different snapshots of the network of fibres for different realisations in the case Ex3R-b. 158
Figure 45 – Homogenised stress components throughout the loading program and critical points for different realisations in the case Ex3R-b. 158
Figure 46 – Initial and final configurations for fibre networks of Study 4. 161
Figure 47 – Homogenised stress responses showing the lack of objectivity in the mechanical response during the post-critical regime. 161

List of Tables

Table 1 – Network parameters to study the effect of fibre area and orientation. * for each level, 3 realisations are considered. 129
Table 2 – Network parameters to study the effect of fibre activation stretch. 132
Table 3 – Network parameters for the study of boundary conditions related to $\widetilde{\mathscr{U}}_{\mu}^{\mathsf{L}}$ and $\widetilde{\mathscr{U}}_{\mu}^{\mathsf{M}}$. 134
Table 4 – Material, geometrical and numerical parameters for the cases in Study 1. $\downarrow_{\max}$: maximum reduction. 147
Table 5 – Material, geometrical and numerical parameters for the cases in Study 2. $\downarrow_{\max}$: maximum reduction. 151
Table 6 – Material, geometrical and numerical parameters for all cases in Study 3 concerning fibre area reduction. $\downarrow_{\max}$: maximum reduction. 154
Table 7 – Material, geometrical and numerical parameters for all cases in Study 3 concerning removal of fibres. Variable (k) is used to identify the realisation. 155
Table 8 – Material, geometrical and numerical parameters for all cases with a vertical band in Study 4. $\downarrow_{\max}$: maximum reduction. 159
Table 9 – Material, geometrical and numerical parameters for all cases with an inclined band in Study 4. 159

List of abbreviations and acronyms

RVE	Representative Volume Element
MMVP	Method of Multiscale Virtual Power
PMVP	Principle of Multiscale Virtual Power
PVP	Principle of Virtual Power
MCKMM	Minimally Constrained Kinematically admissible Multiscale Model
MCS	Minimally Constrained Space (shorter acronym to MCKMM)
LBS	Linear Boundary Space
DBA	Discontinuous Bifurcation Analysis
PKST	(First) Piola-Kirchhoff Stress Tensor
SEF	Strain Energy Function

List of symbols

$\mathrm{n_d}$	Spatial dimension, 2 or 3 in this text.
$\mathbf{e}_1, \ldots, \mathbf{e}_{\mathrm{n_d}}$	Canonical vectors of $\mathbb{R}^{\mathrm{n_d}}$.
$\mathbf{E}_{ij} = \mathbf{e}_i \otimes \mathbf{e}_j, \text{ for } i,j = 1, \ldots \mathrm{n_d}$	2^{nd}-order tensors of the canonical basis of $\mathbb{R}^{\mathrm{n_d} \times \mathrm{n_d}}$.
$\partial_Z(\cdot)$	Alternative notation to $= \frac{\partial(\cdot)}{\partial Z}$.
$\mathbf{a}, \boldsymbol{\mathsf{a}}$	Convention for vectors.
$\mathbf{A}, \boldsymbol{\mathsf{A}}$	Convention for 2^{nd}-order tensors.
$\mathbb{A}$	Convention for 4^{th}-order tensor.
$\mathcal{A}$	Convention for operator or functional.
$\mathscr{A}$	Vector space, manifold or a functional set.
$\mathscr{A}'$	Dual of $\mathscr{A}$.
$\mathrm{Var}_{\mathscr{A}}$ or $\widehat{\mathscr{A}}$	Tangent space (of variations) associated to $\mathscr{A}$.
α	Reserved index to designate fibre properties
A_α	Fibre original transversal area.
L_α	Fibre original length.
$\boldsymbol{\mathsf{a}}_\alpha$	Fibre direction unit vector.
$\boldsymbol{\mathsf{s}}_\alpha$ or $\boldsymbol{\mathsf{s}}_\mu^\alpha$	Generalised fibre stress vector.
$\boldsymbol{\mathsf{g}}_\alpha$ or $\boldsymbol{\mathsf{g}}_\mu^\alpha$	Generalised fibre strain vector.
$\boldsymbol{\mathsf{D}}_\alpha$	Generalised fibre constitutive tangent tensor (2^{nd}-order).
$\boldsymbol{\mathsf{S}}_\alpha$ or $\boldsymbol{\mathsf{S}}_\mu^\alpha$	Generalised fibre stress (2^{nd}-order tensor representation).
$\boldsymbol{\mathsf{G}}_\mu^\alpha$	Generalised fibre strain (2^{nd}-order tensor representation).
$\otimes$	Standard tensor product. It applies both for vectors or 2^{nd}-order tensors.

$\overline{\otimes}$	Non-standard tensor product 2[nd]-order tensors. Defined as

$$(\mathbf{a} \otimes \mathbf{b}) \,\overline{\otimes}\, (\mathbf{c} \otimes \mathbf{d}) = \mathbf{a} \otimes \mathbf{c} \otimes \mathbf{b} \otimes \mathbf{d} \tag{LS.1}$$

$\lvert \cdot \rvert$	Measure of a set or the absolute value of a number.
$\mathrm{tr}(\cdot)$	Trace of the second order tensor $(\cdot)$.
$\overline{(\cdot)}$	Closure of the set $(\cdot)$ (if $(\cdot)$ is a set).
$(\cdot)^\circ$	Interior of the set $(\cdot)$ (if $(\cdot)$ is a set).

Contents

1 Introduction **23**
1.1 Mechanical failure in arterial tissues 24
1.2 Multiscale nature of the arterial tissues 26
1.3 On multiscale theories 29
1.4 Multiscale approaches for fibre networks 31
1.5 Methodology 34
1.6 Main objectives 35
1.7 Scientific Contributions 36
1.8 Organisation 37
2 Variational Foundations of Multiscale Models **39**
2.1 Method of Virtual Power 40
2.1.1 Kinematics 40
2.1.2 Mathematical Duality 40
2.1.3 Principle of Virtual Power 41
2.2 Method of Multiscale Virtual Power 42
2.2.1 Multiscale Kinematics 43
2.2.1.1 Macroscale Kinematics 43
2.2.1.2 Microscale Kinematics 43
2.2.2 Kinematical Admissibility 44
2.2.2.1 Insertion Operators 44
2.2.2.2 Kinematic homogenisation operators 45
2.2.3 Duality 46
2.2.4 Principle of Multiscale Virtual Power 47
2.3 Application in solid mechanics 48
2.3.1 Macroscale model 49
2.3.2 Microscale kinematics 50
2.3.3 Multiscale kinematics 51
2.3.3.1 Specific subspaces of multiscale models 51
2.3.4 Duality and PMVP 52
2.4 Miscelanneous topics 54
2.4.1 Linearisation of the microscale model 54
2.4.2 Homogenised constitutive tangent 54
2.4.2.1 Proof of the major-symmetry 56
2.4.3 Incompressible Materials 57
2.4.3.1 Admissible macroscale displacement set 57
2.4.3.2 Point-valued strain and strain rate set 58

2.4.3.3 Homogenisation formula 58
2.5 Closing remarks 59
3 A Consistent Multiscale Model for Solids with Voids reaching Boundary . . 61
3.1 Multiscale setting and preliminary notation 62
3.2 Kinematics 64
3.2.1 Kinematical insertion 65
3.2.2 Displacement homogenisation 65
3.2.3 Gradient homogenisation 66
3.2.4 Spaces of admissible displacement fluctuations 68
3.3 Principle of Multiscale Virtual Power 69
3.3.1 Variational formulation 69
3.3.2 Homogenisation formulae 70
3.3.3 Micromechanical problem 71
3.3.4 Reactive forces 72
3.3.5 Purely constitutive multiscale formulation 73
3.3.6 Consequences of omitting $\bar{\mathbf{n}}_\mu$ (but $\bar{\mathbf{n}}_\mu \neq \mathbf{0}$) 74
3.4 Closing remarks 75
4 Linking Networks of Fibres to Continua 76
4.1 Features of the fibrous microstructure 76
4.2 Motivation about the transition from continuum media to discrete networks 78
4.2.1 Discrete displacement homogenisation 81
4.2.2 Discrete version for gradient-related integrals 81
4.2.3 Comment on equivalent areas of boundary joints 82
4.3 Kinematics 83
4.3.1 Characterisation of microscale fibre network 83
4.3.2 Microscale displacement 87
4.3.3 Insertion operators 88
4.3.4 Generalised microscale gradient operator 90
4.3.5 Kinematic homogenisation operators 92
4.3.5.1 Homogenisation of displacements 92
4.3.5.2 Homogenisation of generalised microscale gradient 93
4.3.5.3 Space of admissible fluctuations 95
4.3.6 Consistency of kinematical operators 97
4.4 Mathematical duality and virtual power 98
4.5 Principle of Multiscale Virtual Power 99
4.5.1 Stress homogenisation 100
4.5.2 Microscale mechanical equilibrium problem 101
4.6 Reactive forces 102
4.6.1 Stress homogenisation from boundary data 104

4.7 Concluding remarks . . . 105
5 Damage Modelling and Failure Detection in Fibrous Materials . . . 107
5.1 Multiscale model for fibres network revisited . . . 108
5.2 Constitutive models for fibres . . . 110
5.3 Damage modelling . . . 113
5.4 Regularised damage model . . . 115
5.5 Consistent algorithmic tangent . . . 116
5.6 Numerical regularisation based on artificial viscosity . . . 118
5.7 Homogenised constitutive tangent . . . 119
5.8 Discontinuous bifurcation analysis . . . 122
5.9 Method for determining the initial opening direction . . . 123
5.10 Closing Remarks . . . 125
6 Numerical Experiments . . . 126
6.1 Hyperelastic fibre networks . . . 126
6.1.1 Two-dimensional setting simulations . . . 127
6.1.1.1 Random generation of fibrous networks . . . 127
6.1.1.2 Effect of fibre area and fibre orientation . . . 129
6.1.1.3 Effect of the activation stretch . . . 131
6.1.1.4 On the choice of boundary conditions . . . 134
6.1.2 Three-dimensional simulations . . . 141
6.1.2.1 Effect of circumferential angle . . . 141
6.1.3 Discussion . . . 143
6.2 Fibre networks featuring softening . . . 145
6.2.1 Study 1: Detection of critical point, angle and direction of discontinuous bifurcation at macroscale . . . 146
6.2.2 Study 2: Sensitivity of critical point to boundary conditions . . . 150
6.2.3 Study 3: Influence of heterogeneity . . . 153
6.2.4 Study 4: Size-effect during the post-critical regime . . . 158
6.2.5 Discussion . . . 160
6.3 Closing Remarks . . . 162
7 Conclusion . . . 163
7.1 On the contributions of the thesis . . . 163
7.2 Limitations . . . 164
7.3 Towards truly multiscale simulations . . . 165
7.4 Further perspectives . . . 166

Bibliography . . . 168

1 Introduction

Fibre networks are important structural components for many biological and artificial materials and hence are fundamental in a wide spectrum of fields, ranging from medicine and biology to industrial applications. Concerning biological soft materials, most of the cardiovascular tissue in the human and animal bodies, such as arterial walls and the heart, are composed from collagen fibre networks that carry the main structural function (ROBERTSON; WATTON, 2013; HOLZAPFEL; GASSER; OGDEN, 2000). Another important examples of collagenous fibrous tissues are: the connective tissue, comprising tendons and articular cartilage (DAVIS; VITA, 2012; GANGHOFFER et al., 2016; VASSOLER; FANCELLO; A., 2016); the extracellular matrix (ECM), which provides the structural support for cells together with the proteoglycans, for example in the human cornea (CHENG; HATAMI-MARBINI; PINSKY, 2013). Also, there are non-collagenous biological fibrous structures as those found in the cytoskeleton, where F-actin filaments that compose the network structure play not only a structural role but also act upon biochemical regularisation (RANGAMANI; XIONG; IYENGAR, 2014). Additional, examples of non-biological fibrous materials include textiles, paper and rubber-like materials.

From the vast number of soft biological fibrous materials, this thesis found its inspiration in the basic constituents of the arterial walls. This is motivated by the fact that cardiovascular diseases are the leading cause of death worldwide (ROTH et al., 2015). Hence, due to the complexity and importance of the problem, the efforts of the scientific community towards a more detailed understanding of this subject have increased during the last years. Naturally, the computational mechanics approach has become a viable and fundamental methodology to guide research in the field. For this reason, several constitutive models have been proposed in the attempt to improve predictive capabilities of numerical simulations to model the material behaviour of arterial tissue (HOLZAPFEL; OGDEN, 2010; HOLZAPFEL; GASSER; OGDEN, 2000; WEISBECKER; UNTERBERGER; HOLZAPFEL, 2015; GASSER; OGDEN; HOLZAPFEL, 2006).

To gain insight on the onset and progress of some cardiovascular diseases, as well as to improve treatment and surgical planning in medical practice, a detailed characterisation of the mechanical behaviour of the arterial wall is required. This is even more fundamental when studying the tendency of soft tissues to failure after growth, remodelling and damage processes. The classical constitutive modelling approach based purely on phenomenological laws fails in representing the micro-mechanical interactions among tissue constituents, which are fully responsible for disastrous outcomes such as pathological remodelling and, eventually, rupture of these tissues. In turn, the multiscale constitutive modelling raises as a powerful tool which allows to naturally take into account the microscopic details and interactions of the basic unit blocks of the biological tissues, such as collagen fibres, pores, etc.

Before digging into more technical aspects, we address more carefully two questions that are fundamental to understand the motivation of the present work, that is:

1. Why is it important to study failure in arterial tissues? (see Section 1.1).
2. Why is it so important to model the arterial tissue using a multiscale approach? (see Section 1.2).

Still in this chapter we further discuss about generalities concerning multiscale theories in Section 1.3 and also the use of this approach in the field of fibrous materials in Section 1.4. In the sequence of that, the methodology adopted will be discussed in Section 1.5 and objectives of the thesis will be pointed out in Section 1.6, as well as the associated contributions in Section 1.7. For the organisation of the each chapter, see Section 1.8.

1.1 Mechanical failure in arterial tissues

Particularly in the context of the vascular tissues, it has largely been acknowledged the connection between the onset and progress of pathologies with physiological, chemical and mechanical markers (CARO; FITZ-GERALD; SCHROTER, 1971; KU et al., 1985; GIDDENS; ZARINS; GLAGOV, 1993; CHATZIZISIS et al., 2007). While at a large timescale the material response slowly evolves and transforms by means of mechanobiological phenomena, being manifested through growth and remodelling processes (ROBERTSON; WATTON, 2013), at a short timescale, it must be recognised the weakening and rupture preceding such catastrophic events are matter of the domain of failure analysis and/or inelastic constitutive modelling. Moreover, one single common characteristic of most important cardiovascular diseases is the role played by failure and other softening phenomena. Such importance can be seen by the increasing number of scientific contributions in the computational biomechanics field. Below, it follows some example of diseases and their related studies:

1. Atherosclerotic degenerations of the blood vessels lead to the development of atherosclerotic plaques which are one of the fundamental expressions of the onset and progress of cardiovascular diseases. For instance, the simulation of fracturing the iliac atherosclerotic artery using a phase field model was reported in (RAINA; MIEHE, 2015). Using the continuum damage approach, (BALZANI; BRINKHUES; HOLZAPFEL, 2012) simulated inflation of an atherosclerotic artery.

Other contributions in this field have been provided by (FERRARA; PANDOLFI, 2008).

2. The treatment of vessel stenosis targets the opening of lumen area in order to regularise blood pressure and remove obstacles to blood flow. Two common procedures are baloon angioplasty and stent implants. These procedures, however, may severely injure the inner surface of the arterial wall. Ineffective procedures may also result in re-stenosis of the blood vessel, or even in the rupture of atherosclerotic plaque, which can block downstream circulation, causing stroke (brain circulation) or myocardial infarction (coronary circulation). Given the great relevance in understanding and optimising these treatments, (LI et al., 2012) performed the numerical simulation of the ballon-angioplasty and stent implant in an idealised three-layer transversely isotropic artery allowing damage in both collagen and elastin constituents.

3. The laminated structure of the *media* (see Fig. 1), which renders a high strength to the artery, may be also the cause the so-called dissection which is the separation of these lamellae. The dissection phenomena have basically two consequences: it can cause stenosis or it may weaken the artery causing, for instance, the growth of an aneurysm. In this field of research, (GASSER; HOLZAPFEL, 2006) performed numerical simulations of arterial dissection combining transversely isotropic energy density with proper finite element formulations to deal with discontinuous fields. A combined analysis during a ballon-angioplasty intervention was done in (GASSER; HOLZAPFEL, 2007). Other works in this direction are (GASSER; HOLZAPFEL, 2003; FERRARA; PANDOLFI, 2010).

Several studies have been conducted to try to characterise, through ex-vivo experiments, the loss of stiffness either at the level of the entire arterial wall (SANG et al., 2018), or at a layer level (WEISBECKER et al., 2012), just to mention a couple of examples. Many mathematical models have been proposed to explain these observations, see for example (BALZANI; BRINKHUES; HOLZAPFEL, 2012; LI et al., 2012; LI, 2016; PEÑA, 2014). These studies share a similar modelling strategy, that is the characterisation of phenomenological material models to describe the stable material response as well as the identification of the conditions for which the constitutive response starts to feature a softening behaviour (i.e. negative slope in the stress-strain relation), instant at which the failure of the tissue typically begins.

Many other examples could be mentioned, but the important point to highlight at this moment is that none of the aforementioned articles study the failure phenomena using a multiscale paradigm, subject of the next Section 1.2. As it will be seen in the next few sections, the study of the micromechanical environment in fibrous networks is paramount towards a correct understanding of the phenomena involved in the rupture of biological tissues.

1.2 Multiscale nature of the arterial tissues

The human body is a highly complex multiscale system, as in particular the cardiovascular system and the circulation of blood through it. Particularly, the arterial wall tissues are highly heterogeneous, as seen in Figs. 2 and 1. These heterogeneities (for instance, different families of fibres, voids, etc.) govern the mechanical response of the tissue at the macroscopic (observable) scale, which is the level at which the load-bearing function is crucial to properly interact with the forces exerted by the blood. The main structurally important components are elastin, collagen and smooth muscle fibres, as can be seen in Fig. 1. The arterial wall is composed by three layers:

***Intima*:** It consists mainly of elastin, which has almost a linear elastic and isotropic behaviour. Sometimes the endothelium is not considered part of this layer, due to the small thickness and low mechanical relevance.

***Media*:** It is the intermediate layer which comprises most of the artery. It is formed by an elastic and smooth muscle matrix reinforced with collagen fibres. Due to its structure, the mechanical behaviour of this layer is nonlinear and anisotropic.

***Adventia*:** It is the stiffest layer due to the high concentration of collagen fibres immersed in elastin.

Within the characterisation of the arterial tissue, the mechanical relevance of the tunica media and adventitia is of the utmost interest. These layers feature an architecture of elastic and collagen fibres which provide them with particular functional roles (ROBERTSON; WATTON, 2013). The exact composition depends on the type of vessel and, also, on the size of the vessel. However, the fibrous structure is dominant for these two outer layers. From a macroscale viewpoint, these fibres display a certain preferred material orientation around a given direction which, also, depends on the type of vessel. Thus, phenomenological models have introduced the effect of fibres through transversely isotropic constitutive functionals based on direction-dependent invariants also including the effect of fibre dispersion (GASSER; OGDEN; HOLZAPFEL, 2006; HOLZAPFEL; GASSER; OGDEN, 2000). Concerning the fenestrated structure of intima (see Fig. 2), in (GASSER et al., 2010) it is shown the micro-mechanical characterisation of the intra-luminal thrombus tissue in abdominal aortic aneurysms, which can be modelled employing an Representative Volume Element (RVE) with randomly distributed elliptical porous media.

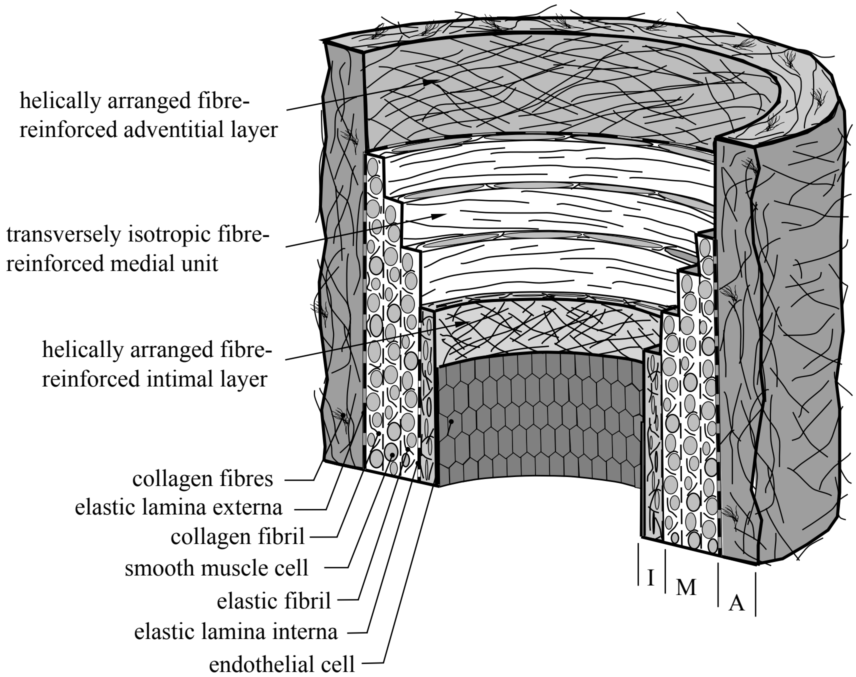

Figure 1 – Arterial wall structure. Asked for permission from (HOLZAPFEL; GASSER; OGDEN, 2000)).

Also, in the context of biological materials displaying a fibrous structure, some works have addressed the importance of the mechanical interaction among fibres at the microscale in the overall response of the tissue. For example, as pointed in (STEIN et al., 2011), the effect of stiffening is not well understood, and considering the non-affinity of deformation in those models it is necessary to gain insight into such phenomenon. In (KABLA; MAHADEVAN, 2007; CHANDRAN; BAROCAS, 2007), the authors attributed the nonlinear mechanical response observed in some experimental tests to two contributing factors: (i) the individual nonlinear constitutive behaviour of each single fibre, and (ii) the non-affine collective deformation of the network. Several non-affinity indexes are proposed and comparison is made in (HATAMI-MARBINI; PICU, 2009). In (PRITCHARD; HUANG; TERENTJEV, 2014), the same features are discussed, plus the recruitment of individual fibres, which is also claimed to play an important role in the nonlinear behaviour observed at the macroscale. All these factors motivate the construction of multiscale models, so that the internal structure of the tissue along with underlying micro-mechanical interactions are taken into account in the resulting material response.

Finally, it is worth mentioning that despite the increasing experimental and computational efforts to investigate failure-related and irreversible effects of soft biological tissue, as those seen in Section 1.1, the underlying degradation mechanisms at the microscale level remain poorly understood. According to (GASSER, 2011), there is still no clear definition of what damage is, and conventional indicators of mechanical injury (such as visible failure and loss of stiffness) may not identify the tissue's tolerance to injury appropriately. For instance, a single scale modelling approach of arterial tissues does not regard explicitly individual collagen fibres and this may obscure the understanding of important microscale constitutive ingredients.

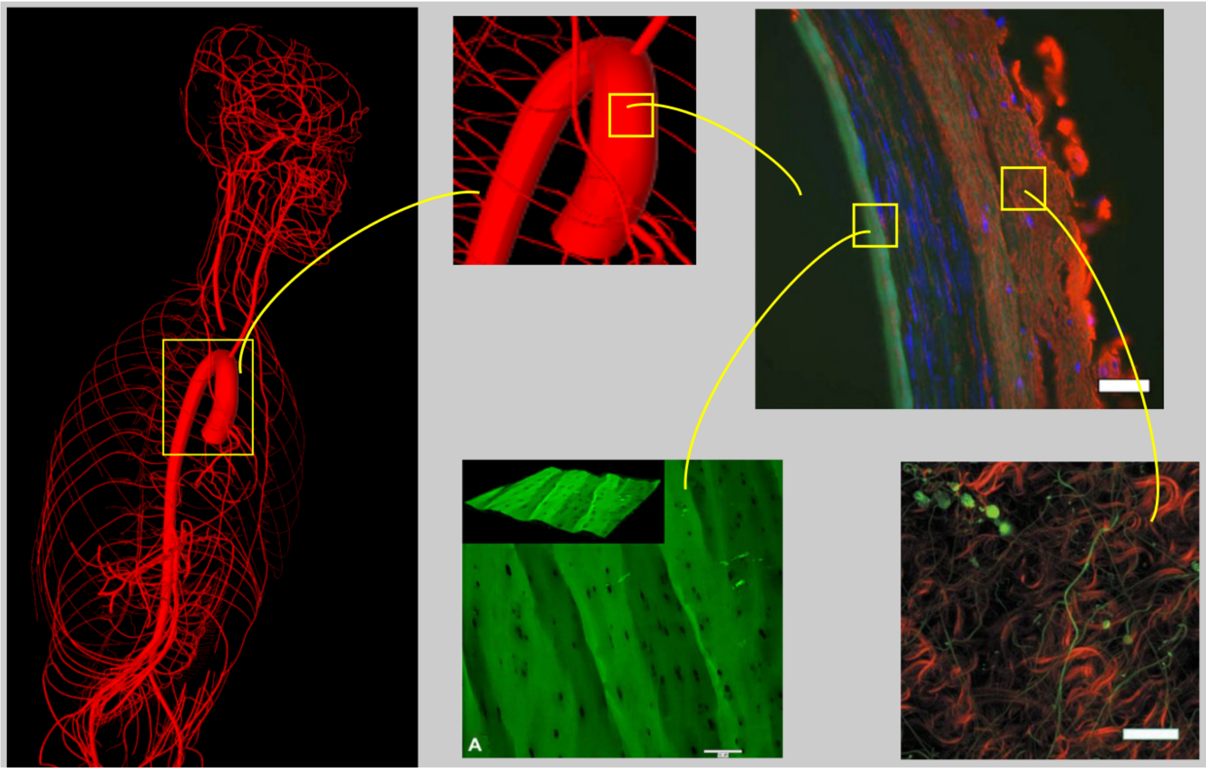

Figure 2 – Overview of several spatial scales in the cardiovascular system. Images extracted from the Adan-Web (http://hemolab.lncc.br/adan-web/) and asked for permission from (ROBERTSON; WATTON, 2013).

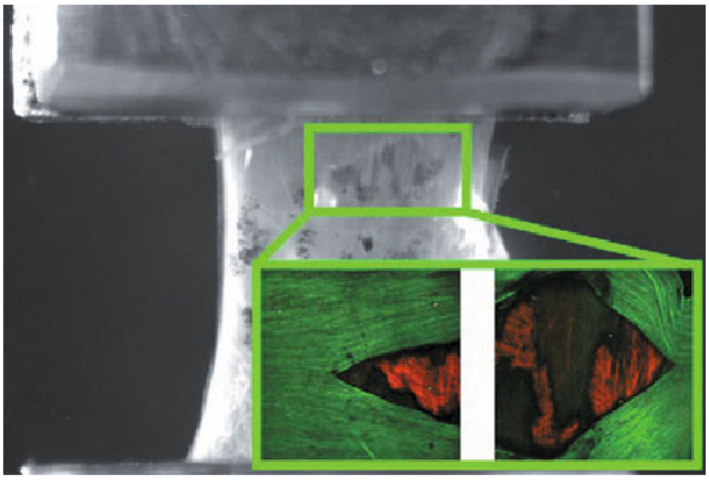

Figure 3 – Arterial tissue rupture (asked for permission from (ROBERTSON; HILL; LI, 2012)).

1.3 On multiscale theories

Nowadays, in order to reach a deeper description of the reality, most of the areas of science involving complex material behavior as well as multi-physics phenomena needs to resort at some point to multiscale modelling techniques. This is motivated by the profound insight about the interplay between observable (macroscale) response and underlying (microscale) physical mechanisms enabled by these techniques, and also by the increasing availability of computational resources (which enable expensive simulations). From the vast number of multiscale methodologies, this thesis focus on a specific class of procedures which rely on the formulation (and solution) of an equilibrium problem at a smaller scale, or simply microscale, and also on the transfer of information between scales through proper insertion and homogenisation formulae. Since the microscale domain, also called microcell, is intended to be as representative as possible, these approaches can be termed as Representative Volume Element (RVE)-base multiscale models. Such literature is vast dating back to the mid of last century (HILL, 1965; MANDEL, 1972) and have been successfully applied in many areas, such as heat transfer (ÖZDEMIR; BREKELMANS; GEERS, 2008), solid mechanics (FEYEL; CHABOCHE, 2000a; MICHEL; MOULINEC; SUQUET, 1999; MIEHE; SCHOTTE; SCHROEDER, 1999; NEMAT-NASSER, 1999), including plasticity (MCDOWELL, 2010), thermoelasticity (BLANCO; GIUSTI, 2014; TEMIZER; WRIGGERS, 2011), material failure (BELYTSCHKO; SONG, 2010; BELYTSCHKO; LOEHNERT; SONG, 2008; SÁNCHEZ et al., 2013; TORO et al., 2014), biomechanics (PAHR; ZYSSET, 2008; SPEIRS; NETO; PERIĆ, 2008; ROCHA et al., 2018), as well as in the field of fluid mechanics (BLANCO; CLAUSSE; FEIJÓO, 2017; SANDSTRÖM; LARSSON, 2013), just to cite few instances. Out of the scope of this thesis, another important lineage of multiscale theories is that based on the asymptotic analysis of partial differential equations with periodic coefficients in the modelling of periodic media, initiated by the landmark contributions of (BENSOUSSAN; LIONS; PAPANICOLAOU, 1978) and (SANCHEZ-PALENCIA, 1980).

It is important to remark that, in order to improve their predictive capacities, phenomenological models make use of two alternative paths: (i) to increase the number of kinematical descriptors (enhanced theories of continuum media) or (ii) to increase the number of internal variables that define the material constitutive response. In the first case, the resultant mechanical model, along with its underlying thermodynamics restrictions, becomes very complex. In the second case, a great number of material parameters need to be adjusted/characterised from experimental tests. As already commented, a natural choice to overcome the drawbacks inherent to phenomenological models is the explicit modelling of the mechanical interactions between basic components of the tissues, through RVE-based strategies. In biological tissues, this aspect is even more important given the current limitations to perform most of the experiments *in-vivo*. In fact, other experimental observations are still needed, as those from the microstructure of the arterial wall obtained from techniques such as multiphoton microscopy, as seen in Fig. 2, available in (ROBERTSON; WATTON, 2013) and references therein, for example. However, we claim that if this kind of enriched information is available, it could be integrated into the model in order to deliver more reliable predictions.

In the selection of a particular multiscale model, two aspects, which affect its predictive capabilities, must be taken into account: i) the definition of the morphology that shapes the RVE, and ii) the definition of the boundary conditions to be applied at the microscale model. In fact, aspects i) and ii) are not totally independent from each other, since the more suitable the boundary conditions, the smaller the size required for the microcell, to be regarded as a RVE, and vice-versa. To be rigorous, the use of the term RVE is inappropriate before performing a rigorous statistical analysis (KANIT et al., 2003; KHISAEVA; OSTOJA-STARZEWSKI, 2006). In fact, the RVE is very clearly defined in two situations only, as stated in (KHISAEVA; OSTOJA-STARZEWSKI, 2006): i) a unit cell in a periodic microstructure, and ii) a volume containing a very large (mathematically infinite) set of microscale elements. Neither of these two assumptions are valid for the problems of this thesis, however we will use the term RVE, sometimes as an abuse of language, even lacking a rigorous statistical analysis.

Regarding the morphology of the RVE for porous materials, we can split these morphologies in three categories: i) RVEs in which voids are confined to the interior of the microscale domain, i.e., voids not reaching the RVE boundary; ii) RVEs with voids reaching the RVE boundary in a structured, periodic pattern and iii) RVEs with voids reaching the RVE boundary following a random pattern. Multiscale models for the group i) and ii) have been consistently formulated, largely tested and widely understood. For case of materials featuring randomly distributed voids or even materials with very high porosity, it is almost impossible to fit those materials in either case i) or ii). In turn, case iii) has not received the same attention by the related literature. The utilisation of the very same concepts borrowed from case i) and ii) to the more complicated situation of case iii) may yield results which are, at least, questionable from the mathematical/physical point of view. Therefore, if we regard the fibrous material as a special case of porous materials with low volume fraction, and thus case iii), a consistent multiscale model to deal with porous continua containing voids reaching the RVE boundary should be formulated properly. Actually this is one of the goals of this thesis (see Section 1.6).

Concerning the choice of the boundary conditions, there is a first fundamental step to overcome. This is related with the definition of lower and upper bounds within which the homogenised material behavior, retrieved from the multiscale model, is expected to be placed. The upper bound for the effective material response (in the sense of the stiffest response) is given by the so-called Taylor model, or also known as mixture model, where the kinematics at microscale is fully prescribed given the macroscale kinematics. This is the situation of maximally constrained kinematics. In turn, the lower bound is the model that features the weakest response measured in some sense, which corresponds to the situation of minimally constrained kinematics at microscale. Actually, it will be seen in this thesis that the determination of the least constrained boundary condition is not a trivial task for the RVEs of the category iii) of the previous paragraph. Notwithstanding, the methodology to be adopted in this thesis (see Section 1.5) provides the necessary tools to derive the minimal admissible kinematical restrictions.

Finally, in contrast to the development of multiscale models for complex materials, whose literature is vast and dates back to the mid of last century (HILL, 1965; MANDEL, 1972), the development of multiscale models for biological tissues has a recent history. Although the natural and increasingly pressing motivation for using multiscale models, there are still many barriers to be overcome before the proliferation of multiscale models in biomechanics. Among these barriers we mention the complexity and computational cost involved in dealing with such multiscale strategies and also empirical issues. In any case, multiscale modelling, which is extremely effective and widely spread in other areas, constitutes the future of material modelling also in the case of living tissues. Up to now, there are really few contributions in biomechanics of soft tissues making use of multiscale methodologies. In fact, and thinking in tissues whose microstructure is made up of fibres, this problem implies the integration between a macroscale continuum mechanical models and microscale fibrous (i.e. discrete) models (STYLIANOPOULOS; BAROCAS, 2007a; STYLIANOPOULOS; BAROCAS, 2007b; SPEIRS; NETO; PERIĆ, 2008; BERKACHE et al., 2017; NADY; GODA; GANGHOFFER, 2016; NADY; GANGHOFFER, 2016), which also comprises the proper characterisation of admissible microscale boundary conditions. In this regard, the present thesis features several scientific contributions to the field (see Section 1.6). Additional literature concerning fibres networks will be considered next in Section 1.4.

1.4 Multiscale approaches for fibre networks

In the last years, current imaging technologies have provided a staggering amount of data to drive the construction and validation of mathematical models featuring increasingly complex descriptive capabilities (STEIN et al., 2008). In this direction, novel experimental settings have enable scientists to study the refined mechanical response of individual collagen fibres or even fibrils, including the mechanisms that lead to the rupture of such components (BLANCO; POLINDARA; GOICOLEA, 2015; ZITNAY et al., 2017).

Up to the authors' knowledge, very few works considered multiscale methodologies to model the material response of a network of fibres in biological tissues. For instance, the work of (SPEIRS; NETO; PERIĆ, 2008) aimed at fitting parameters of some classical strain energy functions by means of homogenisation and optimisation of a multiscale model composed by a continuum matrix of material (representing the elastin content) reinforced with a set of discrete trusses elements representing the collagen fibres. However, and because of the existence of a background continuum elastin matrix, this multiscale approach was entirely based on standard continuum mechanics methods, and no reference to the discrete nature of the fibres network was made.

In the works by (CHANDRAN; BAROCAS, 2007; STYLIANOPOULOS; BAROCAS, 2007a; STYLIANOPOULOS; BAROCAS, 2007b) the so-called collagen hyperelastic network approach is presented and applied in the multiscale analysis of the arterial tissue. These works postulate the homogenisation for the stress measure based on a continuum-like homogenisation procedure, but no detailed discussion about the connection of kinematical descriptors between scales, as well as boundary conditions other than the linear boundary displacement constraint is mentioned. Following a similar approach, although relying on an infinitesimal strain model for individual collagen fibres and also suffering from the same drawbacks than works previously cited in this paragraph, the contributions by (THUNES et al., 2016; THUNES et al., 2018) show interesting predictive capabilities, and considerable advances were achieved towards correlating experimental data of human aorta. Pursuing a different approach, (WITTHOFT et al., 2016) makes use of DFD (Dissipative Particle Dynamics) to model multi-constituent arterial tissues.

Dealing with multiscale methods based on asymptotic analysis and generalised non-Cauchy continuum applied to fibre networks, the recent works of (BERKACHE et al., 2017; NADY; GODA; GANGHOFFER, 2016; NADY; GANGHOFFER, 2016) present important contributions, the later being in the domain of textiles, and including inter-fibre contact. These works are based on a more general procedure published independently by (CAILLERIE; MOURAD; RAOULT, 2003) and (WARREN; BYSKOV, 2002), the so-called discrete homogenisation (in short DH). Importantly, the DH method is restricted to periodic conditions.

Concerning size-effects of the RVE, (BERKACHE et al., 2017; SHAHSAVARI; PICU, 2013) perform convergence analyses of their models and both conclude in favour of the fundamental role played by different boundary conditions in the context of fibre networks. Notwithstanding this, both methodologies fail to provide a clear derivation and interpretation of those boundary conditions. In this direction, this thesis will considerably expand the understanding on this matter by pursuing a multiscale approach based on the Hill-Mandel principle (see Sections 1.6 and 1.5). Also considering the role played by RVE boundary conditions, but not in a context of fibre networks, the work of (CARNIEL; KLAHR; FANCELLO, 2019) presents interesting results for the problem of helically collagen fibres embedded in a softer matrix, by extending the approach of (CARNIEL;

FANCELLO, 2018) applied for the modelling of tendon tissues.

Despite the strides made in this field, the bottom-line mechanisms unfolding in the smallest spatial scales and that lead to the occurrence of large scale mechanical conditions for failure to occur have remained poorly understood. On the one side, this is because the problem poses formidable challenges from the experimental perspective. In fact, the observation and tracking of failures in the small scale tissue constituents, while the tissue specimen is being stretched, is beyond the limits of current technologies, as pointed out recently in (SANG et al., 2018).

In the previous context, the development of mathematical models acquires an even more fundamental character as a rational strategy to guide research in the field. The construction of proper constitutive models based on a multiscale approach provides a natural path to bridge observable rupture phenomena and substratum deterioration. Through such models, it could be possible to provide a typification of the fundamental ingredients responsible for the irruption of a macroscale failure and the softening of individual tissue constituents, that is collagen fibres, delivering a controlled in-silico experimental laboratory to test hypotheses.

The loss of strong ellipticity condition (RICE, 1976), in many cases, visibly coincides with the instant of definition of a strain localisation pattern at the microscale level. Although strain localisation is a quite well documented phenomenon in mechanics (e.g (BIGONI, 2012)), to the authors' knowledge, contributions concerning such study for the material response of fibrous tissues within a multiscale paradigm have not been addressed. We must mention the works of (VANDERHEIDEN; HADI; BAROCAS, 2015; HADI; SANDER; BAROCAS, 2012; SOZUMERT et al., 2018; DEOGEKAR; PICU, 2018) where effect of damaging of fibres has been introduced in a discrete model, but have let the strain localisation and material instability phenomena cursorily analysed. Importantly, the observation of this event is particularly possible if sufficiently generic boundary conditions are available. In this context, the admissible kinematical constraints derived in this thesis will be shown to be of special interest.

In a more general context of material modelling using computational mechanics, not a considerable number of attempts have been made to couple discrete mechanical interactions with continua in a multiscale setting. We highlight the works of (MIEHE; DETTMAR, 2004; MIEHE; DETTMAR; ZAH, 2010), which addressed the homogenisation of a granular microstructure to retrieve standard measures of internal stresses in the material. Other works regarding the homogenisation of atomistic and molecular dynamics interactions are reported in (DAVYDOV; PELTERET; STEINMANN, 2014; STEINMANN; RICKER; AIFANTIS, 2011; LI; E, 2005; LI; URATA, 2016) and in the realm of multiscale modelling of the paper an example is (BOSCO et al., 2017). In fact, in spite of the existence of previous works in this direction, up to the authors' knowledge there is no well-established approach to couple such problems of distinct kinematics between the scales. In this regard, this thesis provides some valuable ingredients to drive the construction of other discrete-continuum models, other than those based in fibres networks.

1.5 Methodology

Towards the construction and full characterisation of a multiscale model, the first challenge lies in the consistent information exchange between scales. Such process implies to characterise the multiscale model in terms of kinematical homogenisation, microscale equilibrium problem and generalised stress-like homogenisation. This problem will be addressed, within the unified framework coined as Method of Multiscale Virtual Power (MMVP), in (BLANCO et al., 2014; BLANCO et al., 2016), providing the basic principles and axiomatic steps to build mechanically coherent multiscale models. Such approach is formulated on the light of variational formulations derived from the Principle of Virtual Power (PVP) (GERMAIN, 1972; MAUGIN, 1980), in which the MMVP can be viewed as an extended format of the PVP suitable to address physical problems in multiscale scenarios.

The main aspect of such theory that justifies its utilisation, as usual in variational formulations, is that it provides a rational justification of classical formulations and facilitates the rigorous construction of new multiscale models in a systematic, well-defined steps. The MMVP, relies on three steps, namely: i) the definition of kinematics at each scale, and the proper transfer of kinematical descriptors between scales, ii) the use of duality arguments to introduce the stress measures as dictated by the virtual power functionals at both scales, and iii) the formulation of the Principle of Multiscale Virtual Power (PMVP), which ensures the physical consistency between scales. This approach was adopted because it is a general methodology that, following well-defined steps, allows to construct new multiscale models based on a minimum set of assumptions. Furthermore, these guidelines lead naturally to a minimal set of kinematical constraints, and thus it is valuable to establish lower bounds for the mechanical response, whose importance was already pointed out in Section 1.3. A deeper presentation of the MMVP is given in Chapter 2.

Moreover, it is worth mentioning that the MMVP has been succesfully applied in a number of different multiscale problems such as the analysis of solid mechanics with microscale inertial effects (NETO et al., 2015); in the connection between second order continua and classical continuum mechanics models (BLANCO et al., 2016), in fluid mechanics (BLANCO; CLAUSSE; FEIJÓO, 2017), thermoelasticity (BLANCO; GIUSTI, 2014) and also to tackle multiscale material failure (SÁNCHEZ et al., 2013; TORO et al., 2014; TORO et al., 2016; TORO et al., 2016).

Finally, concerning the failure and strain localisation detection, this is performed exploiting the method of discontinuous bifurcation analysis (RICE, 1976), in which the so-called acoustic tensor, which is a function of the homogenised constitutive tangent tensor given by the MMVP, is evaluated to detect the loss of strong ellipticity condition.

1.6 Main objectives

Based on the above considerations, this thesis deals with the construction of a multiscale model to characterise the macroscale constitutive behaviour of a fibrous material featuring a discrete microstructure (i.e., a network of collagen fibres) aiming at the detection of failure and strain localisation phenomena. To reach this general goal, we propose the following steps in the form of intermediate goals:

1. As already pointed out in Section 1.3, to drive the construction of the fibre network model, a generalisation of the classical multiscale theory for solids in finite strain regime, that enables the analysis of RVEs with a random distribution of voids, is required. Importantly, the main goal of this step is to develop a truly Minimally Constrained Kinematical Multiscale Model (the MCKMM model) for such kind of RVEs by using the MMVP. As a consequence of the formulation, the proposed MCKMM corresponds to a model with a uniform traction acting over each solid boundary with constant normal vector.

2. Given that a consistent multiscale model for the porous RVEs has been established in the previous step, this step aims at the construction of the multiscale model featuring a classical finite strain solid at macroscale and a discrete network of fibres at the microstructure. This is accomplished by regarding a fibrous RVE as a special case of a fenestrated RVE and then proceed by performing an adequate continuum-to-discrete transition, which, in the end, results in a multiscale model with a fully discrete kinematics at the microscale. Hence, a discrete version for the MCKMM is derived here.

3. The final goal is, on the light of the discrete model derived in the previous step, to investigate the impact that softening fibres in the discrete microscale domain have on the homogenised macroscale response. The critical point, that characterises the macroscale failure initiation, is detected using the discontinuous bifurcation analysis (RICE, 1976). As a subproduct of this process, the microscale failure pattern, i.e., unit normal and crack-opening vectors, shall be determined.

1.7 Scientific Contributions

During the period of the doctorate program, comprised between March 2015 and April 2019, the following scientific reports were elaborated in the context of the thesis:

Full-length articles in journals : Among published, submitted and being revised papers, we have:

- Felipe Figueredo Rocha, Pablo Javier Blanco, Pablo Javier Sánchez, and Raúl Antonino Feijóo. Multi-scale modelling of arterial tissue: Linking networks of fibres to continua. *Computer Methods in Applied Mechanics and Engineering*, 341:740–787, 2018
- Felipe Figueredo Rocha, Pablo Javier Blanco, Pablo Javier Sánchez, Eduardo de Souza Neto, and Raúl Antonino Feijóo. Multiscale modelling of damage-driven strain localisation in fibrous tissues (under review). *Journal of the Mechanics and Physics of Solids*, 2019.
- Pablo Javier Blanco, Pablo Javier Sánchez, Felipe Figueredo Rocha, Sebastián Toro, and Raúl Antonino Feijóo. A consistent multiscale mechanical formulation for media with randomly distributed voids (in submission). *Computer Methods in Applied Mechanics and Engineering*, 2019.

Full-length articles in conferences :

- F.F. Rocha, P.J. Blanco, R.A. Feijóo, P.J. Sánchez, and A.E. Huespe. A multiscale approach to model arterial tissue. *In Ibero-Latin American Congress on Computational Methods in Engineering* (CILAMCE), Rio de Janeiro, 2015. Anais do XXXVI Congresso Ibero-Latino-Americano de Métodos Computacionais em Engenharia.

Extended abstracts in conferences :

- F.F. Rocha; P.J. Blanco ; P.J. Sánchez; R.A. Feijóo. On the constitutive modeling for fibrous tissues. In: International Conference on Computational and Mathematical Biomedical Engineering, 2017, Pittsburgh. International Conference on Computational and Mathematical Biomedical Engineering Proceedings, 2017.

Abstracts in conferences :

- P.J. Blanco, P.J. Sánchez, F.F. Rocha, Toro, S.; R.A. Feijóo. Multiscale formulation for materials with randomly distributed voids: minimally constrained and more restrictive multiscale sub-models. In: XII Argentine Congress on Computational Mechanics, 2018, San Miguel de Tucumán. Mecánica

Computacional. Santa Fé: Asociación Argentina de Mecánica Computacional, 2018. v.XXXVI. p.1683 - 1683

- F.F. Rocha; P.J. Blanco; de Souza Neto, E.; P.J. Sánchez, R.A. Feijóo. Towards post-critical multiscale modelling of damage in biological fibrous tissues. In: XII Argentine Congress on Computational Mechanics, 2018, San Miguel de Tucumán. Mecánica Computacional. Santa Fé: Asociación Argentina de Mecánica Computacional, 2018. v.XXXVI. p.1875 - 1875
- F.F. Rocha, P.J. Blanco, P.J. Sánchez, R.A. Feijóo. A Multiscale Approach to Study Softening Mechanisms in Arterial Tissue In: EMI2017-IC - 2017 EMI International Conference, 2017, Rio de Janeiro. EMI2017-IC - 2017 EMI International Conference Proceedings. , 2017.
- Toro, S., F.F. Rocha, P.J. Sánchez, P.J. Blanco, A.E. Huespe, R.A. Feijóo. Modelado Multiescala de Materiales: Análisis de Condiciones de Borde en Micro-Estructuras con Poros y/o Inclusiones que Alcanzan la Frontera del RVE In: Congreso sobre Métodos Numéricos y sus Aplicaciones, 2017, La Plata. Anais do ENIEF 2017. La Plata: Asociación Argentina de Mecánica Computacional, 2017. v.XXXV. p.1309 -1309

1.8 Organisation

This thesis is divided in 6 chapters (without considering the introduction), briefly described below:

- **Chapter 2) Variational Foundations of Multiscale Models:** In this chapter we review the Method of Multiscale Virtual Power (MMVP) (BLANCO et al., 2014; BLANCO et al., 2016), which is the basic tool used throughout this thesis, already introduced in Section 1.3. Importantly, the abstract theory is applied to the classical multiscale model for solid mechanics, which introduces the standard model of class of problems that this thesis addresses, i.e., the ones in the field of solid mechanics. By including this chapter, our intention is to maintain this thesis as self-contained as possible.
- **Chapter 3) A Consistent Multiscale Model for Solids with Voids reaching Boundary:** This chapter presents the developments associated with the intermediate goal 1) of Section 1.6.
- **Chapter 4) Linking Networks of Fibres to Continua:** Here, we develop the multiscale model for network of fibres, which consists in the intermediate goal 2) of Section 1.6.

- **Chapter 5) Damage Modelling and Failure Detection in Fibrous Materials:** The intermediate goal 3) of Section 1.6 is addressed in details in this chapter.

- **Chapter 6) Numerical Experiments:** Through a set of relevant numerical experiments, in this chapter we demonstrate the potentialities of the framework developed in Chapter 4 and Chapter 5.

- **Chapter 7) Conclusion:** Finally, this chapter is dedicated to the final discussions of the most relevant aspects approached in this thesis. Also, some future lines of research is introduced.

The suggested reading path is the traditional top-down approach, given that the chapters, and section therein, have a clear relation of dependency with the previous ones. The only two exceptions are Section 2.4, which can be skipped in a first reading, and also Chapter 6, in which Section 6.1 can be read right after Chapter 4 for the reader eager to jump into the analysis of some numerical examples.

Note that the three main theoretical cornerstones of the thesis, tackling each one of the major goals established in Section 1.6, are respectively mapped in Chapters 3, 4 and 5. Accordingly, these chapters are associated to the three full-length journal articles of Section 1.7.

2 Variational Foundations of Multiscale Models

...the whole burden of philosophy seems to consist in this - from the phenomena of motions to investigate the forces of nature, and then from these forces to demonstrate the other phenomena.

Isaac Newton (Preface to the first edition of the Principia, 1685).

This chapter aims to describe the basic tools for the multiscale modelling of a physical problem in the context of variational formulations. To reach this goal, we decided to follow a strategy that goes from general setting to specific applications. Considering this, the chapter is divided into three parts. First, Section 2.1 is devoted to presenting in abstract form the standard procedure for modelling a generic physical problem via variational formulations by using the well-known Principle of Virtual Power (GERMAIN, 1972; MAUGIN, 1980). The former section serves as a basis to understand the Method of Multiscale Virtual Power (MMVP) (BLANCO et al., 2014),(BLANCO et al., 2016), which is reviewed in Section 2.2. Finally, in Section 2.3, the MMVP is invoked to model the classical multiscale model for continuum solid mechanics in finite strain regime in a classical setting. The reason for that are twofold: i) exemplify the use of the MMVP in a concrete modelling scenario and ii) provide a basis in which non-standard models is build upon, as example of Chapter 3. Also in the same section, we address more advanced topics such as: the variational treatment for incompressible materials, linearisation of the nonlinear problem for Newton-Raphson procedure, and the macroscale constitutive tangent derivation together with the analysis of its symmetries. These topics are useful for the thesis but are not contemplated in the remaining chapters.

It is worth mentioning that the choice of presenting the abstract formulation is not only aiming to formulate the model in Section 2.3, but is specially useful for the derivation of non-standard models in chapters 3 and 4, providing a sound systematic framework for deriving multiscale theories as well as simplifying the presentation of the following applications.

Note that throughout this section, a basic knowledge of continuum mechanics is assumed. For a reader interested in reviewing these concepts we refer to the classical books (GURTIN, 1981; OGDEN, 1984) but also to the more recent presentation of (HOLZAPFEL, 2000).

2.1 Method of Virtual Power

In this section we present the framework for modelling physical phenomena using the method of virtual power in the context of single scale problems. The generalisation for multiscale problems is considered next in Section 2.2.

2.1.1 Kinematics

Let Ω be a geometrical bounded domain that stands for the configuration occupied by the body $\mathcal{B}$ in which the physical problem to be modelled is defined. Let $\mathbf{x} \in \Omega$ be a point in such domain Ω. The so-called *generalised displacements* u is an entity capable to describe the kinematics (also understood in a generalised sense) of the entire physical model. Depending on the nature of the problem u may assume different representations, e.g., scalar field, vector field, tensor field, or even n-tuples of possible different kind of fields in multi-field problems. Also, these fields are defined in subdomains of Ω (including the case of the entire domain). Mathematically, let us say that u belongs to a space $\mathscr{U}$ that encloses in its definition the adequate representation chosen for modelling a given problem. Also, depending on physical restrictions (e.g. boundary conditions, incompressibility) we may be interested in solutions belonging to a subset of $\mathscr{U}$, let us say $\mathrm{Kin}_{\mathscr{U}} \subset \mathscr{U}$. The set $\mathrm{Kin}_{\mathscr{U}}$ is the set of *kinematically admissible generalised displacements.* Associated to $\mathrm{Kin}_{\mathscr{U}}$, we can define the space of *kinematically admissible generalised virtual actions* as:

$$\mathrm{Var}_{\mathscr{U}} = \{\hat{u} \in \mathscr{U}; \hat{u} = u_1 - u_2; u_1, u_2 \in \mathrm{Kin}_{\mathscr{U}}\}. \tag{2.1}$$

Another important kinematical concept is the *generalised strain*, denoted by $D \in \mathscr{E}$, being $\mathscr{E}$ its corresponding vector space. Similar to u, D may admit very general descriptors, and in general can be understood as a collection of them, which are also defined on subdomains of Ω.

Relating $\mathscr{U}$ and $\mathscr{E}$, there is the so-called *generalised strain rate* operator $\mathcal{D}$ defined as:

$$\begin{aligned} \mathcal{D} :& \mathscr{U} \to \mathscr{E} \\ & u \mapsto D = \mathcal{D}(u). \end{aligned} \tag{2.2}$$

In particular an element $D \in \mathscr{E}$ is said to be *kinematically compatible* if there exist $u \in \mathscr{U}$ such that $D = \mathcal{D}(u)$. Accordingly, for a virtual action $\hat{u}$, we have $\hat{D} = \mathcal{D}(\hat{u})$. The kernel of the operator $\mathcal{D}$, i.e. $\mathrm{Ker}(\mathcal{D}) \subset \mathscr{U}$ (recalling $\mathrm{Ker}(\mathcal{D}) = \{u \in \mathscr{U}; \mathcal{D}(u) = 0\}$), is an important concept to be explored next whose elements are called *rigid generalised displacements.*

2.1.2 Mathematical Duality

The other concept necessary to completely set the physical model is the postulation of two linear functionals, related to the spaces $\mathscr{U}$ and $\mathscr{E}$, known as *external* and *internal*

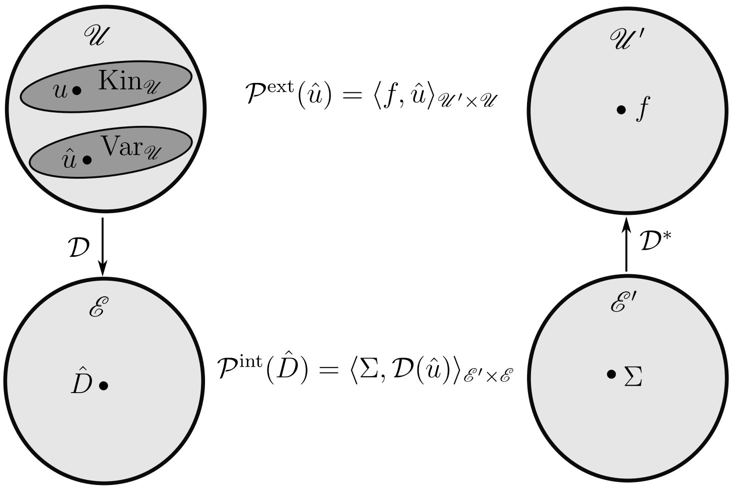

Figure 4 – Duality diagram for the principle of virtual power in single scale.

virtual power functionals respectively. Since, by hypothesis, these functional are linear, they admit representation in the form of duality products as follows

$$\mathcal{P}^{\text{ext}}(u) = \langle f, u\rangle_{\mathscr{U}'\times\mathscr{U}}, \tag{2.3}$$

$$\mathcal{P}^{\text{int}}(D) = \langle \Sigma, D\rangle_{\mathscr{E}'\times\mathscr{E}}, \tag{2.4}$$

where the dual element $f \in \mathscr{U}'$ is so-called *generalised external forces* and $\Sigma \in \mathscr{E}'$ the *generalised internal stress*. Evaluation of $\mathcal{P}^{\text{int}}$ is restricted to admissible strain rates, i.e., $\mathcal{P}^{\text{int}}(\mathcal{D}(\hat{u}))$ with $\hat{u} \in \text{Var}_{\mathscr{U}}$. Therefore, by using the so-called *adjoint operator* $\mathcal{D}' : \mathscr{E}' \to \mathscr{U}'$, we can identify the admissible external forces for the model as the element $f = \mathcal{D}'(\Sigma) \in \mathscr{U}'$, such that

$$\mathcal{P}^{\text{int}}(\mathcal{D}(\hat{u})) = \langle \Sigma, \mathcal{D}(\hat{u})\rangle_{\mathscr{E}'\times\mathscr{E}} = \langle \mathcal{D}'(\Sigma), \hat{u}\rangle_{\mathscr{U}'\times\mathscr{U}} = \langle f, \hat{u}\rangle_{\mathscr{U}'\times\mathscr{U}} \quad \hat{u} \in \text{Var}_{\mathscr{U}}. \tag{2.5}$$

Additionally, also from (2.5), admissible external $f \in \mathscr{U}'$ are such that:

$$\langle f, \hat{u}\rangle_{\mathscr{U}'\times\mathscr{U}} = 0 \quad \hat{u} \in \text{Var}_{\mathscr{U}} \cap \text{Ker}(\mathcal{D}) \tag{2.6}$$

In other words $f \in (\text{Var}_{\mathscr{U}} \cap \text{Ker}(\mathcal{D}))^{\perp}$. For an overview of the whole picture of relations between spaces see Fig. 4.

Remark 1 *The difference between internal and external virtual power is normally referred to in the literature as the so-called total virtual power defined as*

$$\mathcal{P}^{\text{tot}}(u, D) = \mathcal{P}^{\text{int}}(D) - \mathcal{P}^{\text{ext}}(u). \tag{2.7}$$

2.1.3 Principle of Virtual Power

The Principle of Virtual Power (PVP) is the variational statement of the physical problem that tells us about the criterion under which a system is at equilibrium, and it is enunciated as follows:

Principle 1 (Principle of Virtual Power) *Let $f \in \mathscr{U}'$ be an admissible external force, it is said that $\Sigma \in \mathscr{E}'$ is equilibrated if the following variational equation holds*

$$\mathcal{P}^{\text{int}}(\mathcal{D}(\hat{u})) = \mathcal{P}^{\text{ext}}(\hat{u}) \qquad \forall \hat{u} \in \text{Var}_{\mathscr{U}}, \tag{2.8}$$

or equivalently

$$\langle \Sigma, \mathcal{D}(\hat{u}) \rangle_{\mathscr{E}' \times \mathscr{E}} = \langle f, \hat{u} \rangle_{\mathscr{U}' \times \mathscr{U}} \qquad \forall \hat{u} \in \text{Var}_{\mathscr{U}}. \tag{2.9}$$

Remark 2 *In this work we are interested in a common particular case of the Principle 1 in which the generalised internal stress state depends on the history of some (possibly non-linear) generalised strain measure through a given constitutive functional. Let $\mathcal{G} : \mathscr{U} \to \mathscr{E}$ be this generalised strain measure, then $\Sigma = \Sigma(\mathcal{G}^t)$, where $\mathcal{G}^t$ is the history of $\mathcal{G}$ up to a time t that implicitly depends on history of the generalised displacements u^t, i.e., $\mathcal{G}^t = \mathcal{G}(u^t)$. Note that for sake of simplicity no distinction of notation was made between the object and the associated functional. It is worth mentioning that solution of (2.8) in this scenario consists in finding $u \in \text{Kin}_{\mathscr{U}}$ such that (2.9) holds, for the corresponding Σ. Finally, specification of $\mathcal{G}$ naturally induces the strain rate operator as the tangent of this possibly non-linear measure of generalised strain, i.e., by the Gâteaux derivative $\mathcal{D}(\hat{u}) := \left.\dfrac{\mathrm{d}}{\mathrm{d}\tau}\mathcal{G}(u + \tau\hat{u})\right|_{\tau=0}$.*

2.2 Method of Multiscale Virtual Power

The derivation of a multiscale model using the the Method of Multiscale Virtual Power (MMVP) is based on three fundamental concepts described next, following (BLANCO et al., 2014; BLANCO et al., 2016).

1. *Kinematical Admissibility.* The kinematics for both macro and microscale must be first defined, which amounts to define the kinematical descriptors at each scale together with the *generalised gradient* operators. Connection between the scales is established through (i) the *insertion* of macroscale entities into the microscale kinematics and (ii) the *homogenisation* of microscale entities to render corresponding macro-scale kinematical descriptors. The macroscale and the microscale kinematics, and the connection between them in terms of insertion and homogenisation operations are developed in detail in Section 2.3.2. Moreover, the role of the homogenisation operations is to provide an unambiguous set of rules to define constraints for the kinematical descriptors at the microscale, avoiding thus ad-hoc considerations.
2. *Mathematical Duality.* The postulation of the virtual power functionals for each scale is the second step. This amounts to characterise, as power-conjugates to kinematical descriptors, the dual force- and stress-like entities. These entities are thus compatible with the kinematics in each scale. The macro- and microscale

virtual power functionals, which play a key role in the multiscale power balance, are introduced in Section 2.2.3.

3. *Principle of Multiscale Virtual Power* (PMVP). This principle consists in a variational statement and generalisation of the Hill-Mandel Principle of Macrohomogeneity (HILL, 1965; MANDEL, 1972), where the postulated virtual power functionals defined in the different scales are equated. From this principle, the microscale equilibrium problem and the homogenisation formula for the stress measure are derived using variational arguments. The PMVP is developed in Section 2.2.4.

The present work takes advantage of the possibility offered by the MMVP to deal with kinematics at the macroscale and microscale in a systematic form, to be explored in the next chapters.

2.2.1 Multiscale Kinematics

It was seen in Section 2.1.1 the abstract kinematical setting in the context of variational formulations of a single scale physical model. We will reutilise as much as possible the same notation in order to set the multiscale kinematics avoiding repetition of concepts. First, we describe the macro and microscale kinematics independently (as in a single problem) and secondly the apropriate link between both scales is given in Section 2.2.2, as part of the Kinematical Admissibility step for the construction of the model following the MMVP (BLANCO et al., 2014; BLANCO et al., 2016).

2.2.1.1 Macroscale Kinematics

Keeping analogy with the notation defined in Section 2.1.1, but adding a subscript $(\cdot)_M$ whenever necessary, at the macroscale we define Ω_M, $\mathscr{U}_M$, $\mathscr{E}_M$, $\mathrm{Kin}_{\mathscr{U}_M}$ (and consequently $\mathrm{Var}_{\mathscr{U}_M}$) and $\mathcal{D}_M$. We also have $u_M \in \mathscr{U}_M$ and $D_M \in \mathscr{E}_M$, generalised macroscale displacements and strain rates respectively. Points in Ω_M are denoted by $\mathbf{x}_M$ and it is interesting to denote point-valued objects as $u_M|_{\mathbf{x}_M} = u_M(\mathbf{x}_M)$ and $D_M|_{\mathbf{x}_M} = D_M(\mathbf{x}_M)$. Let us denote as $\mathbb{R}^{\mathbf{x}_M}_{\mathscr{U}_M}$ and $\mathbb{R}^{\mathbf{x}_M}_{\mathscr{E}_M}$ the sets in which $u_M|_{\mathbf{x}_M}$ and $D_M|_{\mathbf{x}_M}$ live, respectively. In a given $\mathbf{x}_M \in \Omega_M$ the microscale kinematics is defined as next.

2.2.1.2 Microscale Kinematics

In the similar fashion as for the aforementioned macroscale kinematics setting, we also admit the existence of Ω_μ, $\mathscr{U}_\mu$, $\mathscr{E}_\mu$, and $\mathcal{D}_\mu$, partially defining the microscale kinematics. Points in the RVE domain Ω_μ are denoted by $\mathbf{x}_\mu$. As usual, we have the *generalised microscale displacements* $u_\mu \in \mathscr{U}_\mu$ and *generalised microscale strain rates* $D_\mu \in \mathscr{E}_\mu$. It is worth mentioning that the definition of sets, spaces and operators in microscale is independent to the ones defined for macroscale, i.e., in other words, microscale and macroscale kinematics can be modelled differently.

Note that the missing components to complete the characterisation of the kinematics in microscale are the necessary physical constraints to define $\mathrm{Kin}_{\mathscr{U}_\mu}$ (and consequently $\mathrm{Var}_{\mathscr{U}_\mu}$). This is a matter of the kinematical admissibility step, subject of Section 2.2.2.

2.2.2 Kinematical Admissibility

So far, the kinematics groundwork has been established for both scales separately. Now, it is necessary to define mappings of the macro-scale kinematics at a given macro-scale point $\mathbf{x}_M$ and the microscale kinematics at the corresponding RVE. This amounts to define the so-called *insertion operators* and *homogenisation operators*. The same concept applies to mapping macro- and microscale virtual actions (variations).

Let us assume that $u_\mu \in \mathscr{U}_\mu$ is composed by two parts: i) one determined by the macroscale kinematics through the action of the insertion operators, let us denote $\overline{u}_\mu$ and ii) other remaining part, so-called *fluctuation of the generalised displacements*, denoted by $\tilde{u}_\mu$. Hence, $u_\mu = \overline{u}_\mu + \tilde{u}_\mu$, with $\overline{u}_\mu \in \overline{\mathscr{U}}_\mu$ and $\tilde{u}_\mu \in \widetilde{\mathscr{U}}_\mu$, where $\overline{\mathscr{U}}_\mu$ and $\widetilde{\mathscr{U}}_\mu$ are subspaces of $\mathscr{U}_\mu$.

It is important to mention that the adoption of a definition of insertion operators, although not necessarily unique, should satisfy a certain number of physical reasonable restrictions. Such constraints are emphasised through specific commentaries in this chapter.

2.2.2.1 Insertion Operators

The first insertion operator maps point-valued macroscale generalised displacements to microscale generalised displacements as follows:

$$\begin{aligned} \mathcal{J}_\mu^{\mathscr{U}} : \mathbb{R}^{\mathbf{x}_M}_{\mathscr{U}_M} &\rightarrow \overline{\mathscr{U}}_\mu, \\ u_M|_{\mathbf{x}_M} &\mapsto \mathcal{J}_\mu^{\mathscr{U}}(u_M|_{\mathbf{x}_M}) \end{aligned} \tag{2.10}$$

It is also necessary to define a second insertion operator which maps point-valued macroscale generalised strain rates to microscale generalised displacements as follows:

$$\begin{aligned} \mathcal{J}_\mu^{\mathscr{E}} : \mathbb{R}^{\mathbf{x}_M}_{\mathscr{E}_M} &\rightarrow \overline{\mathscr{U}}_\mu, \\ D_M|_{\mathbf{x}_M} &\mapsto \mathcal{J}_\mu^{\mathscr{E}}(D_M|_{\mathbf{x}_M}) \end{aligned} \tag{2.11}$$

The contribution $\overline{u}_\mu$ is then characterised as follows

$$\overline{u}_\mu = \mathcal{J}_\mu^{\mathscr{U}}(u_M|_{\mathbf{x}_M}) + \mathcal{J}_\mu^{\mathscr{E}}(D_M|_{\mathbf{x}_M}). \tag{2.12}$$

Remark (Operator Restrictions) 1 *Operator $\mathcal{J}_\mu^{\mathscr{U}}$ should be such that*

$$\mathcal{D}_\mu(\mathcal{J}_\mu^{\mathscr{U}}(u_M|_{\mathbf{x}_M})) = 0 \qquad \forall u_M|_{\mathbf{x}_M} \in \mathbb{R}^{\mathbf{x}_M}_{\mathscr{U}_M}, \tag{2.13}$$

i.e. , $\mathcal{J}_\mu^{\mathscr{U}}(u_M|_{\mathbf{x}_M}) \in \mathrm{Ker}(\mathcal{D}_\mu)$*. From the physical point of view the above restriction entails that the inserted generalised displacement from the macroscale does not produce any effect on the generalised strain rates at microscale.*

2.2.2.2 Kinematic homogenisation operators

In this section we define the homogenisation operators which establish the kinematical connection between the kinematics at both scales, providing a sense of kinematic conservation in the multiscale transfer. Furthermore, these operators clearly define the admissible kinematical restrictions to be satisfied by the displacement fluctuations.

First we have the homogenisation operator for the generalised displacement as follows

$$\begin{aligned} \mathcal{H}_\mu^{\mathscr{U}} : \mathscr{U}_\mu &\to \mathbb{R}^{\mathbf{x}_M}_{\mathscr{U}_M}, \\ u_\mu &\mapsto \mathcal{H}_\mu^{\mathscr{U}}(u_\mu). \end{aligned} \tag{2.14}$$

From this operator emerges a physical restriction upon u_μ that has to satisfy

$$\mathcal{H}_\mu^{\mathscr{U}}(u_\mu) = u_M|_{\mathbf{x}_M}. \tag{2.15}$$

Remark (Operator Restrictions) 2 *Operator* $\mathcal{H}_\mu^{\mathscr{U}}$ *should be such that*

$$\mathcal{H}_\mu^{\mathscr{U}}(\mathcal{J}_\mu^{\mathscr{U}}(u_M|_{\mathbf{x}_M})) = u_M|_{\mathbf{x}_M} \qquad \forall u_M|_{\mathbf{x}_M} \in \mathbb{R}^{\mathbf{x}_M}_{\mathscr{U}_M}, \tag{2.16}$$

$$\mathcal{H}_\mu^{\mathscr{U}}(\mathcal{J}_\mu^{\mathscr{E}}(D_M|_{\mathbf{x}_M})) = 0 \qquad \forall D_M|_{\mathbf{x}_M} \in \mathbb{R}^{\mathbf{x}_M}_{\mathscr{E}_M} \tag{2.17}$$

i.e. , $\mathcal{H}_\mu^{\mathscr{U}} \circ \mathcal{J}_\mu^{\mathscr{U}}$ *is the identity operator in* $\mathbb{R}^{\mathbf{x}_M}_{\mathscr{U}_M}$ *and insertion of a pure macroscopic generalised strain rate generates zero homogenised generalised displacement.*

Since the operator $\mathcal{H}_\mu^{\mathscr{U}}$ is linear, this is equivalent to

$$\begin{aligned} \mathcal{H}_\mu^{\mathscr{U}}(u_\mu) &= \mathcal{H}_\mu^{\mathscr{U}}(\overline{u}_\mu) + \mathcal{H}_\mu^{\mathscr{U}}(\tilde{u}_\mu) \\ &= \mathcal{H}_\mu^{\mathscr{U}}(\mathcal{J}_\mu^{\mathscr{U}}(u_M|_{\mathbf{x}_M})) + \mathcal{H}_\mu^{\mathscr{U}}(\mathcal{J}_\mu^{\mathscr{E}}(D_M|_{\mathbf{x}_M})) + \mathcal{H}_\mu^{\mathscr{U}}(\tilde{u}_\mu) = u_M|_{\mathbf{x}_M}, \end{aligned}$$

which implies, from (2.16) and (2.17), that the fluctuation $\tilde{u}_\mu$ must satisfy

$$\mathcal{H}_\mu^{\mathscr{U}}(\tilde{u}_\mu) = 0 \tag{2.18}$$

Next we have the homogenisation operator for the generalised strain rate

$$\begin{aligned} \mathcal{H}_\mu^{\mathscr{E}} : \mathscr{E}_\mu &\to \mathbb{R}^{\mathbf{x}_M}_{\mathscr{E}_M}, \\ D_\mu &\mapsto \mathcal{H}_\mu^{\mathscr{E}}(D_\mu). \end{aligned} \tag{2.19}$$

The physical restriction associated to this operator is postulated naturally as follows

$$\mathcal{H}_\mu^{\mathscr{E}}(D_\mu) = D_M|_{\mathbf{x}_M}. \tag{2.20}$$

Remark (Operator Restrictions) 3 *Operator* $\mathcal{H}_\mu^{\mathscr{E}}$ *should be such that*

$$\mathcal{H}_\mu^{\mathscr{E}}(\mathcal{D}_\mu(\mathcal{J}_\mu^{\mathscr{E}}(D_M|_{\mathbf{x}_M}))) = D_M|_{\mathbf{x}_M} \qquad \forall D_M|_{\mathbf{x}_M} \in \mathbb{R}^{\mathbf{x}_M}_{\mathscr{E}_M}, \tag{2.21}$$

i.e. , $\mathcal{H}_\mu^{\mathscr{U}} \circ \mathcal{D}_\mu \circ \mathcal{J}_\mu^{\mathscr{U}}$ *is the identity operator in* $\mathbb{R}^{\mathbf{x}_M}_{\mathscr{E}_M}$*.*

Since $\mathcal{H}_\mu^{\mathscr{E}}$ and $\mathcal{D}_\mu$ are linear, using (2.21), (2.13) and also $D_\mu = \mathcal{D}_\mu(u_\mu) = \mathcal{D}_\mu(\overline{u}_\mu) + \mathcal{D}_\mu(\tilde{u}_\mu)$ we have

$$\mathcal{H}_\mu^{\mathscr{E}}(D_\mu) = \mathcal{H}_\mu^{\mathscr{E}}(\mathcal{D}_\mu(\mathcal{J}_\mu^{\mathscr{U}}(u_M|_{\mathbf{x}_M}))) + \mathcal{H}_\mu^{\mathscr{E}}(\mathcal{D}_\mu(\mathcal{J}_\mu^{\mathscr{E}}(D_M|_{\mathbf{x}_M}))) + \mathcal{H}_\mu^{\mathscr{E}}(\mathcal{D}_\mu(\tilde{u}_\mu) = D_M|_{\mathbf{x}_M},$$

which yields to

$$\mathcal{H}_\mu^{\mathscr{E}}(\mathcal{D}_\mu(\tilde{u}_\mu)) = 0. \tag{2.22}$$

Note that restrictions (2.15) and (2.20) defines the kinematical admissible set for the microscale generalised displacement as follows

$$\mathrm{Kin}_{\mathscr{U}_\mu} = \Big\{ u_\mu \in \mathscr{U}_\mu \ ; \ \mathcal{H}_\mu^{\mathscr{U}}(u_\mu) = u_M|_{\mathbf{x}_M} \ , \ \mathcal{H}_\mu^{\mathscr{E}}(\mathcal{D}_\mu(u_\mu)) = D_M|_{\mathbf{x}_M} \Big\} \subset \mathscr{U}_\mu. \tag{2.23}$$

As already commented, this was the last ingredient to entirely set the microscale kinematics. An overview about the relation between kinematical spaces in both macro and microscale is provided in Fig. 5.

For our context, it is also interesting to characterise the admissible space of fluctuations, which is as follows [1]:

$$\widetilde{\mathscr{U}}_\mu = \Big\{ \tilde{u}_\mu \in \mathscr{U}_\mu \ ; \ \mathcal{H}_\mu^{\mathscr{U}}(\tilde{u}_\mu) = 0 \ , \ \mathcal{H}_\mu^{\mathscr{E}}(\mathcal{D}_\mu(\tilde{u}_\mu)) = 0 \Big\} \subset \mathscr{U}_\mu. \tag{2.24}$$

Taking differences between any two elements of $\widetilde{\mathscr{U}}_\mu$, it is easy to see that the space of variations of fluctuation coincides with $\widetilde{\mathscr{U}}_\mu$, so the same notation is used for this purpose.

2.2.3 Duality

In the same fashion as in Section 2.1.2 for a single scale problem, we need to set virtual power internal and external functionals for both scales.

Regarding the macroscale let us suppose the existence of linear functionals $\mathcal{P}_M^{\mathrm{int}}$ and $\mathcal{P}_M^{\mathrm{ext}}$, internal and external virtual power functionals for macroscale respectively. As consequence, skipping details for sake of simplicity, the representation of these functionals by duality products define the dual (power-conjugated) objects of the macroscale, the internal generalised stress $\Sigma_M \in (\mathscr{E}_M)'$ and the macroscale external generalised forces $f_M \in (\mathscr{U}_M)'$.

[1] Note that specifically, for ease of notation, we have not used the notation $\mathrm{Kin}_{(\cdot)}$.

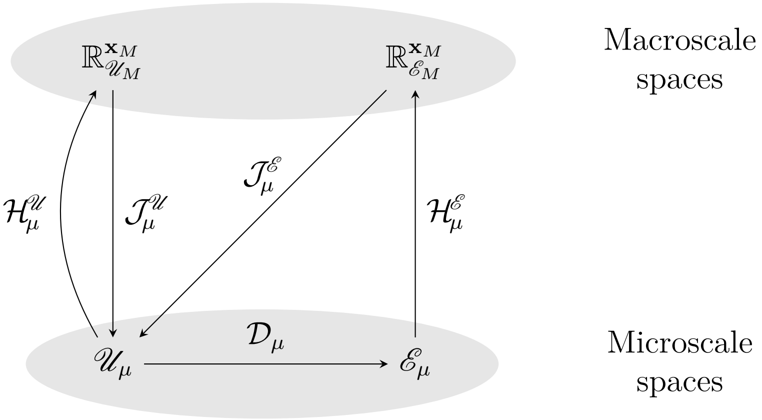

Figure 5 – Diagram of kinematics: relation between spaces and operators found in (2.10), (2.11), (2.10), (2.19), (2.14) and also the generalised deformation operator at microscale ($\mathcal{D}_\mu$) defined analogously as in (2.2).

At a point-wise level, $\mathcal{P}^{\text{int}}_M$ becomes

$$\mathcal{P}^{\text{int}}_{M,\mathbf{x}_M}(\hat{D}_M|_{\mathbf{x}_M}) = \Sigma_M|_{\mathbf{x}_M} \bullet \hat{D}_M|_{\mathbf{x}_M}, \tag{2.25}$$

where operation $(\cdot) \bullet (\cdot)$ is a duality product on $(\mathbb{R}^{\mathbf{x}_M}_{\mathscr{E}_M})' \times \mathbb{R}^{\mathbf{x}_M}_{\mathscr{E}_M}$. This product encloses in its definition proper scalar weights required by modelling purposes as function of the RVE in question. In practical situations we will make this definition explicit.

In a similar way we have the point-wise version $\mathcal{P}^{\text{ext}}_M$ as

$$\mathcal{P}^{\text{ext}}_{M,\mathbf{x}_M}(\hat{u}_M|_{\mathbf{x}_M}) = f_M|_{\mathbf{x}_M} \star \hat{u}_M|_{\mathbf{x}_M}, \tag{2.26}$$

where $\star$ is a duality product on $(\mathbb{R}^{\mathbf{x}_M}_{\mathscr{U}_M})' \times \mathbb{R}^{\mathbf{x}_M}_{\mathscr{U}_M}$ and follows the same comments as for $\bullet$ above.

Analogously, regarding the microscale we admit linear functionals $\mathcal{P}^{\text{int}}_\mu$ and $\mathcal{P}^{\text{ext}}_\mu$, internal and external virtual power functionals for microscale respectively. As usual, their definitions also entail the characterisation internal generalised stress $\Sigma_\mu \in (\mathscr{E}_\mu)'$ and the microscale external generalised forces $f_\mu \in (\mathscr{U}_\mu)'$. It is worth mentioning that arguments of $\mathcal{P}^{\text{int}}_\mu$ can be either $\mathcal{D}_\mu(\hat{u}_\mu) \in \mathcal{D}_\mu(\text{Var}_{\mathscr{U}_\mu})$ or the pair $\left(\hat{D}_M|_{\mathbf{x}_M}, \mathcal{D}_\mu(\hat{\tilde{u}}_\mu)\right) \in \widehat{\mathbb{R}^{\mathbf{x}_M}_{\mathscr{E}_M}} \times \mathcal{D}_\mu(\widetilde{\mathscr{U}_\mu})$ since both spaces are isomorphic. For convenience, no distinction in notation is made. Very same comments apply to $\mathcal{P}^{\text{ext}}_\mu$ because $\hat{u}_\mu \in \text{Var}_{\mathscr{U}_\mu}$ can be identified with the triple $\left(\hat{u}_M|_{\mathbf{x}_M}, \hat{D}_M|_{\mathbf{x}_M}, \hat{\tilde{u}}_\mu\right) \in \widehat{\mathbb{R}^{\mathbf{x}_M}_{\mathscr{U}_M}} \times \mathbb{R}^{\mathbf{x}_M}_{\mathscr{E}_M} \times \widetilde{\mathscr{U}_\mu}$.

2.2.4 Principle of Multiscale Virtual Power

In this section we postulate the principle of generalised equilibrium between scales. To this aim, the Principle of Multiscale Virtual Power (PMVP) and the virtual power functionals defined in Section 2.2.3 are invoked.

The PMVP in the present context can be understood as a generalised formulation of the Hill-Mandel Principle of Macrohomogeneity (HILL, 1965; MANDEL, 1972). This principle states that the total (difference between internal and external) virtual power exerted by macroscale entities at point $\mathbf{x}_M \in \Omega_M$ must equal to the total power exerted in the corresponding microscale (the RVE). Mathematically, this is stated below

Principle 2 ***(of Multiscale Virtual Power)*** *It is said that the elements* $(\Sigma_M|_{\mathbf{x}_M}, f_M|_{\mathbf{x}_M}) \in (\mathbb{R}^{\mathbf{x}_M}_{\mathscr{E}_M})' \times (\mathbb{R}^{\mathbf{x}_M}_{\mathscr{U}_M})'$ *and* $(\Sigma_\mu, f_\mu) \in \mathscr{E}'_\mu \times \mathscr{U}'_\mu$ *are equilibrated if the following variational equation is satisfied*

$$\begin{aligned}\mathcal{P}^{\text{int}}_{M,\mathbf{x}_M}(\hat{D}_M|_{\mathbf{x}_M}) - \mathcal{P}^{\text{ext}}_{M,\mathbf{x}_M}(\hat{u}_M|_{\mathbf{x}_M}) = \mathcal{P}^{\text{int}}_\mu\left(\hat{D}_M|_{\mathbf{x}_M}, \mathcal{D}_\mu(\hat{\tilde{u}}_\mu)\right) - \\ \mathcal{P}^{\text{ext}}_\mu\left(\hat{u}_M|_{\mathbf{x}_M}, \hat{D}_M|_{\mathbf{x}_M}, \hat{\tilde{u}}_\mu\right) \ , \quad \forall \hat{u}_M|_{\mathbf{x}_M}, \hat{D}_M|_{\mathbf{x}_M}, \hat{\tilde{u}}_\mu \ \textit{kin. admissibles}\end{aligned} \tag{2.27}$$

or equivalently

$$\begin{aligned}\Sigma_M|_{\mathbf{x}_M} \bullet \hat{D}_M|_{\mathbf{x}_M} - f_M|_{\mathbf{x}_M} \star \hat{u}_M|_{\mathbf{x}_M} = \\ \langle \Sigma_\mu, \hat{D}_M|_{\mathbf{x}_M} + \mathcal{D}_\mu(\hat{\tilde{u}}_\mu)\rangle_{\mathscr{E}'_\mu \times \mathscr{E}_\mu} - \langle f_\mu, \mathcal{J}^{\mathscr{U}}_\mu(\hat{u}_M|_{\mathbf{x}_M}) + \mathcal{J}^{\mathscr{E}}_\mu(\hat{D}_M|_{\mathbf{x}_M}) + \hat{\tilde{u}}_\mu\rangle_{\mathscr{U}'_\mu \times \mathscr{U}_\mu} \\ \forall (\hat{u}_M|_{\mathbf{x}_M}, \hat{D}_M|_{\mathbf{x}_M}, \hat{\tilde{u}}_\mu) \in \widehat{\mathbb{R}^{\mathbf{x}_M}_{\mathscr{U}_M}} \times \widehat{\mathbb{R}^{\mathbf{x}_M}_{\mathscr{E}_M}} \times \widetilde{\mathscr{U}_\mu}.\end{aligned} \tag{2.28}$$

It follows from (2.28) three variational consequences:

1. Homogenisation of generalised internal stresses: Choosing $\hat{u}_M|_{\mathbf{x}_M} = 0$ and $\hat{\tilde{u}}_\mu = 0$, it is possible to find the explicit expression for $\Sigma_M|_{\mathbf{x}_M}$ in terms of the pair (Σ_μ, f_μ). Along this process the so-called *generalised stress homogenisation operator* $\mathcal{H}^{\mathbf{x}_M}_{\Sigma_M} : \mathscr{E}'_\mu \times \mathscr{U}'_\mu \to (\mathbb{R}^{\mathbf{x}_M}_{\mathscr{E}_M})'$ is identified.

2. Homogenisation of generalised external forces: Choosing $\hat{D}_M|_{\mathbf{x}_M} = 0$ and $\hat{\tilde{u}}_\mu = 0$, an explicit expression for $f_M|_{\mathbf{x}_M}$ as function of f_μ is found. This process also identifies the so-called *generalised external force homogenisation operator* $\mathcal{H}^{\mathbf{x}_M}_{f_M} : \mathscr{U}'_\mu \to (\mathbb{R}^{\mathbf{x}_M}_{\mathscr{U}_M})'$.

3. Equilibrium problem at microscale: Choosing $\hat{u}_M|_{\mathbf{x}_M} = 0$ and $\hat{D}_M|_{\mathbf{x}_M} = 0$ a variational equation for equilibrium problem is derived. As solution of this equation the fluctuation field $\tilde{u}_\mu \in \widetilde{\mathscr{U}_\mu}$ is determined.

The explicit shape of these results is problem dependent. Therefore we will characterise these forms in due time.

2.3 Application in solid mechanics

Let us start with the simplest scenario for the present context, which is that of multiscale modelling in continuum solid mechanics. For the purpose of this work, finite strain regime is adopted for both scales and by convention all fields are defined in the material configuration. Although the problem presented is in the context of first-order (conventional) continuum mechanics, we highlight that the very same methodology has already been proved to be easily extended to other fields as heat transfer (BLANCO; GIUSTI, 2014), fluid mechanics (BLANCO; CLAUSSE; FEIJÓO, 2017), second-order continuum mechanics (BLANCO et al., 2016), etc.

Importantly, we keep presentation brief since the very same steps are repeated in the forthcoming chapters and the model to be presented is classical in the literature, see (NETO et al., 2015) for example. Notwithstanding, the importance of this section is to demonstrate the abstract theoretical setting applied to a standard, well-known model, before moving to non-standard, still not estabilished, multiscale models. We postpone and refer the reader to Chapter 3 for a more detailed explanation.

2.3.1 Macroscale model

At the macroscale we consider a standard model from continuum mechanics in the finite strain regime. Let $\Omega_M \subset \mathbb{R}^{\mathrm{n_d}}$, $\mathrm{n_d} = 2, 3$, be an open set which represents the reference (or material) configuration of the body $\mathcal{B}_M$. Material points in Ω_M are denoted $\mathbf{x}_M$. The boundary of Ω_M, Γ_M, is split into Dirichlet (Γ_M^D) and Neumann (Γ_M^N) parts, whose outward unit normal vector is $\mathbf{n}_M$. This setting is depicted in Fig. 6 (left). Let the displacement be $u_M = \mathbf{u}_M \in \mathscr{U}_M = [H^1(\Omega_M)]^{\mathrm{n_d}}$ and the associated strain rate operator $\mathcal{D}_M = \nabla_{\mathbf{x}_M}$ (note that in this case the strain measure coincides with $\mathcal{D}_M$). This defines $D_M = \mathbf{G}_M = \nabla_{\mathbf{x}_M}\mathbf{u}_M \in \mathcal{D}_M(\mathscr{U}_M) \subset \mathscr{E}_M = [L^2(\Omega_M)]^{\mathrm{n_d}\times\mathrm{n_d}}$. Note that the traditional gradient of deformation is retrieved by $\mathbf{F}_M = \mathbf{I} + \mathbf{G}_M$.

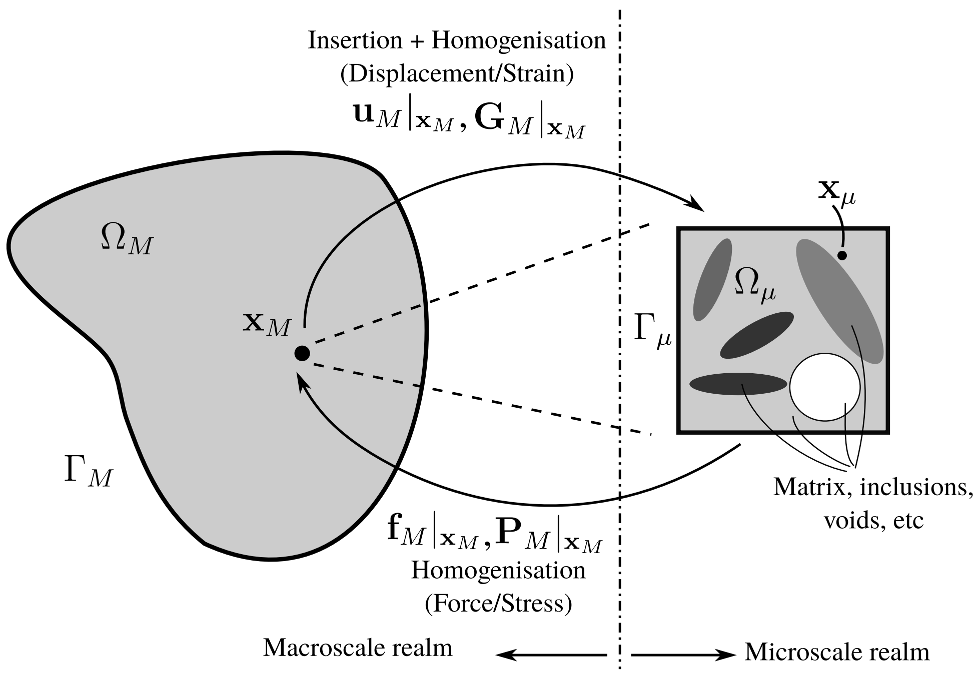

Figure 6 – Multiscale setting for the modelling in continuum solid mechanics.

Concerning Dirichlet boundary conditions, we have $\mathrm{Kin}_{\mathscr{U}_M} = \left\{\mathbf{u}_M \in [H^1(\Omega_M)]^{\mathrm{n_d}}; \mathbf{u}_M = \mathbf{u}_M^D \text{ on } \Gamma_M^D\right\}$ and its space of variations $\mathrm{Var}_{\mathscr{U}_M} = \left\{\hat{\mathbf{u}}_M \in [H^1(\Omega_M)]^{\mathrm{n_d}}; \hat{\mathbf{u}}_M = \mathbf{0} \text{ on } \Gamma_M^D\right\}$. This also defines $\hat{\mathbf{G}}_M = \mathcal{D}_M(\hat{\mathbf{u}}_M)$ for $\hat{\mathbf{u}}_M \in \mathrm{Var}_{\mathscr{U}_M}$. We assume $\mathcal{P}_M^{\mathrm{int}}(\hat{\mathbf{G}}_M) = \int_{\Omega_M} \mathbf{P}_M \cdot \hat{\mathbf{G}}_M \, \mathrm{d}\Omega_M$, where the power-conjugated stress tensor to the adopted strain measure is the first Piola-Kirchhoff stress tensor (PKST) $\Sigma_M = \mathbf{P}_M$. Finally, $\mathcal{P}_M^{\mathrm{ext}}(\hat{\mathbf{u}}_M) = \int_{\Omega_M} \mathbf{b}_M \cdot \hat{\mathbf{u}}_M \, \mathrm{d}\Omega_M + \int_{\Gamma_M^N} \mathbf{t}_M \cdot \hat{\mathbf{u}}_M \, \mathrm{d}\Gamma_M^N$, where the admissible external forces are given by body forces $\mathbf{b}_M \in [L^2(\Omega_M)]^{\mathrm{n_d}}$ and tractions along the Neumann boundary $\mathbf{t}_M \in [L^2(\Gamma_M^N)]^{\mathrm{n_d}}$, this defines $f_M = (\mathbf{b}_M, \mathbf{t}_M)$. All such definitions define the mechanical problem at the macroscale given below.

Problem 1 (Macroscale Mechanical Problem) *Given an admissible external force system* $(\mathbf{b}_M, \mathbf{t}_M)$*, find the displacement field* $\mathbf{u}_M \in \mathrm{Kin}_{\mathscr{U}_M}$ *such that the following variational equation is satisfied*

$$\int_{\Omega_M} \mathbf{P}_M \cdot \hat{\mathbf{G}}_M \, \mathrm{d}\Omega_M = \int_{\Omega_M} \mathbf{b}_M \cdot \hat{\mathbf{u}}_M \, \mathrm{d}\Omega_M + \int_{\Gamma_M^N} \mathbf{t}_M \cdot \hat{\mathbf{u}}_M \, \mathrm{d}\Gamma_M^N \quad \forall \hat{\mathbf{u}}_M \in \mathrm{Var}_{\mathscr{U}_M}, \tag{2.29}$$

where $\mathbf{P}_M$ *is given by some constitutive law of the kind* $\mathbf{P}_M = \mathscr{F}(\mathbf{G}_M^t)$ [2].

Finally, for point-valued versions of the virtual powers at a point $\mathbf{x}_M \in \Omega_M$ we have $\mathcal{P}_{M,\mathbf{x}_M}^{\mathrm{int}}(\hat{\mathbf{G}}_M|_{\mathbf{x}_M}) = \mathbf{P}_M|_{\mathbf{x}_M} \bullet \hat{\mathbf{G}}_M|_{\mathbf{x}_M} = |\Omega_\mu| \mathbf{P}_M|_{\mathbf{x}_M} \cdot \hat{\mathbf{G}}_M|_{\mathbf{x}_M}$ and $\mathcal{P}_{M,\mathbf{x}_M}^{\mathrm{ext}}(\hat{\mathbf{u}}_M|_{\mathbf{x}_M}) = \mathbf{b}_M|_{\mathbf{x}_M} \star \hat{\mathbf{u}}_M|_{\mathbf{x}_M} = |\Omega_\mu| \mathbf{b}_M|_{\mathbf{x}_M} \cdot \hat{\mathbf{u}}_M|_{\mathbf{x}_M}$. Note that the factor $|\Omega_\mu|$ in the definition of $\bullet$ and $\star$ is used to take into account the size of the RVE. Moreover, tractions applied on boundary have no effect in the external virtual power exerted at a point in the bulk of the domain, $\mathbf{x}_M \in \Omega_M$. The above comments are employed in Section 2.3.4.

2.3.2 Microscale kinematics

In terms of kinematics, at microscale we also assume the standard model from continuum mechanics in the finite strain regime. Using an analogous notation we have $\Omega_\mu \subset \mathbb{R}^{\mathrm{n_d}}$, $\mathrm{n_d} = 2, 3$, an open set which represents the reference (or material) configuration of the RVE, with boundary Γ_μ and outward unit normal $\mathbf{n}_\mu$. Material points in Ω_μ are denoted by $\mathbf{x}_\mu$. Also following a similar notation we have $u_\mu = \mathbf{u}_\mu \in \mathscr{U}_\mu = [H^1(\Omega_\mu)]^{\mathrm{n_d}}$, $\mathcal{D}_\mu = \nabla_{\mathbf{x}_\mu}$ and $D_\mu = \mathbf{G}_\mu = \nabla_{\mathbf{x}_\mu} \mathbf{u}_\mu \in \mathcal{D}_\mu(\mathscr{U}_\mu) \subset \mathscr{E}_\mu = [L^2(\Omega_\mu)]^{\mathrm{n_d} \times \mathrm{n_d}}$, for the microscopic displacement, strain rate operator and strain tensor, respectively. It is important to remember that RVE encloses a portion of the body which has a representative structure of the material, being the characteristic size of Ω_μ generally much smaller than the size of Ω_M, but sufficiently large to be considered representative.

2 In a multiscale approach, the constitutive functional $\mathscr{F}$ is implicitly defined by solving a microscale problem (in the RVE) and by applying a certain homogenisation procedure to entities defined at the microscale level. This is one of goals of the forthcoming sections.

2.3.3 Multiscale kinematics

For a given point $\mathbf{x}_M \in \Omega_M$, according to the spaces $\mathscr{U}_M$ and $\mathscr{E}_M$ defined in 2.3.1, we have $\mathbf{u}_M|_{\mathbf{x}_M} = \mathbf{u}_M(\mathbf{x}_M) \in \mathbb{R}^{\mathbf{x}_M}_{\mathscr{U}_M} = \mathbb{R}^{\mathrm{n_d}}$ and $\mathbf{G}_M|_{\mathbf{x}_M} = \mathbf{G}_M(\mathbf{x}_M) \in \mathbb{R}^{\mathbf{x}_M}_{\mathscr{E}_M} = \mathbb{R}^{\mathrm{n_d}\times\mathrm{n_d}}$. Insertion operators are established as $\mathscr{J}^{\mathscr{U}}_\mu(\mathbf{u}_M|_{\mathbf{x}_M}) = \mathbf{u}_M|_{\mathbf{x}_M}$ and $\mathscr{J}^{\mathscr{E}}_\mu(\mathbf{G}_M|_{\mathbf{x}_M}) = \mathbf{G}_M|_{\mathbf{x}_M}(\mathbf{x}_\mu - \mathbf{x}^G_\mu)$, with $\mathbf{x}^G_\mu := \frac{1}{|\Omega_\mu|}\int_{\Omega_\mu} \mathbf{x}_\mu \, \mathrm{d}\Omega_\mu$ (centroid of the RVE), which yields the usual decomposition

$$\mathbf{u}_\mu(\mathbf{x}_\mu) = \mathbf{u}_M|_{\mathbf{x}_M} + \mathbf{G}_M|_{\mathbf{x}_M}(\mathbf{x}_\mu - \mathbf{x}^G_\mu) + \tilde{\mathbf{u}}_\mu(\mathbf{x}_\mu) \qquad \forall \mathbf{x}_\mu \in \Omega_\mu, \tag{2.30}$$

where $\tilde{u}_\mu = \tilde{\mathbf{u}}_\mu \in \widetilde{\mathscr{U}_\mu} \subset \mathscr{U}_\mu$ and $\widetilde{\mathscr{U}_\mu}$ (space of admissible fluctuations) to be defined in the following steps. First, we postulate the kinematical homogenisation operators $\mathscr{H}^{\mathscr{U}}_\mu(\mathbf{u}_\mu) = \frac{1}{|\Omega_\mu|}\int_{\Omega_\mu} \mathbf{u}_\mu \, \mathrm{d}\Omega_\mu$ and $\mathscr{H}^{\mathscr{E}}_\mu(\mathbf{G}_\mu) = \frac{1}{|\Omega_\mu|}\int_{\Omega_\mu} \mathbf{G}_\mu \, \mathrm{d}\Omega_\mu$ and from the basic kinematical conservation restrictions for $\mathscr{H}^{\mathscr{U}}_\mu$ (2.15) and $\mathscr{H}^{\mathscr{E}}_\mu$ (2.20), anagously to (2.24), we arrive at

$$\begin{aligned} \widetilde{\mathscr{U}}^M_\mu &= \left\{ \tilde{\mathbf{u}}_\mu \in \mathscr{U}_\mu \; ; \; \int_{\Omega_\mu} \tilde{\mathbf{u}}_\mu \, \mathrm{d}\Omega_\mu = \mathbf{0} \; , \; \int_{\Omega_\mu} \nabla_{\mathbf{x}_\mu} \tilde{\mathbf{u}}_\mu \, \mathrm{d}\Omega_\mu = \mathbf{O} \right\} \\ &= \left\{ \tilde{\mathbf{u}}_\mu \in \mathscr{U}_\mu \; ; \; \int_{\Omega_\mu} \tilde{\mathbf{u}}_\mu \, \mathrm{d}\Omega_\mu = \mathbf{0} \; , \; \int_{\Gamma_\mu} \tilde{\mathbf{u}}_\mu \otimes \mathbf{n}_\mu \, \mathrm{d}\Gamma_\mu = \mathbf{O} \right\}. \end{aligned} \tag{2.31}$$

This space is the Minimally Constrained Kinematically admissible Multiscale Model (MCKMM), also known as uniform traction model. It consists in the minimally constrained space that can be employed as admissible space of fluctuations. Hereafter, when the context is clear, $\widetilde{\mathscr{U}}^M_\mu$ is simply denoted by $\widetilde{\mathscr{U}_\mu}$. Otherwise $\widetilde{\mathscr{U}_\mu}$ refers to a generic submodel of $\widetilde{\mathscr{U}}^M_\mu$, such that $\widetilde{\mathscr{U}_\mu} \subset \widetilde{\mathscr{U}}^M_\mu$. Examples of that are given in the following.

2.3.3.1 Specific subspaces of multiscale models

So far, only the minimally constrained space of admissible fluctuations $\widetilde{\mathscr{U}}^M_\mu$ (2.31) has been established. Note that any subspace of $\widetilde{\mathscr{U}}^M_\mu$ could be considered in the analysis. In this sense, we present three different subspaces possibilities:

1. Taylor model:

$$\widetilde{\mathscr{U}}^T_\mu := \{\mathbf{0}\} \tag{2.32}$$

2. Linear boundary model:

$$\widetilde{\mathscr{U}}^L_\mu := \{\tilde{\mathbf{u}}_\mu \in \widetilde{\mathscr{U}}^M_\mu ; \tilde{\mathbf{u}}_\mu|_{\Gamma_\mu} = \mathbf{0}\} \tag{2.33}$$

3. Periodic boundary model:

$$\widetilde{\mathscr{U}}^P_\mu := \{\tilde{\mathbf{u}}_\mu \in \widetilde{\mathscr{U}}^M_\mu ; \tilde{\mathbf{u}}_\mu|_{\Gamma^{i,+}_\mu} = \tilde{\mathbf{u}}_\mu|_{\Gamma^{i,-}_\mu}, \forall i = 1\} \tag{2.34}$$

where $\Gamma_\mu = \bigcup_i \left(\Gamma^{i,+}_\mu \cup \Gamma^{i,-}_\mu\right)$, with $\Gamma^{i,+}_\mu$ and $\Gamma^{i,-}_\mu$ disjoints and with opposite outward normal vectors. This model is known to lead to skew-periodic tractions on the boundary.

Note that $\widetilde{\mathscr{U}}_\mu^T \subset \widetilde{\mathscr{U}}_\mu^L \subset \widetilde{\mathscr{U}}_\mu^P \subset \widetilde{\mathscr{U}}_\mu^M$. For the sake of simplicity, when the choice is irrelevant, we use $\widetilde{\mathscr{U}}_\mu$ as notation for any of the particular models.

Alternative boundary conditions (to the linear, periodic and uniform traction models) have been developed in the literature, most of them in an ad-hoc manner. Some examples are the so-called mixed uniform boundary conditions (HAZANOV, 1998; HAZANOV; HUET, 1994), where the linear model is considered for certain components of the displacement field while for the other components a uniform traction approach is postulated. An approach relying on similar ideas was proposed in (PAHR; ZYSSET, 2008) but incorporating periodic conditions in some components of the displacement field and uniform traction for others. More recently, in (SANDSTRÖM; LARSSON, 2017; SANDSTRÖM; LARSSON; RUNESSON, 2014; SVENNING; FAGERSTRÖM; LARSSON, 2016), the so-called weak periodicity was developed as a strategy to continuously range between the uniform traction model and the periodic model.

2.3.4 Duality and PMVP

For the microscopic internal virtual functional we use a similar model than at macroscale, i.e., $\mathcal{P}_\mu^{\text{int}}(\hat{\mathbf{G}}_\mu) = \int_{\Omega_\mu} \mathbf{P}_\mu \cdot \hat{\mathbf{G}}_\mu \, d\Omega_\mu$, where $\Sigma_\mu = \mathbf{P}_\mu$ is the microscopic version of the PKST. Consequently, $\mathcal{P}_\mu^{\text{ext}}(\hat{\mathbf{u}}_\mu) = \int_{\Omega_\mu} \mathbf{b}_\mu \cdot \hat{\mathbf{u}}_\mu \, d\Omega_\mu$, $f_\mu = \mathbf{b}_\mu \in [L^2(\Omega_\mu)]^{\mathrm{n_d}}$ stands for the admissible microscale body forces. Below it is shown the particularisation of the Principle 2 for the context of solid mechanics.

Problem 2 ***(Principle of Multiscale Virtual Power for Solid Mechanics)*** *It is said that the elements* $(\mathbf{P}_M|_{\mathbf{x}_M}, \mathbf{b}_M|_{\mathbf{x}_M}) \in (\mathbb{R}^{\mathbf{x}_M}_{\mathscr{E}_M})' \times \mathbb{R}^{\mathbf{x}_M}_{\mathscr{U}_M})'$ *and* $(\mathbf{P}_\mu, \mathbf{b}_\mu) \in \mathscr{E}_\mu' \times \mathscr{U}_\mu'$ *are equilibrated if the following variational equation is satisfied*

$$
\begin{aligned}
&|\Omega_\mu|\mathbf{P}_M|_{\mathbf{x}_M} \cdot \hat{\mathbf{G}}_M|_{\mathbf{x}_M} - |\Omega_\mu|\mathbf{b}_M|_{\mathbf{x}_M} \cdot \hat{\mathbf{u}}_M|_{\mathbf{x}_M} = \\
&\qquad \int_{\Omega_\mu} \mathbf{P}_\mu \cdot \hat{\mathbf{G}}_\mu \, d\Omega_\mu - \int_{\Omega_\mu} \mathbf{b}_\mu \cdot \hat{\mathbf{u}}_\mu \, d\Omega_\mu \\
&\qquad\qquad \forall (\mathbf{u}_M|_{\mathbf{x}_M}, \hat{\mathbf{G}}_M|_{\mathbf{x}_M}, \hat{\tilde{\mathbf{u}}}_\mu) \in \widehat{\mathbb{R}^{\mathbf{x}_M}_{\mathscr{U}_M}} \times \widehat{\mathbb{R}^{\mathbf{x}_M}_{\mathscr{E}_M}} \times \widetilde{\mathscr{U}}_\mu .
\end{aligned}
\tag{2.35}
$$

Recalling $\hat{\mathbf{u}}_\mu = \hat{\mathbf{u}}_M|_{\mathbf{x}_M} + \hat{\mathbf{G}}_M|_{\mathbf{x}_M}(\mathbf{x}_\mu - \mathbf{x}_\mu^G) + \hat{\tilde{\mathbf{u}}}_\mu$ and $\hat{\mathbf{G}}_\mu = \hat{\mathbf{G}}_M|_{\mathbf{x}_M} + \nabla_{\mathbf{x}_\mu}\hat{\tilde{\mathbf{u}}}_\mu$, replacing into (2.35), after rearranging terms we have:

$$
\begin{aligned}
&\left(\int_{\Omega_\mu} \mathbf{b}_\mu \, d\Omega_\mu - |\Omega_\mu|\mathbf{b}_M|_{\mathbf{x}_M}\right) \cdot \hat{\mathbf{u}}_M|_{\mathbf{x}_M} + \\
&\left(|\Omega_\mu|\mathbf{P}_M|_{\mathbf{x}_M} + \int_{\Omega_\mu} \mathbf{b}_\mu \otimes (\mathbf{x}_\mu - \mathbf{x}_\mu^G) \, d\Omega_\mu - \int_{\Omega_\mu} \mathbf{P}_\mu \, d\Omega_\mu\right) \cdot \hat{\mathbf{G}}_M|_{\mathbf{x}_M} + \\
&\int_{\Omega_\mu} (-\mathbf{P}_\mu \cdot \nabla_{\mathbf{x}_\mu}\hat{\tilde{\mathbf{u}}}_\mu + \mathbf{b}_\mu \cdot \hat{\tilde{\mathbf{u}}}_\mu) \, d\Omega\mu = 0 \quad \forall (\hat{\mathbf{u}}_M|_{\mathbf{x}_M}, \hat{\mathbf{G}}_M|_{\mathbf{x}_M}, \hat{\tilde{\mathbf{u}}}_\mu) \in \widehat{\mathbb{R}^{\mathbf{x}_M}_{\mathscr{U}_M}} \times \widehat{\mathbb{R}^{\mathbf{x}_M}_{\mathscr{E}_M}} \times \widetilde{\mathscr{U}}_\mu
\end{aligned}
\tag{2.36}
$$

Setting in the first place $\hat{\mathbf{G}}_M|_{\mathbf{x}_M} = \mathbf{O}$ and $\hat{\tilde{\mathbf{u}}}_\mu = \mathbf{0}$ in expression (2.36) we get the homogenisation operator for body forces

$$\mathbf{b}_M|_{\mathbf{x}_M} = \mathcal{H}^{\mathbf{x}_M}_{\mathbf{b}_M}(\mathbf{b}_\mu) = \frac{1}{|\Omega_\mu|}\int_{\Omega_\mu} \mathbf{b}_\mu \, \mathrm{d}\Omega_\mu. \tag{2.37}$$

$$\tag{2.38}$$

Secondly, assuming $\hat{\mathbf{u}}_M|_{\mathbf{x}_M} = \mathbf{0}$ and $\hat{\tilde{\mathbf{u}}}_\mu = \mathbf{0}$ in (2.36), then we arrive at the homogenisation operator for PKST, given below:

$$\mathbf{P}_M|_{\mathbf{x}_M} = \mathcal{H}^{\mathbf{x}_M}_{\mathbf{P}_M}(\mathbf{P}_\mu, \mathbf{b}_\mu) = \frac{1}{|\Omega_\mu|}\left(\int_{\Omega_\mu} \mathbf{P}_\mu \, \mathrm{d}\Omega_\mu - \int_{\Omega_\mu} \mathbf{b}_\mu \otimes (\mathbf{x}_\mu - \mathbf{x}^G_\mu) \, \mathrm{d}\Omega_\mu\right) \tag{2.39}$$

Note that, differently from what is usually assumed in the literature, the homogenisation of the stress is not simply the average of microscale stress field, but body forces also play a role.

Finally, setting $\hat{\mathbf{u}}_M|_{\mathbf{x}_M} = \mathbf{0}$ and $\hat{\mathbf{G}}_M|_{\mathbf{x}_M} = \mathbf{O}$ in (2.36) and by assuming a given constitutive law $\mathbf{P}_\mu = \mathscr{F}_\mu(\mathbf{G}_\mu)$ we arrive at a field problem, denoted RVE microscopic equilibrium problem, in which solution is obtained by finding $\tilde{\mathbf{u}}_\mu \in \widetilde{\mathscr{U}}_\mu$ such that

$$\int_{\Omega_\mu} \mathbf{P}_\mu(\mathbf{G}_M|_{\mathbf{x}_M} + \nabla_{\mathbf{x}_\mu}\tilde{\mathbf{u}}_\mu) \cdot \nabla_{\mathbf{x}_\mu}\hat{\tilde{\mathbf{u}}}_\mu \, \mathrm{d}\Omega_\mu - \int_{\Omega_\mu} \mathbf{b}_\mu \cdot \hat{\tilde{\mathbf{u}}}_\mu \, \mathrm{d}\Omega_\mu = 0 \qquad \forall \hat{\tilde{\mathbf{u}}}_\mu \in \widetilde{\mathscr{U}}_\mu. \tag{2.40}$$

By integrating by parts, it follows the resulting Euler-Lagrange equations

$$\begin{cases} \mathrm{div}_{\mathbf{x}_\mu} \mathbf{P}_\mu + \tilde{\mathbf{b}}_\mu = \mathbf{0} & \text{in } \Omega_\mu \\ \mathbf{P}_\mu \mathbf{n}_\mu = \mathbf{P}_M|_{\mathbf{x}_M}\mathbf{n}_\mu & \text{on } \Gamma_\mu \end{cases} \tag{2.41}$$

where $\tilde{\mathbf{b}}_\mu := \mathbf{b}_\mu - \mathbf{b}_M|_{\mathbf{x}_M}$ and $\mathbf{n}_\mu$ is the unit outward normal vector to Γ_μ.

Remark 3 *Alternatively, from (2.39) and using (2.41), it is possible to derive an equivalent homogenisation formula just in terms of boundary data as below*

$$\mathbf{P}_M|_{\mathbf{x}_M} = \mathcal{H}^{\mathbf{x}_M,*}_{\mathbf{P}_M}(\mathbf{t}_\mu) = \frac{1}{|\Omega_\mu|}\int_{\Gamma_\mu} \mathbf{t}_\mu \otimes (\mathbf{x}_\mu - \mathbf{x}^G_\mu) \, \mathrm{d}\Gamma_\mu, \tag{2.42}$$

and $\mathbf{t}_\mu := \mathbf{P}_\mu \mathbf{n}_\mu$ is the microcospic traction vector.

Remark 4 *Also note that if the microscale force per unit volume is constant, say $\mathbf{b}_\mu = \mathbf{b}$, and also from the definition of RVE centroid, the homogenisation formula (2.39) becomes*

$$\mathbf{P}_M|_{\mathbf{x}_M} = \frac{1}{|\Omega_\mu|}\int_{\Omega_\mu} \mathbf{P}_\mu \, \mathrm{d}\Omega_\mu. \tag{2.43}$$

Remark 5 *Recalling from classical continuum mechanics that $(\boldsymbol{\sigma}_M)_m = \frac{1}{\det \mathbf{F}_M}\mathbf{P}_M(\mathbf{F}_M)^T$ is the material description of the Cauchy stress tensor, and noting that $(\boldsymbol{\sigma}_M)_m|_{\mathbf{x}_M} = \frac{1}{\det \mathbf{F}_M|_{\mathbf{x}_M}}\mathbf{P}_M|_{\mathbf{x}_M}(\mathbf{F}_M|_{\mathbf{x}_M})^T$ is the evaluation of the Cauchy stress at the material point $\mathbf{x}_M \in \Omega_M$, we have that the Cauchy stress tensor can be obtained by post-processing the point-valued Piola-Kirchhoff stress tensor $\mathbf{P}_M|_{\mathbf{x}_M}$ resulting from a given homogenisation operator.*

2.4 Miscelanneous topics

This section is devoted to present some additional topics concerning the multiscale solid mechanics model of Section 2.3 that are also useful for other contexts. Section 2.4.1 and Section 2.4.2 are also applied to the model of Chapter 3 and Section 2.4.3 is generic for all kinds of models presented in the thesis.

2.4.1 Linearisation of the microscale model

The nonlinear variational problem in (2.40) needs some adequate special numerical method to be solved. Here we adopt the Newton-Raphson method, and the linearised version can be written as follows: Given $\tilde{\mathbf{u}}_\mu^k \in \widetilde{\mathscr{U}}_\mu$ and $\mathbf{G}_\mu^k = \mathbf{G}_M|_{\mathbf{x}_M} + \nabla_{\mathbf{x}_\mu}\tilde{\mathbf{u}}_\mu^k$, find $\delta\tilde{\mathbf{u}}_\mu^k \in \widetilde{\mathscr{U}}_\mu$ such that:

$$\begin{aligned} &\int_{\Omega_\mu} \mathbb{A}_\mu(\mathbf{G}_\mu^k)\nabla_{\mathbf{x}_\mu}\delta\tilde{\mathbf{u}}_\mu^k \cdot \nabla_{\mathbf{x}_\mu}\hat{\tilde{\mathbf{u}}}_\mu \, d\Omega_m = \\ -&\int_{\Omega_\mu} \mathbf{P}_\mu(\mathbf{G}_\mu^k)\cdot\nabla_{\mathbf{x}_\mu}\hat{\tilde{\mathbf{u}}}_\mu \, d\Omega_\mu + \int_{\Omega_\mu} \mathbf{b}_\mu \cdot \hat{\tilde{\mathbf{u}}}_\mu \, d\Omega_\mu \qquad \forall \hat{\tilde{\mathbf{u}}}_\mu \in \widetilde{\mathscr{U}}_\mu, \end{aligned} \tag{2.44}$$

where the constitutive microscopic tangent tensor is

$$\mathbb{A}_\mu(\mathbf{G}_\mu) = \partial_{\mathbf{G}_\mu}\mathbf{P}_\mu(\mathbf{G}_\mu). \tag{2.45}$$

The next step is to perform the increment of $\tilde{\mathbf{u}}_\mu$ for the next iteration as

$$\tilde{\mathbf{u}}_\mu^{k+1} = \tilde{\mathbf{u}}_\mu^k + \delta\tilde{\mathbf{u}}_\mu^k \tag{2.46}$$

until a convergence criterion is achieved.

Remark 6 *Note that the same procedure is also applied to macroscale mechanical problem. Therefore, there will be the need of the macroscale homogenised constitutive tangent $\mathbb{A}_M$ derived from the homogenised stress. This is subject of the next Section 2.4.2.*

2.4.2 Homogenised constitutive tangent

Similar to (2.45), we define the homogenised tangent tensor as the derivative of $\mathbf{P}_M$, the homogenised PKST, with respect to the macroscale displacement gradient $\mathbf{G}_M$, that is:

$$\mathbb{A}_M(\mathbf{G}_M) := \partial_{\mathbf{G}_M}\mathbf{P}_M(\mathbf{G}_M) \tag{2.47}$$

Considering an infinitesimal perturbation in the component $(\mathbf{G}_M)_{kl}$, for $k, l = 1, \dots \mathrm{n_d}$, we rewrite (2.47) as :

$$\mathbb{A}_M(\mathbf{G}_M) = \lim_{\varepsilon\to 0} \frac{[\mathbf{P}_M(\mathbf{G}_M + \varepsilon\mathbf{e}_k\otimes\mathbf{e}_l) - \mathbf{P}_M(\mathbf{G}_M)]_{ij}}{\varepsilon} \mathbf{e}_i\otimes\mathbf{e}_j\otimes\mathbf{e}_k\otimes\mathbf{e}_l \tag{2.48}$$

Note that although (2.47) is valid for the entire Ω_M, we are looking at a specific point $\mathbf{x}_M \in \Omega_M$. Hence, hereafter consider all objects evaluated for this point. Also, body forces are omitted just for sake of simplicity.

We now set an auxiliar vector $\tilde{\mathbf{u}}_\mu^{kl,\varepsilon} \in \widetilde{\mathscr{U}_\mu}$, which is the the solution of the perturbed microscale fluctuation problem as follows:

$$\int_{\Omega_\mu} \mathbf{P}_\mu(\mathbf{G}_M|_{\mathbf{x}_M} + \varepsilon \mathbf{e}_k \otimes \mathbf{e}_l + \nabla_{\mathbf{x}_\mu} \tilde{\mathbf{u}}_\mu^{kl,\varepsilon}) \cdot \nabla_{\mathbf{x}_\mu} \hat{\tilde{\mathbf{u}}}_\mu \, \mathrm{d}\Omega_\mu = 0 \qquad \forall \hat{\tilde{\mathbf{u}}}_\mu \in \widetilde{\mathscr{U}_\mu} \tag{2.49}$$

Defining $\mathbf{u}_{kl}^{can}$ through the relation:

$$\tilde{\mathbf{u}}_\mu^{kl,\varepsilon} = \tilde{\mathbf{u}}_\mu + \varepsilon \mathbf{u}_{kl}^{can} \tag{2.50}$$

We expand (2.49) by Taylor series

$$\int_{\Omega_\mu} \mathbf{P}_\mu(\mathbf{G}_\mu + \varepsilon \mathbf{e}_k \otimes \mathbf{e}_l + \varepsilon \nabla_{\mathbf{x}_\mu} \mathbf{u}_{kl}^{can}) \cdot \nabla_{\mathbf{x}_\mu} \hat{\tilde{\mathbf{u}}}_\mu \, \mathrm{d}\Omega_\mu = \underbrace{\int_{\Omega_\mu} \mathbf{P}_\mu(\mathbf{G}_\mu) \cdot \nabla_{\mathbf{x}_\mu} \hat{\tilde{\mathbf{u}}}_\mu \mathrm{d}\Omega_\mu}_{:=0 \text{ from } (2.40)} +$$

$$\varepsilon \int_{\Omega_\mu} \mathbb{A}_\mu(\mathbf{G}_\mu)(\mathbf{e}_k \otimes \mathbf{e}_l + \nabla_{\mathbf{x}_\mu} \mathbf{u}_{kl}^{can}) \cdot \nabla_{\mathbf{x}_\mu} \hat{\tilde{\mathbf{u}}}_\mu \, \mathrm{d}\Omega_\mu + \mathcal{O}(\varepsilon^2) = 0 \qquad \forall \hat{\tilde{\mathbf{u}}}_\mu \in \widetilde{\mathscr{U}_\mu}$$

Dividing last equation by ε and since we are interested in the limit when $\varepsilon \to 0$, $\mathcal{O}(\varepsilon^2)/\varepsilon = \mathcal{O}(\varepsilon)$ vanishes, we get the following canonical problem to find $\mathbf{u}_{kl}^{can} \in \widetilde{\mathscr{U}_\mu}$:

$$\int_{\Omega_\mu} \mathbb{A}_\mu(\mathbf{G}_\mu) \nabla_{\mathbf{x}_\mu} \mathbf{u}_{kl}^{can} \cdot \nabla_{\mathbf{x}_\mu} \hat{\tilde{\mathbf{u}}}_\mu \, \mathrm{d}\Omega_\mu = - \int_{\Omega_\mu} \mathbb{A}_\mu(\mathbf{G}_\mu)(\mathbf{e}_k \otimes \mathbf{e}_l) \cdot \nabla_{\mathbf{x}_\mu} \hat{\tilde{\mathbf{u}}}_\mu \, \mathrm{d}\Omega_\mu \qquad \forall \hat{\tilde{\mathbf{u}}}_\mu \in \widetilde{\mathscr{U}_\mu}. \tag{2.51}$$

Developing (2.48) in Taylor expansion for the perturbation in kl we have:

$$\begin{aligned}
&\lim_{\varepsilon \to 0} \frac{1}{\varepsilon} \left[\mathbf{P}_M|_{\mathbf{x}_M}(\mathbf{G}_M|_{\mathbf{x}_M} + \varepsilon \mathbf{e}_k \otimes \mathbf{e}_l) - \mathbf{P}_M|_{\mathbf{x}_M}(\mathbf{G}_M|_{\mathbf{x}_M}) \right] \otimes \mathbf{e}_k \otimes \mathbf{e}_l \\
&= \left[\frac{1}{|\Omega_\mu|} \int_{\Omega_\mu} \lim_{\varepsilon \to 0} \frac{1}{\varepsilon} \Big(\mathbf{P}_\mu(\mathbf{G}_\mu + \varepsilon \mathbf{e}_k \otimes \mathbf{e}_l + \varepsilon \nabla_{\mathbf{x}_\mu} \mathbf{u}_{kl}^{can}) - \mathbf{P}_\mu(\mathbf{G}_\mu) \Big) \, \mathrm{d}\Omega_\mu \right] \otimes \mathbf{e}_k \otimes \mathbf{e}_l \\
&= \left[\frac{1}{|\Omega_\mu|} \int_{\Omega_\mu} \lim_{\varepsilon \to 0} \mathbb{A}_\mu(\mathbf{G}_\mu)(\mathbf{e}_k \otimes \mathbf{e}_l + \nabla_{\mathbf{x}_\mu} \mathbf{u}_{kl}^{can}) + \mathcal{O}(\varepsilon) \, \mathrm{d}\Omega_\mu \right] \otimes \mathbf{e}_k \otimes \mathbf{e}_l \\
&= \left[\frac{1}{|\Omega_\mu|} \int_{\Omega_\mu} [\mathbb{A}_\mu(\mathbf{G}_\mu)]_{ijpq} [\mathbf{e}_k \otimes \mathbf{e}_l + \nabla_{\mathbf{x}_\mu} \mathbf{u}_{kl}^{can}]_{pq} \, \mathrm{d}\Omega_\mu \right] \mathbf{e}_i \otimes \mathbf{e}_j \otimes \mathbf{e}_k \otimes \mathbf{e}_l \\
&= \left[\underbrace{\frac{1}{|\Omega_\mu|} \int_{\Omega_\mu} [\mathbb{A}_\mu(\mathbf{G}_\mu)]_{ijkl} \, \mathrm{d}\Omega_\mu}_{:=[\overline{\mathbb{A}_M}]_{ijkl}} + \underbrace{\frac{1}{|\Omega_\mu|} \int_{\Omega_\mu} [\mathbb{A}_\mu(\mathbf{G}_\mu)]_{ijpq} [\nabla_{\mathbf{x}_\mu} \mathbf{u}_{kl}^{can}]_{pq} \, \mathrm{d}\Omega_\mu}_{:=[\widetilde{\mathbb{A}_M}]_{ijkl}} \right] \mathbf{e}_i \otimes \mathbf{e}_j \otimes \mathbf{e}_k \otimes \mathbf{e}_l
\end{aligned}$$

Thus we have identified above the components that define the Taylor and fluctuation contributions, respectively, as the tensors $\overline{\mathbb{A}_M}$ and $\widetilde{\mathbb{A}_M}$, yielding $\mathbb{A}_M = \overline{\mathbb{A}_M} + \widetilde{\mathbb{A}_M}$. In intrinsic notation we have

$$\overline{\mathbb{A}_M} = \frac{1}{|\Omega_\mu|} \int_{\Omega_\mu} \mathbb{A}_\mu \, \mathrm{d}\Omega_\mu \tag{2.52}$$

and

$$\widetilde{\mathbb{A}_M} = \left[\frac{1}{|\Omega_\mu|} \int_{\Omega_\mu} \mathbb{A}_\mu \nabla_{\mathbf{x}_\mu} \mathbf{u}_{kl}^{can} \, d\Omega_\mu \right] \otimes \mathbf{e}_k \otimes \mathbf{e}_l \tag{2.53}$$

where $\mathbf{u}_{kl}^{can}$, $k, l = 1, \ldots, \mathrm{n_d}$, are the solutions of the canonical problems formulated in (2.51).

2.4.2.1 Proof of the major-symmetry

Now we want to prove an important aspect of $\mathbb{A}_M$, its major symmetry. As a matter of fact, saying that a general fourth-order tensor $\mathbb{A}$ has major symmetry is equivalent to have

$$\mathbb{A}\mathbf{C} \cdot \mathbf{D} = \mathbb{A}\mathbf{D} \cdot \mathbf{C} \quad \text{for any } \mathbf{C}, \mathbf{D} \text{ second-order tensors,} \tag{2.54}$$

where conventional product between fourth-order and second-order tensors as well as the conventional dot product for second-order tensors have been admitted. In cartesian coordinates and using indicial notation this means $[\mathbb{A}]_{ijkl} = [\mathbb{A}]_{klij}$ for any $i, j, k, l \in \{1, 2, \ldots, \mathrm{n_d}\}$.

From (2.52) and by assuming that $\mathbb{A}_\mu$ is major-symmetric, the contribution $\overline{\mathbb{A}_M}$ is major-symmetric. Now we will prove the same property to $\widetilde{\mathbb{A}_M}$. For this aim, first take $\hat{\mathbf{u}}_\mu = \mathbf{u}_{ij}^{can} \in \widetilde{\mathscr{U}_\mu}$ in (2.51), so

$$\begin{aligned}\int_{\Omega_\mu} \mathbb{A}_\mu \nabla_{\mathbf{x}_\mu} \mathbf{u}_{kl}^{can} \cdot \nabla_{\mathbf{x}_\mu} \mathbf{u}_{ij}^{can} \, d\Omega_\mu &= - \int_{\Omega_\mu} \mathbb{A}_\mu (\mathbf{e}_k \otimes \mathbf{e}_l) \cdot \nabla_{\mathbf{x}_\mu} \mathbf{u}_{ij}^{can} \, d\Omega_\mu \\ &= - \int_{\Omega_\mu} \mathbb{A}_\mu^T \nabla_{\mathbf{x}_\mu} \mathbf{u}_{ij}^{can} \cdot (\mathbf{e}_k \otimes \mathbf{e}_l) \, d\Omega_\mu \\ = - \underbrace{\int_{\Omega_\mu} \mathbb{A}_\mu \nabla_{\mathbf{x}_\mu} \mathbf{u}_{ij}^{can} \, d\Omega_\mu}_{:\mathbf{J}_{ij}} &\cdot \underbrace{(\mathbf{e}_k \otimes \mathbf{e}_l)}_{:\mathbf{E}_{kl}} = -\mathbf{J}_{ij} \cdot \mathbf{E}_{kl}\end{aligned} \tag{2.55}$$

On the other hand, we have

$$\int_{\Omega_\mu} \mathbb{A}_\mu \nabla_{\mathbf{x}_\mu} \mathbf{u}_{kl}^{can} \cdot \nabla_{\mathbf{x}_\mu} \mathbf{u}_{ij}^{can} \, d\Omega_\mu = \int_{\Omega_\mu} \mathbb{A}_\mu \nabla_{\mathbf{x}_\mu} \mathbf{u}_{ij}^{can} \cdot \nabla_{\mathbf{x}_\mu} \mathbf{u}_{kl}^{can} \, d\Omega_\mu = -\mathbf{J}_{kl} \cdot \mathbf{E}_{ij} \tag{2.56}$$

Thus, it follows that $\mathbf{J}_{kl} \cdot \mathbf{E}_{ij} = \mathbf{J}_{ij} \cdot \mathbf{E}_{kl}$.

Clearly the set $\{\mathbf{E}_{pq}\}_{p,q=1,\ldots,\mathrm{n_d}}$ is a basis to the second-order tensor space, so $\mathbf{J}_{kl}$ can be expressed as the summation $\mathbf{J}_{kl} = (\mathbf{J}_{kl} \cdot \mathbf{E}_{ij})\mathbf{E}_{ij}$, where Einstein's notation is implied. By using this decomposition we have

$$\begin{aligned}\mathbf{J}_{kl} \otimes \mathbf{E}_{kl} = ((\mathbf{J}_{kl} \cdot \mathbf{E}_{ij})\mathbf{E}_{ij}) \otimes \mathbf{E}_{kl} = \mathbf{E}_{ij} \otimes ((\mathbf{J}_{kl} \cdot \mathbf{E}_{ij})\mathbf{E}_{kl}) = \\ \mathbf{E}_{ij} \otimes ((\mathbf{J}_{ij} \cdot \mathbf{E}_{kl})\mathbf{E}_{kl}) = \mathbf{E}_{ij} \otimes \mathbf{J}_{ij} = \mathbf{E}_{kl} \otimes \mathbf{J}_{kl}.\end{aligned} \tag{2.57}$$

Finally, from the above conclusion and recalling (2.53) we have $\widetilde{\mathbb{A}_M} = \frac{1}{|\Omega_\mu|}\mathbf{J}_{kl} \otimes \mathbf{E}_{kl} = \frac{1}{|\Omega_\mu|}\mathbf{E}_{kl} \otimes \mathbf{J}_{kl}$. Indeed, if a fourth-order tensor satisfies the former commutation property, thus (2.54) holds straightforwardly.

2.4.3 Incompressible Materials

An important class of materials of special interest to the mechanics of soft tissues is the one of incompressible materials. In brief, a material is said to be incompressible if it undergoes a motion without changing of volume locally, i.e., for every material point in the body, the determinant of the deformation gradient is positive unitary. Focusing on the multiscale constitutive modelling of such materials, we are interested in the case in which the macroscale kinematics verifies the incompressibility constraint whilst the microscale kinematic may be compressible, i.e., it does not fulfil the incompressibility constraint point-wisely. Moreover, the resulting homogenised stress only provides a constitutive law for isochoric (or deviatoric) [3] for the PKST.

It is worth mentioning that as our modification of the traditional is postulated at the macroscale level, the proposed procedure is independent of the mechanical model adopted for the microscale. Hence, the very same procedure shown in this section can be applied either for continuum mechanical models at the microscale, as in this chapter, as well as for the discrete mechanical model considered at the microscale which is to be detailed in Chapter 4 for fibrous materials.

2.4.3.1 Admissible macroscale displacement set

Given the scenario described previously, the strategy to address this issue in the framework of the MMVP is straightforward. As usual in variational formulations, the kinematics has to be changed accordingly. Let us admit the space $\mathscr{U}_M$ and an admissible set of displacements $\mathrm{Kin}_{\mathscr{U}_M}$, which is not incompressible yet. In the case of an incompressible macroscale model, the set of kinematically admissible displacement fields is

$$\mathrm{Kin}_{\mathscr{U}_M}^{\mathsf{inc}} = \{\mathbf{u}_M \in \mathrm{Kin}_{\mathscr{U}_M}; \det(\mathbf{I} + \nabla_{\mathbf{x}_M}\mathbf{u}_M) = 1 \text{ in } \Omega_M\}. \tag{2.58}$$

Since the above manifold is nonlinear, the associated space of admissible virtual displacements follows from the corresponding tangent space given below

$$\begin{aligned}\mathrm{Var}_{\mathscr{U}_M}^{\mathsf{inc}} =& \{\hat{\mathbf{u}}_M \in \mathrm{Var}_{\mathscr{U}_M}; (\mathbf{I} + \nabla_{\mathbf{x}_M}\mathbf{u}_M)^{-T} \cdot \nabla\hat{\mathbf{u}}_M = 0 \text{ in } \Omega_M\} \\ =& \{\hat{\mathbf{u}}_M \in \mathrm{Var}_{\mathscr{U}_M}; \operatorname{tr}\left(\nabla_{\mathbf{x}_M}\hat{\mathbf{u}}_M (\mathbf{I} + \nabla_{\mathbf{x}_M}\mathbf{u}_M)^{-1}\right) = 0 \text{ in } \Omega_M\}\end{aligned} \tag{2.59}$$

Accordingly, the variational formulation in Problem 1 needs to be slightly changed by switching $\mathrm{Kin}_{\mathscr{U}_M}$ and $\mathrm{Var}_{\mathscr{U}_M}$ to $\mathrm{Kin}_{\mathscr{U}_M}^{\mathsf{inc}}$ and $\mathrm{Var}_{\mathscr{U}_M}^{\mathsf{inc}}$, respectively.

[3] By isochoric (or deviatoric) part of the PKST we mean that the trace of the corresponding Cauchy stress is zero. The classical transformation between Piola-Kirchhoff and Cauchy stress tensors is recalled in Remark 5.

2.4.3.2 Point-valued strain and strain rate set

For a specific point $\mathbf{x}_M \in \Omega_M$, from the definition in (2.58) and (2.59) it follows

$$\mathbf{G}_M|_{\mathbf{x}_M} \in \mathbb{R}^{\mathbf{x}_M,\mathsf{inc}}_{\mathscr{E}_M} = \{\mathbf{A} \in \mathbb{R}^{\mathrm{n_d}\times\mathrm{n_d}};\ \det(\mathbf{I}+\mathbf{A}) = 1\}, \tag{2.60}$$

$$\hat{\mathbf{G}}_M|_{\mathbf{x}_M} \in \widehat{\mathbb{R}^{\mathbf{x}_M,\mathsf{inc}}_{\mathscr{E}_M}} = \{\hat{\mathbf{A}} \in \mathbb{R}^{\mathrm{n_d}\times\mathrm{n_d}};\ \mathrm{tr}\left(\hat{\mathbf{A}}(\mathbf{I}+\mathbf{G})^{-1}\right) = 0\}. \tag{2.61}$$

The PMVP in Problem 2 is easily cast into the incompressible case by appropriately replacing $\mathbb{R}^{\mathbf{x}_M}_{\mathscr{E}_M}$ and $\widehat{\mathbb{R}^{\mathbf{x}_M}_{\mathscr{E}_M}}$ by the subsets $\mathbb{R}^{\mathbf{x}_M,\mathsf{inc}}_{\mathscr{E}_M}$ and $\widehat{\mathbb{R}^{\mathbf{x}_M,\mathsf{inc}}_{\mathscr{E}_M}}$, respectively (recall that it is assumed $\mathbb{R}^{\mathbf{x}_M}_{\mathscr{E}_M} = \widehat{\mathbb{R}^{\mathbf{x}_M}_{\mathscr{E}_M}} = \mathbb{R}^{\mathrm{n_d}\times\mathrm{n_d}}$).

2.4.3.3 Homogenisation formula

Let us analyse the impact of the modified admissible sets accounting for incompressibility upon the related variational consequences of the PMVP, particularly, in the homogenisation operator. First, let us retake (2.36) for $\hat{\mathbf{u}}_M|_{\mathbf{x}_M} = \mathbf{0}$ and $\hat{\tilde{\mathbf{u}}}_\mu = \mathbf{0}$ and also considering the expression for $\mathcal{H}^{\mathbf{x}_M}_{\mathbf{P}_M}$ in (2.39), then

$$\left(\mathbf{P}_M|_{\mathbf{x}_M} - \mathcal{H}^{\mathbf{x}_M}_{\mathbf{P}_M}(\mathbf{P}_\mu, \mathbf{b}_\mu)\right) \cdot \hat{\mathbf{G}}_M|_{\mathbf{x}_M} = 0 \quad \forall \hat{\mathbf{G}}_M|_{\mathbf{x}_M} \in \widehat{\mathbb{R}^{\mathbf{x}_M}_{\mathscr{E}_M}} \tag{2.62}$$

Now, instead of $\mathbf{P}_M|_{\mathbf{x}_M}$ let us consider $\mathbf{P}^{\mathsf{iso}}_M|_{\mathbf{x}_M}$. Then, replacing $\widehat{\mathbb{R}^{\mathbf{x}_M}_{\mathscr{E}_M}}$ by $\widehat{\mathbb{R}^{\mathbf{x}_M,\mathsf{inc}}_{\mathscr{E}_M}}$ yields

$$\left(\mathbf{P}^{\mathsf{iso}}_M|_{\mathbf{x}_M} - \mathcal{H}^{\mathbf{x}_M}_{\mathbf{P}_M}(\mathbf{P}_\mu, \mathbf{b}_\mu)\right) \cdot \hat{\mathbf{G}}_M|_{\mathbf{x}_M} = 0 \quad \forall \hat{\mathbf{G}}_M|_{\mathbf{x}_M} \in \widehat{\mathbb{R}^{\mathbf{x}_M,\mathsf{inc}}_{\mathscr{E}_M}} \tag{2.63}$$

Using classical tensor identities[4] and noting that $\mathbf{F}_M|_{\mathbf{x}_M} = \mathbf{I} + \mathbf{G}_M|_{\mathbf{x}_M}$ is nonsingular, we have that condition (2.63) is equivalent to

$$\left(\mathbf{P}^{\mathsf{iso}}_M|_{\mathbf{x}_M} - \mathcal{H}^{\mathbf{x}_M}_{\mathbf{P}_M}(\mathbf{P}_\mu, \mathbf{b}_\mu)\right)\mathbf{F}^T_M|_{\mathbf{x}_M} \cdot \hat{\mathbf{G}}_M|_{\mathbf{x}_M}\mathbf{F}^{-1}_M|_{\mathbf{x}_M} = 0 \quad \forall \hat{\mathbf{G}}_M|_{\mathbf{x}_M} \in \mathbb{T}_{\mathsf{inc}}, \tag{2.64}$$

but, since $\mathrm{tr}(\hat{\mathbf{G}}_M|_{\mathbf{x}_M}\mathbf{F}^{-1}_M|_{\mathbf{x}_M}) = 0$, it results

$$\left(\mathbf{P}^{\mathsf{iso}}_M|_{\mathbf{x}_M} - \mathcal{H}^{\mathbf{x}_M}_{\mathbf{P}_M}(\mathbf{P}_\mu, \mathbf{b}_\mu)\right)\mathbf{F}^T_M|_{\mathbf{x}_M} = \beta\mathbf{I}, \tag{2.65}$$

with $\beta \in \mathbb{R}$. Hence $\mathbf{P}^{\mathsf{iso}}_M|_{\mathbf{x}_M}$ is of the form

$$\mathbf{P}^{\mathsf{iso}}_M|_{\mathbf{x}_M} = \mathcal{H}^{\mathbf{x}_M}_{\mathbf{P}_M}(\mathbf{P}_\mu, \mathbf{b}_\mu) + \beta\mathbf{F}^{-T}_M|_{\mathbf{x}_M}. \tag{2.66}$$

Taking β such that $\mathrm{tr}\left(\frac{1}{\det \mathbf{F}_M|_{\mathbf{x}}}\mathbf{P}^{\mathsf{iso}}_M|_{\mathbf{x}_M}\mathbf{F}^T_M|_{\mathbf{x}_M}\right) = 0$ (see Remark 5) we have

$$\beta = -\frac{1}{\mathrm{n_d}}\mathrm{tr}(\mathcal{H}^{\mathbf{x}_M}_{\mathbf{P}_M}(\mathbf{P}_\mu, \mathbf{b}_\mu)\mathbf{F}^T_M|_{\mathbf{x}_M}) = -\frac{1}{\mathrm{n_d}}\mathcal{H}^{\mathbf{x}_M}_{\mathbf{P}_M}(\mathbf{P}_\mu, \mathbf{b}_\mu) \cdot \mathbf{F}_M|_{\mathbf{x}_M}, \tag{2.67}$$

which replaced in (2.66) gives

$$\begin{aligned}\mathbf{P}^{\mathsf{iso}}_M|_{\mathbf{x}_M} &= \mathcal{H}^{\mathbf{x}_M}_{\mathbf{P}_M}(\mathbf{P}_\mu, \mathbf{b}_\mu) - \frac{1}{\mathrm{n_d}}\left(\mathcal{H}^{\mathbf{x}_M}_{\mathbf{P}_M}(\mathbf{P}_\mu, \mathbf{b}_\mu) \cdot \mathbf{F}_M|_{\mathbf{x}_M}\right)\mathbf{F}^{-T}_M|_{\mathbf{x}_M} \\ &= \mathcal{H}^{\mathbf{x}_M}_{\mathbf{P}_M}(\mathbf{P}_\mu, \mathbf{b}_\mu) - \frac{1}{\mathrm{n_d}}(\mathbf{F}^{-T}_M|_{\mathbf{x}_M} \otimes \mathbf{F}_M|_{\mathbf{x}_M})\mathcal{H}^{\mathbf{x}_M}_{\mathbf{P}_M}(\mathbf{P}_\mu, \mathbf{b}_\mu).\end{aligned} \tag{2.68}$$

[4] For any $\mathbf{A}_1$, $\mathbf{A}_2$ and $\mathbf{A}_3$ second order tensors the following identity holds: $\mathbf{A}_1 \cdot \mathbf{A}_2\mathbf{A}_3 = \mathbf{A}_1\mathbf{A}_3^T \cdot \mathbf{A}_2$.

Finally, defining the fourth order tensor

$$\mathbb{T}^{\mathsf{iso}}|_{\mathbf{x}} = \mathbb{I} - \frac{1}{\mathrm{n_d}} \mathbf{F}_M^{-T}|_{\mathbf{x}_M} \otimes \mathbf{F}_M|_{\mathbf{x}_M}, \tag{2.69}$$

with $\mathbb{I}$ being fourth-order identity tensor, we have the isochoric part of the stress, which is

$$\mathbf{P}_M^{\mathsf{iso}}|_{\mathbf{x}_M} = \mathcal{H}_{\mathbf{P}_M}^{\mathbf{x}_M,\mathsf{iso}}(\mathbf{P}_\mu, \mathbf{b}_\mu) = \mathbb{T}^{\mathsf{iso}}|_{\mathbf{x}} \mathcal{H}_{\mathbf{P}_M}^{\mathbf{x}_M}(\mathbf{P}_\mu, \mathbf{b}_\mu). \tag{2.70}$$

We highlight that the only difference between (2.39) and (2.70) is the pre-multiplication of the projection isochoric tensor in the former homogenisation formula. Moreover, by construction the homogenised Piola-Kirchhoff macroscale stress tensor in the incompressible case, transformed into the corresponding Cauchy stress, features null trace.

2.5 Closing remarks

In this chapter we have reviewed the Method of Multiscale Virtual Power (MMVP) (BLANCO et al., 2014; BLANCO et al., 2016), which is the basic tool that will guide the theoretical development of the forthcoming chapters. Such a unified variational theory addresses a general class of multiscale models based on the concept of Representative Volume Element and is based on three fundamental principles: (i) kinematical admissibility, (ii) duality and (ii) the Principle of Multiscale Virtual Power (PMVP). Particularly important is the fact that the MMVP allows the construction of non-standard multiscale models in a relatively intuitive manner, without ambiguities. In fact, as usual in variational formulations, the postulation of the kinematics is the only degree of arbitrariness of the methodology. This was illustrated by presenting the classical multiscale model for solid mechanics.

It is shown that the proposed systematisation of RVE-based multiscale modelling is particularly relevant in the two forthcoming chapters. Firstly, in Chapter 3, in the context of porous micro-structures, we change the definitions of insertion kinematical operators. Thus, macroscale kinematical descriptors are inserted exclusively on the solid part of the RVE domain. This subtle change leads to a novel multiscale formulation which resolves the inconsistencies that may arise when voids reach the RVE boundary in a random manner. Secondly, in Chapter 4, we propose a model with dissimilar kinematics, being a discrete network of fibres at microscale and the usual finite strain continuum at macroscale. Also, it is demonstrated that a postulation of a different kinematical setting at microscale leads to the emergence of non-trivial additional ingredients.

Finally, it is worth mentioning that although this chapter is not devoted to the presentation of the major contributions of this thesis, the topics of Section 2.4 are particularly relevant, since these results are not readily found in the literature in a such level of details. In fact, the demonstration of the major-symmetry of $\mathbb{A}_M$ in Section 2.4.2, at least up to the author's knowledge, is novel. The analogous proof for the homogenised tangent tensor for the fibrous material is presented in Chapter 5 and is also a contribution of this thesis (ROCHA et al., 2019). Note that in the latter context, the major-symmetry has important consequences concerning the discontinuous bifurcation analysis.

3 A Consistent Multiscale Model for Solids with Voids reaching Boundary

Everything should be made as simple as possible, but not simpler.

Albert Einstein

Retaking the problematic about the random porous materials already discussed in Section 1.3, multiscale models relying on the concept of RVE have been consistently formulated, largely tested and widely understood for the cases where either microscopic voids did not reach the RVE boundary or they did reach it in a structured manner. The case of randomly distributed voids which randomly reach the boundary of the RVE has not received the same focus, and the utilisation in this latter case of the concepts and strategies borrowed from the former cases may yield results which are, at least, questionable from the mathematical/physical point of view.

Consider, for example, the fenestrated microcell illustrated in Fig. 7, featuring a random distribution of voids, which ultimately reach the boundary in a truly random manner. A more constrained model (upper bound in stress) is easily postulated using the linear boundary model of the previous chapter (see (2.33)). On the contrary, the definition of a minimally constrained space (lower bound) in this kind of microstructure is problematic, and to some extent debatable. Clearly, if we apply a uniform traction (actually a uniform stress tensor applied over the normal vector to the solid boundary) acting over the solid boundary, the RVE is then subjected to a system of boundary forces which is not self-equilibrated. The lack of self-equilibrium of such uniform traction model is originated from the fact that the solid part of the RVE boundary does not form a *balanced* surface (the integral of the normal vector over solid part of the boundary is not zero). We conclude, then, that the so-called called *uniform traction model* in the previous sense (see (2.31)) has to be revised in the context of RVEs as in Fig. 7. Note that neither can the classical periodic model (see (2.34)) be applied because there is no one-to-one correspondence between material particles oppositely lying at both parallel (vertical and horizontal) sides of the boundary. The naive solution, and actually what is normally employed in the literature, is the utilisation of the linear boundary model. However, while it is a practical solution, it is known that this model can result much stiffer than it should be, not providing insight about the lower bound for the material response.

The case of fibrous materials in which fibres are distributed randomly (also known as non-woven materials) is a typical example of which the hypothesis of periodic structure of voids reaching boundary fails. In this direction, this chapter addresses the construction of a multiscale model for continuum solid media featuring a random distribution of voids (see Fig. 7). Therefore, the target of the present chapter is to provide the theoretical continuum groundwork in which the proper discrete multiscale theory for fibrous materials, to be presented in Chapter 4, is built upon.

The chapter is organised following an analagous structure to that of Section 2.3, in which the standard multiscale model for solid mechanics was presented. Section 3.1 discusses the multiscale setting and also some preliminary notation required for a clear definition of the parts of a porous RVE. Section 3.2 describes the kinematics at the microscale, where subtle differences between the standard model and the proposed one appear, resulting in a novel space of kinematically admissible fluctuation fields. Section 3.3 presents the postulation of the PMVP followed by the derivation of its corollaries. An important attention shall be given to Section 3.3.4, where an analysis based on the concept of Lagrange Multipliers unveils the physical interpretation of the model putting in evidence the principal advantages of the proposed theory. It is worth mentioning that for the sake of readability a lighter notation (if compared to Chapter 2), is adopted hereafter, i.e., less indexes and use of operators. Also, many of the developments of Section 2.3 is reutilised here.

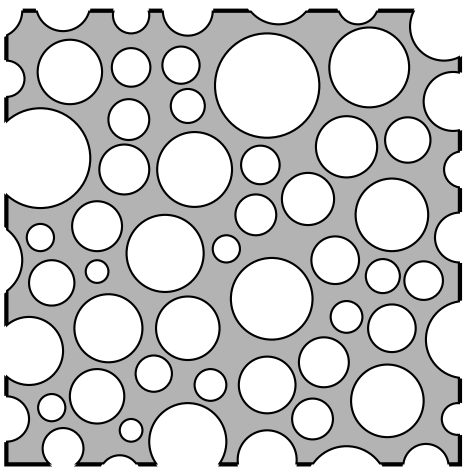

Figure 7 – Microscale domain with random distribution of circular voids. The integral of the normal vector over the solid part of the RVE boundary (in bold) is not zero.

3.1 Multiscale setting and preliminary notation

Consider the multiscale setting shown in Fig. 8 that keeps the very same format to one presented in Section 2.3 (Fig. 6). As it can be appreciated, the only important difference here is the massive presence of voids in the RVE domain, in particular crossing the imaginary square window of observation of the RVE. We refer the reader to Section 2.3.1 for comments concerning the macroscale model. Importantly, we drop subindexes for kinematical and force/stress-like objects, e.g, $\mathbf{G}$ is used instead of $\mathbf{G}_M$ and so on.

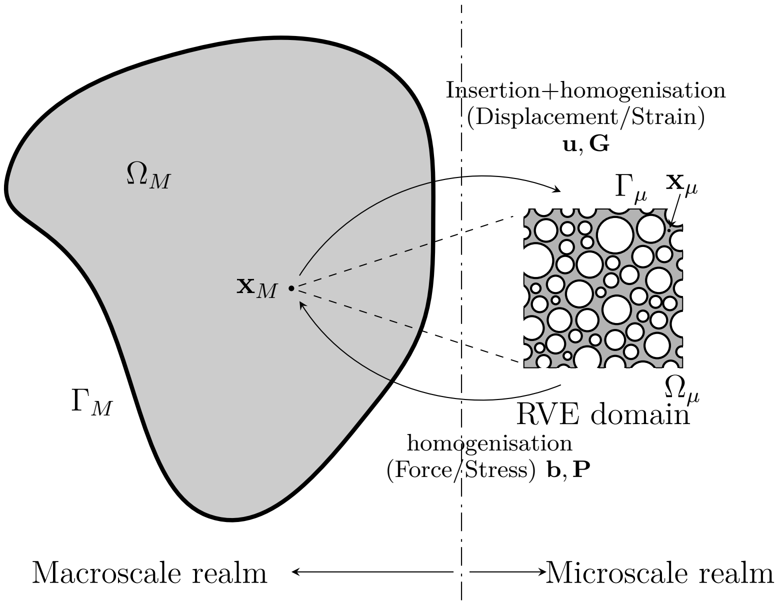

Figure 8 – Multiscale setting for the modelling in continuum mechanics in random porous media.

Let $\Omega_\mu \subset \mathbb{R}^{\mathrm{n_d}}$ be the microscale domain in which the mechanical problem is to be postulated. This domain requires consistent and suitable boundary conditions as we will see. As anticipated in the introduction, we are interested in modelling families of microstructures with aleatory arrangement of voids (periodicity condition is not satisfied). In an attempt to tipify the microscale domain we can isolate a small portion of the material. In doing this, the so-defined RVE domain will feature internal voids, but also parts of these voids will eventually be cut by the RVE boundary (see sketches in Figures 7 and 10). Such general context poses some critical issues for the setting of consistent boundary conditions, as we illustrate in forthcoming sections.

We define the following sets of points in the RVE domain:

- Ω_μ: the entire RVE domain including solid material and voids;
- Ω_μ^s: solid part of the RVE domain;
- Ω_μ^v: region occupied by voids in the RVE domain;

With the previous definitions we have that $\Omega_\mu = (\overline{\Omega_\mu^s \cup \Omega_\mu^v})^\circ$. Thus, we have

- Γ_μ: boundary of the RVE domain;

- Γ_μ^s: boundary of Ω_μ^s;
- $\Gamma_\mu^{s,v}$: boundary of Ω_μ^s shared with the boundaries of the voids (either internal or external voids;
- $\Gamma_\mu^{s,b}$: boundary of Ω_μ^s shared with the RVE boundary.

Some of boundaries are depicted on Figure 9. With the previous definitions it is $\Gamma_\mu^{s,b} = \Gamma_\mu \cap \Gamma_\mu^s$, and also

$$\Gamma_\mu^s = \Gamma_\mu^{s,v} \cup \Gamma_\mu^{s,b}. \tag{3.1}$$

At this point, we introduce a fundamental definition required for the developments to come. We say that the RVE is $\mathbf{n}_\mu$-balanced if the following condition is satisfied

$$\int_{\Gamma_\mu^{s,b}} \mathbf{n}_\mu \, \mathrm{d}\Gamma_\mu = \mathbf{0}, \tag{3.2}$$

where $\mathbf{n}_\mu$ is the outward unit normal vector to $\Gamma_\mu^{s,b}$. If (3.2) is not satisfied, then the RVE is said to be $\mathbf{n}_\mu$-unbalanced.

Remark 7 *Usually, in the literature, the microscale domains regarded in multiscale simulations are such that the entire RVE boundary is solid, or at least periodic, cases in which* (3.2) *trivially holds, and so this kind of RVE choices are $\mathbf{n}_\mu$-balanced (see first and second columns in Figure 10). In general, a RVE may not guarantee* (3.2)*, and so it is $\mathbf{n}_\mu$-unbalanced (see third column in Figure 10).*

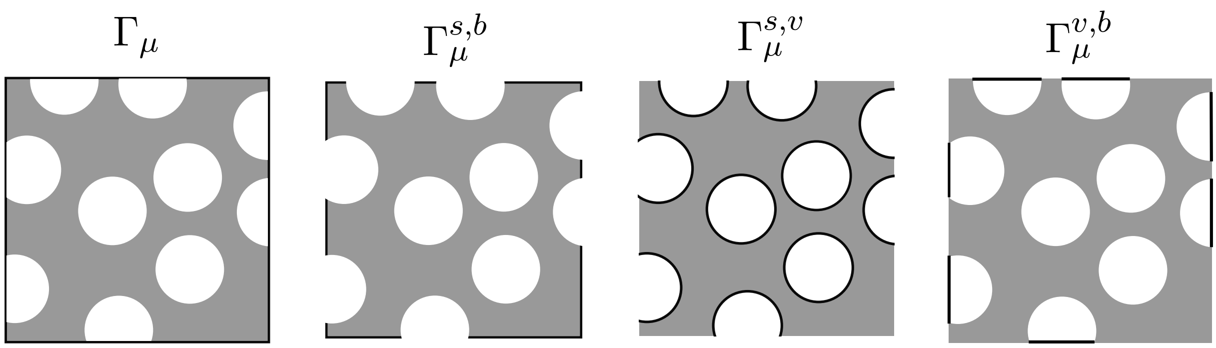

Figure 9 – Scheme of the boundary partitioning for a generic porous RVE geometry.

3.2 Kinematics

Henceforward, we consider the macroscale kinematics at a point $\mathbf{x}_M \in \Omega_M$ defined by $\mathbf{u} \in \mathbb{R}^{\mathrm{n_d}}$ and $\mathbf{G} \in \mathbb{R}^{\mathrm{n_d} \times \mathrm{n_d}}$ (contraction of notations $\mathbf{u}_M|_{\mathbf{x}_M}$ and $\mathbf{G}_M|_{\mathbf{x}_M}$, respectively).

3.2.1 Kinematical insertion

We assume that the displacement $\mathbf{u}$ and the displacement gradient $\mathbf{G}$ are inserted into the solid part of the microscale domain Ω_μ^s following an affine relation, that is

$$\mathbf{u}_\mu(\mathbf{x}_\mu) = \mathbf{u} + \mathbf{G}(\mathbf{x}_\mu - \mathbf{x}_\mu^G) + \tilde{\mathbf{u}}_\mu(\mathbf{x}_\mu) \qquad \mathbf{x}_\mu \in \Omega_\mu^s, \tag{3.3}$$

where $\tilde{\mathbf{u}}_\mu$ is a fluctuating displacement field defined in the microscale solid part of the domain and $\mathbf{x}_\mu^G$ is defined in Section 3.2.2. Hence, we have that $\mathbf{u}_\mu, \tilde{\mathbf{u}}_\mu \in [H^1(\Omega_\mu^s)]^{\mathrm{n_d}}$. Hence, the gradient of the microscale displacement field (3.3) is also defined for the solid part as

$$\mathbf{G}_\mu(\mathbf{x}_\mu) = \nabla_{\mathbf{x}_\mu}\mathbf{u}_\mu(\mathbf{x}_\mu) = \mathbf{G} + \nabla_{\mathbf{x}_\mu}\tilde{\mathbf{u}}_\mu(\mathbf{x}_\mu) \qquad \mathbf{x}_\mu \in \Omega_\mu^s. \tag{3.4}$$

Hereafter we drop the functional dependence for ease of notation.

Remark 8 *Notice that the kinematics is exclusively defined in the solid part of the RVE domain, where actually material particles lie. No kinematics whatsoever is regarded in the empty domain of the voids.*

3.2.2 Displacement homogenisation

Now, we postulate the homogenisation formula for the displacement field as follows

$$\mathbf{u} = \frac{1}{|\Omega_\mu^s|}\int_{\Omega_\mu^s} \mathbf{u}_\mu \, \mathrm{d}\Omega_\mu^s, \tag{3.5}$$

that is, the average of the microscale displacement field in the solid domain Ω_μ^s must be equal to the macroscale displacement field. By introducing (3.3) into (3.5) we have

$$\mathbf{u} = \mathbf{u} + \mathbf{G}\left(\frac{1}{|\Omega_\mu^s|}\int_{\Omega_\mu^s}(\mathbf{x}_\mu - \mathbf{x}_\mu^G)\,\mathrm{d}\Omega_\mu^s\right) + \frac{1}{|\Omega_\mu^s|}\int_{\Omega_\mu^s}\tilde{\mathbf{u}}_\mu\,\mathrm{d}\Omega_\mu^s. \tag{3.6}$$

By considering first $\tilde{\mathbf{u}}_\mu = \mathbf{0}$, (3.6) leads us to

$$\mathbf{x}_\mu^G = \frac{1}{|\Omega_\mu^s|}\int_{\Omega_\mu^s}\mathbf{x}_\mu\,\mathrm{d}\Omega_\mu^s. \tag{3.7}$$

Inserting (3.7) into the homogenisation rule (3.6) we have that it is trivially verified provided that the fluctuation field $\tilde{\mathbf{u}}_\mu$ satisfies the following constraint

$$\int_{\Omega_\mu^s}\tilde{\mathbf{u}}_\mu\,\mathrm{d}\Omega_\mu^s = \mathbf{0}. \tag{3.8}$$

To end this section, it is worth noting that the constraint (3.8) and the definition (3.7) are consequences of applying the kinematically admissibility concept to the macro and microscale displacement fields, which are connected through the homogenisation operator (3.5), as postulated in the framework of the MMVP in Chapter 2.

3.2.3 Gradient homogenisation

The homogenisation formula for the first order gradient of the microscale displacement field is postulated as follows

$$\mathbf{G} = \frac{1}{|\Omega_\mu^s|}\left[\int_{\Omega_\mu^s} \nabla_{\mathbf{x}_\mu}\mathbf{u}_\mu \,\mathrm{d}\Omega_\mu^s - \int_{\Gamma_\mu^{s,v}} \tilde{\mathbf{u}}_\mu \otimes \mathbf{n}_\mu \,\mathrm{d}\Gamma_\mu - \int_{\Gamma_\mu^{s,b}} \tilde{\mathbf{u}}_\mu \otimes \bar{\mathbf{n}}_\mu \,\mathrm{d}\Gamma_\mu\right], \tag{3.9}$$

where $\mathbf{n}_\mu$ is the outward unit normal vector to the solid boundary Γ_μ^s.

Regarding the classical model of the Section 2.3 three major differences are worth to be commented:

1. First, by the fact of the insertion of the macroscale kinematics is now only defined for the solid domain, we have $|\Omega_\mu^s|$ instead of $|\Omega_\mu|$ in the denominator of the leading fraction.
2. Also because of the insertion definition, fluctuations are only defined in the solid part of the domain, which induces the introduction of the second integral in (3.9) in order to accommodate the fluctuations over the solid-void boundary. This modification and the latter do not change the final multiscale model in terms of admissible fluctuation space.
3. Finally, a novel term appears in (3.9) which is related to a vector denoted by $\bar{\mathbf{n}}_\mu$. This new term is motivated by the fact that the homogenisation formula per se, i.e. without considering any other restriction on $\tilde{\mathbf{u}}_\mu$, must be such that no spurious gradient should appear when considering a uniform displacement fluctuation field. In fact, this fundamental notion of invariance to rigid translations is a basic property that any homogenisation formula must guarantee. Mathematically, introducing a fluctuation field of the form $\tilde{\mathbf{u}}_\mu = \mathbf{c}$, i.e., an arbitrary uniform field, we can express this fact as follows

$$\mathcal{H}_\mu^{\mathscr{E}}(\mathcal{D}_\mu(\mathbf{u} + \mathbf{G}(\mathbf{x}_\mu - \mathbf{x}_\mu^G) + \mathbf{c})) = \mathbf{G}, \tag{3.10}$$

where the operator $\mathcal{H}_\mu^{\mathscr{E}} \circ \mathcal{D}_\mu$ is defined by (3.9), where $\mathcal{D}_\mu$ coincides with the gradient in the solid part of domain as in (3.4), but should be understood in a more general sense for the solid boundary.

To check the effect of property (3.10) above, let us use the Green formula in the first term of the right hand side, and recall (3.1), therefore equation (3.9) is rewritten as

$$\mathbf{O} = \frac{1}{|\Omega_\mu^s|}\left[\int_{\Gamma_\mu^s} \tilde{\mathbf{u}}_\mu \otimes \mathbf{n}_\mu \,\mathrm{d}\Gamma_\mu - \int_{\Gamma_\mu^{s,v}} \tilde{\mathbf{u}}_\mu \otimes \mathbf{n}_\mu \,\mathrm{d}\Gamma_\mu - \int_{\Gamma_\mu^{s,b}} \tilde{\mathbf{u}}_\mu \otimes \bar{\mathbf{n}}_\mu \,\mathrm{d}\Gamma_\mu\right] = \frac{1}{|\Omega_\mu^s|}\left[\int_{\Gamma_\mu^{s,b}} \tilde{\mathbf{u}}_\mu \otimes (\mathbf{n}_\mu - \bar{\mathbf{n}}_\mu) \,\mathrm{d}\Gamma_\mu\right]. \tag{3.11}$$

Hence, making $\tilde{\mathbf{u}}_\mu = \mathbf{c}$ above gives the definition of the vector $\bar{\mathbf{n}}_\mu$

$$\bar{\mathbf{n}}_\mu = \frac{1}{|\Gamma_\mu^{s,b}|} \int_{\Gamma_\mu^{s,b}} \mathbf{n}_\mu \, \mathrm{d}\Gamma_\mu, \tag{3.12}$$

such that property (3.10) holds. Note that

$$\bar{\mathbf{n}}_\mu \begin{cases} = \mathbf{0} & \text{RVE is } \mathbf{n}_\mu\text{-balanced}, \\ \neq \mathbf{0} & \text{RVE is } \mathbf{n}_\mu\text{-unbalanced}, \end{cases} \tag{3.13}$$

Remark 9 *Property (3.10) applied to the novel homogenisation formula proposed in (3.9) univocally led us to the form of vector $\bar{\mathbf{n}}_\mu$ (see (3.12)). Moreover, it has fundamental mechanical consequences related to the (self-) equilibrium of tractions distributed over the RVE boundary. This is discussed in detail in forthcoming sections.*

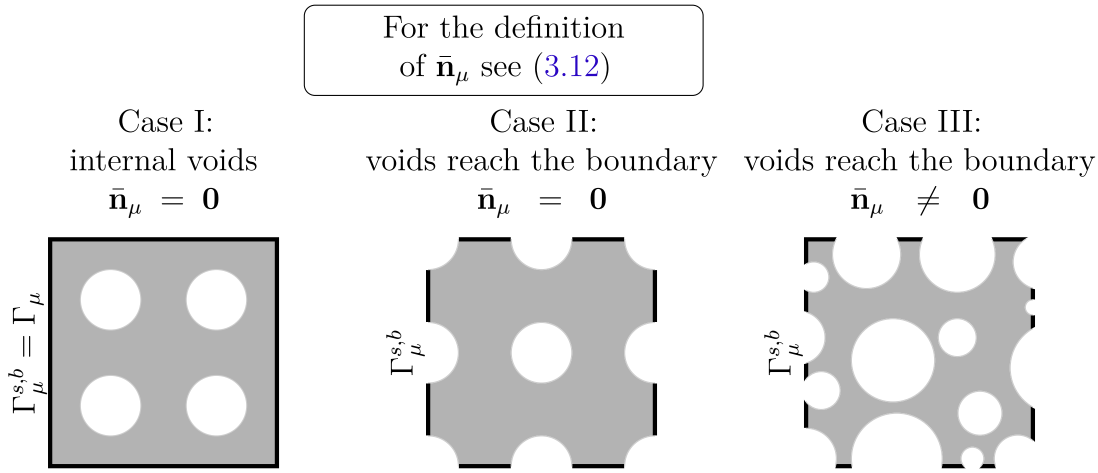

Figure 10 – Different types of RVE domains with the corresponding denomination for the different parts of the boundaries. Case I: internal voids imply that the RVE is $\mathbf{n}_\mu$-balanced ($\bar{\mathbf{n}}_\mu = \mathbf{0}$). Case II: voids reach the boundary, but due to the structured arrangement of the voids the RVE is $\mathbf{n}_\mu$-balanced ($\bar{\mathbf{n}}_\mu = \mathbf{0}$). Case III: voids reach the boundary in a random manner, so the RVE is $\mathbf{n}_\mu$-unbalanced ($\bar{\mathbf{n}}_\mu \neq \mathbf{0}$).

Now, by introducing (3.4) into (3.9) we obtain

$$\mathbf{G} = \frac{1}{|\Omega_\mu^s|}\left[\int_{\Omega_\mu^s} \left[\mathbf{G} + \nabla_{\mathbf{x}_\mu} \tilde{\mathbf{u}}_\mu\right] \mathrm{d}\Omega_\mu^s - \int_{\Gamma_\mu^{s,v}} \tilde{\mathbf{u}}_\mu \otimes \mathbf{n}_\mu \, \mathrm{d}\Gamma_\mu - \int_{\Gamma_\mu^{s,b}} \tilde{\mathbf{u}}_\mu \otimes \bar{\mathbf{n}}_\mu \, \mathrm{d}\Gamma_\mu \right] =$$
$$\mathbf{G} + \frac{1}{|\Omega_\mu^s|} \int_{\Gamma_\mu^{s,b}} \tilde{\mathbf{u}}_\mu \otimes (\mathbf{n}_\mu - \bar{\mathbf{n}}_\mu) \, \mathrm{d}\Gamma_\mu, \tag{3.14}$$

and, so, (3.9) holds provided that the fluctuation displacement field satisfies the following constraint

$$\int_{\Gamma_\mu^{s,b}} \tilde{\mathbf{u}}_\mu \otimes (\mathbf{n}_\mu - \bar{\mathbf{n}}_\mu) \, \mathrm{d}\Gamma_\mu = \mathbf{O}. \tag{3.15}$$

As before, observe that the constraint (3.15) and the characterisation given by (3.12) are simple consequences of imposing the kinematically admissibility concept to the macro and microscale displacement gradients related through the homogenisation operator (3.9), just as stipulated in the MMVP.

3.2.4 Spaces of admissible displacement fluctuations

Let us provide the characterisation of kinematically admissible fluctuation displacement fields. Within the present theory (see (BLANCO et al., 2014; BLANCO et al., 2016)) and from the kinematical restrictions imposed over the fluctuation fields, as given by (3.8) and (3.15), we say that a fluctuation field is kinematically admissible if it belongs to the following space

$$\widetilde{\mathscr{U}}_\mu^M = \left\{ \tilde{\mathbf{u}}_\mu \in [H^1(\Omega_\mu^s)]^{\mathrm{n_d}};\ \int_{\Omega_\mu^s} \tilde{\mathbf{u}}_\mu \, \mathrm{d}\Omega_\mu^s = \mathbf{0},\ \int_{\Gamma_\mu^{s,b}} \tilde{\mathbf{u}}_\mu \otimes (\mathbf{n}_\mu - \bar{\mathbf{n}}_\mu) \, \mathrm{d}\Gamma_\mu = \mathbf{O} \right\}. \tag{3.16}$$

As stated in the introduction, the aim of the present work is to define, through (3.16), the minimally constrained space of kinematically admissible displacement fluctuation fields, that is the MCKMM, in the general case of porous media with a random distribution of voids. In other words, the model proposed here provides a mechanically consistent lower bound concerning the homogenised response of the material. Consequently, any space $\widetilde{\mathscr{U}}_\mu$ satisfying $\widetilde{\mathscr{U}}_\mu \subset \widetilde{\mathscr{U}}_\mu^M$ can be regarded as kinematically admissible, and can be consistently employed in the mechanical analysis of arbitrary porous materials, keeping in mind that it will result in a more constrained kinematical model (i.e. a stiffer model).

Remark 10 *If the RVE is $\mathbf{n}_\mu$-balanced, that is, if it verifies $\bar{\mathbf{n}}_\mu = \mathbf{0}$ (see (3.2)), space $\widetilde{\mathscr{U}}_\mu^M$ defined in (3.16) becomes*

$$\widetilde{\mathscr{U}}_\mu^{M,0} = \left\{ \tilde{\mathbf{u}}_\mu \in [H^1(\Omega_\mu^s)]^{\mathrm{n_d}};\ \int_{\Omega_\mu^s} \tilde{\mathbf{u}}_\mu \, \mathrm{d}\Omega_\mu^s = \mathbf{0},\ \int_{\Gamma_\mu^{s,b}} \tilde{\mathbf{u}}_\mu \otimes \mathbf{n}_\mu \, \mathrm{d}\Gamma_\mu = \mathbf{O} \right\}, \tag{3.17}$$

which coincides with the classical definition of the MCKMM as in (2.31), if the solid domain covers all the RVE, i.e., $\Omega_\mu^s = \Omega_\mu$. In the purely constitutive case (see Section 3.3.5), even for $\Omega_\mu^s \subset \Omega_\mu$ (proper subset) but $\Gamma_\mu^s = \Gamma_\mu$.

Space $\widetilde{\mathscr{U}}_\mu^{M,0}$ is valid and consistent when the whole RVE boundary contains material particles, or in situations where the microstructure is periodic (see first and second columns in Figure 10). In a general setting these specific situations do not hold (see third column in Figure 10) and the definition provided in (3.16) has to be used in order to ensure a lower bound model, also avoiding mechanical inconsistencies, as we shall discuss in Section 3.3.6.

A typical space of admissible fluctuation fields employed in multiscale simulations of porous materials with random distribution of voids is the so-called *linear boundary* *model*. This implies in considering the space $\widetilde{\mathscr{U}}_\mu^L$ defined by

$$\widetilde{\mathscr{U}}_\mu^L = \left\{ \tilde{\mathbf{u}}_\mu \in [H^1(\Omega_\mu^s)]^{\mathrm{n_d}};\ \int_{\Omega_\mu^s} \tilde{\mathbf{u}}_\mu \, \mathrm{d}\Omega_\mu^s = \mathbf{0}, \tilde{\mathbf{u}}_\mu = \mathbf{0} \text{ on } \Gamma_\mu^{s,b} \right\}. \tag{3.18}$$

The resulting mechanical response associated to fluctuations in $\widetilde{\mathscr{U}}_\mu^L$ ($\subset \widetilde{\mathscr{U}}_\mu^M$) may be too constrained in certain applications. This is the case where strain localisation mechanisms develop in the microscale. Here, the fact that the fluctuation component of the displacement field is set to zero over the boundary implies in an exaggeratedly stiff model. This could be mitigated by increasing the microcell size, in detriment of more expensive multiscale simulations.

Hereafter, for the sake of simplicity and unless stated otherwise, we consider $\widetilde{\mathscr{U}}_\mu = \widetilde{\mathscr{U}}_\mu^M$.

It is worth mentioning that in addition to the alternative models already commented in Section 2.3.3.1, in (DIRRENBERGER; FOREST; JEULIN, 2014), a different type of boundary condition was tested as a generalisation of the proposal presented in (HAZANOV; HUET, 1994), which is a mixed boundary condition that changes according to the type of loading applied to the MC to solve networks of fibers embedded in an empty space. Notwithstanding the authors managed to set a kinematical model less constrained than the linear model over microcells with arbitrary distribution of voids (the empty space), it is not a lower bound for this kind of micro-structure. However, in these works, the consideration of truly random distributions of voids within the RVE (and over its boundary) was not tackled.

3.3 Principle of Multiscale Virtual Power

Finally, the last pillar in the context of the MMVP is the Principle of Multiscale Virtual Power (PMVP) (BLANCO et al., 2014; BLANCO et al., 2016), which is employed to mechanically connect both scales. In this context no major differences with respect to Section 2.3 are introduced, however their forthcoming consequences for the new kinematical setting are important. Then, we derive the generalised (force and stress) homogenisation formulae implied by the PMVP, and we characterise the mechanical equilibrium problem in variational and strong forms.

3.3.1 Variational formulation

As it is classic for models in solid mechanics, the total virtual power exerted at a point $\mathbf{x}_M$ in the macroscale, related to the microscale domain of size $|\Omega_\mu|$, is expressed as a linear functional of the pair $(\hat{\mathbf{u}}, \hat{\mathbf{G}})$, that is

$$\mathcal{P}_{M,\mathbf{x}_M}^{\mathrm{tot}}(\hat{\mathbf{u}}, \hat{\mathbf{G}}) = |\Omega_\mu| \Big[\mathbf{P} \cdot \hat{\mathbf{G}} - \mathbf{b} \cdot \hat{\mathbf{u}} \Big], \tag{3.19}$$

where $\mathbf{P}$ is the macroscale PKST and $\mathbf{b}$ is the macroscale force.

In turn, keeping the present analysis in the context of finite strain solid mechanics, the total virtual power in the microscale domain results

$$\mathcal{P}_\mu^{\mathrm{tot}}(\hat{\mathbf{u}}_\mu, \nabla_{\mathbf{x}_\mu}\hat{\mathbf{u}}_\mu) = \int_{\Omega_\mu^s} \left[\mathbf{P}_\mu \cdot \nabla_{\mathbf{x}_\mu}\hat{\mathbf{u}}_\mu - \mathbf{b}_\mu \cdot \hat{\mathbf{u}}_\mu\right] \mathrm{d}\Omega_\mu^s, \tag{3.20}$$

where $\mathbf{P}_\mu$ is the microscale PKST (for which a constitutive model is required) and $\mathbf{b}_\mu$ is a vector force field per unit volume defined in the microscale domain. Observe that the microscale virtual power is exclusively exerted in the solid domain Ω_μ^s.

The PMVP is then stated as follows

$$\mathbf{P} \cdot \hat{\mathbf{G}} - \mathbf{b} \cdot \hat{\mathbf{u}} = \frac{1}{|\Omega_\mu|} \int_{\Omega_\mu^s} \left[\mathbf{P}_\mu \cdot \nabla_{\mathbf{x}_\mu}\hat{\mathbf{u}}_\mu - \mathbf{b}_\mu \cdot \hat{\mathbf{u}}_\mu\right] \mathrm{d}\Omega_\mu^s \qquad \forall(\hat{\mathbf{u}}, \hat{\mathbf{G}}, \hat{\tilde{\mathbf{u}}}_\mu) \in \mathbb{R}^{\mathrm{n_d}} \times \mathbb{R}^{\mathrm{n_d}\times\mathrm{n_d}} \times \widetilde{\mathscr{U}}_\mu. \tag{3.21}$$

Introducing (3.3)-(3.4) into (3.21) yields

$$\mathbf{P} \cdot \hat{\mathbf{G}} - \mathbf{b} \cdot \hat{\mathbf{u}} = \frac{1}{|\Omega_\mu|} \int_{\Omega_\mu^s} \left[\mathbf{P}_\mu \cdot (\hat{\mathbf{G}} + \nabla_{\mathbf{x}_\mu}\hat{\tilde{\mathbf{u}}}_\mu) - \mathbf{b}_\mu \cdot (\hat{\mathbf{u}} + \hat{\mathbf{G}}(\mathbf{x}_\mu - \mathbf{x}_\mu^G) + \hat{\tilde{\mathbf{u}}}_\mu)\right] \mathrm{d}\Omega_\mu^s \qquad \forall(\hat{\mathbf{u}}, \hat{\mathbf{G}}, \hat{\tilde{\mathbf{u}}}_\mu) \in \mathbb{R}^{\mathrm{n_d}} \times \mathbb{R}^{\mathrm{n_d}\times\mathrm{n_d}} \times \widetilde{\mathscr{U}}_\mu. \tag{3.22}$$

3.3.2 Homogenisation formulae

Consider first $\hat{\mathbf{G}} = \mathbf{O}$ and $\hat{\tilde{\mathbf{u}}}_\mu = \mathbf{0}$ in (3.22). Then, we obtain

$$\mathbf{b} \cdot \hat{\mathbf{u}} = \frac{1}{|\Omega_\mu|} \int_{\Omega_\mu^s} \mathbf{b}_\mu \cdot \hat{\mathbf{u}} \, \mathrm{d}\Omega_\mu^s \qquad \forall \hat{\mathbf{u}} \in \mathbb{R}^{\mathrm{n_d}}, \tag{3.23}$$

which gives the homogenisation formula for the macroscale force per unit volume $\mathbf{b}$

$$\mathbf{b} = \frac{1}{|\Omega_\mu|} \int_{\Omega_\mu^s} \mathbf{b}_\mu \, \mathrm{d}\Omega_\mu^s. \tag{3.24}$$

Note that the integration takes place in the solid domain Ω_μ^s, but it is normalised to the size of the whole RVE domain Ω_μ.

Now, take $\hat{\mathbf{u}} = \mathbf{0}$ and $\hat{\tilde{\mathbf{u}}}_\mu = \mathbf{0}$ in (3.22), which results in

$$\mathbf{P} \cdot \hat{\mathbf{G}} = \frac{1}{|\Omega_\mu|} \int_{\Omega_\mu^s} \left[\mathbf{P}_\mu \cdot \hat{\mathbf{G}} - \mathbf{b}_\mu \cdot (\hat{\mathbf{G}}(\mathbf{x}_\mu - \mathbf{x}_\mu^G))\right] \mathrm{d}\Omega_\mu^s \quad \forall \hat{\mathbf{G}} \in \mathbb{R}^{\mathrm{n_d}\times\mathrm{n_d}}. \tag{3.25}$$

This implies in the following homogenisation formula for the macroscale stress tensor

$$\mathbf{P} = \frac{1}{|\Omega_\mu|} \int_{\Omega_\mu^s} \left[\mathbf{P}_\mu - \mathbf{b}_\mu \otimes (\mathbf{x}_\mu - \mathbf{x}_\mu^G)\right] \mathrm{d}\Omega_\mu^s. \tag{3.26}$$

As with (3.24), while the integration takes place in Ω_μ^s, the normalisation is ruled by the size of the RVE domain Ω_μ.

Remark 11 *The same comments of remarks 4 and 3 (Chapter 2) apply here, but they need to be slightly rephrased. Naturally, in Remark 4, the integral over the entire RVE (Ω_μ) changes to an integral over the solid part of the RVE (Ω_μ^s), i.e., where stress is defined, while in Remark 3 the boundary integral is only considered over the solid boundary of RVE ($\Gamma_\mu^{s,b}$), i.e., where tractions are actually defined (see in the following (3.30)).*

3.3.3 Micromechanical problem

Once the homogenisation formulae have been established, the expression (3.22) results in the following variational formulation for the microscale equilibrium problem

$$\int_{\Omega_\mu^s} \Big[\mathbf{P}_\mu \cdot \nabla_{\mathbf{x}_\mu} \hat{\tilde{\mathbf{u}}}_\mu - \mathbf{b}_\mu \cdot \hat{\tilde{\mathbf{u}}}_\mu\Big] \, \mathrm{d}\Omega_\mu^s = 0 \qquad \forall \hat{\tilde{\mathbf{u}}}_\mu \in \widetilde{\mathscr{U}}_\mu. \tag{3.27}$$

Let us obtain the strong form of the equilibrium and, at the same time, characterise the system of reactive forces which are power-conjugate to the constraints considered in the definition of the space $\widetilde{\mathscr{U}}_\mu$ (see (3.16)), i.e. for the MCKMM. Accordingly, in the variational equation (3.27), instead of the space $\widetilde{\mathscr{U}}_\mu$ we consider the unconstrained space $[H^1(\Omega_\mu^s)]^{\mathrm{n_d}}$, but we introduce the constraints (3.8) and (3.15) through corresponding Lagrange multipliers, say $\boldsymbol{\Theta} \in \mathbb{R}^{\mathrm{n_d}}$ and $\boldsymbol{\Lambda} \in \mathbb{R}^{\mathrm{n_d}\times\mathrm{n_d}}$, respectively, as follows

$$\begin{aligned}
&\int_{\Omega_\mu^s} \Big[\mathbf{P}_\mu \cdot \nabla_{\mathbf{x}_\mu} \hat{\tilde{\mathbf{u}}}_\mu - \mathbf{b}_\mu \cdot \hat{\tilde{\mathbf{u}}}_\mu\Big] \, \mathrm{d}\Omega_\mu^s + \boldsymbol{\Theta} \cdot \int_{\Omega_\mu^s} \hat{\tilde{\mathbf{u}}}_\mu \, \mathrm{d}\Omega_\mu^s + \hat{\boldsymbol{\Theta}} \cdot \int_{\Omega_\mu^s} \tilde{\mathbf{u}}_\mu \, \mathrm{d}\Omega_\mu^s \\
&\qquad - \boldsymbol{\Lambda} \cdot \int_{\Gamma_\mu^{s,b}} \hat{\tilde{\mathbf{u}}}_\mu \otimes (\mathbf{n}_\mu - \bar{\mathbf{n}}_\mu) \, \mathrm{d}\Gamma_\mu - \hat{\boldsymbol{\Lambda}} \cdot \int_{\Gamma_\mu^{s,b}} \tilde{\mathbf{u}}_\mu \otimes (\mathbf{n}_\mu - \bar{\mathbf{n}}_\mu) \, \mathrm{d}\Gamma_\mu = 0 \\
&\qquad\qquad \forall (\hat{\tilde{\mathbf{u}}}_\mu, \hat{\boldsymbol{\Theta}}, \hat{\boldsymbol{\Lambda}}) \in [H^1(\Omega_\mu^s)]^{\mathrm{n_d}} \times \mathbb{R}^{\mathrm{n_d}} \times \mathbb{R}^{\mathrm{n_d}\times\mathrm{n_d}}.
\end{aligned} \tag{3.28}$$

The equations associated to arbitrary variations $\hat{\boldsymbol{\Theta}}$ and $\hat{\boldsymbol{\Lambda}}$ naturally lead to the constraints (3.8) and (3.15). So, consider now $\hat{\boldsymbol{\Theta}} = \mathbf{0}$ and $\hat{\boldsymbol{\Lambda}} = \mathbf{O}$. Thus, by integrating by parts the first term in (3.28), arranging terms and recalling (3.1), yields

$$\begin{aligned}
&- \int_{\Omega_\mu^s} \Big[\operatorname{div}_{\mathbf{x}_\mu} \mathbf{P}_\mu + \mathbf{b}_\mu - \boldsymbol{\Theta}\Big] \cdot \hat{\tilde{\mathbf{u}}}_\mu \, \mathrm{d}\Omega_\mu^s + \int_{\Gamma_\mu^{s,v}} \mathbf{P}_\mu \mathbf{n}_\mu \cdot \hat{\tilde{\mathbf{u}}}_\mu \, \mathrm{d}\Gamma_\mu \\
&\qquad + \int_{\Gamma_\mu^{s,b}} \Big[\mathbf{P}_\mu \mathbf{n}_\mu - \boldsymbol{\Lambda}(\mathbf{n}_\mu - \bar{\mathbf{n}}_\mu)\Big] \cdot \hat{\tilde{\mathbf{u}}}_\mu \, \mathrm{d}\Gamma_\mu = 0 \quad \forall \hat{\tilde{\mathbf{u}}}_\mu \in [H^1(\Omega_\mu^s)]^{\mathrm{n_d}}.
\end{aligned} \tag{3.29}$$

Using now classical arguments from the calculus of variations we readily obtain the equilibrium problem in its strong form

$$\begin{cases}
-\operatorname{div}_{\mathbf{x}_\mu} \mathbf{P}_\mu = \mathbf{b}_\mu - \boldsymbol{\Theta} & \text{in } \Omega_\mu^s, \\
\mathbf{P}_\mu \mathbf{n}_\mu = \mathbf{0} & \text{on } \Gamma_\mu^{s,v}, \\
\mathbf{P}_\mu \mathbf{n}_\mu = \boldsymbol{\Lambda}(\mathbf{n}_\mu - \bar{\mathbf{n}}_\mu) & \text{on } \Gamma_\mu^{s,b}.
\end{cases} \tag{3.30}$$

Remark 12 *It is important to note that, unlike the multiscale formulations available in the literature, the novel homogenisation formula proposed in* (3.9) *results in a uniform traction model, on* $\Gamma_\mu^{s,b}$*, whose strong formulation is* (3.30)*, in which the traction over such boundary is obtained by projecting the constant tensor* $\boldsymbol{\Lambda}$ *over the vector* $\mathbf{n}_\mu - \bar{\mathbf{n}}_\mu$*. This enables the model to have an equilibrated system of reactive boundary forces per unit area over* $\Gamma_\mu^{s,b}$*. This fundamental issue is illustrated next (and also addressed in Section 3.3.6).*

3.3.4 Reactive forces

In this section we provide a deeper characterisation of the Lagrange multiplers $\boldsymbol{\Theta}$ and $\boldsymbol{\Lambda}$ appearing in (3.28) and (3.30), again in the particular context of the MCKMM.

Consider in (3.28) that $\hat{\hat{\mathbf{u}}}_\mu = \hat{\mathbf{c}}$ is a uniform field. Then, we have

$$-\hat{\mathbf{c}} \cdot \left(\int_{\Omega_\mu^s} \mathbf{b}_\mu \, \mathrm{d}\Omega_\mu^s \right) + |\Omega_\mu^s| \hat{\mathbf{c}} \cdot \boldsymbol{\Theta} - \boldsymbol{\Lambda} \cdot \left(\hat{\mathbf{c}} \otimes \int_{\Gamma_\mu^{s,b}} (\mathbf{n}_\mu - \bar{\mathbf{n}}_\mu) \, \mathrm{d}\Gamma_\mu \right) = 0 \qquad \forall \hat{\mathbf{c}} \in \mathbb{R}^{\mathrm{n_d}}. \tag{3.31}$$

Because of the definition of $\bar{\mathbf{n}}_\mu$ introduced in (3.12), expression (3.31) gives

$$\boldsymbol{\Theta} = \frac{1}{|\Omega_\mu^s|} \int_{\Omega_\mu^s} \mathbf{b}_\mu \, \mathrm{d}\Omega_\mu^s = \frac{|\Omega_\mu|}{|\Omega_\mu^s|} \mathbf{b}. \tag{3.32}$$

Hence, the reaction $\boldsymbol{\Theta}$ balances the forces per unit volume, if any, which are characterised by $\mathbf{b}_\mu$ in the microscale. This is a remarkable fact, because, in the proposed model, $\boldsymbol{\Theta}$ is not intended to play any role in providing mechanical balance to the tractions that arise over the solid RVE boundary. Indirectly, (3.32) establishes that the system of reactive forces over the solid boundary $\Gamma_\mu^{s,b}$ is equilibrated as a consequence of the ingredients embedded in the formulation. This is appreciated by dropping the third term in expression (3.31), precluding $\boldsymbol{\Lambda}$ from appearing in (3.32).

On the other hand, the following identity

$$\int_{\Omega_\mu^s} \mathbf{P}_\mu \, \mathrm{d}\Omega_\mu^s = -\int_{\Omega_\mu^s} \mathrm{div}_{\mathbf{x}_\mu} \mathbf{P}_\mu \otimes (\mathbf{x}_\mu - \mathbf{x}_\mu^G) \, \mathrm{d}\Omega_\mu^s + \int_{\Gamma_\mu^s} \mathbf{P}_\mu \mathbf{n}_\mu \otimes (\mathbf{x}_\mu - \mathbf{x}_\mu^G) \, \mathrm{d}\Gamma_\mu, \tag{3.33}$$

enables us to rewrite (3.26), by exploiting the strong forms of the equilibrium (3.30), which together with the definition of $\mathbf{x}_\mu^G$ in (3.7) and the domain spliting given in (3.1), leads to

$$\begin{aligned}\mathbf{P} = \frac{1}{|\Omega_\mu|}\Bigg[-\int_{\Omega_\mu^s} \Big[\mathrm{div}_{\mathbf{x}_\mu} \mathbf{P}_\mu + \mathbf{b}_\mu\Big] \otimes (\mathbf{x}_\mu - \mathbf{x}_\mu^G)\, \mathrm{d}\Omega_\mu^s \\ + \int_{\Gamma_\mu^s} \mathbf{P}_\mu \mathbf{n}_\mu \otimes (\mathbf{x}_\mu - \mathbf{x}_\mu^G)\, \mathrm{d}\Gamma_\mu \Bigg] = \\ \frac{1}{|\Omega_\mu|}\Bigg[-\boldsymbol{\Theta} \otimes \int_{\Omega_\mu^s} (\mathbf{x}_\mu - \mathbf{x}_\mu^G)\, \mathrm{d}\Omega_\mu^s + \int_{\Gamma_\mu^{s,b}} \boldsymbol{\Lambda}(\mathbf{n}_\mu - \bar{\mathbf{n}}_\mu) \otimes (\mathbf{x}_\mu - \mathbf{x}_\mu^G)\, \mathrm{d}\Gamma_\mu \Bigg] = \\ \frac{1}{|\Omega_\mu|} \boldsymbol{\Lambda} \int_{\Gamma_\mu^{s,b}} (\mathbf{n}_\mu - \bar{\mathbf{n}}_\mu) \otimes (\mathbf{x}_\mu - \mathbf{x}_\mu^G)\, \mathrm{d}\Gamma_\mu = \\ \frac{1}{|\Omega_\mu|} \boldsymbol{\Lambda} \int_{\Gamma_\mu^{s,b}} (\mathbf{n}_\mu - \bar{\mathbf{n}}_\mu) \otimes \mathbf{x}_\mu\, \mathrm{d}\Gamma_\mu. \end{aligned} \tag{3.34}$$

where, from the definition of $\bar{\mathbf{n}}_\mu$, we can omit $\mathbf{x}_\mu^G$ in the last equality above. Finally, we obtain

$$\boldsymbol{\Lambda} = |\Omega_\mu| \mathbf{P} \left[\int_{\Gamma_\mu^{s,b}} (\mathbf{n}_\mu - \bar{\mathbf{n}}_\mu) \otimes \mathbf{x}_\mu\, \mathrm{d}\Gamma_\mu \right]^{-1}. \tag{3.35}$$

The homogenisation formula (3.35) is a novel formula when compared to the specialised literature. In the present work, this formula has been molded directly by the new kinematical constraint (3.15). Furthermore, such formula holds whether the RVE is $\mathbf{n}_\mu$-balanced or not.

Remark 13 *Particularly, if the RVE is $\mathbf{n}_\mu$-balanced, and the RVE boundary is entirely solid media ($\Gamma_\mu = \Gamma_\mu^{s,b}$), we have that (3.2) holds, and then $\bar{\mathbf{n}}_\mu = \mathbf{0}$ (see (3.12)). In such case, (3.35) becomes*

$$\boldsymbol{\Lambda} = |\Omega_\mu| \mathbf{P} \left[\int_{\Gamma_\mu} \mathbf{n}_\mu \otimes \mathbf{x}_\mu\, \mathrm{d}\Gamma_\mu \right]^{-1} = \mathbf{P}. \tag{3.36}$$

Therefore, the present formulation reduces to the classical one under the corresponding hypotheses. This fact indicates the only situation in which the Lagrange multiplier associated to the imposition of the MCKMM has exactly the meaning of the PKST.

3.3.5 Purely constitutive multiscale formulation

Consider the scenario in which forces per unit volume in the microscale are set to zero. This is the case of pure constitutive modelling, in which the interest resides in building a constitutive law relating the macroscale stress $\mathbf{P}$ to a macroscale measure of strain, in this case $\mathbf{G}$.

Since $\mathbf{b}_\mu = \mathbf{0}$, from (3.24) we get $\mathbf{b} = \mathbf{0}$, and the homogenisation formula for the stress reduces to the classical one

$$\mathbf{P} = \frac{1}{|\Omega_\mu|} \int_{\Omega_\mu^s} \mathbf{P}_\mu\, \mathrm{d}\Omega_\mu^s. \tag{3.37}$$

Moreover, by virtue of (3.32), we conclude that the reactive force per unit volume is $\boldsymbol{\Theta} = \mathbf{0}$.

Thus, the variational form of the equilibrium (3.27) turns into

$$\int_{\Omega_\mu^s} \mathbf{P}_\mu \cdot \nabla_{\mathbf{x}_\mu} \hat{\tilde{\mathbf{u}}}_\mu \, \mathrm{d}\Omega_\mu^s = 0 \qquad \forall \hat{\tilde{\mathbf{u}}}_\mu \in \widetilde{\mathscr{U}}_\mu. \tag{3.38}$$

The strong formulation of the equilibrium results

$$\begin{cases} \operatorname{div}_{\mathbf{x}_\mu} \mathbf{P}_\mu = \mathbf{0} & \text{in } \Omega_\mu^s, \\ \mathbf{P}_\mu \mathbf{n}_\mu = \mathbf{0} & \text{on } \Gamma_\mu^{s,v}, \\ \mathbf{P}_\mu \mathbf{n}_\mu = \boldsymbol{\Lambda}(\mathbf{n}_\mu - \bar{\mathbf{n}}_\mu) & \text{on } \Gamma_\mu^{s,b}. \end{cases} \tag{3.39}$$

3.3.6 Consequences of omitting $\bar{\mathbf{n}}_\mu$ (but $\bar{\mathbf{n}}_\mu \neq \mathbf{0}$)

Consider the constitutive multiscale model from Section 3.3.5. Let us take an arbitrary RVE, which is in general $\mathbf{n}_\mu$-unbalanced. Suppose that we neglect the last term in (3.9) which brings the contribution of the average normal vector $\bar{\mathbf{n}}_\mu$ to the gradient homogenisation formula. This is equivalent to considering, in the variational statement of the equilibrium (3.38), the space of kinematically admissible fluctuation displacements $\widetilde{\mathscr{U}}_\mu^0$ defined in (3.17), that is

$$\int_{\Omega_\mu^s} \mathbf{P}_\mu \cdot \nabla_{\mathbf{x}_\mu} \hat{\tilde{\mathbf{u}}}_\mu \, \mathrm{d}\Omega_\mu^s = 0 \qquad \forall \hat{\tilde{\mathbf{u}}}_\mu \in \widetilde{\mathscr{U}}_\mu^0. \tag{3.40}$$

Next, let us introduce the Lagrange multipliers, denoted correspondingly by $\boldsymbol{\Theta}^0$ and $\boldsymbol{\Lambda}^0$, to remove the kinematical constraints from the space $\widetilde{\mathscr{U}}_\mu^0$. The variational equilibrium equation associated to the admissible variation of the fluctuation displacement field turns into

$$\int_{\Omega_\mu^s} \mathbf{P}_\mu \cdot \nabla_{\mathbf{x}_\mu} \hat{\tilde{\mathbf{u}}}_\mu \, \mathrm{d}\Omega_\mu^s + \boldsymbol{\Theta}^\circ \cdot \int_{\Omega_\mu^s} \hat{\tilde{\mathbf{u}}}_\mu \, \mathrm{d}\Omega_\mu^s - \boldsymbol{\Lambda}^\circ \cdot \int_{\Gamma_\mu^{s,b}} \hat{\tilde{\mathbf{u}}}_\mu \otimes \mathbf{n}_\mu \, \mathrm{d}\Gamma_\mu = 0$$
$$\forall \hat{\tilde{\mathbf{u}}}_\mu \in [H^1(\Omega_\mu^s)]^{\mathrm{n_d}}. \tag{3.41}$$

Going ahead as in (3.31), we consider now the uniform fluctuation $\hat{\tilde{\mathbf{u}}}_\mu = \hat{\mathbf{c}}$, which in (3.41) yields

$$\hat{\mathbf{c}} \cdot \left(|\Omega_\mu^s| \boldsymbol{\Theta}^\circ - |\Gamma_\mu^{s,b}| \boldsymbol{\Lambda}^\circ \bar{\mathbf{n}}_\mu \right) = 0 \qquad \forall \hat{\mathbf{c}} \in \mathbb{R}^{\mathrm{n_d}}, \tag{3.42}$$

where we have used the definition (3.12). From (3.42) we can observe that since the RVE is $\mathbf{n}_\mu$-unbalanced, a reactive force per unit volume $\boldsymbol{\Theta}^0$ emerges in order to equilibrate the uniform traction acting over the RVE boundary, which is characterised by $\boldsymbol{\Lambda}^0$. This spurious reactive force is

$$\boldsymbol{\Theta}^0 = \frac{|\Gamma_\mu^{s,b}|}{|\Omega_\mu^s|} \boldsymbol{\Lambda}^\circ \bar{\mathbf{n}}_\mu. \tag{3.43}$$

The smaller the unbalance, that is, the smaller the magnitude of the vector $|\Gamma_\mu^{s,b}|\bar{\mathbf{n}}_\mu$, the smaller the reaction force. Also the larger the size of the RVE, the smaller the $\mathbf{\Theta}^0$. This implies that by enlarging the microcell size we can mitigate the effect of this spurious reactive force. However, enlarging the microcell size implies in solving larger problems, which is not a viable solution in many cases.

Remark 14 *As a consequence of neglecting the fact that the RVE is $\mathbf{n}_\mu$-unbalanced, the property* (3.10) *is violated, which has a profound impact, in the sense that the reactive force over the boundary $\Gamma_\mu^{s,b}$ is not equilibrated, requiring the appearance of a spurious force per unit volume. In this context, we say that the use of the space $\widetilde{\mathscr{U}}_\mu$ (see* (3.16)*) instead of $\widetilde{\mathscr{U}}_\mu^0$ (see* (3.17)*) is mechanically consistent, delivering a system of reactive boundary forces which is equilibrated.*

3.4 Closing remarks

It is important to remark that in addition to the inherent importance of the developments presented in this chapter for the context for random porous RVEs, such consistent model has also a very close relation with the main topic of this thesis, which is the multiscale modelling of fibrous materials. Such connection is developed in detail in Section 4.2.

We highlight that the subject of this chapter is the substrate of another contribution of this thesis (BLANCO et al., 2019). In fact, the discrete model for fibre network (see Chapter 4) has served as a concrete motivation to revise the standard model for multiscale solid mechanics in order deal with a random pattern of voids reaching boundary, aspect that had been neglected in the literature. A preliminary version of this model can also be found in (ROCHA et al., 2018).

4 Linking Networks of Fibres to Continua

All models are wrong, but some are useful.

George Box

This chapter constitutes in some sense the core of the thesis. So far, the variational theory for the formulation of RVE-based multiscale models has been set in an abstract format in Chapter 2 and used to systematically derive a consistent model for microstructures in continuum media featuring random porous patterns in Chapter 3. Hereafter, while the macroscale solid kinematics is modelled using a standard continuum approach in the finite strain regime, the microscale mechanics is modelled using a discrete kinematics. The continuum theory for solids is used as motivation to derive the discrete model and once the discrete setting is established we proceed with a rigourous presentation of the discrete model in the light of the MMVP. In the sense of models featuring different kinematics, and in the context of applications of the MMVP, the present work is novel and can be used to drive the construction of multiscale models with similar features in other applications, such as those encountered in the modelling of textiles, polymeric materials and granular materials.

The present chapter is organised as follows. In Section 4.1, we introduce some hypotheses and the most important features of the proposed multiscale model for fibres. For a reader interested in a continuum motivation of the discrete model to be derived next, in Section 4.2 the continuum model with pores reaching boundary is used to motivate the model of discrete fibres. The former section is not of mandatory reading. Concerning the development of the model itself, it is divided in three parts, presented in Section 4.3 (kinematics), Section 4.4 (duality) and Section 4.5 (PMVP). Some theoretical aspects of the present multiscale model are discussed in Section 4.6, particularly those related to the mechanical significance of the generalised forces associated to the kinematical restrictions. Section 5.2 is devoted to the constitutive modelling of fibres at the microscale, and numerical tests are presented in Section 6.1. Extensions to the present model and limitations are discussed in Section 6.1.3. Final remarks are outlined in Section 4.7. Throughout the manuscript, an informative parallel with continuum multiscale formulations is discussed in a series of remarks termed "(Continuum Case)".

4.1 Features of the fibrous microstructure

The present model aims to simulate the constitutive behaviour of biological tissues with an underlying fibrous architecture, with special emphasis in arterial tissues for which

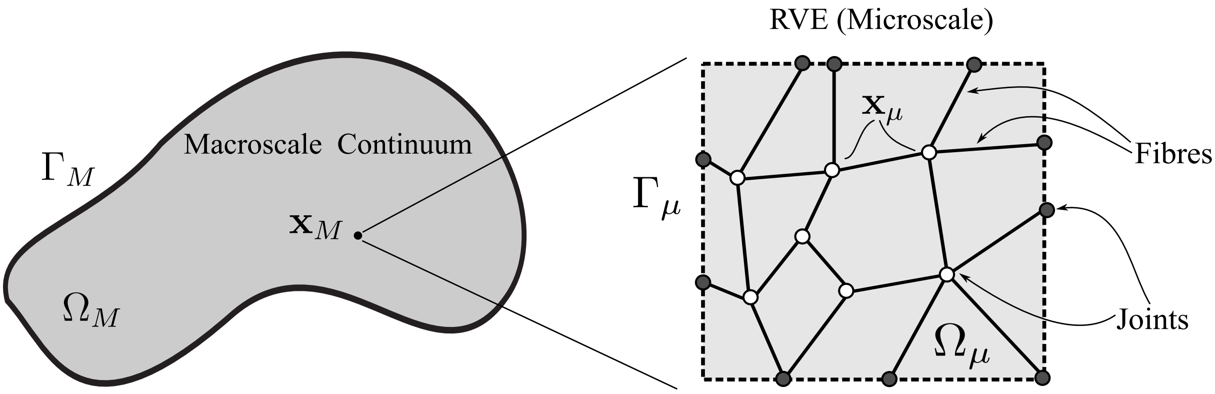

Figure 11 – Macroscale continuum and discrete microscale RVE domains.

the network of collagen fibres is the structural element.

The fibres are very slender components, and therefore their behaviour is considered through one-dimensional structural components. The basic hypotheses about the network of fibres are the following:

- The network of fibres is an interconnected network of nonlinear rectilinear trusses. Therefore, bending, shear and torsional effects in the fibres are neglected.
- Fibres are connected through perfect joints which neither detach nor offer resistance to the relative change of direction of the fibres.
- Body forces per unit volume are neglected in the network.
- No matrix is considered as ground substance for the network, then the fibres are surrounded by "empty space".

Remark 15 *For all purpose of this work, as "empty space" we consider a medium which is mechanically irrelevant. For instance, in the case of a fluid surrounding the fibres, if dissipative effects are disregarded, the contribution in stress state would be irrelevant, however it could add a kinematical constraint to the overall behaviour of the material, turning the tissue into an incompressible medium. Incompressibility is addressed in a series of remarks throughout the manuscript.*

Remark 16 *Other constituents of arterial tissue such as elastin fibres and smooth muscle cells could also be coupled with the present multiscale model, but their incorporation in the present model is out of the scope of this work.*

These hypotheses are physically reasonable and have been already proposed in literature (see for example (STYLIANOPOULOS; BAROCAS, 2007a; STYLIANOPOULOS; BAROCAS, 2007b)). Particularly, with respect to the interconnected network structure, in (CHANDRAN, 2005) it is argued that isolated fibres tend to spontaneously cross-link in order to stabilise the structure.

Networks of fibres can be artificially generated using specific algorithms. Previous works used Voronoi (ZHANG et al., 2012) and Delaunay (HADI; BAROCAS, 2013) tessellations, as well as the so-called Mikado networks (HEUSSINGER; FREY, 2006), which are randomly generated straight lines with cross-links identified at each crossing of lines. Another alternative algorithm for network generation, similar to Mikado networks, was presented in (STYLIANOPOULOS; BAROCAS, 2007a), but in such case, instead of line segments, the nodes are primarily generated randomly. One may also want to consider the segmentation of real microscopic images as in (STEIN et al., 2008).

Concerning the individual fibres, we take the following assumptions:

- Each single fibre is a straight segment [1] with uniform cross-sectional area, material properties and strain.
- Fibres only support tensile stress in axial direction, or even they just may be activated after exceeding a certain stretch, called *activation stretch*.
- A fibre features a hyperelastic behaviour inspired in phenomenological models.

These hipotheses are considered for the sake of simplicity, but do not impose serious limitations to the formulation of the proposed multiscale model, which is the main focus of our work. Again, analogous assumptions were already regarded in previous works (STYLIANOPOULOS; BAROCAS, 2007a; STYLIANOPOULOS; BAROCAS, 2007b).

For those readers interested in a more sophisticated model in terms of fibre kinematics, we refer to recent works including the geometrically exact beam theory accounting different kinds of contacts between fibres (CYRON et al., 2013; MEIER et al., 2017).

4.2 Motivation about the transition from continuum media to discrete networks

In this section our aim is to succinctly retake the consistent formulation for pores reaching the RVE boundary, presented in Chapter 3, which could be understood as the groundwork for our model of a fibre networks. What is shown here is somewhat informal and the rigorous presentation is postponed to the next section of this chapter.

[1] The physical effect of waviness will considered in the constitutive law for each fibre but not in its geometrical description.

One important consideration to be highlighted once again is that our point of depart is a formulation that is itself not classical in multiscale theory. Particularly, this is because the displacement field is not well defined in the absence of material points, that is, in the void (empty) domain. This is of crucial relevance if the RVE is basically composed by empty space, as it is the case of fibrous materials.

Now, consider in a typical porous microstructure that the voids grow sufficiently so that the solid part can be portioned in a number of slender parts (each one representing a bundle of fibres) and in their intersections (joints) as in Fig. 12. As usual, $\Omega_\mu \subset \mathbb{R}^{\mathrm{n_d}}$ is an open bounded set that stands for the entire RVE domain. The domain $\Omega_\mu^f \subset \Omega_\mu$ denotes the volume occupied by a fibre indexed with the integer $f \in \{1, 2, \ldots, N_{fibres}\}$ and $\Omega_\mu^j \subset \Omega_\mu$ is the domain of a joint indexed by $j \in \{1, 2, \ldots, N_{joints}\}$. Also, let us define the following auxiliary notations

$$\begin{aligned} &\Omega_\mu^F = \bigcup_{f=1}^{N_{fibres}} \Omega_\mu^f \ , \ \Omega_\mu^J = \bigcup_{j=1}^{N_{joints}} \Omega_\mu^i \ , \ \Omega_\mu^s = \overline{\Omega_\mu^F \cup \Omega_\mu^N} \ , \ \Omega_\mu^v = \Omega_\mu \backslash \Omega_\mu^s \\ &\Gamma_\mu^{r,t} = \Gamma_\mu^r \cap \Gamma_\mu^t \quad \text{for } r, t \in \{f, j, F, J, s, v\} \end{aligned} \tag{4.1}$$

Further, note that $\Gamma_\mu^{s,b} = \cup_{j=1}^{N_{joints}} \Gamma_\mu^{j,b}$, i.e., the fibres are assumed to be always connected to the boundary through a joint. By convention, a normal vector $\mathbf{n}^{r,t}$ of a surface $\Gamma_\mu^{r,t}$, always points from Ω_μ^r to Ω_μ^t, for $r, t \in \{f, j, F, J, s, v\}$.

It is important to remark here that in the following developments our aim is to arrive at the same kinematics hypotheses as described in Section 4.1. Therefore, now we introduce what we call the *Hypothesis of Small Joints* (HSJ) and *Hypothesis of truss* (HT) which relies on the assumptions.

HSJ.1) For a given integrable function φ defined in Ω_μ^s of any type value (scalar, vector, tensor value), with reasonable same order of magnitude in Ω_μ^s, the approximation

$$\sum_{f=1}^{N_{fibres}} \int_{\Omega_\mu^f} \varphi \, \mathrm{d}\Omega_\mu^f \gg \sum_{j=1}^{N_{joints}} \int_{\Omega_\mu^j} \varphi \, \mathrm{d}\Omega_\mu^j, \tag{4.2}$$

holds. One first corollary is that

$$|\Omega_\mu^s| = \sum_{f=1}^{N_{fibres}} |\Omega_\mu^f| + \sum_{j=1}^{N_{joints}} |\Omega_\mu^j| \approx \sum_{f=1}^{N_{fibres}} |\Omega_\mu^f| = |\Omega_\mu^F|, \tag{4.3}$$

which is obtained by taking $\varphi = 1$.

HSJ.2) The joints are so small that material points $\mathbf{x}_\mu \in \Omega_\mu^j$ can be approximated by the point $\bar{\mathbf{x}}_\mu^j$ at the centroid of Ω_μ^j. For continuous vector fields (e.g displacements, fluctuations of displacements, etc), let us say $\mathbf{v} : \Omega_\mu^j \to \mathbb{R}^{\mathrm{n_d}}$, it is reasonable that:

$$\mathbf{v}(\mathbf{x}_\mu) \approx \mathbf{v}(\bar{\mathbf{x}}_\mu^j) := \mathbf{v}^j, \quad \forall \mathbf{x}_\mu \in \Omega_\mu^j. \tag{4.4}$$

Hence, the above assumption and with HSJ.1 guide the future discrete structure in form of nodal values in the network model.

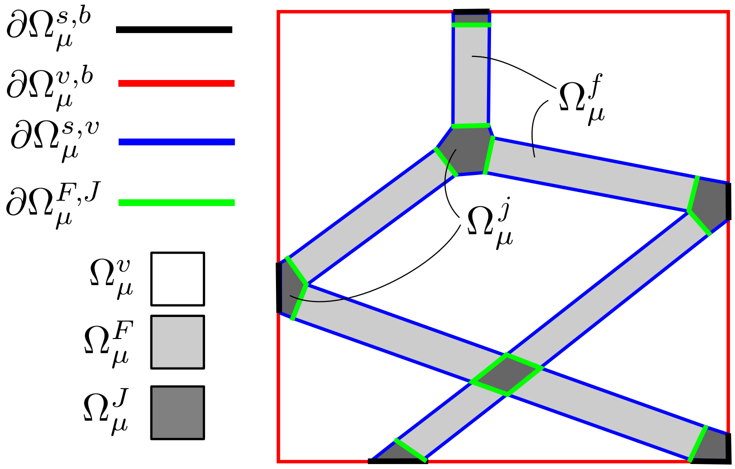

Figure 12 – Example of a porous RVE featuring connected slender structural components.

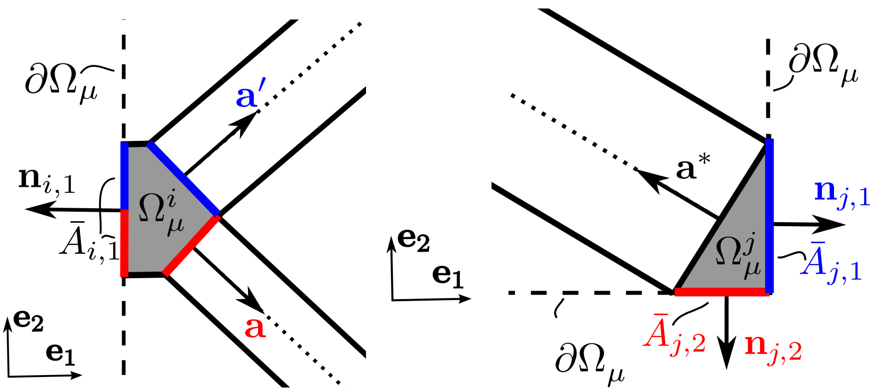

(a) On an RVE side.

(b) At an RVE corner.

Figure 13 – Typical joints reaching the RVE boundary.

HT) The slender parts of the solid are so slender that allow them to be modelled as straight trusses with constant cross sections, denoted by A_f, and length L_f. The displacement at each bar must be constant in the cross section of the bar and is given by the linear interpolation between the displacement at the initial, $\mathbf{x}_\mu^{i_f} \in \Gamma_\mu^f \cap \Gamma_\mu^{i_f}$, and at the end, $\mathbf{x}_\mu^{j_f} \in \Gamma_\mu^f \cap \Gamma_\mu^{j_f}$ points of the centreline of the bar. The above considerations define the displacement field along the fibre $\mathbf{u}_\mu^f$ as a linear field, that is

$$
\begin{aligned}
\mathbf{u}_\mu^f(s) &:= \left(1 - \frac{s}{L_f}\right)\mathbf{u}_\mu(\mathbf{x}_\mu^{i_f}) + \frac{s}{L_f}\mathbf{u}_\mu(\mathbf{x}_\mu^{j_f}) \\
&= \left(1 - \frac{s}{L_f}\right)\mathbf{u}_\mu^{i_f} + \frac{s}{L_f}\mathbf{u}_\mu^{j_f} \qquad s \in [0, L_f].
\end{aligned} \tag{4.5}
$$

Here, $\mathbf{x}_\mu^{i_f}$ and $\mathbf{x}_\mu^{j_f}$ are points characterising the joints $\Omega_\mu^{i_f}$ and $\Omega_\mu^{j_f}$, with $i_f, j_f \in \{1, 2, \ldots, N_{joints}\}$, respectively. As a straightforward corollary of this assumption is that the non null part of $\nabla_{\mathbf{x}_\mu}\mathbf{u}_\mu$ in Ω_μ^f is given by $\frac{\mathrm{d}}{\mathrm{d}s}(\mathbf{u}_\mu^f(s)) \otimes \mathbf{t}_f$, i.e.,

$$\nabla_{\mathbf{x}_\mu}\mathbf{u}_\mu\Big|_{\Omega_\mu^f} = \frac{\mathrm{d}}{\mathrm{d}s}\mathbf{u}_\mu^f(s) \otimes \mathbf{t}_f = \frac{1}{L_f}(\mathbf{u}_\mu^{j_f} - \mathbf{u}_\mu^{i_f}) \otimes \mathbf{t}_f, \tag{4.6}$$

where $\mathbf{t}_f$ is a unit vector pointing from $\mathbf{x}_\mu^{i_f}$ towards $\mathbf{x}_\mu^{j_f}$.

4.2.1 Discrete displacement homogenisation

Now, let us investigate the impact of the HSJ.1 and HT for the expressions related to the homogenisation of the displacement field from Chapter 3. Recalling (3.5), it is easy to see that the following simplifications holds

$$\begin{aligned}\frac{1}{|\Omega_\mu^s|}\int_{\Omega_\mu^s} \mathbf{u}_\mu \mathrm{d}\Omega_\mu^s &= \frac{1}{|\Omega_\mu^s|}\left(\sum_{f=1}^{N_{fibres}} \int_{\Omega_\mu^f} \mathbf{u}_\mu \mathrm{d}\Omega_\mu^s + \sum_{j=1}^{N_{joints}} \int_{\Omega_\mu^j} \mathbf{u}_\mu \,\mathrm{d}\Omega_\mu^s\right) \\ &\approx \frac{1}{|\Omega_\mu^F|}\sum_{f=1}^{N_{fibres}} \int_{\Omega_\mu^f} \mathbf{u}_\mu \,\mathrm{d}\Omega_\mu^s \approx \frac{1}{|\Omega_\mu^F|}\sum_{f=1}^{N_{fibres}} \frac{|\Omega_\mu^f|}{2}(\mathbf{u}_\mu^{i_f} + \mathbf{u}_\mu^{j_f}).\end{aligned} \tag{4.7}$$

The result above also leads to analogous specific expressions for the centroid and restriction over the fluctuation field, to be seen in Section 4.3.

4.2.2 Discrete version for gradient-related integrals

We now investigate the impact of the HSJ.1 in the expression of the homogenisation of the gradient field of Chapter 3. Firsly, working with the first two integrals of (3.9) we have

$$\begin{aligned}&\int_{\Omega_\mu^s} \nabla_{\mathbf{x}_\mu}\mathbf{u}_\mu \,\mathrm{d}\Omega_\mu^s - \int_{\Gamma_\mu^{s,v}} \tilde{\mathbf{u}}_\mu \otimes \mathbf{n}_\mu^{s,v} \,\mathrm{d}\Gamma_\mu^{s,v} = \\ &\sum_{j=1}^{N_{joints}}\left(\int_{\Omega_\mu^j} \nabla_{\mathbf{x}_\mu}\mathbf{u}_\mu \,\mathrm{d}\Omega_\mu^i - \int_{\Gamma_\mu^{j,v}} \tilde{\mathbf{u}}_\mu \otimes \mathbf{n}_\mu^{j,v} \,\mathrm{d}\Gamma_\mu^{j,v}\right) \\ &+ \sum_{f=1}^{N_{fibres}}\left(\int_{\Omega_\mu^f} \nabla_{\mathbf{x}_\mu}\mathbf{u}_\mu \,\mathrm{d}\Omega_\mu^f - \int_{\Gamma_\mu^{f,v}} \tilde{\mathbf{u}}_\mu \otimes \mathbf{n}_\mu^{f,v} \,\mathrm{d}\Gamma_\mu^{f,v}\right) \\ \approx &\sum_{j=1}^{N_{joints}}\left(\int_{\Gamma_\mu^{j,F}} \tilde{\mathbf{u}}_\mu \otimes \mathbf{n}_\mu^{j,F} \,\mathrm{d}\Gamma_\mu^{j,F} + \int_{\Gamma_\mu^{j,b}} \tilde{\mathbf{u}}_\mu \otimes \mathbf{n}_\mu^{j,b}\, \Gamma_\mu^{j,b}\right) + \\ &+ \sum_{f=1}^{N_{fibres}}\left(\int_{\Omega_\mu^f} \nabla_{\mathbf{x}_\mu}\mathbf{u}_\mu \,\mathrm{d}\Omega_\mu^f - \int_{\Gamma_\mu^{f,v}} \tilde{\mathbf{u}}_\mu \otimes \mathbf{n}_\mu^{f,v}\, \Gamma_\mu^{f,v}\right).\end{aligned} \tag{4.8}$$

Considering the last part of (4.8) (after the approximation sign), it can be still rewritten by taking into account HSJ.2 yielding

$$\sum_{j=1}^{N_{joints}}\left(\int_{\Gamma_\mu^{j,F}}\tilde{\mathbf{u}}_\mu^j\otimes\mathbf{n}_\mu^{j,F}\,\mathrm{d}\Gamma_\mu^{j,F}+\int_{\Gamma_\mu^{j,b}}\tilde{\mathbf{u}}_\mu^j\otimes\mathbf{n}_\mu^{j,b}\,\mathrm{d}\Gamma_\mu^{j,b}\right)+ \\ +\sum_{f=1}^{N_{fibres}}\left(\int_{\Omega_\mu^f}\nabla_{\mathbf{x}_\mu}\mathbf{u}_\mu\,\mathrm{d}\Omega_\mu^f-\int_{\Gamma_\mu^{f,v}}\tilde{\mathbf{u}}_\mu\otimes\mathbf{n}_\mu^{f,v}\,\mathrm{d}\Gamma_\mu^{f,v}\right). \tag{4.9}$$

Now, introducing HT and (4.6) into (4.9) we have

$$\sum_{j=1}^{N_{joints}}\sum_{f=1}^{N_{fibres}}|\Gamma_\mu^{f,j}|\tilde{\mathbf{u}}_\mu^j\otimes\mathbf{n}_\mu^{j,f}+\sum_{j=1}^{N_{joints}}|\Gamma_\mu^{j,b}|\tilde{\mathbf{u}}_\mu^j\otimes\mathbf{n}_\mu^{j,b} \\ +\sum_{f=1}^{N_{fibres}}L_fA_f\left(\frac{1}{L_f}(\mathbf{u}_\mu^{j_f}-\mathbf{u}_\mu^{i_f})\otimes\mathbf{t}_f\right). \tag{4.10}$$

Note that $|\Gamma_\mu^{f,j}|=\begin{cases}0 & \text{if } \Gamma_\mu^{f,j}=\emptyset\\ A_f & \text{otherwise}\end{cases}$. Moreover, we are supposing that the normal vectors to the surfaces are aproximately constant. In Section 4.2.3 we show an estimate for $|\Gamma_\mu^{j,b}|$ and $\mathbf{n}_\mu^{j,b}$ as a function of known properties of the structural components.

Now let us simplify the third integral in (3.9). Using HSJ.2 we have

$$\int_{\Gamma_\mu^{s,b}}\tilde{\mathbf{u}}_\mu\otimes\bar{\mathbf{n}}_\mu\,\mathrm{d}\Gamma_\mu^{s,b}=\sum_{j=1}^{N_{joints}}\int_{\Gamma_\mu^{j,b}}\mathbf{u}_\mu\otimes\bar{\mathbf{n}}_\mu\,\mathrm{d}\Gamma_\mu^{j,b} \\ \approx\sum_{j=1}^{N_{joints}}|\Gamma_\mu^{j,b}|\tilde{\mathbf{u}}_\mu^j\otimes\bar{\mathbf{n}}_\mu. \tag{4.11}$$

4.2.3 Comment on equivalent areas of boundary joints

Finally, the boundary areas are computed by projecting the fibre areas arriving at a certain joint over the corresponding normal vector. For example, for the case of Fig. 13a we have just one boundary surface, then

$$\bar{A}_{i,1}=|\mathbf{n}_{i,1}\cdot\mathbf{a}|A+|\mathbf{n}_{i,1}\cdot\mathbf{a}'|A', \tag{4.12}$$

where A and A' are the areas related to the fibres with unit vector $\mathbf{a}$ and $\mathbf{a}'$, respectively. For the case of Fig. 13a we have two boundary surfaces, then

$$\bar{A}_{j,1}=|\mathbf{n}_{j,1}\cdot\mathbf{a}^*|A^*, \tag{4.13}$$

$$\bar{A}_{j,2}=|\mathbf{n}_{j,2}\cdot\mathbf{a}^*|A^*, \tag{4.14}$$

where A^* is the area associated to fibre whose unit vector is $\mathbf{a}^*$. These ideas are of easy generalisation as defined in (4.30). Equivalent areas and normals are obtained using (4.31) and (4.32), respectively. In the case of Fig. 13a, these expressions trivially lead to $\bar{A}_i:=|\Gamma_\mu^{i,b}|=\bar{A}_{i,1}$ and $\mathbf{n}^i:=\mathbf{n}_{i,1}$. For the case of Fig. 13b, it is easy to verify that $\bar{A}_j:=|\Gamma_\mu^{j,b}|=A^*$ and $\mathbf{n}^j:=-\mathbf{a}^*$.

4.3 Kinematics

In this section we present the microscale kinematical setting for the network of fibres and its connection to the macroscale kinematics within the framework of the MMVP, which is illustrated in Figure 11. The adopted macroscale kinematics is equal to the previous chapters and we refer to Section 2.3.1 to recall the notation. For the sake of simplicity, we shorten the notation to the point-valued kinematical entities evaluated at the point $\mathbf{x}_M \in \Omega_M$, then hereafter $\mathbf{u}_M|_{\mathbf{x}_M}$ simplifies to $\mathbf{u}$ and $\mathbf{G}_M|_{\mathbf{x}_M}$ becomes $\mathbf{G}$, where the same notation is applied to the their variations. Also to keep the presentation simple, we admit $\mathbf{u} \in \mathbb{R}^{\mathrm{n_d} \times \mathrm{n_d}}$ $\mathbf{G} \in \mathbb{R}^{\mathrm{n_d} \times \mathrm{n_d}}$, however it was already seen that the MMVP is suffient general to handle other situations such as those arising in the case of incompressibility (see Section 2.4.3). Finally, Section 4.3.1 is devoted to present the discrete structure that partially fills the volume $\Omega_\mu \subset \mathbb{R}^{\mathrm{n_d}}$ (the RVE associated to the macroscale point).

4.3.1 Characterisation of microscale fibre network

Before providing the specific description of the microscale kinematics, in this section we introduce some basic notations. As already commented, our microscale network model consists of interconnected straight trusses, which models the real fibrous structure at the microscale. Each truss is an idealisation of a collagen bundle (a group of collagen fibres in the present context) and is geometrically represented by a line segment between two points. As an abuse of notation, when referring to a truss we simply call it *fibre*. For more considerations and its constitutive implications, see Section 5.2.

The other object that has to be modelled in the network is the joint that interconnects fibre segments, which represents the interaction between two or more bundle of collagen fibres crossing each other. In this work, there is no relative displacement among the fibres reaching the joint. Moreover, as the characteristic size of a joint is much smaller than that of fibres, we idealise these entities as *nodes* (or simply points), that is, geometrical entities without dimension.

Next, the kinematical framework for the components at microscale in a pure discrete form is presented. As already shown, the justifications for this model from a continuum perspective has been discussed in Section 4.2.

To denote the set of fibres which are interconnected through nodes we introduce the following notation

$$\begin{aligned}\mathcal{N}_{\text{net}} &= \text{list of nodes in the network} \\ &= \{i;\, i = 1, 2, \dots, N_{joints}\}, \end{aligned} \tag{4.15}$$

$$\begin{aligned}\mathcal{F}_{\text{net}} &= \text{list of fibres in the network} \\ &= \{\alpha = (i_\alpha, j_\alpha) \in \mathcal{N}_{\text{net}} \times \mathcal{N}_{\text{net}};\, i_\alpha \neq j_\alpha\}, \end{aligned} \tag{4.16}$$

where i_α and j_α stand for initial and final node of fibre α, respectively.

To complement the geometrical characterisation of the oriented graph $(\mathcal{N}_{\text{net}}, \mathcal{F}_{\text{net}})$, we introduce the following sets

$$\mathcal{N}_{\text{net}}^{\Gamma} = \text{boundary nodes in the network } (\mathcal{N}_{\text{net}}^{\Gamma} \subset \mathcal{N}_{\text{net}}), \tag{4.17}$$

$$\mathring{\mathcal{N}}_{\text{net}} = \text{interior nodes in the network} = \mathcal{N}_{\text{net}} \backslash \mathcal{N}_{\text{net}}^{\Gamma}, \tag{4.18}$$

$$\mathcal{X}_{\text{net}} = \text{node positions} = \{\mathbf{x}_\mu^i \in \Omega_\mu,\ i \in \mathcal{N}_{\text{net}}\}, \tag{4.19}$$

$$\mathcal{A}_{\text{net}} = \text{fibre transversal areas} = \{A_\alpha \in \mathbb{R}^+,\ \alpha \in \mathcal{F}_{\text{net}}\}. \tag{4.20}$$

Then, the representation of the network of fibres is fully characterised by the following object

$$\text{NET} = (\mathcal{N}_{\text{net}}^{\Gamma}, \mathring{\mathcal{N}}_{\text{net}}, \mathcal{F}_{\text{net}}, \mathcal{X}_{\text{net}}, \mathcal{A}_{\text{net}}), \tag{4.21}$$

which for brevity is simply called *Network*, and whose basic elements are schematically shown in Fig. 14. Note that $\mathcal{N}_{\text{net}}$ is already implicit in (4.21) since $\mathcal{N}_{\text{net}} = \mathcal{N}_{\text{net}}^{\Gamma} \cup \mathring{\mathcal{N}}_{\text{net}}$.

It is worth mentioning that the property $\mathcal{A}_{\text{net}}$ equips the one-dimensional discrete model with a realistic three-dimensional structure of the continuum model, which is further complemented by the *activation stretch* that is related to the tortuosity of the real fibre. This is taken into account later in Section 5.2 when addressing the constitutive behaviour of the fibres.

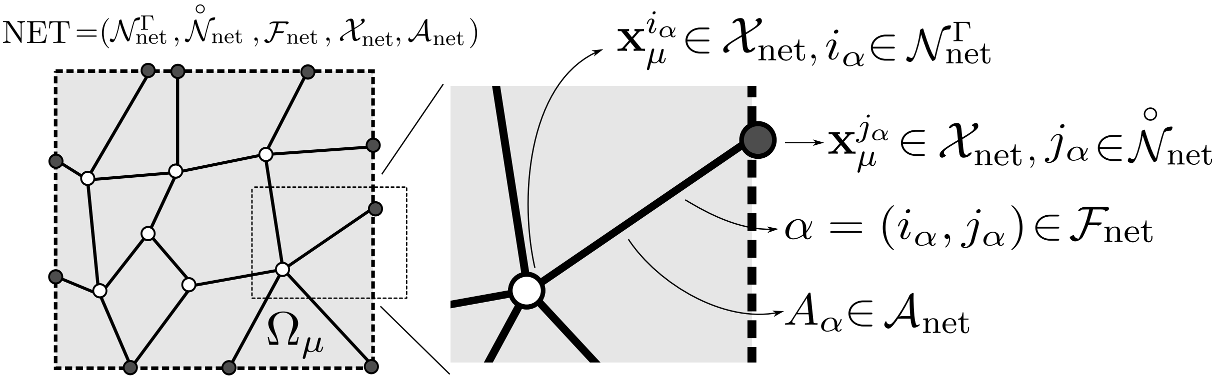

Figure 14 – Notation and basic ingredients in the geometrical/topological description of the *Network* of fibres.

Consider now the length of fibre α given by

$$L_\alpha = \|\mathbf{x}_\mu^{j_\alpha} - \mathbf{x}_\mu^{i_\alpha}\|_2, \tag{4.22}$$

where $\|\cdot\|_2$ is the standard Euclidean norm in $\mathbb{R}^{\text{n}_\text{d}}$. Let us define the volume of the fibre V_α and the measure of the whole set of fibres $|\mathcal{F}_{\text{net}}|$ as follows

$$V_\alpha = A_\alpha L_\alpha, \quad \alpha \in \mathcal{F}_{\text{net}}, \tag{4.23}$$

$$|\mathcal{F}_{\text{net}}| = \sum_{\alpha \in \mathcal{F}_{\text{net}}} V_\alpha. \tag{4.24}$$

The difference between any generic variable related to extreme points of fibre α, that is, $(\cdot)^{j_\alpha} - (\cdot)^{i_\alpha}$, is denoted by the following operator

$$\Delta^\alpha(\cdot) := (\cdot)^{j_\alpha} - (\cdot)^{i_\alpha}. \tag{4.25}$$

In addition, we introduce the *fibre-node signal brackets* $[\cdot,\cdot]$ defined by

$$[\alpha, i] = \begin{cases} 1 & \text{if } j_\alpha = i, \\ -1 & \text{if } i_\alpha = i, \\ 0 & \text{otherwise.} \end{cases} \tag{4.26}$$

This operation contains the same information as the standard fibre (mesh) connectivity data structure, being an alternative way to describe it, but significantly simplifies the derivations in this work. Note that $[\alpha, i]$ is different from zero only when α is in the set

$$\begin{aligned} \mathcal{F}^i_{\text{net}} &= \text{fibres sharing node } i \\ &= \{\alpha = (i_\alpha, j_\alpha) \in \mathcal{F}_{\text{net}},\ i_\alpha = i \text{ or } j_\alpha = i\}. \end{aligned} \tag{4.27}$$

Operator Δ^α can be expressed in terms of the *fibre-node signal brackets* as follows

$$\Delta^\alpha(\cdot) = \sum_{i \in \mathcal{N}_{\text{net}}} [\alpha, i](\cdot)^i. \tag{4.28}$$

Also, we introduce the unit vector $\mathbf{a}_\alpha$ defined by fibre α and directed from the initial node i_α to the final node j_α, that is

$$\mathbf{a}_\alpha = \frac{1}{L_\alpha}\Delta^\alpha \mathbf{x}_\mu. \tag{4.29}$$

Associated to each node $i \in \mathcal{N}^\Gamma_{\text{net}}$, lying over the boundary of the RVE, we have the *node boundary area(s)* $\bar{A}_{i,k}$ and the *node boundary normal vector(s)* $\mathbf{n}_{i,k}$, where $k \in \{1, \ldots, k_i^{max}\}$, being k_i^{max} the number of RVE faces sharing node i. For example, for a two-dimensional squared RVE as in Fig. 14, for a node $i \in \mathcal{N}^\Gamma_{\text{net}}$ over a RVE corner corresponds $k_i^{max} = 2$, otherwise it is $k_i^{max} = 1$. In a three-dimensional cubic RVE, k_i^{max} may assume the values of 3 (at vertices), 2 (on edges) or 1 (over faces).

The area(s) $\bar{A}_{i,k}$ is(are) calculated accounting for the area A_α and direction of fibres $\mathbf{a}_\alpha$ that reach the boundary at a node $i \in \mathcal{N}^\Gamma_{\text{net}}$ and its/their respective normal(s) $\mathbf{n}_{i,k}$, which is(are) the corresponding outward unit normal vector(s) to the boundary Γ_μ, as follows

$$\bar{A}_{i,k} = \sum_{\alpha \in \mathcal{F}^i_{\text{net}}} |\mathbf{n}_{i,k} \cdot \mathbf{a}_\alpha| A_\alpha \quad \text{for } i \in \mathcal{N}^\Gamma_{\text{net}}, k \in \{1, \ldots, k_i^{max}\}. \tag{4.30}$$

The geometrical interpretation can be found in Section 4.2.3 where typical examples of joints are analysed in Fig. 13 and equations therein.

To shorten notation let us introduce the *equivalent boundary area* and *normal* for a node over the boundary as

$$\bar{A}_i = \left\| \sum_{k=1}^{k_i^{max}} \bar{A}_{i,k}\mathbf{n}_{i,k} \right\|_2, \tag{4.31}$$

$$\mathbf{n}_i = \frac{1}{\bar{A}_i} \sum_{k=1}^{k_i^{max}} \bar{A}_{i,k}\mathbf{n}_{i,k}. \tag{4.32}$$

Now, let us define the *joint normal vector* $\mathbf{m}_i$ for every $i \in \mathcal{N}_{\text{net}}$ accounting for the surface integral of the normals for a given joint collapsed into its corresponding node. As explained in 4.2, the surface considered is the internal solid surface, which means the intersection of the joint and fibres for internal nodes, added to the intersection between joint and RVE borders for boundary nodes. Using definitions (4.31) and (4.32) we can define $\mathbf{m}_i$ as:

$$\mathbf{m}_i = \begin{cases} -\sum_{\alpha \in \mathcal{F}^i_{\text{net}}} [\alpha, i] A_\alpha \mathbf{a}_\alpha & i \in \mathring{\mathcal{N}}_{\text{net}}, \\ \bar{A}_i \mathbf{n}_i - \sum_{\alpha \in \mathcal{F}^i_{\text{net}}} [\alpha, i] A_\alpha \mathbf{a}_\alpha & i \in \mathcal{N}^{\Gamma}_{\text{net}}. \end{cases} \tag{4.33}$$

Note that the negative sign and fibre-node signal brackets in the definition naturally accommodates the orientation of fibre unit vector to point outwards the joint domain as can be appreciated in Fig. 15.

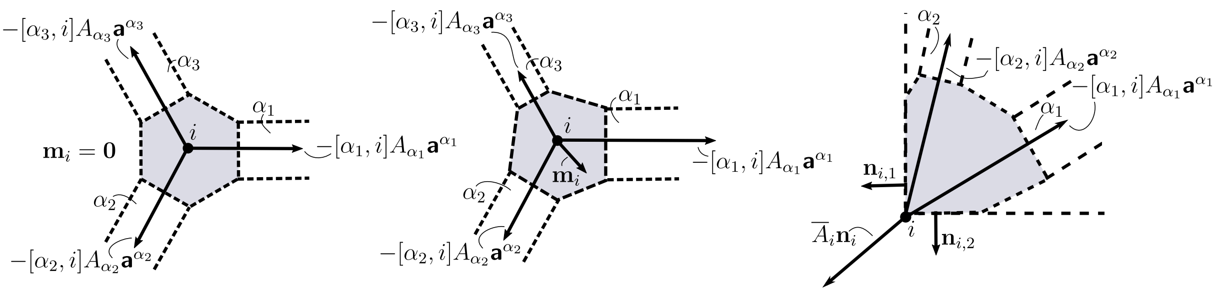

Figure 15 – Concept of joint normal vector in different situations. Left inset: regular hexagonally-shaped joint with $A_{\alpha_1} = A_{\alpha_2} = A_{\alpha_3}$, yielding $\mathbf{m}_i = \mathbf{0}$. Middle inset: arbitrary joint with $A_{\alpha_1} \neq A_{\alpha_2} \neq A_{\alpha_3}$ and so $\mathbf{m}_i \neq \mathbf{0}$. Right inset: Joint at a corner.

In the present framework, the discrete structure of NET of an RVE is just admissible when the graph $(\mathcal{N}_{\text{net}}, \mathcal{F}_{\text{net}})$ is connected, that is, any two nodes of the network are connected by at least one path of fibres.

Remark 17 *Hereafter, in order to facilitate the reading of the manuscript, we adopt different fonts to represent tensorial (including vectors) quantities associated to fibres and* *nodes, such as* $\mathbf{a}_\alpha$ $(\alpha \in \mathcal{F}_{\text{net}})$ *for fibre and* $\mathbf{x}^i_\mu$ $(i \in \mathcal{N}_{\text{net}})$ *for nodes. For n-tuples of tensors we consider Blackboard bold fonts, for example* $\mathbb{A} = \{\mathbf{a}_\alpha\}_{\alpha\in\mathcal{F}_{\text{net}}}$*, generally with the same letter to represent the n-tuple as well as its elements. This notation is extensively used in the forthcoming sections.*

4.3.2 Microscale displacement

Given a NET we are interested in describing the *displacement* experienced by material points in this *Network*. By material points we have the joints (nodes) and the points that compose the fibres (points of the straight lines).

The displacement at the nodes is an element of the following vector space

$$\mathscr{U}^N_\mu = \{\mathbb{U}^N_\mu = \{\mathbf{u}^i_\mu\}_{i\in\mathcal{N}_{\text{net}}}; \mathbf{u}^i_\mu \in \mathbb{R}^{\text{n}_\text{d}},\ i \in \mathcal{N}_{\text{net}}\}. \tag{4.34}$$

It consists of a $|\mathcal{N}_{\text{net}}|$-tuple of vectors ($|\mathcal{N}_{\text{net}}|$ the cardinality of $\mathcal{N}_{\text{net}}$) in the n_d-dimensional space, each vector representing the displacement at each node of the *Network*, thus we denote $\mathbf{u}^i_\mu$ the displacement of node $i \in \mathcal{N}_{\text{net}}$.

For a given $\mathbb{U}^N_\mu \in \mathscr{U}^N_\mu$, the fibre displacements fields are in the vector functional space

$$\begin{aligned}\mathscr{U}^F_\mu := \{\mathbb{U}^F_\mu = \{\mathbf{u}^\alpha_\mu\}_{\alpha\in\mathcal{F}_{\text{net}}}; \mathbf{u}^\alpha_\mu : [0, L_\alpha] \to \mathbb{R}^{\text{n}_\text{d}};&\\ \mathbf{u}^\alpha_\mu(s) = \Big(1 - \tfrac{s}{L_\alpha}\Big)\mathbf{u}^{i_\alpha}_\mu + \tfrac{s}{L_\alpha}\mathbf{u}^{j_\alpha}_\mu, s \in [0, L_\alpha], \alpha = (i_\alpha, j_\alpha) \in \mathcal{F}_{\text{net}}\},&\end{aligned} \tag{4.35}$$

where the vector field $\mathbf{u}^\alpha_\mu$ associated to each fibre $\alpha \in \mathcal{F}_{\text{net}}$ represents the displacement field along the centreline of the fibre in the n_d-dimensional space. Notice that, the space $\mathscr{U}^F_\mu$ is univocally established once $\mathbb{U}^N_\mu \in \mathscr{U}^N_\mu$ is specified. As a consequence, if two fibres share a node, the displacement at such node is the same, which is one of the hypotheses considered in this work.

Therefore, the displacement in the network is completely characterised by the space

$$\mathscr{U}_\mu := \{\mathbb{U}_\mu = (\mathbb{U}^N_\mu, \mathbb{U}^F_\mu) \in \mathscr{U}^N_\mu \times \mathscr{U}^F_\mu\}. \tag{4.36}$$

The operation of addition in $\mathscr{U}_\mu$ is such that for $\mathbb{W}_1, \mathbb{W}_2 \in \mathscr{U}_\mu$ yields $\mathbb{W}_3 = \mathbb{W}_1 + \mathbb{W}_2 \in \mathscr{U}_\mu$ with

$$\mathbf{w}^i_3 = \mathbf{w}^i_1 + \mathbf{w}^i_2 \qquad \forall i \in \mathcal{N}_{\text{net}}, \tag{4.37}$$

$$\mathbf{w}^\alpha_3(s) = \mathbf{w}^\alpha_1(s) + \mathbf{w}^\alpha_2(s) \qquad \forall \alpha \in \mathcal{F}_{\text{net}}, \forall s \in [0, L_\alpha], \tag{4.38}$$

where $\mathbb{W}_k = (\{\mathbf{w}^i_k\}_{i\in\mathcal{N}_{net}}, \{\{\mathbf{w}^\alpha_k\}_{\alpha\in\mathcal{F}_{net}}\})$, $k = 1, 2, 3$. The zero element in this space is denoted by $\mathbb{O}$ in such way that $\mathbb{W} + \mathbb{O} = \mathbb{W},\ \forall \mathbb{W} \in \mathscr{U}_\mu$, which means that $\mathbb{O}$ has zero-valued vectors for the nodes part and zero-valued constant vector functions for the fibre part. Analogous interpretation of addition is considered for any other space to be defined in terms of tuples in this manuscript.

Remark 18 *From the definition of $\mathscr{U}_\mu^F$ in (4.35), it is easy to see that the space $\mathscr{U}_\mu$ has the same dimension than $\mathscr{U}_\mu^N$. In other words, an element $\mathbb{U}_\mu \in \mathscr{U}_\mu$ is uniquely determined by a choice of $\mathbb{U}_\mu^N \in \mathscr{U}_\mu^N$. We extensively use this property overall the manuscript by defining quantities exclusively in terms of $\mathbb{U}_\mu^N$.*

4.3.3 Insertion operators

So far, the discrete kinematics groundwork has been established for a network of fibres. Now, in the same spirit of Section 2.2.2.1, we estabilish that the macroscale displacement at point $\mathbf{x}_M \in \Omega_M$ is mapped into the microscale kinematics using the following operator

$$\begin{aligned} \mathcal{J}_\mu^{\mathscr{U}} &: \mathbb{R}^{\mathrm{n_d}} \to \mathscr{U}_\mu, \\ &\mathbf{u} \mapsto \mathcal{J}_\mu^{\mathscr{U}}(\mathbf{u}) = (\mathcal{J}_\mu^{\mathscr{U},N}(\mathbf{u}), \mathcal{J}_\mu^{\mathscr{U},F}(\mathbf{u})), \end{aligned} \tag{4.39}$$

defined by

$$[\mathcal{J}_\mu^{\mathscr{U},N}(\mathbf{u})]^i = \mathbf{u} \qquad i \in \mathcal{N}_{\mathrm{net}}, \tag{4.40}$$

$$[\mathcal{J}_\mu^{\mathscr{U},F}(\mathbf{u})]^\alpha(s) = \mathbf{u} \qquad \alpha \in \mathcal{F}_{\mathrm{net}}, s \in [0, L_\alpha], \tag{4.41}$$

i.e.,. the macroscale displacement at point $\mathbf{x}_M$ is inserted uniformly in the network (joints and trusses). The macroscale gradient tensor at point $\mathbf{x}$ is mapped into the microscale kinematics through the following operator

$$\begin{aligned} \mathcal{J}_\mu^{\mathscr{E}} &: \mathbb{R}^{\mathrm{n_d} \times \mathrm{n_d}} \to \mathscr{U}_\mu, \\ &\mathbf{G} \mapsto \mathcal{J}_\mu^{\mathscr{E}}(\mathbf{G}) = (\mathcal{J}_\mu^{\mathscr{E},N}(\mathbf{G}), \mathcal{J}_\mu^{\mathscr{E},F}(\mathbf{G})), \end{aligned} \tag{4.42}$$

defined by

$$[\mathcal{J}_\mu^{\mathscr{E},N}(\mathbf{G})]^i = \mathbf{G}(\mathbf{x}_\mu^i - \mathbf{x}_\mu^G), \qquad i \in \mathcal{N}_{\mathrm{net}}, \tag{4.43}$$

$$[\mathcal{J}_\mu^{\mathscr{E},F}(\mathbf{G})]^\alpha(s) = \mathbf{G}\left(\left(1 - \frac{s}{L_\alpha}\right)\mathbf{x}_\mu^{i_\alpha} + \frac{s}{L_\alpha}\mathbf{x}_\mu^{j_\alpha} - \mathbf{x}_\mu^G\right), \qquad \alpha \in \mathcal{F}_{\mathrm{net}}, s \in [0, L_\alpha]. \tag{4.44}$$

where $\mathbf{x}_\mu^G$ is the geometric center for the network of fibres, still to be defined in (4.56).

Remark 19 *The macroscale displacement and gradient are only inserted in the material domain, that is, in the locus of material particles at the microscale, specifically at nodes and in fibres. The empty space surrounding the network plays no role in the definition of the microscale kinematics.*

We introduce the so-called microscale displacement fluctuations $\tilde{\mathbb{U}}_\mu \in \mathscr{U}_\mu$ (see Remark 20) such that the microscale displacement (and its virtual variations) can be expressed through the following expansion

$$\mathbb{U}_\mu = \mathcal{J}_\mu^{\mathscr{U}}(\mathbf{u}) + \mathcal{J}_\mu^{\mathscr{E}}(\mathbf{G}) + \tilde{\mathbb{U}}_\mu, \tag{4.45}$$

which, in the nodal-wise sense results

$$\mathbf{u}_\mu^i = \mathbf{u} + \mathbf{G}(\mathbf{x}_\mu^i - \mathbf{x}_\mu^G) + \tilde{\mathbf{u}}_\mu^i \quad i \in \mathcal{N}_{\mathrm{net}}, \tag{4.46}$$

where $\tilde{\mathbf{u}}_\mu^i$ is the displacement fluctuations of a node $i \in \mathcal{N}_{\mathrm{net}}$ of the generalised fluctuation $\tilde{\mathbb{U}}_\mu$ (notation is as in (4.34)).

Remark 20 *Fluctuations $\tilde{\mathbb{U}}_\mu$ is not an arbitrary element of $\mathscr{U}_\mu$ but it belongs to a specific space (subspace of $\mathscr{U}_\mu$), the so-called space of admissible displacement fluctuations, denoted by $\widetilde{\mathscr{U}}_\mu$. So far, it is only important to keep in mind that the different manners to define $\widetilde{\mathscr{U}}_\mu$ imply in more or less constrained kinematics, as illustrated in Fig. 16. The mathematical characterisation of this family of spaces is subject of Section 4.3.5.3.*

Remark 21 *From definition (4.45), the triple $(\mathbf{u}, \mathbf{G}, \tilde{\mathbb{U}}_\mu) \in \mathbb{R}^{\mathrm{n_d}} \times \mathbb{R}^{\mathrm{n_d} \times \mathrm{n_d}} \times \widetilde{\mathscr{U}}_\mu$ (see Remark 20) uniquely characterises the displacement $\mathbb{U}_\mu \in \mathscr{U}_\mu$. This connection is used in Section 4.3.4.*

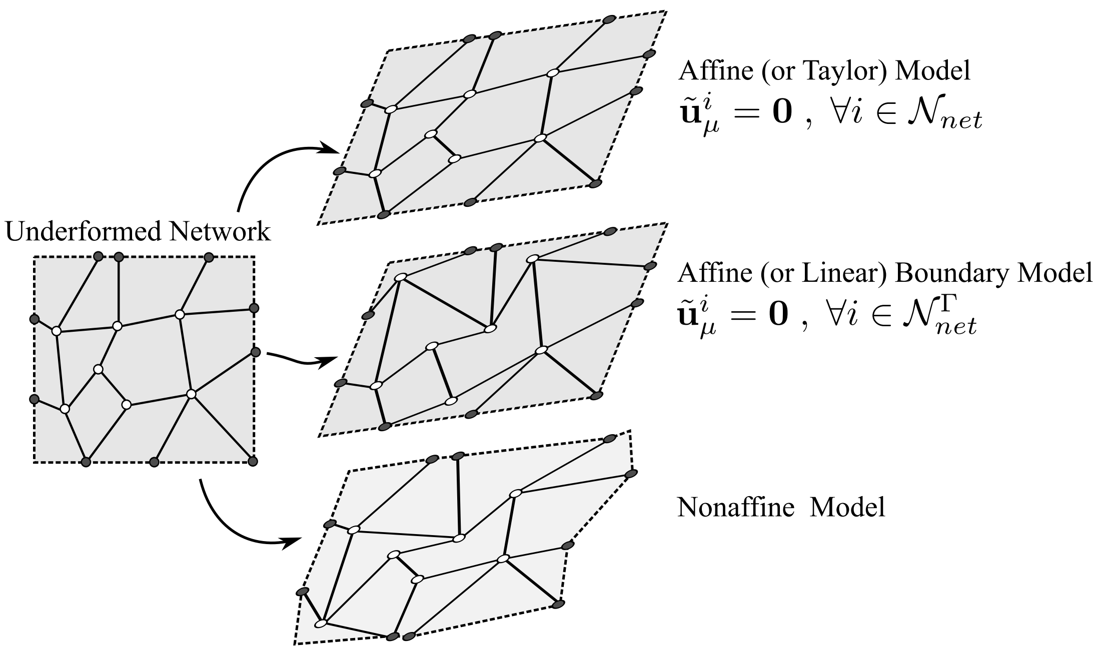

Figure 16 – Affine kinematics and nonaffine kinematics due to the existence of fluctuations.

4.3.4 Generalised microscale gradient operator

In this section we define the *generalised gradient* operation in the microscale reference configuration. This operator, similarly to the gradient in continuum mechanics, provides the measure of the first order variation of the displacement field defined in the network.

Associated to $\mathscr{U}_\mu$, we have the space of *generalised gradients* given by

$$\mathscr{E}_\mu = \{\mathbb{G}_\mu = (\{\mathbf{G}^i_\mu\}_{i\in\mathcal{N}_{\rm net}}, \{\mathsf{G}^\alpha_\mu\}_{\alpha\in\mathcal{F}_{\rm net}}); \\ \mathbf{G}^i_\mu \in \mathbb{R}^{\rm n_d\times n_d},\ i\in\mathcal{N}_{\rm net}, \mathsf{G}^\alpha_\mu \in \mathbb{R}^{\rm n_d\times n_d},\ \alpha\in\mathcal{F}_{\rm net}\}. \tag{4.47}$$

The addition in $\mathscr{E}_\mu$ is defined in the same sense as in (4.37)-(4.38).

For a given *NET-gradient* $\mathbb{G}_\mu \in \mathscr{E}_\mu$, we denote the *N-gradient* $\mathbf{G}^i_\mu$ a generalised gradient measure at node $i \in \mathcal{N}_{\rm net}$ and the *F-gradient* G^α_μ a generalised gradient for fibre $\alpha \in \mathcal{F}_{\rm net}$. The relation between node displacements and the generalised gradients in nodes and fibres is given through the *generalised microscale gradient operator*

$$\begin{aligned} \mathcal{D}_\mu : \mathscr{U}_\mu &\to \mathscr{E}_\mu, \\ \mathbb{U}_\mu &\mapsto \mathbb{G}_\mu = \mathcal{D}_\mu(\mathbb{U}_\mu), \end{aligned} \tag{4.48}$$

where $\mathbb{G}_\mu = (\{\mathbf{G}^i_\mu\}_{i\in\mathcal{N}_{\rm net}}, \{\mathsf{G}^\alpha_\mu\}_{\alpha\in\mathcal{F}_{\rm net}})$ is defined through

$$\mathbf{G}^i_\mu := \tilde{\mathbf{u}}^i_\mu \otimes \mathbf{m}_i \qquad \forall i \in \mathcal{N}_{\rm net}, \tag{4.49}$$

$$\mathsf{G}^\alpha_\mu := \frac{1}{L_\alpha}\Delta^\alpha \mathbb{U}_\mu \otimes \mathsf{a}_\alpha \qquad \forall \alpha \in \mathcal{F}_{\rm net}, \tag{4.50}$$

with $\mathbf{m}_i$ being the *joint normal vector* defined in (4.33). An alternative form to (4.50) is given by

$$\mathsf{G}^\alpha_\mu = \mathbf{G}\mathsf{a}_\alpha \otimes \mathsf{a}_\alpha + \frac{1}{L_\alpha}\Delta^\alpha \tilde{\mathbb{U}}_\mu \otimes \mathsf{a}_\alpha. \tag{4.51}$$

The definition of the *N-gradient*, given by (4.49), is reached by considering the integral of the gradient of the displacement field in the domain of a joint, as detailed in Section 4.2.2, where it can be appreciated the correspondence with the first two summations of (4.10). Hence, if we understand the gradient as a measure of the non-homogeneity of the displacement field, the *N-gradient* amounts to the total non-homogeneity lumped at a joint connecting a certain number of concurrent fibres. As can also be appreciated in Section 4.2.2, it can be proved that only fluctuations play an important role in our model in which joints are idealised to be small.

Definition (4.50) can be regarded as the gradient of the displacement field in some fixed (global) coordinate frame of a straight truss. Remember that for the truss the only mechanically relevant kinematics is along its axial coordinate. The alternative expression

(4.51) is obtained by the replacing (4.45) into (4.50). It is important to remember that the full derivations in the continuum setting are exposed in Section 4.2, where the result obtained in (4.6) was a consequence of the truss hypothesis.

The physical meaning of the F-gradient[2] in each fibre is such that a vector $\mathbf{q}_\mu^\alpha = (\mathbf{I} + \mathbf{G}_\mu^\alpha)\mathbf{a}_\alpha$ is pointed towards the actual direction of the fibre and its euclidean norm is the stretch of the fibre (ratio between actual and original lengths). This motivates the definition of the so-called *generalised fibre strain vector* as

$$\mathbf{g}_\mu^\alpha := \mathbf{G}_\mu^\alpha \mathbf{a}_\alpha \tag{4.52}$$

The representation using the vector $\mathbf{g}_\mu^\alpha$ instead of the second-order tensor $\mathbf{G}_\mu^\alpha$ is preferred in Chapter 5.

It is important to remember that the *NET-gradient* $\mathbb{G}_\mu$ collects generalised gradients from two different kinds of components, i.e., nodes and fibres, being these, respectively, zero-dimensional and one-dimensional entities. Therefore, units are not homogeneous between *N-gradient* and *F-gradient*. Specifically in the case of *N-gradient*, it is not dimensionless, as classical gradients are, but it already has units of volume (this is actually a matter of convention). Although not classical, our special definition for $\mathbb{G}_\mu$ shows to be particularly suitable when we postulate the homogenisation for gradients in Section 4.3.5.2.

Remark 22 *At this point, it is important to highlight that the RVE domain Ω_μ and the network of fibres* NET *are different concepts. Domain Ω_μ is understood as an observational window of the macroscale point $\mathbf{x}_M \in \Omega_M$, while* NET *is the collection of material particles for which a minimum set of geometrical and topological information was endowed to adequately describe the discrete kinematical structure for the problem. The RVE domain Ω_μ contains the* NET *and empty space surrounding the* NET*. Hence, the* NET *provides the material substrate on top of which kinematical quantities and generalised gradient measures are defined.*

Remark 23 *Both definitions, (4.49) and (4.50), imply certain geometrical considerations. In the former, only the solid part of the joint boundary is considered as it comes from the definition of* joint normal vector *in (4.33). In the later, only the axial part of the gradient plays a role for the strain tensor as dictated by the one-dimensional character of fibres. As discussed in Section 4.3.5, these two model simplifications have to be taken into consideration when homogenisation operators are postulated.*

[2] Instead of $\mathbf{G}_\mu^\alpha$ as primary generalised gradient variable, we can equivalently define $\mathbf{F}_\mu^\alpha = (\mathbf{I} + \mathbf{G}_\mu^\alpha)$ as the generalised deformation gradient associated to $\mathbf{G}_\mu^\alpha$, which leads to an equivalent formulation.

4.3.5 Kinematic homogenisation operators

Based on what has been discussed in Section 4.2.1 and Section 4.2.2, in this section we define the homogenisation operators providing a sense of kinematic conservation in the transfer between both scales.

4.3.5.1 Homogenisation of displacements

First, consider the homogenisation operator for the displacement field (and for its virtual variations) defined as

$$\begin{aligned} &\mathcal{H}_\mu^{\mathscr{U}} : \mathscr{U}_\mu \to \mathbb{R}^{\mathrm{n_d}}, \\ &\mathbb{U}_\mu \mapsto \mathcal{H}_\mu^{\mathscr{U}}(\mathbb{U}_\mu) = \frac{1}{|\mathcal{F}_{\mathrm{net}}|} \sum_{\alpha \in \mathcal{F}_{\mathrm{net}}} \frac{V_\alpha}{2} (\mathbf{u}_\mu^{i_\alpha} + \mathbf{u}_\mu^{j_\alpha}). \end{aligned} \tag{4.53}$$

Note that (4.53) is inspired by (4.7) and by construction, $\mathcal{H}_\mu^{\mathscr{U}}$ satisfies

$$\mathcal{H}_\mu^{\mathscr{U}}(\mathcal{J}_\mu^{\mathscr{U}}(\mathbf{u})) = \mathbf{u}. \tag{4.54}$$

We also require

$$\mathcal{H}_\mu^{\mathscr{U}}(\mathcal{J}_\mu^{\mathscr{E}}(\mathbf{G})) = \mathbf{0}, \tag{4.55}$$

that leads to

$$\mathbf{x}_\mu^G = \frac{1}{|\mathcal{F}_{\mathrm{net}}|} \sum_{\alpha \in \mathcal{F}_{\mathrm{net}}} \frac{V_\alpha}{2} (\mathbf{x}_\mu^{i_\alpha} + \mathbf{x}_\mu^{j_\alpha}), \tag{4.56}$$

whose proof is given in Section 4.3.6. Note that constraint (4.55) is needed for the homogenised displacement to be independent from the macroscale gradient.

The macroscale and microscale displacement fields (or its virtual variations) are constrained to satisfy the following

$$\mathcal{H}_\mu^{\mathscr{U}}(\mathbb{U}_\mu) = \mathbf{u}. \tag{4.57}$$

Since the operator is linear, this is equivalent to

$$\mathcal{H}_\mu^{\mathscr{U}}(\mathbb{U}_\mu) = \mathcal{H}_\mu^{\mathscr{U}}(\mathcal{J}_\mu^{\mathscr{U}}(\mathbf{u})) + \mathcal{H}_\mu^{\mathscr{U}}(\mathcal{J}_\mu^{\mathscr{E}}(\mathbf{G})) + \mathcal{H}_\mu^{\mathscr{U}}(\tilde{\mathbb{U}}_\mu) = \mathbf{u}, \tag{4.58}$$

which implies, from (4.54) and (4.55), that the fluctuation $\tilde{\mathbb{U}}_\mu$ must satisfy

$$\mathcal{H}_\mu^{\mathscr{U}}(\tilde{\mathbb{U}}_\mu) = \frac{1}{|\mathcal{F}_{\mathrm{net}}|} \sum_{\alpha \in \mathcal{F}_{\mathrm{net}}} \frac{V_\alpha}{2} (\tilde{\mathbf{u}}_\mu^{i_\alpha} + \tilde{\mathbf{u}}_\mu^{j_\alpha}) = \mathbf{0}. \tag{4.59}$$

Note that (4.53) is a discrete counterpart of the standard displacement homogenisation for continua as presented in Section 2.3.2.

4.3.5.2 Homogenisation of generalised microscale gradient

We propose the homogenisation operator for the generalised microscale gradient (and for its virtual variations)

$$\begin{aligned} \mathcal{H}_\mu^{\mathscr{E}} : \mathscr{E}_\mu &\to \mathbb{R}^{\mathrm{n_d}\times\mathrm{n_d}}, \\ \mathbb{G}_\mu &\mapsto \mathcal{H}_\mu^{\mathscr{E}}(\mathbb{G}_\mu), \end{aligned} \tag{4.60}$$

defined by

$$\mathcal{H}_\mu^{\mathscr{E}}(\mathbb{G}_\mu) = \frac{1}{|\mathcal{F}_{\mathrm{net}}|}\left(\sum_{\alpha\in\mathcal{F}_{\mathrm{net}}} V_\alpha \mathbf{G}_\mu^\alpha + \sum_{i\in\mathcal{N}_{\mathrm{net}}} \mathbf{G}_\mu^i - \sum_{i\in\mathcal{N}_{\mathrm{net}}^\Gamma} \bar{A}_i \tilde{\mathbf{u}}_\mu^i \otimes \bar{\mathbf{n}}_\mu\right)\mathbf{B}^{-1}, \tag{4.61}$$

where $\mathbf{B}$ is an invertible second order tensor called *structural tensor* and $\bar{\mathbf{n}}_\mu$ is the *average normal vector*. These two geometric objects are defined in (4.65) and (4.69), respectively. Note that (4.61) can be seen as a discrete counterpart of the integral of the gradient of the displacement field in the material domain plus the incorporation of additional terms that make the homogenisation consistent. The full justification, based on the kinematics of continua, is found in Section 4.2, where the first two summations of the (4.61) are found in (4.10) and the last summation in (4.11).

Before proceeding with the definitions for $\mathbf{B}$ and $\bar{\mathbf{n}}_\mu$, let us first rewrite (4.61). Let us simplify the first two summations in (4.61), by using (4.49) and (4.51), as next

$$\begin{aligned} &\sum_{\alpha\in\mathcal{F}_{\mathrm{net}}} V_\alpha \mathbf{G}_\mu^\alpha + \sum_{i\in\mathcal{N}_{\mathrm{net}}} \mathbf{G}_\mu^i = \\ &\quad\sum_{\alpha\in\mathcal{F}_{\mathrm{net}}} V_\alpha\left(\mathbf{G}\mathbf{a}_\alpha \otimes \mathbf{a}_\alpha + \frac{1}{L_\alpha}\Delta^\alpha \tilde{\mathbb{U}}_\mu \otimes \mathbf{a}_\alpha\right) + \sum_{i\in\mathcal{N}_{\mathrm{net}}} \tilde{\mathbf{u}}_\mu^i \otimes \mathbf{m}_i = \\ &\quad\sum_{\alpha\in\mathcal{F}_{\mathrm{net}}} V_\alpha \mathbf{G}\mathbf{a}_\alpha \otimes \mathbf{a}_\alpha + \sum_{i\in\mathcal{N}_{\mathrm{net}}}\sum_{\alpha\in\mathcal{F}_{\mathrm{net}}^i} [\alpha, i] A_\alpha \tilde{\mathbf{u}}_\mu^i \otimes \mathbf{a}_\alpha \\ &+ \sum_{i\in\mathring{\mathcal{N}}_{\mathrm{net}}} \tilde{\mathbf{u}}_\mu^i \otimes \left(-\sum_{\alpha\in\mathcal{F}_{\mathrm{net}}^i} [\alpha, i] A_\alpha \mathbf{a}_\alpha\right) + \sum_{i\in\mathcal{N}_{\mathrm{net}}^\Gamma} \tilde{\mathbf{u}}_\mu^i \otimes \left(\bar{A}_i \mathbf{n}_i - \sum_{\alpha\in\mathcal{F}_{\mathrm{net}}^i} [\alpha, i] A_\alpha \mathbf{a}_\alpha\right) = \\ &\quad\sum_{\alpha\in\mathcal{F}_{\mathrm{net}}} V_\alpha \mathbf{G}\mathbf{a}_\alpha \otimes \mathbf{a}_\alpha + \sum_{i\in\mathcal{N}_{\mathrm{net}}^\Gamma} \bar{A}_i \tilde{\mathbf{u}}_\mu^i \otimes \mathbf{n}_i. \end{aligned} \tag{4.62}$$

Replacing the above expression into (4.61) we get the equivalent homogenisation relation below

$$\mathcal{H}_\mu^{\mathscr{E}}(\mathbb{G}_\mu) = \frac{1}{|\mathcal{F}_{\mathrm{net}}|}\left(\sum_{\alpha\in\mathcal{F}_{\mathrm{net}}} V_\alpha \mathbf{G}\mathbf{a}_\alpha \otimes \mathbf{a}_\alpha + \sum_{i\in\mathcal{N}_{\mathrm{net}}^\Gamma} \bar{A}_i \tilde{\mathbf{u}}_\mu^i \otimes (\mathbf{n}_i - \bar{\mathbf{n}}_\mu)\right)\mathbf{B}^{-1}. \tag{4.63}$$

The first fundamental requirement the operator $\mathcal{H}_\mu^{\mathscr{E}}(\cdot)$ must fulfill is that, for an affine model (i.e. $\tilde{\mathbb{U}}_\mu = \mathbb{O}$), one has to retrieve the macroscale gradient $\mathbf{G}$, that is

$$\mathcal{H}_\mu^{\mathscr{E}}(\mathbb{G}_\mu\big|_{\tilde{\mathbb{U}}_\mu=\mathbb{O}}) = \mathbf{G}, \tag{4.64}$$

then, from (4.63) we are led to the definition of $\mathbf{B}$ as

$$\mathbf{B} := \frac{1}{|\mathcal{F}_{\text{net}}|}\left(\sum_{\alpha\in\mathcal{F}_{\text{net}}} V_\alpha \mathbf{a}_\alpha \otimes \mathbf{a}_\alpha\right). \tag{4.65}$$

This tensor, named here as *structural tensor* (also called *orientation tensor*), is a concept which has also been found in the phenomenological modelling (GASSER; OGDEN; HOLZAPFEL, 2006; ZHANG et al., 2012). This theoretical connection can be regarded as a mathematical justification for the phenomenological importance of this tensor.

In turn, a second fundamental property of operator $\mathcal{H}_\mu^{\mathscr{E}}(\cdot)$ is that, for a uniform fluctuation field ($\tilde{\mathbb{U}}_\mu = \mathbb{C}$), we get the very same macroscale gradient, this means

$$\mathcal{H}_\mu^{\mathscr{E}}(\mathbb{G}_\mu\big|_{\tilde{\mathbb{U}}_\mu=\mathbb{C}}) = \mathbf{G}. \tag{4.66}$$

Since $\mathcal{H}_\mu^{\mathscr{E}}$ is a linear operator, from (4.66) we obtain

$$\mathcal{H}_\mu^{\mathscr{E}}(\mathbb{G}_\mu|_{\tilde{\mathbb{U}}_\mu=\mathbb{C}}) = \mathcal{H}_\mu^{\mathscr{E}}(\mathbb{G}_\mu\big|_{\tilde{\mathbb{U}}_\mu=\mathbb{O}}) + \mathcal{H}_\mu^{\mathscr{E}}(\mathbb{G}_\mu\big|_{\mathbf{G}=\mathbf{O},\tilde{\mathbb{U}}_\mu=\mathbb{C}}) = \mathbf{G}, \tag{4.67}$$

which gives $\mathcal{H}_\mu^{\mathscr{E}}(\mathbb{G}_\mu\big|_{\mathbf{G}=\mathbf{O},\tilde{\mathbb{U}}_\mu=\mathbb{C}}) = \mathbf{O}$ by using (4.64). Finally, since

$$\mathcal{H}_\mu^{\mathscr{E}}(\mathbb{G}_\mu\big|_{\mathbf{G}=\mathbf{O},\tilde{\mathbb{U}}_\mu=\mathbb{C}}) = \frac{1}{|\mathcal{F}_{\text{net}}|}\left(\sum_{i\in\mathcal{N}_{\text{net}}^{\Gamma}} \bar{A}_i \tilde{\mathbf{u}}_\mu^i \otimes (\mathbf{n}_i - \bar{\mathbf{n}}_\mu)\right)\mathbf{B}^{-1} = \mathbf{O}, \tag{4.68}$$

we obtain the definition for the vector $\bar{\mathbf{n}}_\mu$ as

$$\bar{\mathbf{n}}_\mu := \frac{1}{\sum\limits_{i\in\mathcal{N}_{\text{net}}^{\Gamma}} \bar{A}_i}\left(\sum_{i\in\mathcal{N}_{\text{net}}^{\Gamma}} \bar{A}_i \mathbf{n}_i\right). \tag{4.69}$$

Remark 24 *Note that the final expression for $\bar{\mathbf{n}}_\mu$ in (4.69) is simply the average normal over the solid boundary. The* average normal vector *is a measure of the geometric unbalance in the solid part of the RVE boundary and, as we will see, it plays a fundamental role in the minimally constrained kinematical model, and consequently in the characterization of the dual entities.*

Remark 25 *Properties (4.64) and (4.66), which ensure the conservation of the deformation gradient and kinematical consistency of our model, naturally and univocally shape the tensor $\mathbf{B}$ and the vector $\bar{\mathbf{n}}_\mu$. In other words, the expressions (4.65) and (4.69) result from the homogenisation of gradient postulated in (4.61), which embodies the choice for the NET-gradient in (4.48), altogether with the considerations taken for the structural elements in the network (nodes and bars).*

Analogously to (4.57), the microscale gradient measure is constrained to satisfy the following

$$\mathcal{H}_\mu^{\mathscr{E}}(\mathbb{G}_\mu) = \mathbf{G}, \tag{4.70}$$

which implies, by linearity, that the fluctuation must satisfy

$$\mathcal{H}_\mu^{\mathscr{E}}(\mathbb{G}_\mu\big|_{\mathbf{G}=\mathbf{O}}) = \mathbf{O}, \tag{4.71}$$

or, more explicitly, and by using (4.63), the fluctuation must be compliant with the following constraint

$$\mathcal{H}_\mu^{\mathscr{E}}(\mathbb{G}_\mu|_{\mathbf{G}=\mathbf{O}}) = \frac{1}{|\mathcal{F}_{\text{net}}|}\Bigg(\sum_{i\in\mathcal{N}_{\text{net}}^{\Gamma}} \bar{A}_i \tilde{\mathbf{u}}_\mu^i \otimes (\mathbf{n}_i - \bar{\mathbf{n}}_\mu)\Bigg)\mathbf{B}^{-1} = \mathbf{O}. \tag{4.72}$$

The fact that (4.72) solely depends on boundary data is reasonable as one should expect to be able to control the RVE deformation exclusively by using the displacement field defined over the material points of the RVE that reach the boundary.

Remark 26 (Continuum Case) *As the tensor* $\mathbf{B}$ *is assumed to be invertible, post-multiplication of* (4.72) *by* $\mathbf{B}$ *leads to the alternative restriction*

$$\sum_{i\in\mathcal{N}_{\text{net}}^{\Gamma}} \bar{A}_i \tilde{\mathbf{u}}_\mu^i \otimes (\mathbf{n}_i - \bar{\mathbf{n}}_\mu) = \mathbf{O}. \tag{4.73}$$

This last expression has a clear parallel with that one encountered in multiscale models with voids reaching boundary as in Chapter 3 (see (3.15)*) We highlight that in our context, i.e., fibrous materials, the empty space between fibres (voids) is in general the major part of the RVE boundary, making the proposed generalisation of the classical constraint a true cornerstone.*

4.3.5.3 Space of admissible fluctuations

Using kinematical constraints given in (4.57) and (4.70), which ensure preservation of kinematical descriptors between macro and micro scales, we arrive respectively to the restrictions (4.59) and (4.73) for fluctuations. This allows us to define the largest space of kinematically admissible displacement fluctuations (and its virtual variations)

$$\widetilde{\mathscr{U}}_\mu^{\mathsf{M}} = \Bigg\{\tilde{\mathbb{U}}_\mu \in \mathscr{U}_\mu;\ \sum_{\alpha\in\mathcal{F}_{\text{net}}} \frac{V_\alpha}{2}(\tilde{\mathbf{u}}_\mu^{i_\alpha} + \tilde{\mathbf{u}}_\mu^{j_\alpha}) = \mathbf{0};\ \sum_{i\in\mathcal{N}_{\text{net}}^{\Gamma}} \bar{A}_i \tilde{\mathbf{u}}_\mu^i \otimes (\mathbf{n}_i - \bar{\mathbf{n}}_\mu) = \mathbf{O}\Bigg\}. \tag{4.74}$$

The space $\widetilde{\mathscr{U}}_\mu^{\mathsf{M}}$ is a subspace of $\mathscr{U}_\mu$ whose elements satisfy the minimum set of constraints such that kinematic conservation is guaranteed. Hence, space $\widetilde{\mathscr{U}}_\mu^{\mathsf{M}}$ defines the *minimally constrained multiscale model* (MCMM), also known in literature as *uniform traction model* for the very same reasons as in (2.41). As usual, other more constrained models, defined by corresponding spaces $\widetilde{\mathscr{U}}_\mu^*$ are also possible, provided they satisfy $\widetilde{\mathscr{U}}_\mu^* \subset \widetilde{\mathscr{U}}_\mu^{\mathsf{M}}$. Three sub-models with theoretical and practical relevance are the following:

1. Affine model (also called Taylor model or *rule of mixtures*): this model does not allow fluctuations neither in interior nodes neither on the boundary, being the most kinematically constrained scenario. Such model can be obtained as sub-model of the MCMM proposed here by taking

$$\widetilde{\mathscr{U}}_\mu^{\mathsf{T}} = \{\tilde{\mathbb{U}}_\mu \in \mathscr{U}_\mu;\ \tilde{\mathbf{u}}_\mu^i = \mathbf{0},\ i \in \mathcal{N}_{\text{net}}\}. \tag{4.75}$$

2. Affine boundary model (also called linear boundary model): this model allows nonzero fluctuations only in interior nodes which renders this scenario be less constrained than the Affine model. Mathematically we have

$$\widetilde{\mathscr{U}}_\mu^{\mathsf{L}} = \{\tilde{\mathbb{U}}_\mu \in \mathscr{U}_\mu;\ \mathcal{H}_\mu^{\mathscr{U}}(\tilde{\mathbb{U}}_\mu) = \mathbf{0}, \tilde{\mathbf{u}}_\mu^i = \mathbf{0},\ i \in \mathcal{N}_{\text{net}}^\Gamma\}. \tag{4.76}$$

3. Periodic boundary model [3]: Still less constrained than the Affine boundary model, this model allows nonzero fluctuations over the RVE boundary such that

$$\begin{aligned}\widetilde{\mathscr{U}}_\mu^{\mathsf{P}} = \{\tilde{\mathbb{U}}_\mu \in \mathscr{U}_\mu;\ \mathcal{H}_\mu^{\mathscr{U}}(\tilde{\mathbb{U}}_\mu) = \mathbf{0}, \tilde{\mathbf{u}}_\mu^{i_+} = \tilde{\mathbf{u}}_\mu^{i_-}, \\ (i_+, i_-) \in (\mathcal{N}_{\text{net}}^\Gamma)^+ \times (\mathcal{N}_{\text{net}}^\Gamma)^- \text{ is a periodic pair } \},\end{aligned} \tag{4.77}$$

where by periodic pair it is meant that $\bar{A}_{i_+,k_+} = \bar{A}_{i_-,k_-}$ and $\mathbf{n}_{i_+,k_+} = -\mathbf{n}_{i_-,k_-}$, given that $\{(\mathcal{N}_{\text{net}}^\Gamma)^+, (\mathcal{N}_{\text{net}}^\Gamma)^-\}$ is a partition of $\mathcal{N}_{\text{net}}^\Gamma$. Since $\bar{\mathbf{n}}_\mu = \mathbf{0}$ in this case, it is not difficult to see that $\widetilde{\mathscr{U}}_\mu^{\mathsf{P}} \subset \widetilde{\mathscr{U}}_\mu^{\mathsf{M}}$.

As already pointed out, the characterisation of the minimal set of kinematical constraints in the present context is a valuable aspect of the proposed model, because the space $\widetilde{\mathscr{U}}_\mu^{\mathsf{M}}$ established the admissible kinematical ground to derive other sub-models whose admissibility is guaranteed. An example of a non-classical subspace, not yet explored in the literature, is given by splitting the summation appearing in (4.73) and enforcing each of these parts to be zero.

Note that the aforementioned spaces satisfy the following hierarchy $\widetilde{\mathscr{U}}_\mu^{\mathsf{T}} \subset \widetilde{\mathscr{U}}_\mu^{\mathsf{L}} \subset \widetilde{\mathscr{U}}_\mu^{\mathsf{P}} \subset \widetilde{\mathscr{U}}_\mu^{\mathsf{M}}$. A helpful visualisation to show the transition from a more constrained model to a less constrained one is seen in Fig. 16. In particular, numerical examples presented in Section 6.1 address the effect of the choice of the fluctuation displacement spaces in the homogenised stress tensor at macro scale.

Finally, hereafter we denote $\widetilde{\mathscr{U}}_\mu$ to the space $\widetilde{\mathscr{U}}_\mu^{\mathsf{M}}$. In turn, the space of kinematically admissible virtual variations associated to $\widetilde{\mathscr{U}}_\mu$ is itself $\widetilde{\mathscr{U}}_\mu$, i.e., if $\hat{\tilde{\mathbb{U}}}_\mu = (\tilde{\mathbb{U}}_\mu)_1 - (\tilde{\mathbb{U}}_\mu)_2$ with $(\tilde{\mathbb{U}}_\mu)_1, (\tilde{\mathbb{U}}_\mu)_2 \in \widetilde{\mathscr{U}}_\mu$, hence $\hat{\tilde{\mathbb{U}}}_\mu \in \widetilde{\mathscr{U}}_\mu$.

[3] It requires geometric periodicity of fibres reaching the boundary in terms of direction, area and position.

4.3.6 Consistency of kinematical operators

In order to finalise the presentation of the multiscale kinematical for network of fibres model, we provide the proofs of consistency for all new discrete kinematical operators proposed. By consistency here we mean the fulfilment of certain kinematical restrictions to be satisfied by operators $\mathcal{J}_\mu^{\mathscr{U}}$, $\mathcal{J}_\mu^{\mathscr{E}}$, $\mathcal{D}_\mu$, $\mathcal{H}_\mu^{\mathscr{U}}$, $\mathcal{H}_\mu^{\mathscr{E}}$. In the original works (BLANCO et al., 2016; BLANCO et al., 2014), and as reviewed in Chapter 2, it was seen that the functional forms of the insertion, deformation and homogenisation operators can be arbitrarily defined provided they keep some relation between them. These relations were emphasised during the text, but in some cases the proof was skipped. This section aims to present the rigorous justifications (not necessarily proofs) for all necessary relations between operators proposed in this work, confirming that the formulation proposed is consistent with abstract framework constructed in (BLANCO et al., 2016; BLANCO et al., 2014).

First, consider the operators $\mathcal{J}_\mu^{\mathscr{U}}$, $\mathcal{J}_\mu^{\mathscr{E}}$, $\mathcal{D}_\mu$, $\mathcal{H}_\mu^{\mathscr{U}}$, $\mathcal{H}_\mu^{\mathscr{E}}$ as defined in (4.39), (4.42), (4.48), (4.53) and (4.60), respectively. Given $\mathbf{u} \in \mathbb{R}^{\mathrm{n_d}}, \mathbf{G} \in \mathbb{R}^{\mathrm{n_d}\times\mathrm{n_d}}$ and $\tilde{\mathbb{U}}_\mu \in \widetilde{\mathscr{U}_\mu}$ the following relations are satisfied:

1. $\mathcal{D}_\mu(\mathcal{J}_\mu^{\mathscr{U}}(\mathbf{u})) = \mathbf{O}$.
2. $\mathcal{H}_\mu^{\mathscr{U}}(\mathcal{J}_\mu^{\mathscr{U}}(\mathbf{u})) = \mathbf{u}$.
3. $\mathcal{H}_\mu^{\mathscr{E}}(\mathcal{D}_\mu(\mathcal{J}_\mu^{\mathscr{E}}(\mathbf{G}))) = \mathbf{G}$.
4. $\mathcal{H}_\mu^{\mathscr{U}}(\mathcal{J}_\mu^{\mathscr{E}}(\mathbf{G}))) = \mathbf{0}$.
5. $\mathcal{H}_\mu^{\mathscr{U}}(\tilde{\mathbb{U}}_\mu) = \mathbf{0}$.
6. $\mathcal{H}_\mu^{\mathscr{E}}(\mathcal{D}_\mu(\tilde{\mathbb{U}}_\mu))) = \mathbf{O}$.

Below, the proofs for these propositions follow.

1. From the definitions of the operators, for any $\alpha \in \mathcal{F}_{\text{net}}$ we have

$$\left[\mathcal{D}_\mu(\mathcal{J}_\mu^{\mathscr{U}}(\mathbf{u}))\right]^\alpha = \frac{1}{L_\alpha}\Delta^\alpha \mathcal{J}_\mu^{\mathscr{U}}(\mathbf{u}) \otimes \mathbf{a}_\alpha = \frac{1}{L_\alpha}(\mathbf{u}-\mathbf{u}) \otimes \mathbf{a}_\alpha = \mathbf{O}.$$

   Recalling that joint gradients only depend on the fluctuations, for any $i \in \mathcal{N}_{\text{net}}$ we have

$$\left[\mathcal{D}_\mu(\mathcal{J}_\mu^{\mathscr{U}}(\mathbf{u}))\right]^i = \mathbf{O}.$$

   Finally we conclude that $\mathcal{D}_\mu(\mathcal{J}_\mu^{\mathscr{U}}(\mathbf{u})) = \mathbf{O}$.

2. Take

$$\mathscr{H}_\mu^{\mathscr{U}}(\mathscr{J}_\mu^{\mathscr{U}}(\mathbf{u})) = \frac{1}{|\mathcal{F}_{\text{net}}|}\sum_{\alpha\in\mathcal{F}_{\text{net}}}\frac{V_\alpha}{2}([\mathscr{J}_\mu^{\mathscr{U}}(\mathbf{u})]^{i_\alpha} + [\mathscr{J}_\mu^{\mathscr{U}}(\mathbf{u})]^{j_\alpha}) = \frac{1}{|\mathcal{F}_{\text{net}}|}\sum_{\alpha\in\mathcal{F}_{\text{net}}}\frac{V_\alpha}{2}(\mathbf{u}+\mathbf{u}) = \frac{1}{|\mathcal{F}_{\text{net}}|}\Big(\sum_{\alpha\in\mathcal{F}_{\text{net}}}V_\alpha\Big)\mathbf{u} = \mathbf{u},$$

so, the result follows.

3. First recalling that joint gradients only depend on the fluctuations we have

$$\mathscr{H}_\mu^{\mathscr{E}}(\mathcal{D}_\mu(\mathscr{J}_\mu^{\mathscr{E}}(\mathbf{G}))) = \frac{1}{|\mathcal{F}_{\text{net}}|}\Big(\sum_{\alpha\in\mathcal{F}_{\text{net}}}V_\alpha\left[\mathcal{D}_\mu(\mathscr{J}_\mu^{\mathscr{E}}(\mathbf{G}))\right]^\alpha\Big)\mathbf{B}^{-1} = \frac{1}{|\mathcal{F}_{\text{net}}|}\Big(\sum_{\alpha\in\mathcal{F}_{\text{net}}}V_\alpha\mathbf{G}\mathbf{a}_\alpha\otimes\mathbf{a}_\alpha\Big)\mathbf{B}^{-1} = \mathbf{G}\underbrace{\frac{1}{|\mathcal{F}_{\text{net}}|}\Big(\sum_{\alpha\in\mathcal{F}_{\text{net}}}V_\alpha\mathbf{a}_\alpha\otimes\mathbf{a}_\alpha\Big)}_{=\mathbf{B}\text{ from (4.65)}}\mathbf{B}^{-1} = \mathbf{G},$$

and the result is verified.

4. Take now

$$\mathscr{H}_\mu^{\mathscr{U}}(\mathscr{J}_\mu^{\mathscr{E}}(\mathbf{G})) = \frac{1}{|\mathcal{F}_{\text{net}}|}\sum_{\alpha\in\mathcal{F}_{\text{net}}}\frac{V_\alpha}{2}([\mathscr{J}_\mu^{\mathscr{E}}(\mathbf{G})]^{i_\alpha} + [\mathscr{J}_\mu^{\mathscr{E}}(\mathbf{G})]^{j_\alpha}) = \frac{1}{|\mathcal{F}_{\text{net}}|}\sum_{\alpha\in\mathcal{F}_{\text{net}}}\frac{V_\alpha}{2}\mathbf{G}(\mathbf{x}_\mu^{i_\alpha}+\mathbf{x}_\mu^{j_\alpha}-2\mathbf{x}_\mu^G) = \mathbf{G}\Big(\underbrace{\frac{1}{|\mathcal{F}_{\text{net}}|}\sum_{\alpha\in\mathcal{F}_{\text{net}}}\frac{V_\alpha}{2}(\mathbf{x}_\mu^{i_\alpha}+\mathbf{x}_\mu^{j_\alpha})}_{=\mathbf{x}_\mu^G\text{ from (4.56)}} - \frac{1}{|\mathcal{F}_{\text{net}}|}\Big(\sum_{\alpha\in\mathcal{F}_{\text{net}}}V_\alpha\Big)\mathbf{x}_\mu^G\Big) = \mathbf{0},$$

so the statement holds.

5. This restriction is directly taken into account in the definition of the space $\widetilde{\mathscr{U}}_\mu$ (see (4.74)).

6. Also, this restriction is also directly enforced in the space $\widetilde{\mathscr{U}}_\mu$.

4.4 Mathematical duality and virtual power

In this section the virtual power functionals at both scales are postulated according to the kinematical framework considered at each scale.

At the macroscale, and in view of the model already presented in Section 2.3.1, we recall that the internal virtual power exerted at a given point $\mathbf{x}_M$ in a volume $|\Omega_\mu|$ is characterised as follows $\mathcal{P}^{\text{int}}_{M|\mathbf{x}}(\hat{\mathbf{G}}) = |\Omega_\mu|\mathbf{P}\cdot\hat{\mathbf{G}}$ where $\mathbf{P}$ stands for $\mathbf{P}_M|_{\mathbf{x}_M}$ and $|\Omega_\mu|$ is the volume of the microscale domain (void and solid) where, from the macroscale standpoint, the internal power is considered to be exerted. As already commented, body forces are disregarded in this model for sake of simplicity, so external macroscale virtual power vanishes.

Regarding the microscale, and according to the microscale kinematical setting presented in Section 4.3.1, the internal virtual power is a linear functional of $\hat{\mathbb{G}}_\mu$. Then, by duality arguments it admits the following characterisation

$$\widetilde{\mathcal{P}_\mu^{\text{int}}}(\hat{\mathbb{G}}_\mu) = \sum_{\alpha\in\mathcal{F}_{\text{net}}} V_\alpha \mathbf{S}_\mu^\alpha \cdot \hat{\mathbf{G}}_\mu^\alpha + \sum_{i\in\mathcal{N}_{\text{net}}} \mathbf{S}_\mu^i \cdot \hat{\mathbf{G}}_\mu^i, \tag{4.78}$$

where $\mathbf{S}_\mu^\alpha$ and $\mathbf{S}_\mu^i$ are generalised stresses for a fibre $\alpha \in \mathcal{F}_{\text{net}}$ and for a node $i \in \mathcal{N}_{\text{net}}$, respectively.

Hence, the model allows the N-gradient at each node to be different from zero as would be the case of torsional resistance at fibre connections because of fibre entanglement. However, as postulated earlier in this work, we admit that the generalised stress at nodes is zero, then (4.78) becomes

$$\mathcal{P}_\mu^{\text{int}}(\hat{\mathbb{G}}_\mu) = \sum_{\alpha\in\mathcal{F}_{\text{net}}} V_\alpha \mathbf{S}_\mu^\alpha \cdot \hat{\mathbf{G}}_\mu^\alpha, \tag{4.79}$$

which is the final format for the microscale internal virtual power used in the following developments.

According to (4.50), the stress tensor $\mathbf{S}_\mu^\alpha$ has the structure $\mathbf{S}_\mu^\alpha = \mathbf{s}_\mu^\alpha \otimes \mathbf{a}_\alpha$ with $\mathbf{s}_\mu^\alpha \in \mathbb{R}^{\text{n}_\text{d}}$ [4]. Then, the stress field in the entire network $\mathbb{S}_\mu^F$ is a field

$$\mathscr{S}_\mu = \{\mathbb{S}_\mu^F = \{\mathbf{S}_\mu^\alpha\}_{\alpha\in\mathcal{F}_{\text{net}}} : \mathcal{F}_{\text{net}} \to \mathbb{R}^{\text{n}_\text{d}\times\text{n}_\text{d}},\ \mathbf{S}_\mu^\alpha = \mathbf{s}_\mu^\alpha \otimes \mathbf{a}_\alpha,\ \mathbf{s}_\mu^\alpha \in \mathbb{R}^{\text{n}_\text{d}}\}. \tag{4.80}$$

Remark 27 *Note that the microscale stress field is defined just in $\mathcal{F}_{\text{net}}$ and not in $\mathcal{N}_{\text{net}} \times \mathcal{F}_{\text{net}}$ as in $\mathscr{E}_\mu$ (see definition (4.47)). This is a primary consequence of (4.79) that led to the definition of the internal virtual power in the microscale, which neglects any virtual power exerted at the nodes in the network.*

4.5 Principle of Multiscale Virtual Power

In this section the PMVP (see Section 2.2.4) is postulated for the case of networks of fibres in which virtual power functionals defined in Section 4.4 are invoked. Mathematically, this is

$$\mathcal{P}_{M|\mathbf{x}}^{\text{int}}(\hat{\mathbf{G}}) = \mathcal{P}_\mu^{\text{int}}(\hat{\mathbb{G}}_\mu) \quad \forall(\hat{\mathbf{G}}, \hat{\mathbb{G}}_\mu) \text{ kinematically admissible}, \tag{4.81}$$

[4] The vector $\mathbf{s}_\mu^\alpha$ is the so-called *generalised fibre stress vector* and in fact is the power-conjugate of the fibre strain vector $\mathbf{g}_\mu^\alpha$, defined in (4.52). These representations are particularly useful in Chapter 5.

where $\hat{\mathbb{G}}_\mu = \hat{\mathbb{G}}_\mu(\hat{\mathbf{G}}, \hat{\tilde{\mathbb{U}}}_\mu)$. Using the virtual power functionals for the previous section and also (4.51) we formulate the PMVP as follows.

Problem 3 (Principle of multiscale Virtual Power) *For the macroscale gradient measure $\mathbf{G} \in \mathbb{R}^{\mathrm{n_d}\times\mathrm{n_d}}$, it is said that the macroscale stress tensor at this point, $\mathbf{P}$, is in mechanical equilibrium with the network stress state, $\mathbb{S}_\mu^F = \{\mathbf{S}_\mu^\alpha\}_{\alpha\in\mathcal{F}_{\mathrm{net}}}$, if the following variational equation is satisfied*

$$\mathbf{P}\cdot\hat{\mathbf{G}} = \frac{1}{|\Omega_\mu|}\sum_{\alpha\in\mathcal{F}_{\mathrm{net}}} V_\alpha \mathbf{S}_\mu^\alpha \cdot \left(\hat{\mathbf{G}}\mathbf{a}_\alpha \otimes \mathbf{a}_\alpha + \frac{1}{L_\alpha}\Delta^\alpha \hat{\tilde{\mathbb{U}}}_\mu \otimes \mathbf{a}_\alpha\right)$$
$$\forall(\hat{\mathbf{G}}, \hat{\tilde{\mathbb{U}}}_\mu) \in \mathbb{R}^{\mathrm{n_d}\times\mathrm{n_d}} \times \widetilde{\mathscr{U}}_\mu. \quad (4.82)$$

As natural consequences of the PMVP we have: (i) the homogenisation formula for $\mathbf{P}$ (see Section 4.5.1), and (ii) the variational problem that characterises the mechanical equilibrium at the microscale in terms of the fluctuations of the displacement field (see Section 4.5.2).

Remark 28 *In variational equation (4.82), it is clear the distinction between the RVE domain, called Ω_μ, and the network* NET*, as already pointed by Remark 22. While the microscale virtual power is truly exerted in the trusses that form the* NET*, from the macroscale point of view this corresponds to a subdomain of macro-continuum material whose size is defined to be $|\Omega_\mu|$. This RVE volume is partially filled by $|\mathcal{F}_{\mathrm{net}}|$ plus the surrounding substance, as already discussed in Remark 15.*

4.5.1 Stress homogenisation

Let us take $\hat{\tilde{\mathbb{U}}}_\mu = \mathbb{O}$ in (4.82). We then derive the homogenisation formula for the stress tensor $\mathbf{P}$ at point $\mathbf{x}_M$ as follows

$$\mathbf{P}\cdot\hat{\mathbf{G}} = \frac{1}{|\Omega_\mu|}\sum_{\alpha\in\mathcal{F}_{\mathrm{net}}} V_\alpha \mathbf{S}_\mu^\alpha \cdot (\hat{\mathbf{G}}\mathbf{a}_\alpha \otimes \mathbf{a}_\alpha) \quad \forall\hat{\mathbf{G}} \in \mathbb{R}^{\mathrm{n_d}\times\mathrm{n_d}}, \tag{4.83}$$

which yields

$$\left(\mathbf{P} - \frac{1}{|\Omega_\mu|}\sum_{\alpha\in\mathcal{F}_{\mathrm{net}}} V_\alpha \mathbf{S}_\mu^\alpha \mathbf{a}_\alpha \otimes \mathbf{a}_\alpha\right)\cdot\hat{\mathbf{G}} = 0 \quad \forall\hat{\mathbf{G}} \in \mathbb{R}^{\mathrm{n_d}\times\mathrm{n_d}}. \tag{4.84}$$

Therefore, the homogenisation of the PKST follows

$$\mathbf{P} = \frac{1}{|\Omega_\mu|}\sum_{\alpha\in\mathcal{F}_{\mathrm{net}}} V_\alpha \mathbf{S}_\mu^\alpha \mathbf{a}_\alpha \otimes \mathbf{a}_\alpha. \tag{4.85}$$

Using the representation $\mathbf{S}_\mu^\alpha = \mathbf{s}_\mu^\alpha \otimes \mathbf{a}_\alpha$ (see (4.80)) we have

$$\mathbf{S}_\mu^\alpha \mathbf{a}_\alpha \otimes \mathbf{a}_\alpha = (\mathbf{s}_\mu^\alpha \otimes \mathbf{a}_\alpha)\mathbf{a}_\alpha \otimes \mathbf{a}_\alpha = \mathbf{s}_\mu^\alpha \otimes \mathbf{a}_\alpha = \mathbf{S}_\mu^\alpha, \tag{4.86}$$

and, so, the *Stress Homogenisation* operator results

$$\begin{aligned}
&\mathcal{H}_{\mathbf{P}} : \mathscr{S}_\mu \to \mathbb{R}^{\mathrm{n_d}\times\mathrm{n_d}} \\
&\mathbb{S}^F_\mu \mapsto \mathcal{H}_{\mathbf{P}}(\mathbb{S}^F_\mu) := \frac{1}{|\Omega_\mu|}\sum_{\alpha\in\mathcal{F}_{\mathrm{net}}} V_\alpha \mathbf{S}^\alpha_\mu = \frac{1}{|\Omega_\mu|}\sum_{\alpha\in\mathcal{F}_{\mathrm{net}}} V_\alpha \mathbf{s}^\alpha_\mu \otimes \mathbf{a}_\alpha,
\end{aligned} \tag{4.87}$$

in such way that $\mathbf{P} = \mathcal{H}_{\mathbf{P}}(\mathbb{S}^F_\mu)$.

It is also possible to derive a homogenisation formula completely equivalent to (4.87) but depending only on boundary data, i.e.., on the stress state of fibres that reach the boundary (see Section 4.6).

4.5.2 Microscale mechanical equilibrium problem

Now, taking $\hat{\mathbf{G}} = \mathbf{O}$ in (4.82) yields

$$\sum_{\alpha\in\mathcal{F}_{\mathrm{net}}} V_\alpha \mathbf{S}^\alpha_\mu \cdot \left(\frac{1}{L_\alpha}\Delta^\alpha \hat{\tilde{\mathbb{U}}}_\mu \otimes \mathbf{a}_\alpha\right) = \sum_{\alpha\in\mathcal{F}_{\mathrm{net}}} A_\alpha (\mathbf{S}^\alpha_\mu \mathbf{a}_\alpha)\cdot \Delta^\alpha \hat{\tilde{\mathbb{U}}}_\mu = \\ \sum_{\alpha\in\mathcal{F}_{\mathrm{net}}} A_\alpha \mathbf{s}^\alpha_\mu \cdot \Delta^\alpha \hat{\tilde{\mathbb{U}}}_\mu = 0 \quad \forall \hat{\tilde{\mathbb{U}}}_\mu \in \widetilde{\mathscr{U}}_\mu. \tag{4.88}$$

Consequently we have the following problem to be solved at the RVE.

Problem 4 (Microscale mechanical equilibrium) *Given* $\mathbf{G} \in \mathbb{R}^{\mathrm{n_d}\times\mathrm{n_d}}$*, find* $\tilde{\mathbb{U}}_\mu \in \widetilde{\mathscr{U}}_\mu$ *such that the stress vector* $\{\mathbf{s}^\alpha_\mu\}_{\alpha\in\mathcal{F}_{\mathrm{net}}}$ *is such that the following variational equation holds*

$$\sum_{\alpha\in\mathcal{F}_{\mathrm{net}}} A_\alpha \mathbf{s}^\alpha_\mu \cdot \Delta^\alpha \hat{\tilde{\mathbb{U}}}_\mu = 0 \quad \forall \hat{\tilde{\mathbb{U}}}_\mu \in \widetilde{\mathscr{U}}_\mu, \tag{4.89}$$

where $\mathbf{s}^\alpha_\mu$ *is related to* $\mathbf{G}^\alpha_\mu = \mathbf{G}\mathbf{a}_\alpha \otimes \mathbf{a}_\alpha + \frac{1}{L_\alpha}\Delta^\alpha \tilde{\mathbb{U}}_\mu \otimes \mathbf{a}_\alpha$ *through a microscale constitutive functional of the form* $\mathbf{s}^\alpha_\mu = \mathscr{F}^\alpha_\mu(\mathbf{G}^\alpha_\mu)$*.*

Once Problem 4 is solved, the evaluation of the microscale fibre stresses is straightforward, from which the homogenisation of the macroscale PKST follows directly using (4.87). For details concerning the constitutive law for the fibre, see Section 5.2.

In practice, constitutive and geometrical nonlinearities present in variational equation (4.89) can be addressed using the classical Newton-Raphson linearisation strategy. We omit the details here for the sake of brevity, but this issue is addressed in Problem 7 of Chapter 5, in the context of fibres, but has also been presented in Section 2.4.1 for the continuum formulation. Also in Chapter 5, in Section 5.2, we discuss the issue of for the constitutive laws for fibres.

The kinematical constraints in $\widetilde{\mathscr{U}}_\mu$ (see (4.57) and (4.70)) are imposed using the saddle point problem associated to (4.89) in which Lagrange multipliers are added to relax such constraints. This is detailed in Section 4.6.

Remark 29 *The Variational formulation (4.89) for the microscale problem is the classical problem of nonlinear trusses connected at end points with the exception of the specific constraints in the spaces of admissible functions. A standard approach to this problem is presented in (WRIGGERS, 2008, Chapter 9), where elemental stiffness matrices and residual vectors are derived in a reference frame aligned with the truss, and then properly rotated to assemble them in the global system of equations. The present formulation is absolutely equivalent to such classical formulation (proof omitted for the sake of brevity). The difference is that in the present work a global reference frame has been employed, which is advantageous to deal more directly with the kinematical constraints imposed by the kinematic coupling between scales.*

4.6 Reactive forces

To investigate the reactive forces, in the same fashion as done in Section 3.3.4 for porous RVEs, in this section we aim to rewrite Problem 4 relaxing the constrains in space $\widetilde{\mathscr{U}}_\mu$ through the introduction of Lagrange multipliers. Thus, we have the following problem.

Problem 5 (Lagrange multiplier formulation for the RVE problem) *Given* $\mathbf{G} \in \mathbb{R}^{\mathrm{n_d}\times\mathrm{n_d}}$, *find* $(\tilde{\mathbb{U}}_\mu, \boldsymbol{\Lambda}, \boldsymbol{\Theta}) \in \mathscr{U}_\mu \times \mathbb{R}^{\mathrm{n_d}\times\mathrm{n_d}} \times \mathbb{R}^{\mathrm{n_d}}$ *such that*

$$\sum_{\alpha\in\mathcal{F}_{\mathrm{net}}} A_\alpha \mathbf{s}^\alpha_\mu \cdot \Delta^\alpha \hat{\tilde{\mathbb{U}}}_\mu - \boldsymbol{\Lambda} \cdot \left(\sum_{i\in\mathcal{N}^\Gamma_{\mathrm{net}}} \bar{A}_i \hat{\tilde{\mathbf{u}}}^i_\mu \otimes (\mathbf{n}_i - \bar{\mathbf{n}}_\mu) \right) - \hat{\boldsymbol{\Lambda}} \cdot \left(\sum_{i\in\mathcal{N}^\Gamma_{\mathrm{net}}} \bar{A}_i \tilde{\mathbf{u}}^i_\mu \otimes (\mathbf{n}_i - \bar{\mathbf{n}}_\mu) \right)$$
$$+ \boldsymbol{\Theta} \cdot \left(\sum_{\alpha\in\mathcal{F}_{\mathrm{net}}} \frac{V_\alpha}{2} (\hat{\tilde{\mathbf{u}}}^{i_\alpha}_\mu + \hat{\tilde{\mathbf{u}}}^{j_\alpha}_\mu) \right) + \hat{\boldsymbol{\Theta}} \cdot \left(\sum_{\alpha\in\mathcal{F}_{\mathrm{net}}} \frac{V_\alpha}{2} (\tilde{\mathbf{u}}^{i_\alpha}_\mu + \tilde{\mathbf{u}}^{j_\alpha}_\mu) \right) = 0$$
$$\forall (\hat{\tilde{\mathbb{U}}}_\mu, \hat{\boldsymbol{\Lambda}}, \hat{\boldsymbol{\Theta}}) \in \mathscr{U}_\mu \times \mathbb{R}^{\mathrm{n_d}\times\mathrm{n_d}} \times \mathbb{R}^{\mathrm{n_d}}, \quad (4.90)$$

where $\mathbf{s}^\alpha_\mu = \mathscr{F}^\alpha_\mu(\mathbf{G}^\alpha_\mu)$, *with* $\mathbf{G}^\alpha_\mu = \mathbf{G}\mathbf{a}_\alpha \otimes \mathbf{a}_\alpha + \frac{1}{L_\alpha} \Delta^\alpha \tilde{\mathbb{U}}_\mu \otimes \mathbf{a}_\alpha$.

First, taking $\hat{\tilde{\mathbb{U}}}_\mu = \mathbb{O}$ and $\hat{\boldsymbol{\Theta}} = \mathbf{0}$ in (4.90) we retrieve, now as a natural consequence of the variational equation, the kinematical restriction (4.73), which is equivalent to $\mathcal{H}^{\mathscr{E}}_\mu(\mathcal{D}_\mu(\tilde{\mathbb{U}}_\mu)) = \mathbf{O}$. Secondly, taking $\hat{\tilde{\mathbb{U}}}_\mu = \mathbb{O}$ and $\hat{\boldsymbol{\Lambda}} = \mathbf{O}$ we arrive at (4.59), i.e., $\mathcal{H}^{\mathscr{U}}_\mu(\tilde{\mathbb{U}}_\mu) = \mathbf{0}$. Thirdly, taking $\hat{\boldsymbol{\Lambda}} = \mathbf{O}$ and $\hat{\boldsymbol{\Theta}} = \mathbf{0}$ result in

$$\sum_{\alpha\in\mathcal{F}_{\mathrm{net}}} A_\alpha \mathbf{s}^\alpha_\mu \cdot \Delta^\alpha \hat{\tilde{\mathbb{U}}}_\mu - \boldsymbol{\Lambda} \cdot \left(\sum_{i\in\mathcal{N}^\Gamma_{\mathrm{net}}} \bar{A}_i \hat{\tilde{\mathbf{u}}}^i_\mu \otimes (\mathbf{n}_i - \bar{\mathbf{n}}_\mu) \right)$$
$$+ \boldsymbol{\Theta} \cdot \left(\sum_{\alpha\in\mathcal{F}_{\mathrm{net}}} \frac{V_\alpha}{2} (\hat{\tilde{\mathbf{u}}}^{i_\alpha}_\mu + \hat{\tilde{\mathbf{u}}}^{j_\alpha}_\mu) \right) = 0 \qquad \forall \hat{\tilde{\mathbb{U}}}_\mu \in \mathscr{U}_\mu. \quad (4.91)$$

In particular, expression (4.91) is valid for $\hat{\hat{\mathbb{U}}}_\mu = \mathbb{C}$ (an uniform fluctuation field, i.e., $\hat{\hat{\mathbf{u}}}^i_\mu = \mathbf{c}$, $\forall i \in \mathcal{N}_{\text{net}}$). After some manipulation we have

$$\left(- \boldsymbol{\Lambda} \left(\sum_{i \in \mathcal{N}^{\Gamma}_{\text{net}}} \bar{A}_i (\mathbf{n}_i - \bar{\mathbf{n}}_\mu) \right) + |\mathcal{F}_{\text{net}}| \boldsymbol{\Theta} \right) \cdot \mathbf{c} = 0, \tag{4.92}$$

and by the fact that $\mathbf{c}$ is arbitrary and using the definition of $\bar{\mathbf{n}}_\mu$ in (4.69), we arrive at

$$\boldsymbol{\Theta} = \boldsymbol{\Lambda} \left(\frac{1}{|\mathcal{F}_{\text{net}}|} \sum_{i \in \mathcal{N}^{\Gamma}_{\text{net}}} \bar{A}_i (\mathbf{n}_i - \bar{\mathbf{n}}_\mu) \right) = \mathbf{0}. \tag{4.93}$$

Finally, rewriting (4.91) by taking into account (4.28) and (4.93) and splitting summations into interior and boundary nodes we have

$$\sum_{i \in \mathcal{N}^{\Gamma}_{\text{net}}} \left(\left(\sum_{\alpha \in \mathcal{F}^i_{\text{net}}} [\alpha, i] A_\alpha \mathbf{s}^\alpha_\mu \right) - \bar{A}_i \boldsymbol{\Lambda} (\mathbf{n}_i - \bar{\mathbf{n}}_\mu) \right) \cdot \hat{\hat{\mathbf{u}}}^i_\mu + \sum_{i \in \mathring{\mathcal{N}}_{\text{net}}} \left(\sum_{\alpha \in \mathcal{F}^i_{\text{net}}} [\alpha, i] A_\alpha \mathbf{s}^\alpha_\mu \right) \cdot \hat{\hat{\mathbf{u}}}^i_\mu = 0 \quad \forall \hat{\hat{\mathbb{U}}}_\mu \in \mathscr{U}_\mu. \tag{4.94}$$

This leads to the Euler-Lagrange equations

$$\begin{cases} \sum_{\alpha \in \mathcal{F}^i_{\text{net}}} [\alpha, i] A_\alpha \mathbf{s}^\alpha_\mu = \mathbf{0} & \forall i \in \mathring{\mathcal{N}}_{\text{net}}, \\ \sum_{\alpha \in \mathcal{F}^i_{\text{net}}} [\alpha, i] A_\alpha \mathbf{s}^\alpha_\mu = \bar{A}_i \boldsymbol{\Lambda} (\mathbf{n}_i - \bar{\mathbf{n}}_\mu) & \forall i \in \mathcal{N}^{\Gamma}_{\text{net}}. \end{cases} \tag{4.95}$$

The first equation expresses the equilibrium of fibre forces at each interior node. The second equation stands for the equilibrium between forces at the nodes over the RVE boundary. This equilibrium is satisfied by the summation of fibre forces $[\alpha, i] A_\alpha \mathbf{s}^\alpha_\mu$, $\alpha \in \mathcal{F}^i_{\text{net}}$, and by the reactive force $\bar{A}_i \boldsymbol{\Lambda} (\mathbf{n}_i - \bar{\mathbf{n}}_\mu)$ (usually acknowledged as a uniform traction). This later expression also gives a first physical interpretation for the Lagrange multiplier $\boldsymbol{\Lambda}$[5]. In fact, the total force (traction $\mathbf{t}_i = \bar{A}_i \boldsymbol{\Lambda} (\mathbf{n}_i - \bar{\mathbf{n}}_\mu)$) supported by the bars reaching the boundary node $i \in \mathcal{N}^{\Gamma}_{\text{net}}$ depends on the constant second-order tensor $\boldsymbol{\Lambda}$ and the difference between the unitary outward normal vector of the RVE and the average normal vector.

Remark 30 *By construction of* (4.93) *the reactive force* $\boldsymbol{\Theta}$ *is zero. Therefore, from* (4.95) *(first line) the forces per unit area over the RVE boundary are self-equilibrated.*

Remark 31 (Continuum Case) *We can understand the Euler-Lagrange equations* (4.95) *as discrete counterparts of the continuum formulation for porous RVEs in strong form (partial differential equations form) given in* (3.39)*, the part of* $\mathring{\mathcal{N}}_{\text{net}}$ *related to the divergence and the part* $\mathcal{N}^{\Gamma}_{\text{net}}$ *corresponding to boundary tractions.*

[5] Connection between $\boldsymbol{\Lambda}$ and the homogenised stress tensor $\mathbf{P}$ is addressed in Section 4.6.1

4.6.1 Stress homogenisation from boundary data

We focus now on finding an alternative expression for the homogenisation of the stress tensor depending only on boundary data. As an additional consequence, an alternative physical interpretation for the Lagrange Multiplier $\mathbf{\Lambda}$ is also achieved.

Considering (4.95) for the boundary nodes, let us call $\bar{A}_i\mathbf{\Lambda}(\mathbf{n}_i - \bar{\mathbf{n}}_\mu) = \mathbf{t}_i$ (traction) and consider the summation over $i \in \mathcal{N}_{\text{net}}^{\Gamma}$ as follows

$$
\begin{aligned}
\sum_{i\in\mathcal{N}_{\text{net}}^{\Gamma}} \left(\bar{A}_i\mathbf{\Lambda}(\mathbf{n}_i - \bar{\mathbf{n}}_\mu)\right) \otimes (\mathbf{x}_\mu^i - \mathbf{x}_\mu^G) = \sum_{i\in\mathcal{N}_{\text{net}}^{\Gamma}} \mathbf{t}_i \otimes (\mathbf{x}_\mu^i - \mathbf{x}_\mu^G) = \\
\sum_{i\in\mathcal{N}_{\text{net}}^{\Gamma}} \left(\sum_{\alpha\in\mathcal{F}_{\text{net}}^i} [\alpha, i] A_\alpha \mathbf{s}_\mu^\alpha \right) \otimes (\mathbf{x}_\mu^i - \mathbf{x}_\mu^G) + \\
\sum_{i\in\overset{\circ}{\mathcal{N}}_{\text{net}}} \underbrace{\left(\sum_{\alpha\in\mathcal{F}_{\text{net}}^i} [\alpha, i] A_\alpha \mathbf{s}_\mu^\alpha \right)}_{=\mathbf{0} \text{ from } (4.95)} \otimes (\mathbf{x}_\mu^i - \mathbf{x}_\mu^G) = \\
\sum_{i\in\mathcal{N}_{\text{net}}} \sum_{\alpha\in\mathcal{F}_{\text{net}}^i} [\alpha, i] A_\alpha \mathbf{s}_\alpha \otimes (\mathbf{x}_\mu^i - \mathbf{x}_\mu^G) = \\
\sum_{\alpha\in\mathcal{F}_{\text{net}}} A_\alpha \mathbf{s}_\alpha \otimes \Delta^\alpha \mathbf{x}_\mu = \sum_{\alpha\in\mathcal{F}_{\text{net}}} V_\alpha \mathbf{s}_\alpha \otimes \mathbf{a}_\alpha = |\Omega_\mu|\mathbf{P},
\end{aligned}
\tag{4.96}
$$

where we have also used (4.28) and (4.29). From the development in (4.96), before adding the summation over internal nodes, we have that $\mathbf{P}$ depends only on boundary information, that is

$$
\mathbf{P} = \frac{1}{|\Omega_\mu|} \sum_{i\in\mathcal{N}_{\text{net}}^{\Gamma}} \mathbf{t}_i \otimes (\mathbf{x}_\mu^i - \mathbf{x}_\mu^G). \tag{4.97}
$$

The homogenisation for stress given by (4.97) is completely equivalent to that derived in (4.87). The former can be understood as the discrete counterpart of the well known homogenisation formula for stress based only on boundary data in classical continuum shown in (2.42).

Now, let us define the auxiliary tensor

$$
\mathbf{B}^\Gamma := \frac{1}{|\Omega_\mu|} \sum_{i\in\mathcal{N}_{\text{net}}^{\Gamma}} \bar{A}_i(\mathbf{n}_i - \bar{\mathbf{n}}_\mu) \otimes (\mathbf{x}_\mu^i - \mathbf{x}_\mu^G). \tag{4.98}
$$

With (4.98) into (4.96), and since $\mathbf{\Lambda}$ is a constant tensor, we have

$$
|\Omega_\mu|\mathbf{\Lambda}\mathbf{B}^\Gamma = |\Omega_\mu|\mathbf{P}, \tag{4.99}
$$

which leads us to conclude that

$$
\mathbf{\Lambda} = \mathbf{P}(\mathbf{B}^\Gamma)^{-1}. \tag{4.100}
$$

This establishes that the reactive generalised force due to the imposition of the minimum kinematical constraint of the space $\widetilde{\mathscr{U}}_\mu^{\mathsf{M}}$ is in direct connection with the homogenised stress tensor.

Remark 32 *Recall that the very same analysis for the continuum limit has been performed in Section 3.3.4, and as commented in Remark 13, just in the particular case without pores over the boundary, we have $\boldsymbol{\Lambda} = \mathbf{P}$. Moreover, from a purely geometrical perspective, the well-posedness of the present multiscale formulation is inherently built upon the fact that $\mathbf{B}$ and $\mathbf{B}^{\Gamma}$, defined in* (4.65) *and* (4.98) *respectively, are non-singular second order tensors.*

4.7 Concluding remarks

In this chapter, a multiscale model for microscopic fibre networks has been developed in order to retrieve an homogenised constitutive response corresponding to that of a continuum. Although the focus has been on modelling arterial tissue, the theory is general and can be applied to any fibrous material. The main contributions of the present work consists in a rigorous and general derivation of the micro-mechanical equilibrium problem as well as of the homogenisation formula for the dual stress entity from a minimum set of basic kinematical hypotheses and through the use of the Principle of Multiscale Virtual Power (BLANCO et al., 2016; BLANCO et al., 2014). Furthermore, intrinsic to the proposed multiscale formulation is the construction of the so-called minimally constrained model, resulting in a lower bound for the homogenised mechanical response, of great theoretical and practical interest. As a sub-product of the proposed variational setting, a specific homogenisation formula for incompressible materials has also been established. In addition, we have also shown that the proposed minimally constrained multiscale model is equivalent to setting a uniform traction model, and an alternative formulation of practical interest has been reported resorting to the theory of Lagrange Multipliers.

A definite motivation for the development of this kind of multiscale model is the modelling of fibre damage processes, and the impact of these mechanisms into the macromechanics of materials. Clearly, loading of fibrous specimens featuring damage yields more intricate mechanical interactions, which makes even more complex the constitutive analysis because of the highly heterogeneous strain patterns developed in the fibre network. In essence, the consideration of degradation processes weakens some parts of the networks as a consequence of the fibre geometry, orientation, history of loadings, etc. This is known in the continuum mechanics realm as strain localisation phenomena and results in the softening of the overall constitutive response. It has already been experimentally shown that in biological fibrous tissues the unstable part of the constitutive response is characterised by a series of bumps in the stress-stretch response, that is a series of softening and hardening stages. Classical phenomenological damage modelling usually associates a single damage parameter for each fibre family (BALZANI; BRINKHUES; HOLZAPFEL, 2012; LI; ROBERTSON, 2009), which seems not to be enough to precisely model such complex interplay involving deactivation, activation, reorientation and degradation of fibres. In this direction, we oversee a great applicability of the proposed theoretical multiscale model, which is addressed in detail in Chapter 5.

Finally, several numerical experiments showing different key aspects of the theory are demonstrated in Chapter 6, particularly in Section 6.1. For the interested reader in these examples, Chapter 5 can be skipped in a first reading. In these numerical studies, special emphasis is given to the study of the sensitivity of the homogenised constitutive with respect to different kinds of heterogeneities in the fibrous network architecture and with respect to the choice of kinematically admissible boundary conditions for the micro-mechanical equilibrium problem. The present theoretical framework and the aforementioned numerical examples constitute a further contribution of this thesis (ROCHA et al., 2018).

5 Damage Modelling and Failure Detection in Fibrous Materials

L'endommagement, comme le diable, invisible mais redoutable.[a]

---

[a] Damage, like the devil, invisible but fearsome. (free translation)

Jean Lemaître and Jean-Louis Chaboche (LEMAITRE; CHABOCHE, 1990)

Material rupture is usually driven by micromechanical failure mechanisms. In the case of biological fibrous tissues, whose main load-bearing constituents at the microscale are arranged as a fibre network, strain localisation due to progressive damage evolution in the fibres is the main cause of nucleation of macroscale cracks. As already commented, the consideration of the novel Minimally Constrained Model (proposed in Chapter 4) is an important springboard to perform multiscale analyses and comparisons with existing models which already exploit, due to its simplicity, the Affine Boundary Model. Moreover, noting that an important characteristic of the aforementioned damage process is the propagation of a strain localisation band throughout the network of fibres, a less constrained kinematics over boundary is required in order not to preclude these deformation modes from unfolding naturally. This main characteristic motivates the construction of the model to be proposed in this chapter.

Hence, in this chapter, we investigate the application of the RVE-based multiscale formulation for fibres networks presented in Chapter 4, but within a framework in which microscale fibre damage can lead to macroscale localisation phenomena. For such an analysis, as required, the homogenised tangent tensor is derived and afterward utilised to detect the so-called bifurcation point (also called critical instant, or critical point). In addition, special attention is given to the regularised damage model adopted for the fibre, as well as the consistent algorithmic tangent for the fibres for the adopted time-discrete scheme to be employed.

This chapter is organised as follows. In Section 5.1, the multiscale model for fibres of Chapter 4 is briefly revisited. Also, notation is slightly adapted for sake of convenience to the present context of inelastic behaviour. Section 5.2 is devoted to the constitutive modelling of the fibres and the framework utilised for modelling damage processes is presented in Section 5.3. The regularisation of this damage model is the subject of Section 5.4. Section 5.5 is devoted to the derivation of the consistent algorithmic tangent for the adopted damage model and for a given time-discrete integration scheme. Related to that, a strategy for numerical solution of the nonlinear problem is proposed in Section

5.6. Concerning the bifurcation analysis, whose aim is the detection of the critical point, Section 5.5 provides the derivation of homogenised tangent tensor that is employed in the discontinuous bifurcation analysis (DBA) of Section 5.8, followed by an alternative method proposed to find the initial opening direction at the critical instant. In Section 5.10 we outline the final remarks.

Finally, the proposed analysis is able to precisely determine the instant at which the macroscale problem becomes ill-posed. At such point, the spectral analysis provides information about the macroscale failure pattern (unit normal and crack opening vectors). Numerical examples showing the suitability of the present methodology is shown in Chapter 6, specifically in Section 6.2. Relevant discussions are provided in Section 6.2.5.

5.1 Multiscale model for fibres network revisited

In this section we briefly revisit and extend the model of Chapter 4, depicted in Fig. 11, to model inelastic mechanisms taking place at the microscale. For this aim, an additional hypothesis to the those already presented in Section 4.1 is needed. Now, each fibre behaves inelastically and to model this feature an internal variable is introduced at the fibre level. The same way that strain and material properties are supposed to be homogeneous for each fibre segment, the internal variable is also constant along each fibre segment. For the sake of convenience, first consider some notational changes and comments below:

- Hereafter, boldface fonts are preferred, instead of blackboard bold ones, to designate displacements in the fibre network. Thus, $\mathbf{u}_\mu$ replaces $\mathbb{U}_\mu \in \mathscr{U}_\mu$, $\tilde{\mathbf{u}}_\mu$ stands for $\tilde{\mathbb{U}}_\mu \in \widetilde{\mathscr{U}}_\mu$, and so on.

- The kinematical setting in both scales is identical to that introduced in Chapter 4. Importantly, for a purely constitutive theory (no body forces involved), $\mathbf{G} \in \mathbb{R}^{\mathrm{n_d}\times\mathrm{n_d}}$ is inserted the macroscale point $\mathbf{x}_M$ into the microscale domain Ω_μ. For computational convenience, at the microscale, instead of using the second-order tensor G^α_μ to describe the strain at a fibre, we use the *generalised strain vector* $\mathbf{g}_\alpha$ already defined in (4.52). Here, we rewrite the definition of this vector in terms of displacements as

$$\mathbf{g}_\alpha := \frac{1}{L_\alpha}\Delta^\alpha \mathbf{u}_\mu = \mathbf{G}\mathbf{a}_\alpha + \frac{1}{L_\alpha}\Delta^\alpha \tilde{\mathbf{u}}_\mu, \tag{5.1}$$

  where the index $(\cdot)_\mu$ or $(\cdot)^\mu$ is dropped for ease of notation. Note that the ratio between the actual length of the fibre, ℓ_α, and its original length L_α, known as *fibre stretch* (see Fig. 17), is defined as

$$\lambda_\alpha = \frac{\ell_\alpha}{L_\alpha} = \|\mathbf{a}_\alpha + \mathbf{g}_\alpha\|_2 \tag{5.2}$$

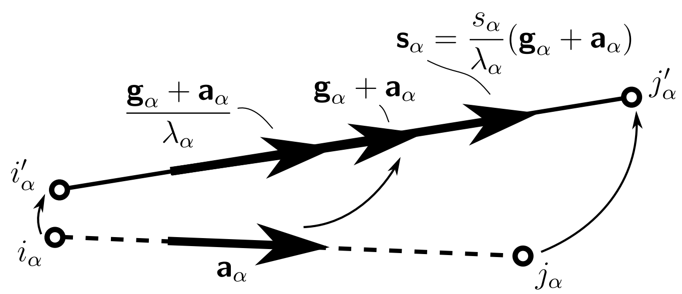

Figure 17 – Fibre in its material and spatial configurations, and interpretation of the generalised strain and stress vectors.

- As already pointed out in Section 4.4, power-conjugated to $\mathbf{g}_\alpha$ we have the *generalised fibre stress vector* $\mathbf{s}_\alpha$. Then, some constitutive functional $\mathscr{F}^\alpha$ has to be provided such that $\mathbf{s}_\alpha = \mathscr{F}^\alpha(\mathbf{g}^t_\alpha)$, where $(\cdot)^t$ represents the history of the variable $(\cdot)$ up to the pseudo-time t. Actually, it is proved in Section 5.2 that

$$\mathbf{s}_\alpha = \frac{s_\alpha}{\lambda_\alpha}(\mathbf{a}_\alpha + \mathbf{g}_\alpha), \tag{5.3}$$

  where s_α is the scalar axial stress of the fibre and, from (5.2), $\frac{(\mathbf{a}_\alpha + \mathbf{g}_\alpha)}{\lambda_\alpha}$ is a unitary vector pointing towards the actual direction of the fibre (see Fig. 17). Thus, s_α solely takes into account the constitutive aspects of the fibre which is supposed to depend only on the history of the uniaxial stretch, so $s_\alpha = \mathscr{F}^\alpha((\lambda_\alpha)^t) = \mathscr{F}^\alpha(\lambda_\alpha, \mathbf{\Pi}_\alpha)$ where $\mathbf{\Pi}_\alpha$ represents the actual state of internal variables that encloses all necessary historical information related to λ_α, as it is traditional to the realm of theories relying on internal variables. Details are discussed in Section 5.3.

- Accordingly, the macroscopic stress tensor $\mathbf{P} = \mathscr{F}(\mathbf{G}^t) = \mathscr{F}(\mathbf{G}, \mathbf{\Pi})$, where $\mathbf{\Pi}$ is a generic set of internal variables. In a pseudo-time stepping procedure, it may be useful to express this constitutive functional for the pseudo-time increment from t_{n-1} to t_n as $\mathbf{P}^n = \overline{\mathscr{F}}(\mathbf{G}^n, \mathbf{\Pi}^{n-1})$, where $\mathbf{\Pi}^{n-1}$ is a generic set of internal variables at the instant t_{n-1} and $\overline{\mathscr{F}}$ stands for the time-discrete constitutive functional. As usual, in a multiscale approach, the constitutive functional $\mathscr{F}$ (and consequently $\overline{\mathscr{F}}$) is implicitly defined through the microscale mechanical equilibrium and by the application of a certain homogenisation procedure, recalled in Problem 6 and in (5.5), respectively. Note that in this case $\mathbf{\Pi} = \{\mathbf{\Pi}_\alpha\}_{\alpha \in \mathcal{F}_{\text{net}}}$ stands for the collection of the internal variables of all fibres of the network.

With the above comments, and using the very same statement of the PMVP for fibres networks as in Problem 3, now are able to recall its the variational consequences adapted to the present context. First, the microscale mechanical equilibrium problem is formulated as follows:

Problem 6 (Microscale mechanical equilibrium) *Given a macroscale gradient* $\mathbf{G} \in \mathbb{R}^{\mathrm{n_d} \times \mathrm{n_d}}$ [1] *and the known set of internal variables* $\mathbf{\Pi} = \{\mathbf{\Pi}_\alpha\}_{\alpha \in \mathcal{F}_{\mathrm{net}}}$ *find* $\tilde{\mathbf{u}}_\mu \in \widetilde{\mathscr{U}_\mu}$ *such that the following variational equation is satisfied:*

$$\sum_{\alpha \in \mathcal{F}_{\mathrm{net}}} A_\alpha \mathbf{s}_\alpha \cdot \Delta^\alpha \hat{\tilde{\mathbf{u}}}_\mu = 0 \quad \forall \hat{\tilde{\mathbf{u}}}_\mu \in \widetilde{\mathscr{U}_\mu}. \tag{5.4}$$

Secondly, the macroscale stress is given by the following homogenisation rule

$$\mathbf{P} = \frac{1}{|\Omega_\mu|} \sum_{\alpha \in \mathcal{F}_{\mathrm{net}}} V_\alpha \mathbf{s}_\alpha \otimes \mathbf{a}_\alpha. \tag{5.5}$$

In the same fashion as in Section 2.4.1, the nonlinear Problem 6 needs to be solved through an adequate iterative method. Here, we use the Newton-Raphson method, where (5.4) is linearised, leading to the following linear problem, which is solved iteratively until a given convergence criterion is achieved.

Problem 7 (Newton-Raphson Iteration) *From same conditions as Problem 6, find the incremental displacement fluctuation* $\delta \tilde{\mathbf{u}}_\mu \in \widetilde{\mathscr{U}_\mu}$ *such that:*

$$\sum_{\alpha \in \mathcal{F}_{\mathrm{net}}} \frac{A_\alpha}{L_\alpha} \mathbf{D}_\alpha \Delta^\alpha \delta \tilde{\mathbf{u}}_\mu \cdot \Delta^\alpha \hat{\tilde{\mathbf{u}}}_\mu = - \sum_{\alpha \in \mathcal{F}_{\mathrm{net}}} A_\alpha \mathbf{s}_\alpha \cdot \Delta^\alpha \hat{\tilde{\mathbf{u}}}_\mu \quad \forall \hat{\tilde{\mathbf{u}}}_\mu \in \widetilde{\mathscr{U}_\mu}, \tag{5.6}$$

where $\mathbf{D}_\alpha = \partial_{\mathbf{g}_\alpha} \mathbf{s}_\alpha$ *is the constitutive second-order tangent tensor for a fibre.*

As it is well-known that the quadratic convergence rate ensured by the Newton method can be achieved only if $\mathbf{D}_\alpha$ is obtained consistently, i.e., by considering in its derivation the integration scheme for the constitutive law (SIMO; TAYLOR, 1985). Here, the consistent algorithmic tangent is presented in Section 5.5 for the fibre constitutive model to be shown in Section 5.3.

Remark 33 *Solution of the Problem 6 together with the homogenisation in (5.5) determines the constitutive functional* $\mathscr{F}$ *(or* $\overline{\mathscr{F}}$*). For a the pseudo-time increment from* t_{n-1} *to* t_n*, in the setting of Problem 6, we need to understand* $\mathbf{G}$ *as* $\mathbf{G}^n$ *and* $\mathbf{\Pi}$ *as* $\mathbf{\Pi}^{n-1}$*, hence delivering* $\mathbf{P}^n = \overline{\mathscr{F}}(\mathbf{G}^n, \mathbf{\Pi}^{n-1})$.

5.2 Constitutive models for fibres

This section discusses the most relevant constitutive aspects of a *fibre* (more precisely, of a bundle of collagen fibres). First, for the sake of simplicity, dissipative effects

[1] For sake of simplicity consider the space to be $\mathbb{R}^{\mathrm{n_d} \times \mathrm{n_d}}$, but the model also remains valid for subsets of it as extensively discussed in the work (ROCHA et al., 2018), specified for the case of incompressible materials.

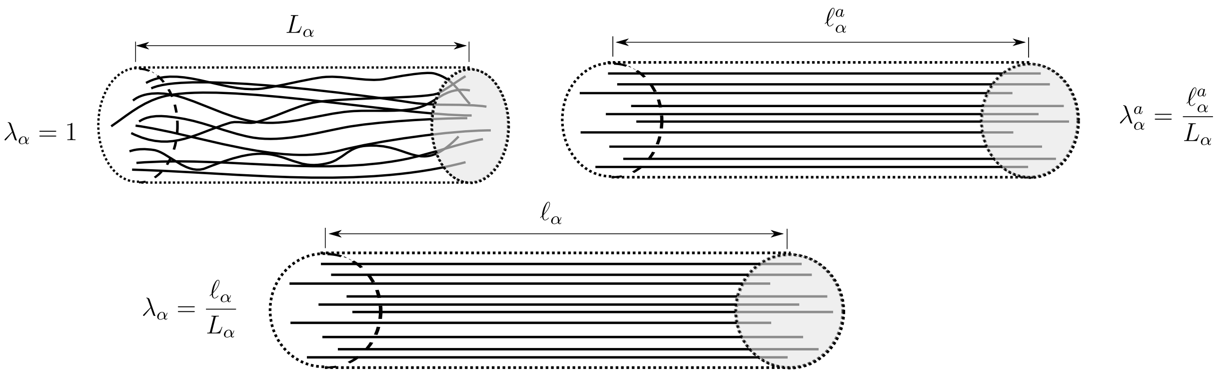

Figure 18 – Imaginary cylinder (truss) in different deformed configurations enclosing a bundle of collagen fibres.

such as damage or viscoelasticity are neglected, and are posteriorly incorporated in Section 5.3. For other approaches, see (VITA, 2005) and (BALZANI; BRINKHUES; HOLZAPFEL, 2012) for the consideration of these phenomena.

It is well-known in the biomechanics field (e.g. (VITA, 2005; DAVIS; VITA, 2012) and references therein) that collagen molecules are packed in form of collagen fibrils, which, in turn, aggregate to form collagen fibres. Collagen fibres are arranged in distinct and parallel bundles (also called fascicles), which are, in general, wavily deposited in a load-free state. This scale can be visualised in Fig. 18 for a fibre bundle $\alpha \in \mathcal{F}_{\text{net}}$, where L_α is the length of an imaginary cylinder embracing fibres featuring similar waviness and directions. When this cylinder is stretched up to a length ℓ^a_α, the fibres align and start bearing axial load. This defines the *activation stretch* (also called *recruitment stretch*) as the ratio:

$$\lambda^a_\alpha = \frac{\ell^a_\alpha}{L_\alpha}. \tag{5.7}$$

The focus of the present contribution is at the scale of the network of fibre bundles, while the detailed description of smaller scales, ranging from collagen molecules up to bundle of fibres is out of scope of this contribution.

For this aim, let

$$\begin{aligned} \Psi^0_\alpha : \mathbb{R} &\to \mathbb{R}^+ \\ \lambda_\alpha &\mapsto \Psi^0_\alpha(\lambda_\alpha) \end{aligned} \tag{5.8}$$

be an hyperelastic strain energy function (SEF) representing the rate-independent behaviour of a collagen bundle $\alpha \in \mathcal{F}_{\text{net}}$ (or simply fibre segment) without experiencing damage. Here, we use the super-index $(\cdot)^0$ to indicates undamaged quantities, in contrast to the damaged ones to be introduced in Section 5.3. This potential is assumed to be convex in terms of λ_α (i.e. $\partial^2_{\lambda_\alpha} \Psi^0_\alpha \geq 0$ for the entire range of stretches) and also the fibre only bears load in tension and once the activation stretch is reached.

Under standard assumptions, the Clausius-Duhem inequality can be written for a single fibre as follows

$$\mathcal{D}_{\alpha}^{\int} = s_{\alpha}\dot{\lambda}_{\alpha} - \dot{\Psi}_{\alpha}^{0} \geq 0, \tag{5.9}$$

for any admissible $\dot{\lambda}_{\alpha}$. Remembering that for the moment the fibre is considered hyperelastic we have $\mathcal{D}_{\alpha}^{\int} = 0$ and thus

$$s_{\alpha}^{0}\dot{\lambda}_{\alpha} - \partial_{\lambda_{\alpha}}\Psi_{\alpha}^{0}\dot{\lambda}_{\alpha} = 0, \tag{5.10}$$

which defines the scalar uniaxial stress s_{α}^{0} as

$$s_{\alpha}^{0}(\lambda_{\alpha}) = \partial_{\lambda_{\alpha}}\Psi_{\alpha}^{0}(\lambda_{\alpha}) \tag{5.11}$$

Examples of SEFs are:

1. In (THUNES et al., 2016), the following SEF that yields to a linear constitutive law for the stress is used:

$$\Psi_{\alpha}^{0}(\lambda_{\alpha}) = \begin{cases} \dfrac{E_{\alpha}}{2}(\lambda_{\alpha} - \lambda_{\alpha}^{a})^{2} & \lambda_{\alpha} > \lambda_{\alpha}^{a}, \\ 0 & \text{otherwise} \end{cases} \tag{5.12}$$

Parameters of this equation are the elastic modulus E_{α} and the activation stretch λ_{α}^{a}.

2. In (LI; OGDEN; HOLZAPFEL, 2016), the following SEF that yields to a quadratic constitutive law [2] is employed:

$$\Psi_{\alpha}^{0}(\lambda_{\alpha}) = \begin{cases} k_{1}^{\alpha}\left(\lambda_{\alpha}^{2} - (\lambda_{\alpha}^{a})^{2})\right)^{2} & \lambda_{\alpha} > \lambda_{\alpha}^{a}, \\ 0 & \text{otherwise} \end{cases} \tag{5.13}$$

The elastic parameter k_{1}^{α} and the already defined λ_{α}^{a} characterise this SEF.

As anticipated in Section 5.1 we need expressions for $\mathbf{s}_{\alpha}^{0}$ and $\mathbf{D}_{\alpha}^{0}$ (undamaged versions of $\mathbf{s}_{\alpha}$ and $\mathbf{D}_{\alpha}$ respectively). From the very same argument of (5.9) and (5.10), we can define $\mathbf{s}_{\alpha}^{0}$ as below

$$\mathbf{s}_{\alpha}^{0}(\mathbf{g}_{\alpha}) := \partial_{\mathbf{g}_{\alpha}}\Psi_{\alpha}^{0}(\mathbf{g}_{\alpha}) = \underbrace{\partial_{\lambda_{\alpha}}\Psi_{\alpha}^{0}(\lambda_{\alpha})}_{=s_{\alpha}^{0}}\left(\frac{\mathbf{a}_{\alpha} + \mathbf{g}_{\alpha}}{\lambda_{\alpha}}\right), \tag{5.14}$$

[2] The term $(\lambda_{\alpha})^{2}$ is analogous to the invariant I_{4} defined for transversally isotropic materials and the energy is equal to the first nonzero term of the Taylor expansion for the exponential model evaluated at $(\lambda_{\alpha})^{2} = (\lambda_{\alpha}^{a})^{2}$ (see (HOLZAPFEL; OGDEN, 2010) for example). Then (5.13) is considered linear in the measure $I_{4} = (\lambda_{\alpha})^{2}$.

where (5.2) and the chain rule have been used. Note that (5.14) proves (5.3) for the undamaged case. Proceeding to compute $\mathbf{D}_\alpha^0$, also by successive applications of the chain rule we have

$$\mathbf{D}_\alpha^0 := \partial_{\mathbf{g}_\alpha} \mathbf{s}_\alpha^0 = \frac{s_\alpha^0}{\lambda_\alpha}\mathbf{I} + \frac{1}{(\lambda_\alpha)^2}\left(c_\alpha^0 - \frac{s_\alpha^0}{\lambda_\alpha}\right)\mathbf{A}_\alpha \tag{5.15}$$

with

$$c_\alpha^0 := \partial_{\lambda_\alpha} s_\alpha^0, \tag{5.16}$$

being the scalar fibre tangent, and with the auxiliary second-order tensor

$$\mathbf{A}_\alpha := (\mathbf{a}_\alpha + \mathbf{g}_\alpha) \otimes (\mathbf{a}_\alpha + \mathbf{g}_\alpha). \tag{5.17}$$

We recall that the second-order stress tensor, used in Chapter 4, is retrieved from $\mathbf{s}_\alpha^0$ by taking $(\mathbf{S}_\mu^\alpha)^0 = \mathbf{s}_\alpha^0 \otimes \mathbf{a}_\alpha$.

At this point it is important to highlight that E_α, k_1^α and λ_α^a, parameters of the SEFs (5.12) and (5.13), have to be understood as homogenised quantities which arise from smaller spatial length scales. We also note that the stress derived from this energy function is non-linear with respect to the stretch λ_α (but it is less steep than exponential models (HOLZAPFEL; GASSER; OGDEN, 2000)). It is believed that such nonlinearity, emerges from geometrical aspects related to the collagen fibres (tortuosity) and from the fact that bending phenomena are neglected (see (COMNINOU; YANNAS, 1976), where the assumption of a sinusoidal shape for the fibre leads to an analytical expression for the axial stress under tension). Another source of nonlinearity comes from the progressive fibre activations taking place within the bundle (VITA, 2005). An analogous effect, but at the scale of the network, is investigated in Section 6.1.1.3, where we reproduce a similar result as a consequence of the heterogeneities in the definition of λ_α^a among the fibres of the network.

Finally, it is important to mention that (CHANDRAN; BAROCAS, 2007) reported that the qualitative network behaviour is largely independent from the constitutive equation assigned to individual fibres. Furthermore in physiological ranges of stretches caused by arterial pressure, most of fibre bundles act on tension (STYLIANOPOULOS; BAROCAS, 2007a). Thus, it is expected that even when picking a relatively simple constitutive model for individual fibres several important features of the multiscale model are manifested.

5.3 Damage modelling

In order to model softening effects we propose the use a standard continuum damage approach with one scalar damage variable d_α per fibre $\alpha \in \mathcal{F}_{\text{net}}$, whose evolution is considered in the light of the framework introduced by (SIMO; JU, 1987) reviewed below (recall that t is a generic pseudo-time):

$$r_\alpha(t) = \max_{\tau\in[0,t]}(\sqrt{2\Psi^0_\alpha(\lambda_\alpha(\tau))}, r^0_\alpha), \quad t > 0, \tag{5.18a}$$

$$\dot{q}_\alpha(t) = H_\alpha(r_\alpha(t))\,\dot{r}_\alpha(t), \tag{5.18b}$$

$$d_\alpha(t) = 1 - \frac{q_\alpha(t)}{r_\alpha(t)}\ ,\ d_\alpha \in [0,1], \tag{5.18c}$$

$$r_\alpha(0) = r^0_\alpha\ ,\ q_\alpha(0) = q^0_\alpha\ ,\ q^0_\alpha = r^0_\alpha \tag{5.18d}$$

Note that two additional auxiliary variables were introduced, r_α and q_α. The parameter r^0_α represents the threshold where the damage evolution begins and H_α is the so-called softening modulus. The relation between the three entities are such that it guarantees $d_\alpha \in [0,1]$, where $d_\alpha = 0$ represents the pristine material and $d_\alpha = 1$ the fully degraded material. Moreover, due to thermodynamical arguments the evolution of damage satisfies: $\dot{d}_\alpha \geq 0$ (see 5.4). Setting $\mathbf{\Pi}_\alpha = \{r_\alpha, q_\alpha, d_\alpha\}$ the damaged stress is then defined as below:

$$s_\alpha(\lambda_\alpha, \mathbf{\Pi}_\alpha) = (1 - d_\alpha)s^0_\alpha(\lambda_\alpha) \tag{5.19}$$

Furthermore, the choices of the functions Ψ^0_α and H_α fully define the constitutive behaviour of one single fibre. Functional expressions Ψ^0_α have been presented in (5.12) and (5.13). For H_α, in this work, we assume to be the following:

$$H_\alpha(r_\alpha) = -H^0_\alpha \exp\left[-H^0_\alpha\left(\frac{r_\alpha - r^0_\alpha}{r^0_\alpha}\right)\right], \tag{5.20}$$

where H^0_α (> 0) is a parameter that dictates the softening behaviour. As it is justified next in Section 5.4, it is possible to characterise H^0_α in terms of the Fracture Energy, G^f_α, which is considered as a material parameter for each fibre, as follows:

$$H^0_\alpha = \left[\frac{G^f_\alpha}{(r^0_\alpha)^2 L_\alpha} - \frac{1}{2}\right]^{-1}. \tag{5.21}$$

Here we note that for r^0_α sufficiently small (or conversely G^f_α large) it is assured that $H^0_\alpha > 0$.

Recalling (5.11), the energy function assumed in (5.12) leads to a linear stress-strain relation $s^0_\alpha = E_\alpha(\lambda_\alpha - \lambda^a_\alpha)$, where $\varepsilon_\alpha = \lambda_\alpha - \lambda^a_\alpha$ can be seen as a strain measure. Particularly for this case of strain energy, it is easy to see that $r^0_\alpha = \frac{s^u_\alpha}{\sqrt{E_\alpha}}$, where s^u_α represents the damage threshold stress that triggers the inelastic behaviour of the fibre. For the sake of clarity, s^u_α will be the default parameter, instead of r^0_α (the material parameter to be characterised), acting as a damage initiation threshold in the numerical experiments of Section 6.2. Note that just (5.12) is considered in these numerical experiments, but a similar arrange of variables, in terms of s^u_α, can be considered for (5.13), if necessary.

Despite its simplicity, the linear stress-strain is widely used in the literature (e.g (THUNES et al., 2016)), but the homogenised response of a fibre network ensemble may not be so simple. This is because of several reasons, some of are the topological arrangement of fibres, heterogeneous material behaviour, nonlinear character of the damage model, and the nonlinearity of the geometry of large strains and deformations of the fibres.

Finally, the fibre stress vector for the damaged case is retrieved replacing Ψ_α^0 by Ψ_α in (5.14), which yields

$$\mathbf{s}_\alpha = \mathbf{s}_\alpha(\mathbf{g}_\alpha, \mathbf{\Pi}_\alpha) = s_\alpha(\lambda_\alpha(\mathbf{g}_\alpha), \mathbf{\Pi}_\alpha) \left(\frac{\mathbf{a}_\alpha + \mathbf{g}_\alpha}{\lambda_\alpha} \right). \tag{5.22}$$

The damaged version of the fibre tangent tensor in (5.15) follows directly from the very same reasoning as above. We postpone this presentation to Section 5.5, when presenting the consistent algorithmic tangent.

5.4 Regularised damage model

In this section, we perform a dissipation analysis to justify the adoption of (5.21). We highlight that we designate the damage model, with the specific choice of (5.21) for H_α^0, as regularised, since it ensures that the physical quantity of Fracture Energy G_α^f (energy per unit area) is dissipated regardless the size of the fibre segment L_α. Hence, L_α acts as characteristic length parameter in (5.21).

For this aim, first let the SEF accounting for damage be defined as

$$\Psi_\alpha(\lambda_\alpha, d_\alpha) = (1 - d_\alpha)\Psi_\alpha^0(\lambda_\alpha). \tag{5.23}$$

Now, let us invoke the Clausius-Duhem inequality (5.9) by considering the above damaged SEF (5.23). Hence, we get

$$\mathcal{D}_\alpha^{\text{int}} = \left(s_\alpha - (1 - d_\alpha)\partial_{\lambda_\alpha}\Psi_\alpha^0 \right) \dot{\lambda}_\alpha + \dot{d}_\alpha \Psi_\alpha^0 \tag{5.24}$$

where we recall that $\mathcal{D}_\alpha^{\text{int}}$ is the dissipation per unit volume of the fibre.

The first term vanishes by considering the constitutive law introduced in (5.19) and the second term is the only responsible for the dissipation process, then

$$\mathcal{D}_\alpha^{\text{int}} = \dot{d}_\alpha \Psi_\alpha^0. \tag{5.25}$$

In a monotone loading regime the dissipation can be rewritten in terms of the auxiliary variables q_α and r_α introduced in (5.18) as follows

$$\mathcal{D}_\alpha^{\text{int}} = \frac{1}{2}(r_\alpha)^2 \frac{q_\alpha \dot{r}_\alpha - \dot{q}_\alpha r_\alpha}{(r_\alpha)^2} = \frac{1}{2}(q_\alpha - H_\alpha r_\alpha)\dot{r}_\alpha \tag{5.26}$$

Integrating the dissipation in time and space yields the total energy dissipated by the single fibre, say $\mathcal{G}_\alpha^f$. By changing variables we get

$$\int_{t_0}^{t_\infty} \int_{\Omega_\alpha} \mathcal{D}_\alpha^{\text{int}} \, \mathrm{d}t\mathrm{d}V = A^\alpha L^\alpha \int_{r_\alpha^0}^{r_\alpha^\infty} \frac{1}{2}(q_\alpha(r) - H_\alpha(r)r)\mathrm{d}r = \mathcal{G}_\alpha^f, \tag{5.27}$$

where Ω_α is the fibre domain.

The regularised damage model proposed here assures that, for each fibre undergoing damage, the integration of the dissipation, in time and space, yields the Fracture Energy G_α^f (energy per unit area) times the fibre area. The Fracture Energy, G_α^f, is a material parameter for each fibre, defined as follows

$$G_\alpha^f = \frac{\mathcal{G}_\alpha^f}{A_\alpha}. \tag{5.28}$$

For the specific choice of the softening-hardening function given in (5.20) and by taking the limit $r_\alpha^\infty \to \infty$ after analytically solving the above integral we have

$$H_\alpha^0 = \left[\frac{G_\alpha^f}{(r_\alpha^0)^2 L_\alpha} - \frac{1}{2} \right]^{-1}. \tag{5.29}$$

Here, if $r_\alpha^0 < \sqrt{2\frac{G_\alpha^f}{L_\alpha}}$ the condition $H_\alpha^0 > 0$ is satisfied, leading to a pure softening behaviour ruled by (5.20) as already discussed. Moreover, when the characteristic length L_α is small (which is mostly idealistic in cases where this length is the mesh size in finite element simulation) the expression is simplified as

$$H_\alpha^0 = \frac{(r_\alpha^0)^2 L_\alpha}{G_\alpha^f}. \tag{5.30}$$

Both formats, (5.29) and (5.30), are used in the literature for the same purposes. The former is identical to one appearing in (COMELLAS; BELLOMO; OLLER, 2015) [3], in the context of damage modelling in biomechanics, and the latter has been applied to modelling concrete (SÁNCHEZ et al., 2012). It is worth mentioning that the derivation of the regularised parameter is independent from the SEF adopted.

5.5 Consistent algorithmic tangent

In Section 5.3 the one dimensional problem has been presented in a continuous framework, but now let us first show the leading incremental expressions and also derive the algorithmic tangent for the case of problems in three-dimensional space, required for the iterative solution by the Newton-Raphson method in Problem 7.

[3] For complete analogy with (COMELLAS; BELLOMO; OLLER, 2015) set $H_0 = -A$, $r = \tau$ and $r_0 = S_0^d$.

In time-discrete form we have

$$s_\alpha^n(\lambda_\alpha^n, \boldsymbol{\Pi}_\alpha^{n-1}) = (1 - d_\alpha^n)\partial_{\lambda_\alpha^n}\Psi_\alpha^0(\lambda_\alpha^n), \tag{5.31}$$

where:

$$r_\alpha^n = \max\left(r_\alpha^{n-1}, \sqrt{2\Psi_\alpha^0(\lambda_\alpha^n)}\right), \tag{5.32a}$$

$$r_\alpha^{n,\omega} = (1-\omega)r_\alpha^{n-1} + \theta r_\alpha^n, \tag{5.32b}$$

$$q_\alpha^n = q_\alpha^{n-1} + H_\alpha(r_\alpha^{n,\omega})(r_\alpha^n - r_\alpha^{n-1}), \tag{5.32c}$$

$$d_\alpha^n = 1 - \frac{q_\alpha^n}{r_\alpha^n}. \tag{5.32d}$$

For convenience, for all the numerical examples of Section (6.2), we assume $\omega = \frac{1}{2}$ (mid-point rule) to integrate the model. Note that the time-discrete damage evolution law is implicit regardless of the value of ω. We highlight that $\boldsymbol{\Pi}_\alpha^n$, the updated internal variable vector, is fully defined in (5.32).

The consistent algorithmic tangent for this one-dimensional model is defined by

$$\begin{aligned} c_\alpha^{n,alg} &:= \partial_{\lambda_\alpha^n} s_\alpha^n \\ &= \begin{cases} (1-d_\alpha^n)\partial^2_{\lambda_\alpha^n}\Psi_\alpha^0 & r_\alpha^n = r_\alpha^{n-1} \\ (1-d_\alpha^n)\partial^2_{\lambda_\alpha^n}\Psi_\alpha^0 - \frac{1}{r_\alpha^n}(\partial_{r_\alpha^n} d_\alpha^n)\left(\partial_{\lambda_\alpha^n}\Psi_\alpha^0\right)^2 & r_\alpha^n > r_\alpha^{n-1} \end{cases}, \end{aligned} \tag{5.33}$$

with

$$\partial_{r_\alpha^n} d_\alpha^n = \frac{1}{(r_\alpha^n)^2}\left[q_\alpha^n - \left(H_\alpha(r_\alpha^{n,\omega}) + \omega H'_\alpha(r_\alpha^{n,\omega})(r_\alpha^n - r_\alpha^{n-1})\right) r_\alpha^n\right]. \tag{5.34}$$

Using the chain rule, the algorithmic tangent is determined by

$$\begin{aligned} \mathbf{D}_\alpha^{n,alg} :=& \partial_{\mathbf{g}_\alpha^n}\mathbf{s}_\alpha^n \\ =& \frac{s_\alpha^n}{\lambda_\alpha^n}\mathbf{I} + \frac{1}{(\lambda_\alpha^n)^2}\left(c_\alpha^{n,alg} - \frac{s_\alpha^n}{\lambda_\alpha^n}\right)\mathbf{A}_\alpha^n \end{aligned} \tag{5.35}$$

with $c_\alpha^{n,alg}$ given in (5.33) and

$$\mathbf{A}_\alpha^n = (\mathbf{a}_\alpha + \mathbf{g}_\alpha^n) \otimes (\mathbf{a}_\alpha + \mathbf{g}_\alpha^n). \tag{5.36}$$

Remark 34 *Regarding the positive-definiteness of the tangent tensor, we have that, for a generic non-zero vector* $\mathbf{w} \in \mathbb{R}^{\mathrm{n_d}}$*,*

$$\begin{aligned} \mathbf{D}_\alpha^{n,alg}\mathbf{w}\cdot\mathbf{w} &= \frac{s_\alpha^n}{\lambda_\alpha^n}\left(\|\mathbf{w}\|^2 - \frac{(\mathbf{w}\cdot(\mathbf{a}_\alpha + \mathbf{g}_\alpha))^2}{(\lambda_\alpha^n)^2}\right) + \frac{(\mathbf{w}\cdot(\mathbf{a}_\alpha + \mathbf{g}_\alpha))^2}{(\lambda_\alpha^n)^2}c_\alpha^{n,alg} \\ &= \|\mathbf{w}\|^2\left(\frac{s_\alpha^n}{\lambda_\alpha^n}(1-\cos^2\phi) + \cos^2\phi\, c_\alpha^{n,alg}\right) > 0, \end{aligned} \tag{5.37}$$

where ϕ is the angle between $\mathbf{w}$ and $\mathbf{a}_\alpha + \mathbf{g}_\alpha$. When $\mathbf{w}$ is parallel to $\mathbf{a}_\alpha + \mathbf{g}_\alpha$ the positive-definiteness condition is only based on the one-dimensional tangent of the fibre be positive, i.e.

$$c_\alpha^{n,alg} > 0. \tag{5.38}$$

On the other hand, if $\mathbf{w}$ is perpendicular to $\mathbf{a}_\alpha + \mathbf{g}_\alpha$ the positive definiteness follows trivially since s_α^n and λ_α^n are always positive if the fibre is bearing axial load. In other words, the three-dimensional format of the fibre tangent has the same properties as the one-dimensional constitutive law. In particular, if a fibre is in softening regime (i.e. $c_\alpha^{n,alg} < 0$), its corresponding tangent tensor $\mathbf{D}_\alpha^{n,alg}$ is not definite-positive.

Remark 35 *Numerically the loss of positive-definiteness of the consistent algorithmic tangent renders severe difficulties for the convergence of the Newton-Raphson procedure in Problem 7. To circumvent this issue, as detailed in 5.6, whenever necessary a fictitious viscosity parameter was incorporated into the one-dimensional fibre constitutive law. This modification perturbs the tangent, improving the convergence of the iterative scheme in the vicinity of critical points. Accordingly, the perturbation in the stress vanishes when convergence has been achieved, up to the convergence tolerance.*

5.6 Numerical regularisation based on artificial viscosity

As already commented, the numerical solution of the nonlinear problem associated to the model proposed is extremely challenging. The reason for that is twofold: first, our fibres (trusses) behave indeed like forceless components (cables) when the fibre stretch in below the activation stretch; second, the damage model considered is updated using a fully implicit numerical scheme. These two characteristics are well-known in the literature to affect smoothness, and thus the numerical computations in the problem (BELYTSCHKO; MISH, 2001). In other words, the robustness of the Newton-Raphson method is affected by the aforementioned factors which deteriorate the positive-definiteness of the global stiffness matrix resulting from the linearisation process. Even so, we decided not to use more robust integration schemes as the so-called Implex method (OLIVER; HUESPE; CANTE, 2008), because one of the drawbacks of the method is the presence of spurious oscillations in the stress that could easily mask the physical ones that undeniably take place in the material response of fibrous materials. In fact, the Implex method was tested, but the results are not reported here. In turn, as explained in the sections describing the numerical experiments, the strategies employed (which resulting in a convergent algorithm) were: firstly, the adaptive selection of the pseudo-time step; and secondly, the consideration of a numerical viscosity in the fibre material model, presented below.

For the sake of simplicity, only in this section we consider that all variables correspond to a single fibre $\alpha \in \mathcal{F}_{\text{net}}$, actual pseudo-time n and for the current Newton-Raphson iteration k, and so all indexes (α, n and k) are dropped everywhere. Consider now that the stress state also depends on the stretch unbalance with the previous iteration $(k-1)$ following a Kelvin-Voigt-like [4] model coupled with damage, that is:

$$s_\eta = s_\eta(\lambda, d) = (1-d)\partial_\lambda \Psi^0(\lambda) + \eta(\lambda - \lambda^{(k-1)}), \tag{5.39}$$

where the subscript η in the stress highlights the difference with the inviscid form, here represented by s_0. Noticing that

$$s_\eta = s_0 + \eta(\lambda - \lambda^{(k-1)}), \tag{5.40}$$

the algorithmic tangent is:

$$c_\eta^{alg} := \partial_\lambda s_\eta = \partial_\lambda s_0 + \eta \partial_\lambda (\lambda - \lambda^{(k-1)}) = c_0^{alg} + \eta, \tag{5.41}$$

where we have used (5.33).

Thus, we briefly conclude from (5.41) and (5.40) that the viscous numerical regularisation affects by a constant term the LHS (delaying the fibre loss of positive-definiteness, now $c_0^{alg} < -\eta$) and by a consistent term (vanishing together with the convergence) the RHS in Problem 7.

It is important to underline that this modification only alters the tangent used in the solution of the equilibrium problem, and so it does not affect the final converged solution of Problem 6 by using Problem 7, nor all subsequent computations (solution of the canonical problem, homogenisation of stress and tangent, determination of the acoustic tensor, etc). Note that these calculations are performed in the other sections of this chapter without making use of the numerical viscosity.

5.7 Homogenised constitutive tangent

In a multiscale analysis, the linearisation of the homogenisation formulae is fundamental for the solution of the macroscale nonlinear equations through any gradient-based method (such as the Newton-Raphson method). In the case of materials which undergo degradation and failure, the calculation of the tangent operator also provides further insight about the mechanical state of the microstructure, in fact, it makes possible to carry out a discontinuous bifurcation analysis (DBA) to be considered next in Section 5.8. For convenience, right below in Problem 8 we summarise the necessary procedures for

[4] Although we have used the viscosity simply for numerical purposes, the Kelvin-Voigt model has already been used in the biomechanical literature to model some collagenous tissues such as tendons (VITA, 2005), where viscosity effects are more pronounced. Also, viscous damage has also been considered for arterial tissues in the work of (PEÑA, 2011).

obtaining computing homogenised constitutive tangent for fibre networks, and the rest of the section is dedicated to make the origin of these calculations explicit.

Problem 8 (Homogenised constitutive tangent for fibre networks) *The homogenised tangent tensor results from the contribution of two terms (see (5.46) and the derivations below) in the form*

$$\mathbb{A}_M = \overline{\mathbb{A}_M} + \widetilde{\mathbb{A}_M} \tag{5.42}$$

with $\overline{\mathbb{A}_M}$ being the so-called Taylor contribution, given by:

$$\overline{\mathbb{A}_M} = \frac{1}{|\Omega_\mu|} \sum_{\alpha \in \mathcal{F}_{\text{net}}} V_\alpha \mathbf{D}_\alpha \overline{\otimes} (\mathbf{a}_\alpha \otimes \mathbf{a}_\alpha), \tag{5.43}$$

where operation $\overline{\otimes}$ is a non-standard tensor product defined in (LS.1). In turn, the fluctuation contribution $\widetilde{\mathbb{A}_M}$ to the tangent, in Cartesian coordinates, is

$$\widetilde{\mathbb{A}_M} = \frac{1}{|\Omega_\mu|} \sum_{\alpha \in \mathcal{F}_{\text{net}}} A_\alpha (\mathbf{D}_\alpha \Delta^\alpha \mathbf{u}_{kl}^{can}) \otimes \mathbf{a}_\alpha \otimes \mathbf{e}_k \otimes \mathbf{e}_l \tag{5.44}$$

where $\mathbf{u}_{kl}^{can}$, for fixed $k, l = 1, \dots, \mathrm{n_d}$, is the solution of the following linear variational problem: find $\mathbf{u}_{kl}^{can} \in \widetilde{\mathscr{U}_\mu}$ such that:

$$\sum_{\alpha \in \mathcal{F}_{\text{net}}} \frac{A_\alpha}{L_\alpha} \mathbf{D}_\alpha \Delta^\alpha \mathbf{u}_{kl}^{can} \cdot \Delta^\alpha \hat{\tilde{\mathbf{u}}}_\mu = - \sum_{\alpha \in \mathcal{F}_{\text{net}}} A_\alpha [\mathbf{a}_\alpha]_l (\mathbf{D}_\alpha \mathbf{e}_k) \cdot \Delta^\alpha \hat{\tilde{\mathbf{u}}}_\mu, \quad \forall \hat{\tilde{\mathbf{u}}}_\mu \in \widetilde{\mathscr{U}_\mu}. \tag{5.45}$$

Note that the tensor $\mathbf{D}_\alpha$ is evaluated at the solution $\tilde{\mathbf{u}}_\mu \in \widetilde{\mathscr{U}_\mu}$ of the microscale equilibrium Problem 6.

In what follows, the detailed derivation of the ingredients in Problem 8 is presented. For ease of notation, just in this section we omit the constitutive dependence of the internal variables and incremental superscripts. Thus, for instance, in the actual value for $\mathbf{G} = \mathbf{G}^n$, then $\mathbf{P} = \mathbf{P}(\mathbf{G})$ actually means $\mathbf{P}^n = \overline{\mathscr{F}}(\mathbf{G}^n, \mathbf{\Pi}^{n-1})$. The same holds for quantities at the fibre level, for example $\mathbf{s}_\alpha = \mathbf{s}_\alpha(\mathbf{g}_\alpha)$, and also for the fluctuation $\tilde{\mathbf{u}}_\mu = \tilde{\mathbf{u}}_\mu(\mathbf{G})$ (solution of Problem 6).

From the definition of the constitutive tangent operator we have:

$$\mathbb{A}_M(\mathbf{G}) := \partial_{\mathbf{G}} \mathbf{P}(\mathbf{G}) = \lim_{\tau \to 0} \left[\frac{\mathbf{P}(\mathbf{G} + \tau \mathbf{e}_k \otimes \mathbf{e}_l) - \mathbf{P}(\mathbf{G})}{\tau} \right] \otimes \mathbf{e}_k \otimes \mathbf{e}_l \tag{5.46}$$

where $\mathbf{e}_k$ and $\mathbf{e}_l$ are the unitary canonical vectors in which the macroscale strain is perturbed. Hereafter, for ease of notation let us use $\mathbf{E}_{kl} = \mathbf{e}_k \otimes \mathbf{e}_l$. Definining the perturbed generalised fibre strain as

$$(\mathbf{g}_\alpha)_{kl}^\tau = (\mathbf{G} + \tau \mathbf{E}_{kl}) \mathbf{a}_\alpha + \frac{1}{L_\alpha} \Delta^\alpha \left(\tilde{\mathbf{u}}_\mu(\mathbf{G}) + \tau \mathbf{u}_{kl}^{can}(\mathbf{G} + \tau \mathbf{E}_{kl}) \right), \tag{5.47}$$

where $\mathbf{u}_{kl}^{can}$, to be determined next, accounts for the derivative of the fluctuation field with respect to the macroscale strain tensor. Rewriting (5.46) by using the homogenisation formula given in (5.5) we obtain

$$\mathbb{A}_M = \frac{1}{|\Omega_\mu|} \sum_{\alpha \in \mathcal{F}_{\text{net}}} V_\alpha \underbrace{\left[\lim_{\tau \to 0} \frac{\mathbf{s}_\alpha((\mathbf{g}_\alpha)_{kl}^\tau) - \mathbf{s}_\alpha(\mathbf{g}_\alpha)}{\tau} \right]}_{:=\mathbf{w}_{kl}^{\alpha,\tau}} \otimes \mathbf{a}_\alpha \otimes \mathbf{E}_{kl}, \tag{5.48}$$

which is explicitly given in Cartesian components as

$$[\mathbb{A}_M]_{ijkl} = \frac{1}{|\Omega_\mu|} \sum_{\alpha \in \mathcal{F}_{\text{net}}} V_\alpha [\mathbf{w}_{kl}^{\alpha,\tau}]_i [\mathbf{a}_\alpha]_j \tag{5.49}$$

Now, let us characterise the elements $\mathbf{w}_{kl}^{\alpha,\tau}$. By taking the Taylor expansion to the perturbed fibre stress we get

$$\mathbf{s}_\alpha((\mathbf{g}_\alpha)_{kl}^\tau) = \mathbf{s}_\alpha(\mathbf{g}_\alpha) + \tau \mathbf{D}_\alpha(\mathbf{g}_\alpha) \left((\mathbf{e}_k \otimes \mathbf{e}_l)\mathbf{a}_\alpha + \frac{1}{L_\alpha} \Delta^\alpha \mathbf{u}_{kl}^{can} \right) + o(\tau^2). \tag{5.50}$$

Hence, we finally arrive at

$$\mathbf{w}_{kl}^{\alpha,\tau} = \mathbf{D}_\alpha(\mathbf{g}_\alpha) \left((\mathbf{a}_\alpha)_l \mathbf{e}_k + \frac{1}{L_\alpha} \Delta^\alpha \mathbf{u}_{kl}^{can} \right). \tag{5.51}$$

Replacing (5.51) into (5.49) we get

$$[\mathbb{A}_M]_{ijkl} = \left(\frac{1}{|\Omega_\mu|} \sum_{\alpha \in \mathcal{F}_{\text{net}}} V_\alpha [\mathbf{D}_\alpha]_{ik} [\mathbf{a}_\alpha]_j [\mathbf{a}_\alpha]_l \right) + \left(\frac{1}{|\Omega_\mu|} \sum_{\alpha \in \mathcal{F}_{\text{net}}} A_\alpha [\mathbf{D}_\alpha]_{ip} [\Delta^\alpha \mathbf{u}_{kl}^{can}]_p [\mathbf{a}_\alpha]_j \right), \tag{5.52}$$

or equivalently

$$\mathbb{A}_M = \overbrace{\frac{1}{|\Omega_\mu|} \sum_{\alpha \in \mathcal{F}_{\text{net}}} V_\alpha \mathbf{D}_\alpha \overline{\otimes} (\mathbf{a}_\alpha \otimes \mathbf{a}_\alpha)}^{\overline{\mathbb{A}_M}} + \overbrace{\frac{1}{|\Omega_\mu|} \sum_{\alpha \in \mathcal{F}_{\text{net}}} A_\alpha (\mathbf{D}_\alpha \Delta^\alpha \mathbf{u}_{kl}^{can}) \otimes \mathbf{a}_\alpha \otimes \mathbf{E}_{kl}}^{\widetilde{\mathbb{A}_M}}, \tag{5.53}$$

where the operation $\overline{\otimes}$ is a non-standard tensor product defined in (LS.1).

The characterisation of $\mathbf{u}_{kl}^{can}$ follows from the microscale mechanical problem stated in Problem 6. Recalling, for a given perturbed macroscopic strain $\mathbf{G} + \tau \mathbf{E}_{kl}$, find $(\tilde{\mathbf{u}}_\mu + \tau \mathbf{u}_{kl}^{can}) \in \widetilde{\mathscr{U}}_\mu$ such that

$$\sum_{\alpha \in \mathcal{F}_{\text{net}}} A_\alpha \mathbf{s}_\alpha((\mathbf{g}_\alpha)_{kl}^\tau) \cdot \Delta^\alpha \hat{\mathbf{u}}_\mu = 0 \quad \forall \hat{\mathbf{u}}_\mu \in \widetilde{\mathscr{U}}_\mu, \tag{5.54}$$

with $(\mathbf{g}_\alpha)_{kl}^\tau$ given by (5.47). From (5.54), considering the Taylor expansion in (5.50), noticing that $\tilde{\mathbf{u}}_\mu \in \widetilde{\mathscr{U}}_\mu$ satisfies the microscale mechanical equilibrium for the macroscale gradient $\mathbf{G}$, and by the fact $\widetilde{\mathscr{U}}_\mu$ is a vector space, we have to find $\mathbf{u}_{kl}^{can} \in \widetilde{\mathscr{U}}_\mu$ such that:

$$\sum_{\alpha \in \mathcal{F}_{\text{net}}} \frac{A_\alpha}{L_\alpha} \mathbf{D}_\alpha \Delta^\alpha \mathbf{u}_{kl}^{can} \cdot \Delta^\alpha \hat{\mathbf{u}}_\mu = - \sum_{\alpha \in \mathcal{F}_{\text{net}}} A_\alpha [\mathbf{a}_\alpha]_l (\mathbf{D}_\alpha \mathbf{e}_k) \cdot \Delta^\alpha \hat{\mathbf{u}}_\mu \quad \forall \hat{\mathbf{u}}_\mu \in \widetilde{\mathscr{U}}_\mu. \tag{5.55}$$

Now we want to prove the major symmetry of $\mathbb{A}_M$ (remember (2.54)). From definition of $\overline{\otimes}$ in (LS.1) and (5.53), the contribution $\overline{\mathbb{A}_M}$ is major-symmetric. Now we prove the same property to $\widetilde{\mathbb{A}_M}$. For this aim, firstly take $\hat{\mathbf{u}} = \mathbf{u}_{ij}^{can} \in \widetilde{\mathscr{U}_\mu}$ in (5.55), so

$$\sum_{\alpha\in\mathcal{F}_{\text{net}}} \frac{A_\alpha}{L_\alpha}\mathbf{D}_\alpha \Delta^\alpha \mathbf{u}_{kl}^{can} \cdot \mathbf{u}_{ij}^{can} = -\sum_{\alpha\in\mathcal{F}_{\text{net}}} A_\alpha [\mathbf{a}_\alpha]_l (\mathbf{D}_\alpha \mathbf{e}_k) \cdot \Delta^\alpha \mathbf{u}_{ij}^{can}\, \mathrm{d}\Omega_\mu$$
$$= -\underbrace{\sum_{\alpha\in\mathcal{F}_{\text{net}}} (A_\alpha \mathbf{D}_\alpha \Delta^\alpha \mathbf{u}_{ij}^{can} \otimes \mathbf{a}_\alpha)}_{:=\mathbf{J}_{ij}} \cdot \mathbf{E}_{kl} = -\mathbf{J}_{ij}\cdot\mathbf{E}_{kl}. \tag{5.56}$$

On the other hand, since $\mathbf{D}_\alpha$ is symmetric (see (5.35)), we have

$$\sum_{\alpha\in\mathcal{F}_{\text{net}}} \frac{A_\alpha}{L_\alpha}\mathbf{D}_\alpha \Delta^\alpha \mathbf{u}_{kl}^{can} \cdot \mathbf{u}_{ij}^{can} = \sum_{\alpha\in\mathcal{F}_{\text{net}}} \frac{A_\alpha}{L_\alpha}\mathbf{D}_\alpha \Delta^\alpha \mathbf{u}_{ij}^{can} \cdot \mathbf{u}_{kl}^{can} = -\mathbf{J}_{kl}\cdot\mathbf{E}_{ij}. \tag{5.57}$$

These two former results show that $\mathbf{J}_{kl}\cdot\mathbf{E}_{ij} = \mathbf{J}_{ij}\cdot\mathbf{E}_{kl}$.

Clearly the set $\{\mathbf{E}_{pq}\}_{p,q=1,\dots,\mathrm{n_d}}$ is a basis to the second-order tensor space, so $\mathbf{J}_{kl}$ can be expressed as the summation $\mathbf{J}_{kl} = (\mathbf{J}_{kl}\cdot\mathbf{E}_{ij})\mathbf{E}_{ij}$, where Einstein's notation is implied. By using this decomposition we have

$$\mathbf{J}_{kl}\otimes\mathbf{E}_{kl} = ((\mathbf{J}_{kl}\cdot\mathbf{E}_{ij})\mathbf{E}_{ij})\otimes\mathbf{E}_{kl} = \mathbf{E}_{ij}\otimes((\mathbf{J}_{kl}\cdot\mathbf{E}_{ij})\mathbf{E}_{kl}) =$$
$$\mathbf{E}_{ij}\otimes((\mathbf{J}_{ij}\cdot\mathbf{E}_{kl})\mathbf{E}_{kl}) = \mathbf{E}_{ij}\otimes\mathbf{J}_{ij} = \mathbf{E}_{kl}\otimes\mathbf{J}_{kl}. \tag{5.58}$$

Finally, from the above conclusion and recalling (5.53) we have $\widetilde{\mathbb{A}_M} = \frac{1}{|\Omega_\mu|}\mathbf{J}_{kl}\otimes\mathbf{E}_{kl} = \frac{1}{|\Omega_\mu|}\mathbf{E}_{kl}\otimes\mathbf{J}_{kl}$. Indeed, if a fourth-order tensor satisfies the former commutation property, thus (2.54) holds straightforwardly.

5.8 Discontinuous bifurcation analysis

Now we are able to describe how the discontinuous bifurcation analysis (DBA) is performed in the same spirit of (RICE, 1976). The aforementioned criterion detects the loss of strong ellipticity of the macroscale response, based on the spectral properties of the so-called *localisation tensor* or *acoustic tensor* $\mathbf{Q}$, to be defined next.

Consider now the instant $t = t_N$ at which a discontinuity surface in the macroscale nucleates. The gradient of displacement rate is assumed to have the following tensor structure (known as Maxwell's kinematical compatibility condition (THOMAS, 1961)) [5]:

$$[\![\dot{\mathbf{G}}]\!] = \dot{\zeta}\boldsymbol{\beta}\otimes\mathbf{n}, \tag{5.59}$$

where $\mathbf{n}$ is the unit normal vector of the surface, $\boldsymbol{\beta}$ is the unit opening direction vector, and $\dot{\zeta}$ is the non-negative normalised opening rate at that instant. The latter is not relevant

[5] Note that given a surface S with normal $\mathbf{n}$ we denote $[\![(\cdot)]\!] = (\cdot)|_{(\mathbf{x}+\mathrm{d}\mathbf{x})} - (\cdot)|_{(\mathbf{x}-\mathrm{d}\mathbf{x})}$, $\forall\mathbf{x}\in S$, with $\mathrm{d}\mathbf{x}$ parallel to the direction of $\mathbf{n}$ and $\|\mathrm{d}\mathbf{x}\|\to 0$.

for the purposes of this work and will be omitted if necessary. Enforcing the traction continuity across the discontinuity surface, we arrive at the condition in which the strong ellipticity is lost, here also referred to as discontinuous bifurcation condition:

$$[\![\dot{\mathbf{P}}\mathbf{n}]\!] = [\![\mathbb{A}_M(\mathbf{G})\dot{\mathbf{G}}]\!]\mathbf{n} = \dot{\zeta}(\mathbb{A}_M(\mathbf{G})\boldsymbol{\beta} \otimes \mathbf{n})\mathbf{n} := \dot{\zeta}\mathbf{Q}(\mathbf{G},\mathbf{n})\boldsymbol{\beta} = \mathbf{0} \qquad \text{for any } \boldsymbol{\beta} \in \mathbb{R}^{\mathrm{n_d}}, \dot{\zeta} > 0, \quad (5.60)$$

where, in our multiscale modelling scenario, $\mathbf{Q} = \mathbf{Q}(\mathbf{G}, \mathbf{n})$ is the homogenised localisation tensor. In Cartesian coordinates, $\mathbf{Q}$ is such that $[\mathbf{Q}]_{ik} = [\mathbb{A}_M]_{ijkl}[\mathbf{n}]_j[\mathbf{n}]_l$. Expression (5.60) has non-trivial solutions if and only if $\mathbf{Q}$ is a singular tensor. Hence, if at a given instant $t = t_N$ with macroscale gradient $\mathbf{G}_N$ there exists an unit vector $\mathbf{n}_N$ such that

$$\det \mathbf{Q}(\mathbf{G}_N, \mathbf{n}_N) = 0, \quad (5.61)$$

then we say that a discontinuous bifurcation (loss of strong ellipticity) has been detected, and t_N and $\mathbf{n}_N$ are the nucleation pseudo-time and normal direction of the corresponding opening macrocrack, respectively.

In practice, we determine the time instants $t_N - \mathrm{d}t$ and t_N, where the minimum of $\det \mathbf{Q}$ for any possible direction $\mathbf{n}$, changes sign and becomes negative. Hence, determination of $\boldsymbol{\beta}$ at time $t = t_N$ as the eigenvector of $\mathbf{Q}$, associated to a null eigenvalue, turns out to be inaccurate. This problem is circumvented by introducing the auxiliary complementary tensor $\overline{\mathbf{Q}} = \overline{\mathbf{Q}}(\mathbf{G}, \boldsymbol{\beta})$, defined in Cartesian coordinates, $[\overline{\mathbf{Q}}]_{jl} = [\mathbb{A}_M]_{ijkl}[\boldsymbol{\beta}]_i[\boldsymbol{\beta}]_k$ (see Section 5.9 for its justification). The determination of $\boldsymbol{\beta}$ in the critical instant is analogous to the process of finding $\mathbf{n}$ through the minimisation of $\det \mathbf{Q}$.

5.9 Method for determining the initial opening direction

As already discussed, the direct determination of the eigenvector $\boldsymbol{\beta}$ that solves $\mathbf{Q}\boldsymbol{\beta} = \mathbf{0}$ is not precise since the critical instant for which $\mathbf{Q}$ becomes singular is never exactly determined. This section aims to propose an alternative path to overcome this issue. Next, we present the basis upon which a heuristic strategy is proposed. This heuristic is proven to yield consistent results in all examples tested along the present investigation.

The problem of interest can be cast equivalently as follows: find $\boldsymbol{\beta} \in \mathbb{R}^{\mathrm{n_d}}$ such that

$$\mathbf{Q}\boldsymbol{\beta} \cdot \mathbf{v} = 0 \qquad \forall \mathbf{v} \in \mathbb{R}^{\mathrm{n_d}}. \quad (5.62)$$

Rearranging terms we have

$$\begin{aligned} \mathbf{Q}\boldsymbol{\beta} \cdot \mathbf{v} &= [\mathbf{Q}]_{ik}[\boldsymbol{\beta}]_k[\mathbf{v}]_i \\ &= [\mathbb{A}_M]_{ijkl}[\mathbf{n}]_j[\mathbf{n}]_l[\boldsymbol{\beta}]_k[\mathbf{v}]_i = \overline{\mathbf{Q}}_{\mathbf{v}}\mathbf{n} \cdot \mathbf{n} = 0 \qquad \forall \mathbf{v} \in \mathbb{R}^{\mathrm{n_d}}, \end{aligned} \quad (5.63)$$

where $\overline{\mathbf{Q}}_{\mathbf{v}} = \overline{\mathbf{Q}}_{\mathbf{v}}(\mathbf{G}, \boldsymbol{\beta})$ is defined by

$$[\overline{\mathbf{Q}}_{\mathbf{v}}]_{jl} := [\mathbb{A}_M]_{ijkl}[\mathbf{v}]_i[\boldsymbol{\beta}]_k. \tag{5.64}$$

Consider a fixed and non-null vector $\mathbf{v}$. Then, expression (5.63) is verified if:

1. Vector $\mathbf{n}$ is in the kernel of tensor $\overline{\mathbf{Q}}_{\mathbf{v}}$, that is, if $\overline{\mathbf{Q}}_{\mathbf{v}}\mathbf{n} = \mathbf{0}$. So, the nontrivial solution of this system implies that we must search for the vector $\boldsymbol{\beta}$ such that:

$$\det \overline{\mathbf{Q}}_{\mathbf{v}} = 0 \tag{5.65}$$

2. Vector $\overline{\mathbf{Q}}_{\mathbf{v}}\mathbf{n}$ is orthogonal to $\mathbf{n}$, that is $\overline{\mathbf{Q}}_{\mathbf{v}}\mathbf{n} = \boldsymbol{\tau}$, with $\boldsymbol{\tau} \perp \mathbf{n}$. For sake of convenience, assuming the spatial dimension to be $\mathrm{n_d} = 2$, without loss of generality, the orthogonal vector is characterised as $\boldsymbol{\tau} = -n_2\mathbf{e}_1 + n_1\mathbf{e}_2$, where n_1 and n_2 are Cartesian components of vector $\mathbf{n}$. Taking the matrix representation $\overline{\mathbf{Q}}_{\mathbf{v}} = \begin{bmatrix} a_{11} & a_{12} \\ a_{21} & a_{22} \end{bmatrix}$ we have

$$\begin{bmatrix} a_{11} & a_{12} \\ a_{21} & a_{22} \end{bmatrix} \begin{bmatrix} n_1 \\ n_2 \end{bmatrix} = \begin{bmatrix} -n_2 \\ n_1 \end{bmatrix}, \tag{5.66}$$

leading to

$$\begin{bmatrix} a_{11} & a_{12}+1 \\ a_{21}-1 & a_{22} \end{bmatrix} \begin{bmatrix} n_1 \\ n_2 \end{bmatrix} = \begin{bmatrix} 0 \\ 0 \end{bmatrix}, \tag{5.67}$$

and thus

$$\det \begin{pmatrix} a_{11} & a_{12}+1 \\ a_{21}-1 & a_{22} \end{pmatrix} = a_{11}a_{22} - a_{12}a_{21} + 1 + a_{12} - a_{21} = 0, \tag{5.68}$$

leading to

$$\det \overline{\mathbf{Q}}_{\mathbf{v}} = a_{21} - a_{12} - 1. \tag{5.69}$$

Note that (5.63) should be valid for all $\mathbf{v} \in \mathbb{R}^{\mathrm{n_d}}$. However, at the time-discrete level, one should never expect that (5.63) is verified exactly, since the critical pseudo-time instant is an unknown in the problem and can be determined up to an error of $\Delta t = t_n - t_{n-1}$. In our experience, the sensitivity of the problem to the choice of $\mathbf{v}$ is quite large, and after a trial and error process we have been able to identify a heuristic procedure. This heuristic consists in fixing a particular $\mathbf{v}$ such that some desirable properties are satisfied and, more importantly, the results are physically consistent in terms of what is expected in fully controlled scenarios. To this end, we recall that the determinant of $\mathbf{Q}$ is positive during the earliest stages of the loading program, $\mathbf{Q}$ is symmetric and positive-definite and, thus, all its eigenvalues are positive. Therefore, we found that by selecting $\mathbf{v} = \boldsymbol{\beta}$, the tensor $\overline{\mathbf{Q}}_{\mathbf{v}=\beta}$ (hereafter just $\overline{\mathbf{Q}}$), features the following properties:

1. $\overline{\mathbf{Q}}$ has (in all numerical experiments) a positive determinant in early stages of the loading program, resembling to $\mathbf{Q}$. For other choices of $\mathbf{v}$, the tensor $\overline{\mathbf{Q}}_{\mathbf{v}}$ failed to hold this property.

2. $\overline{\mathbf{Q}}$ is symmetric (see (5.64) and recall that $\mathbb{A}_M$ does have major symmetry). This guarantees that (5.69) simplifies to $\det \overline{\mathbf{Q}} = -1$, which facilitates our analysis since it follows from the previous property that (5.65) is always verified earlier than (5.69). For this reason, it is sufficient to test (5.65).

The comparison between $\overline{\mathbf{Q}}$ and $\mathbf{Q}$ indicates that in general $\overline{\mathbf{Q}} \neq \mathbf{Q}$ since $\mathbb{A}_M$ has no minor symmetries[6] (recall expressions (5.42), (5.43) or (5.44)). Moreover, $\mathbf{Q}$ and $\overline{\mathbf{Q}}$ are both second order symmetric tensors, since $\mathbb{A}_M$ does have major symmetry[7], this fact yields the existence of only real eigenvalues. Furthermore, the pseudo-time instants at which conditions $\det \mathbf{Q} = 0$ and $\det \overline{\mathbf{Q}} = 0$ hold coincides in every numerical experiment, which tells us that both computations are consistent.

5.10 Closing Remarks

In this work, by exploiting a multiscale paradigm, we have presented a novel framework to represent the connection between microscale damage processes occurring in networks of fibres from biological tissues and the associated macroscale material response corresponding to a continuum model. Through the combination of a multiscale model suitably constructed to allow the evolution of localisation regions in the microscale domain, and a specific discontinuous bifurcation analysis, our model provides the theoretical ingredients to analyse the impact of material and geometrical heterogeneities in the microscale domain not only in the effective material response, but also in the instant of the loading program at which the macroscale strong ellipticity condition is lost, and the nucleation of a macroscale crack is required to recover well-posedness of the macroscale equilibrium problem.

We highlight that the numerical experiments showing the suitability of the present methodology are found next in Chapter 6, particularly in Section 6.2. The theoretical framework of this chapter, together with the aforementioned numerical experiments, is another contribution of this thesis (ROCHA et al., 2019).

[6] Note that in a theory formulated in terms of symmetric stress and strain tensors, the tangent tensor does have minor simmetries and $\overline{\mathbf{Q}}$ would coincide with $\mathbf{Q}$.

[7] This is true for a vast majority of constitutive laws, including hyperelasticity and continuum damage models, which are sufficient for the present work. One classical example that violates this assumption is non-associative plasticity, not considered in this work.

6 Numerical Experiments

Anything that can go wrong will go wrong.

Murphy's law

In this chapter, we present numerical experiments concerning the simulation of fibrous materials microstructures with the proposed multiscale methodology developed in this thesis. We cover both materials with fibres featuring pure hyperelastic constitutive behaviour as well as those subjected to a level of inelastic dissipation modelled by continuum damage theory, which are presented in two distinct parts. Section 6.1 addresses two-dimensional (Section 6.1.1) and three-dimensional (Section 6.1.2) hyperelastic fibre networks focusing on the analysis of different sources of heterogeneities and their influence on the homogenised mechanical response. This former section is independent of the theoretical framework developed in Chapter 5. Later, Section 6.2 mainly analyses the phenomena of strain localisation in fibrous materials by using the concept of discontinuous bifurcation analysis (DBA). Extensive discussions of results are provided for each type of study and special attention is given for the advantages of the MKCMM for modelling fibrous materials.

The numerical core of the implementation was programmed in Fortran 90 using some of the infrastructure available in the in-house code SolverGP (URQUIZA; VéNERE, 2002) that, among other third-parties libraries, uses parallel linear algebra solvers provided by the PETSC library (BALAY et al., 2018). The network of fibres generation was coded in Python by using Numpy/Scipy (WALT; COLBERT; VAROQUAUX, 2011; JONES et al., 2001–) facilities for creating Delaunay triangulations (in 2D) as well as the open source library Voro++ (RYCROFT, 2009) and its wrapper for Python pyvoro[1] for the construction of tridimensional networks by using the Voronoi algorithm. Details are discussed in the specific sections.

6.1 Hyperelastic fibre networks

In this section we investigate the constitutive behaviour of fibrous specimens as predicted by the proposed multiscale model particularly in the presence of heterogeneities along the network. We report simulations in two-dimensional and three-dimensional settings, in Section 6.1.1 and Section 6.1.2, respectively.

[1] URL: https://pypi.org/project/pyvoro/1.3.1/.

6.1.1 Two-dimensional setting simulations

More precisely in the two-dimensional contexts, by heterogeneities we mean any kind of deviation from a homogeneous network (as in Fig. 19). In a homogeneous network, fibres associated to the same family set have the same properties, i.e. (i) the same fiber orientation θ (associated to $\mathbf{a}_\alpha$), (ii) the same length, (iii) the same area, A, and (iv) the same activation stretch λ^a [2]. In particular we denote X*-heterogeneous network*, the fibrous RVE, obtained from a homogeneous network, whenever property X has lost its homogeneity character, where $X \in \{\theta, A, \lambda^a\}$. Cases in which two properties become heterogeneous the notation becomes $X_1 X_2$*-heterogeneous network*, with $X_1, X_2 \in \{\theta, A, \lambda^a\}$.

It is important to note that, in the field of materials science, any network of fibres is naturally a heterogeneous media, and particularly anisotropic due to the intrinsic preferred directional distribution of the properties in the RVE domain. Therefore, the characterisation employed here for a network as homogeneous (heterogeneous) must not be confused with the classical concept of homogeneous (heterogeneous) material.

In this context, several realisations of fibrous RVEs are generated and compared for different spaces of kinematically admissible fluctuation fields, specifically for the minimally constrained space $\widetilde{\mathscr{U}}_\mu^{\mathsf{M}}$ (see (4.74)) and for the linear displacement space $\widetilde{\mathscr{U}}_\mu^{\mathsf{L}}$ (see (4.76)).

The generation of the fibrous networks, together with the definition of the properties is outlined in Section 6.1.1.1. As it will be seen, the aim of this kind of study is to analyse the sensitivity of the constitutive response to such heterogeneities as well as the sensitivity to the choice of boundary conditions for the RVE.

In order to quantify the impact of topological and material RVE heterogeneities in the solution of the microscale equilibrium problem, a measure of the non-affinity of the fluctuation field is proposed, called *non-affinity index*, as follows

$$I_{\mathrm{NA}} := \frac{1}{|\mathcal{F}_{\mathrm{net}}|} \sum_{\alpha \in \mathcal{F}_{\mathrm{net}}} \frac{V_\alpha}{2} (\|\tilde{\mathbf{u}}_\mu^{i_\alpha}\| + \|\tilde{\mathbf{u}}_\mu^{j_\alpha}\|), \tag{6.1}$$

where V_α is the volume of fibre α and $|\mathcal{F}_{\mathrm{net}}|$ is the volume of all fibres.

6.1.1.1 Random generation of fibrous networks

The network of fibres is computationally generated by providing a set of target properties. Initially, for a given average fibre orientation, say θ, (measured from x-axis) and for a certain number of fibres n_{fib}, a homogeneous network is generated containing two families of fibres symmetrically oriented, as in the example shown in Fig. 19. As already said, crossing-points are junctions, which are the extremes of computational fibres.

[2] For sake of simplicity, λ^a is the only source of heterogeneity in the constitutive response of individual fibres since k_1^α is kept constant in the strain energy (5.13) for all fibres.

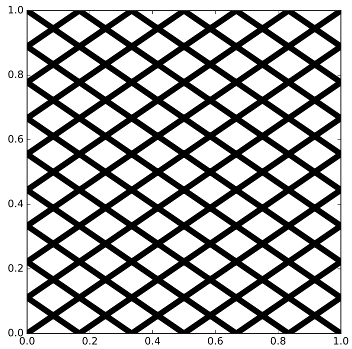

Figure 19 – Example of homogeneous network.

In a second stage, the position of each node is individually perturbed in a random magnitude and direction. The maximum perturbation is limited by a given number $\delta_{\max}$. As outcome, we obtain the networks illustrated in Fig. 20 (second row) for two different values of $\delta_{\max}$. This kind of alteration in the network will render the irregularities in the fibre orientations and lengths. Since orientations are relatively more affected than fibre lengths, in what follows we simply refer to it as θ-heterogeneity.

The two other sources of geometrical and material heterogeneities are in the choice of fibre areas and activation stretches, also called A-heterogeneity and λ^a-heterogeneity respectively. These values are taken from probability distributions with mean value m_A (m_{λ^a}) and standard deviation s_A (s_{λ^a}) for fibre area (activation stretch). Specifically, for the case of heterogeneous activation stretches, the deviation from the unit value was assumed to follow a Gamma-distribution [3] as suggested experimentally by the work of (HILL et al., 2012). In turn, the fibre area is assumed to be normally distributed with negative values disregarded.

For convenience, let us recall the most important parameters that define the characteristics of a certain realisation of a network (i.e. a random generation of the network). The set of parameters is: $\theta, n_{fib}, \delta_{\max}, m_A, s_A, m_{\lambda^a}, s_{\lambda^a}$, and are defined for all the examples presented below.

When referring to numerical examples, the characteristics that govern the randomness of the network generation, such as $\delta_{\max}$ or s_A, for example, are denoted by $p^{l,k}$ meaning that the k-th realisation of the network was generated with level l for the property p. The k value acts as a label of the initialisation of the pseudo-random number generator. That is, we may have different values of k for the same level l, which means that different realisations were taken from the same value of property. In addition, it is possible to have different levels l for the k-th realisation, which means that the deviations

[3] From (DEGROOT; SCHERVISH, 2012), the pdf of the Gamma-distribution is defined as $f_{\alpha,\beta}(x) = (\beta^\alpha/\Gamma(\alpha))x^{\alpha-1}e^{-\beta x}$ for $x > 0$ (zero otherwise), with expected value and variance only function of the two parameters $\alpha > 0$ and $\beta > 0$. Given the values of m_{λ^a} and s_{λ^a} we have $\alpha = (m_{\lambda^a}/s_{\lambda^a})^2$ and $\beta = m_{\lambda^a}/(s_{\lambda^a})^2$.

are magnified but the random pattern remains the same.

6.1.1.2 Effect of fibre area and fibre orientation

In this section we test the effect of two sources of heterogeneities separately, namely: fibre area and fibre orientation. In order to assess the impact of each parameter, 18 network realisations were generated by the procedure described in Section 6.1.1.1. Within this set, 9 networks feature heterogenous fibre area and have a homogeneous fibre orientation, similar to Fig. 19. The remaining 9 networks have heterogeneous fibre orientation, and constant fibre area, for which some realisations representing different levels of node perturbation are found in Fig. 20 (second row). Parameters that control the heterogeneities are the area standard deviation s_A and the node perturbation $\delta_{\max}$, which are set corresponding to three different levels with 3 realisations each, as summarised in Table 1.

All Realisations	θ $33.69°$	n_{fib} 216	m_{λ^a} 1.0	s_{λ^a} 0.0
Levels*	l_1	l_2	l_3	$\delta_{\max} = 0.0[L]$
$s_A[L^2]$	0.002	0.004	0.006	
Levels*	l_1	l_2	l_3	$s_A = 0.0[L^2]$
$\delta_{\max}[L]$	0.002	0.004	0.006	

Table 1 – Network parameters to study the effect of fibre area and orientation. * for each level, 3 realisations are considered.

The constitutive behaviour of single fibres at the microscale is characterised by the strain energy function (5.13), with parameter $k_1^\alpha = 900[F/L^2]$ constant for all fibres. A progressive stretch in the horizontal direction was applied with macroscale gradient given by

$$\mathbf{G}_t = \begin{bmatrix} t & 0 \\ 0 & 0 \end{bmatrix}, \tag{6.2}$$

where t is a parameter in the range $[0, 1]$ that increases linearly and monotonically through 50 load steps.

Fig. 21, on the left column, shows the dominant component of the PKST (P_{11}, from $\mathbf{P} = \left(\begin{smallmatrix} P_{11} & P_{12} \\ P_{21} & P_{22} \end{smallmatrix}\right)$) homogenised according to the proposed multiscale methodology as a function of the macroscale stretch λ, i.e. $\lambda = t + 1$, for the different sets of parameters. To better understand the role of the displacement fluctuations in the constitutive response, the right column in the same figure displays the non-affinity index I_{NA} (see (6.1)) which measures the magnitude of the fluctuation field. In both cases (A-heterogeneity or θ-heterogeneity) it is observed that the smaller the dispersion, the stiffer the constitutive

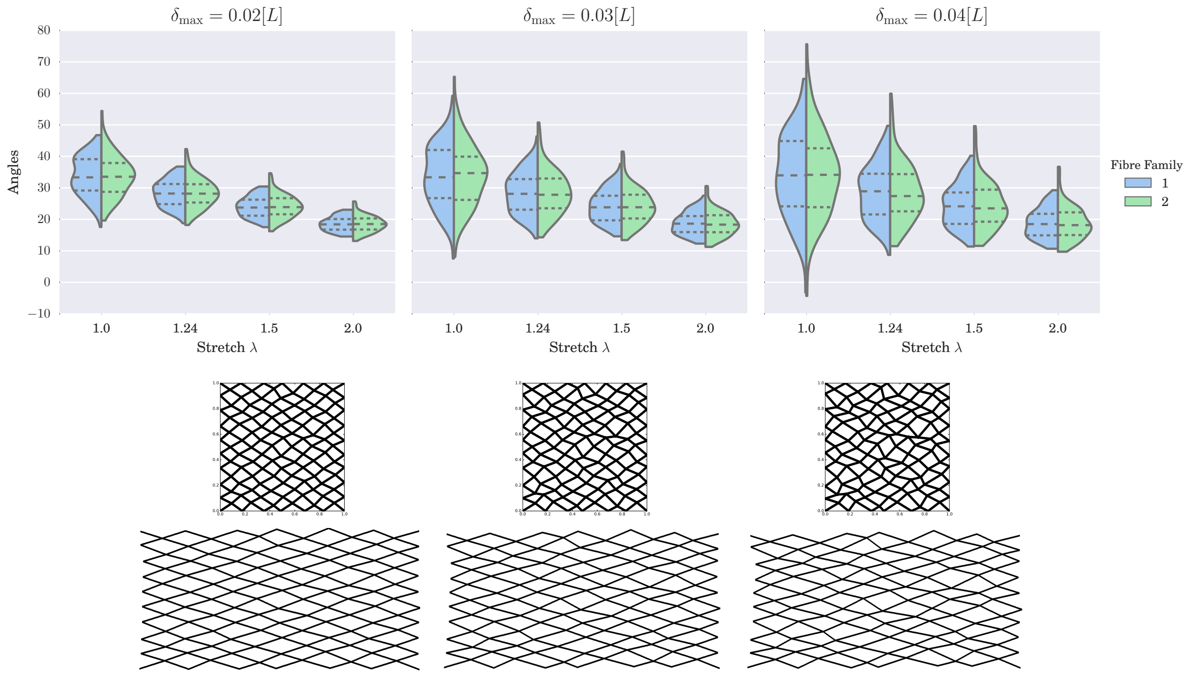

Figure 20 – Reorientation of fibre families considering different fibre orientation angles due to three different node perturbations (realisations for a fixed random seed value). The angle distribution as a function of the macroscale stretch (top row) and the topology of fibres in the original (mid row) and the deformed network at the maximum level of stretch $\lambda = 2.0$ (bottom row).

response. Specifically, for the proposed scenarios, the mechanical response is more sensitive to the definition of fibre area than to the fibre orientation.

Note that, when the fibre area is heterogeneous (see levels l_2 and l_3), the index I_{NA} doubles that obtained when the fibre orientation is heterogeneous. Therefore, we conclude that the determination of fibre areas is a sensitive aspect in the conformation of a fibrous network, even more than the definition of fibre orientation angles.

From this study, it is also possible to analyse the reorientation of fibre families and the resulting angle dispersion in the RVE as the deformation takes place. This is reported in Fig. 20 (top row), where it is seen that the fibre dispersion diminishes as the macroscale stretch increases, providing a sense of fibre orientation around an average value. As expected, such average fibre angle reduces with the increasing stretch. Also, the examples of the network realisations for $\delta^{l_1,1}_{\max}, \delta^{l_2,1}_{\max}, \delta^{l_3,1}_{\max}$ are illustrated in Fig. 20 (bottom and mid rows).

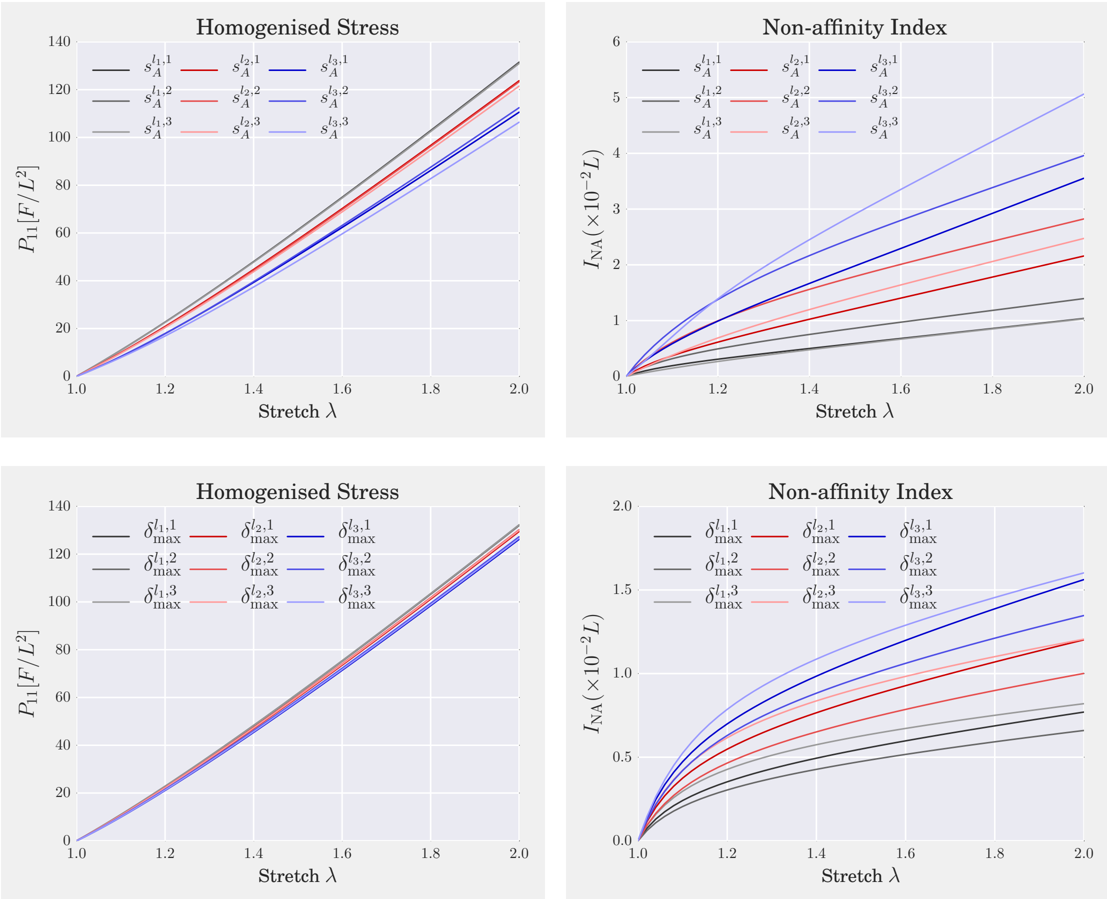

Figure 21 – Homogenised constitutive response (left column) and non-affinity index (right column) considering fibre area variation (top row) and fibre orientation (bottom row).

6.1.1.3 Effect of the activation stretch

In this section, we study the impact of potential heterogeneities in the definition of the fibre activation stretch parameter throughout the network. To this end, we consider 6 random network realisations parameterised as described in Table 2. Each realisation corresponds to a pair $(m_{\lambda^a}, s_{\lambda^a})$, equivalently denoted by $(m,s)_{\lambda^a}$, which aims to control the activation stretch of fibres in the network. Since the definition of the activation stretches does not affect the network configuration (position of nodes, connectivity, etc), the topology is fixed for all realisations (same seed is used in the pseudo-random algorithm). Fig. 22 presents the distribution of the activation stretch as a function of the pair $(m,s)_{\lambda^a}$.

The macroscale gradient applied to the specimens is that given by (6.2), and the constitutive equation of individuals fibres follows (5.13). In this specific case, at early stretching stages the RVE may be highly unstable because of the lack of fibre activation. To circumvent this phase, a neo-hookean material 10^{-3} times softer than the fibre material is considered to be a ground substance. Clearly, this is a pure numerical strategy necessary to stabilise the problem in cases where just few (or even none) fibres are bearing load,

All Realisations		θ	n_{fib}	$\delta_{\max}[L]$	$m_A[L^2]$	$s_A[L^2]$
		33.69°	216	0.03	0.01	0.001
Realisation	1	2	3	4	5	6
m_{λ^a}	0.4	0.4	0.5	0.5	0.6	0.6
s_{λ^a}	0.2	0.4	0.2	0.4	0.2	0.4

Table 2 – Network parameters to study the effect of fibre activation stretch.

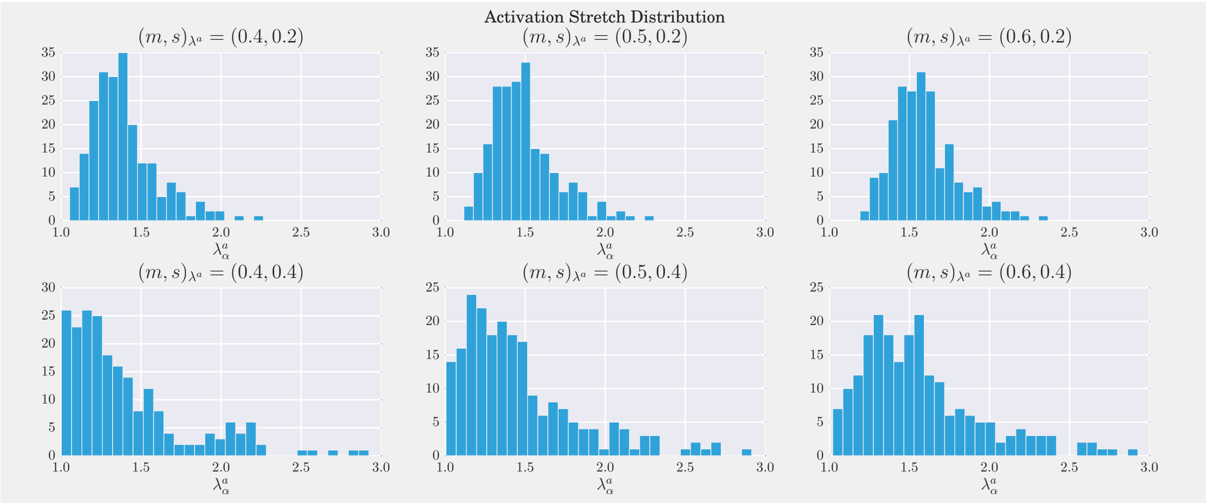

Figure 22 – Histogram of the activation stretch following a Gamma-distribution for the different realisations defined in terms of the pair $(m, s)_{\lambda^a}$.

but which introduces no artificial ingredients in the constitutive response once the fibres activate start to be activated, as will be seen next.

Fig. 23 displays the homogenised P_{11} component, of the PKST, for the 6 realisations. In general, the stress curves are right-shifted towards the value determined by m_{λ^a}, while the lower the standard deviation s_{λ^a} the more pronounced the uprise in the stress value. More specifically, three regions can be distinguished in each curve: toe-region, transition and linear regime. For instance, for the realisation $(m, s)_{\lambda^a} = (0.4, 0.2)$, these regions correspond approximately to the stretch intervals $[1.0, 1.3]$, $[1.3, 1.6]$ and $[1.6, 2.0]$, respectively. In order to quantify the fibres that are effectively bearing load, Fig. 24a features the relative number of fibres whose stretch exceeds the activation stretch for all the realisations[4]. Clearly, the three regions referred to before are unveiled. The toe region has none-to-few activated fibres, while most of the fibres are engaged in the transition region, leading to the recruitment of almost all fibres in the linear regime. Such mechanism is described in the specialised literature, see for example (HILL et al., 2012). From a phenomenological point of view, this is modelled at the macroscale either using exponential strain energy function or a linear strain energy function convoluted with a probability density function.

[4] A schematic representation of activated fibres in deformed networks is presented in the next numerical experiment, specifically in Figs. 27 and 28.

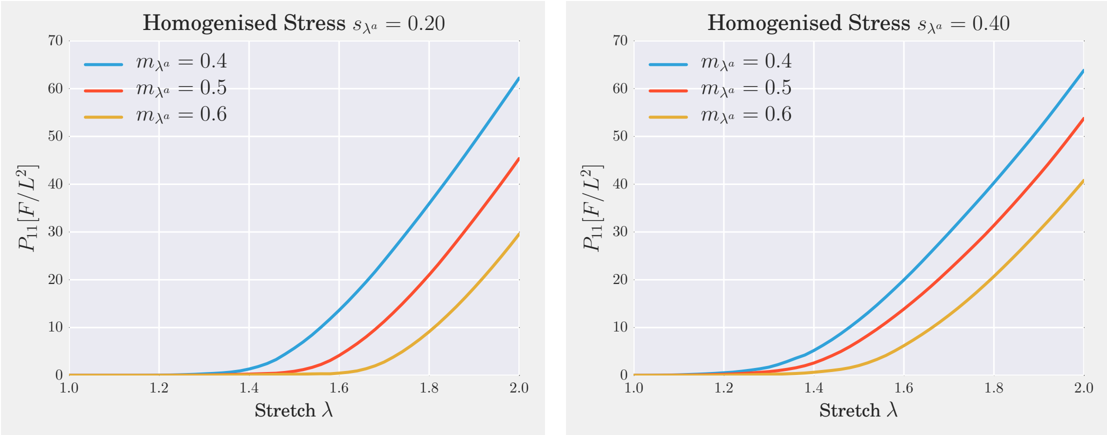

Figure 23 – Homogenised constitutive response for different distributions of the activation stretch parameter.

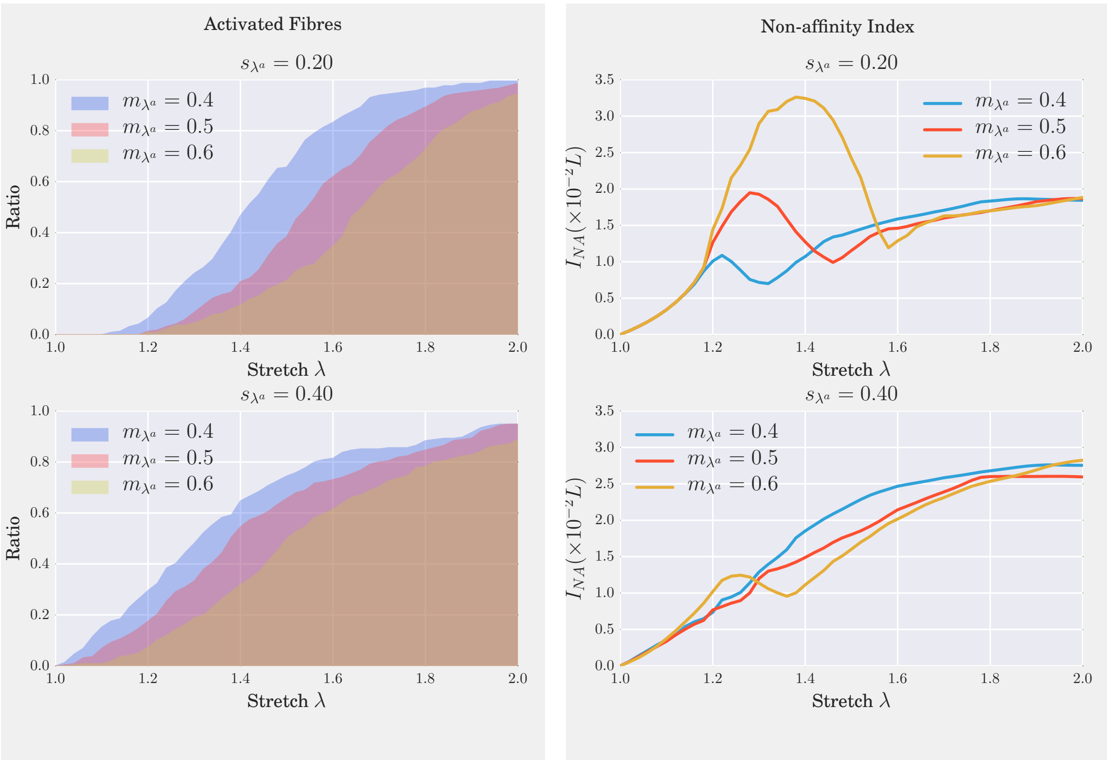

(a) Ratio of activated fibres.

(b) Non-affinity index

Figure 24 – λ^a-heterogeneity in the RVE for the different realisations: impact on the non-affinity and overall activation ratio.

The heterogeneity in the fibre activation stretch leads to a complex pattern of fibre engagement, which in turn affects the magnitude of the fluctuating component of the displacement field in the network. This is manifested through the non-affinity index I_{NA}, as appreciated in Fig. 24b. While I_{NA} is almost monotonously increasing with respect to the stretch for wide activation stretch distributions (e.g. for $s_{\lambda^a} = 0.4$), it features a non-monotonic behaviour when the distribution is sharp ($s_{\lambda^a} = 0.2$), and the magnitude of the fluctuation field becomes significantly bigger in the transition region. However, for both cases, at late loading stages, the fluctuations accommodate to a certain value, which suggests that the mechanical response has reached a stable regime.

6.1.1.4 On the choice of boundary conditions

In this last section, we aim to investigate the sensitivity of the constitutive response with respect to the fibres network size, considering different sub-models from Section 4.3.5.3. This raises a sense of convergence as the network size is increased and the homogenised solution becomes independent from the choice of boundary conditions. Specifically, two choices are analysed, the Affine Boundary Model, $\widetilde{\mathscr{U}}_\mu^{\mathsf{L}}$ (see (4.76)), and the Minimally Constrained Model, $\widetilde{\mathscr{U}}_\mu^{\mathsf{M}}$ (see (4.74)). In the present case, the fibrous specimens to be analysed feature heterogeneities of different kinds (fibre area, orientation and activation stretch).

Firstly, two levels of perturbations were considered for the heterogeneities as detailed in Table 3. These parameters were used to generate corresponding fibres networks which have been replicated horizontally and vertically by a multiplication factor of 2, 3, 4 and 5. The value for m_{λ^a} is such that all fibres are activated when 50% of axial stretch is reached. The resulting networks are shown in Fig. 25.

$\widetilde{\mathscr{U}}_\mu^{\mathsf{M}}$ and $\widetilde{\mathscr{U}}_\mu^{\mathsf{L}}$	θ 33.69°	n_{fib} 96	$m_A[L^2]$ 0.02	m_{λ^a} 1.366	s_{λ^a} 0.2
Levels	l_1		l_2		
$s_A[L^2]$	0.025		0.075		
$\delta_{\max}[L]$	0.025		0.075		

Table 3 – Network parameters for the study of boundary conditions related to $\widetilde{\mathscr{U}}_\mu^{\mathsf{L}}$ and $\widetilde{\mathscr{U}}_\mu^{\mathsf{M}}$.

As in the previous section, the loading protocol is defined by the macroscale gradient. Also as before, the single fibre constitutive response is as in (5.13). Two strain paths were considered with pseudo-time $t \in [0, 1]$ sampled in 50 equally spaced increments for both cases:

1. Axial stretch (pure axial test): Identically to experiments from previous sections, and repeated here for convenience:

$$\mathbf{G}_t = \begin{bmatrix} t & 0 \\ 0 & 0 \end{bmatrix}. \tag{6.3}$$

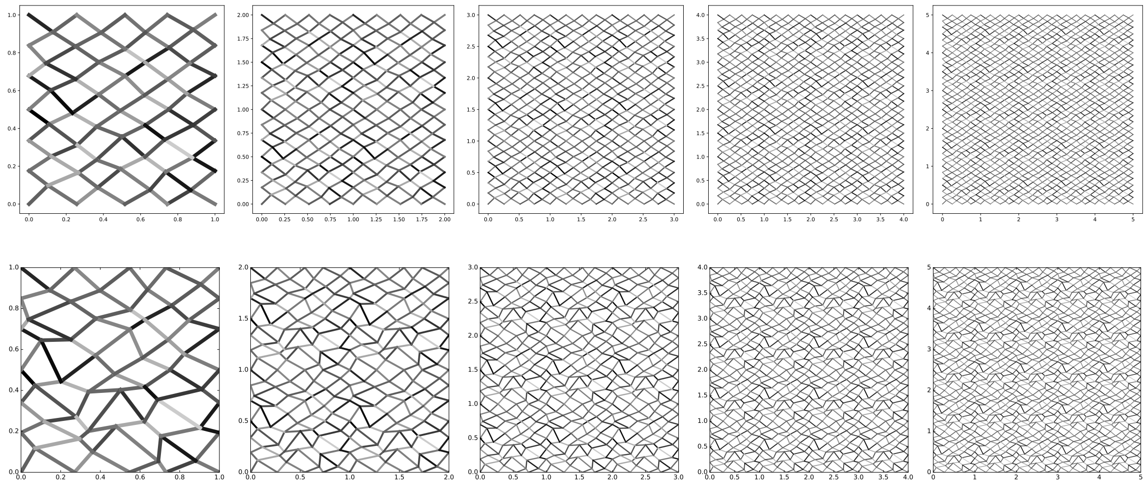

Figure 25 – Network of fibres generation through the replication of a basic unit pattern (multiplication factor from 1 to 5, i.e. left to right panels). Perturbation level l_1 in top row, and perturbation level l_2 in the bottom row. Gray color stands for the fibre transversal area values (darker color indicates larger area).

2. Early axial stretch and late shear-like distortion (combined axial-shear test): In this case the macroscale gradient is

$$\mathbf{G}_t = \begin{bmatrix} \min(t, t_0) & \max(0, t - t_0) \\ 0 & 0 \end{bmatrix}, \tag{6.4}$$

where $t_0 = 0.5$ for the reported numerical examples. Observe that $(\mathbf{G}_t)_{11}$ increases linearly for $t < t_0$, when this component saturates, whilst the shear component $(\mathbf{G}_t)_{12}$ only assumes non-zeros values for $t > t_0$. Around the maximum level of axial stretch ($t = t_0$), we have a minimum number of fibres activated necessary to make the network stable during shear loading stage.

Fig. 26 displays the unit networks warped with the displacement fluctuation field, where we can clearly appreciate how the selection of specific boundary conditions affects the mechanical equilibrium in the RVE. As expected, the fluctuation displacement field is larger in the $\widetilde{\mathscr{U}}_\mu^{\mathsf{M}}$ model, because it is not constrained to be null over the boundary as in the $\widetilde{\mathscr{U}}_\mu^{\mathsf{L}}$ model. This reflects the expected less stiff response of the $\widetilde{\mathscr{U}}_\mu^{\mathsf{M}}$ model.

Concerning the activation of fibres, Figs. 27 and 28 illustrate, for the pure axial and the combined axial-shear tests, respectively, the progression of activated fibres along the pseudo-time. For the sake of simplicity, only perturbation level l_2 is reported in Fig. 27 and just level l_1 is presented in Fig. 28, both for the $\widetilde{\mathscr{U}}_\mu^{\mathsf{M}}$ model. In the pure axial test the ratio of activation fibres increases monotonically and there is no clear tendency concerning the spatial distribution of activation fibres. On the other hand, in the combined axial-shear test and when distortion becomes increasingly important, some fibres even deactivate along one preferred family, maintaining an activation trend in the other family.

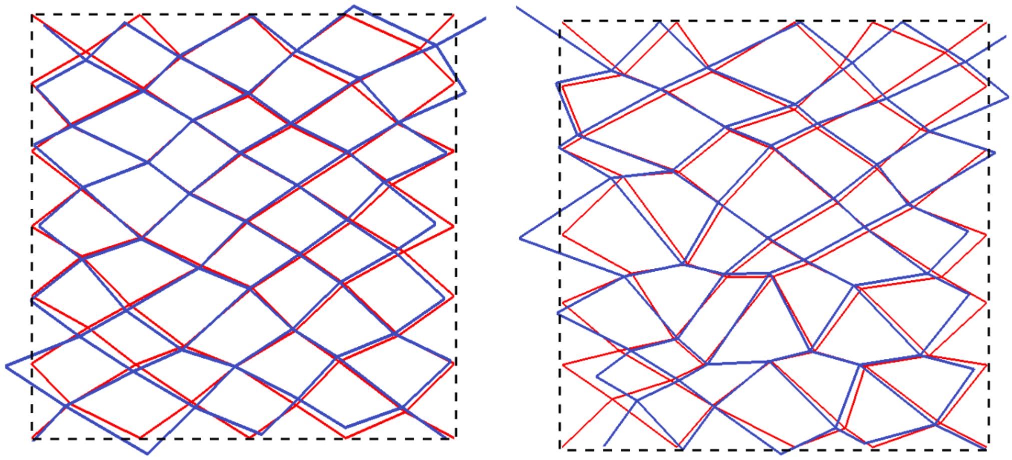

(a) Perturbation l_1 .

(b) Perturbation l_2 .

Figure 26 – The impact of boundary conditions on the displacement fluctuation field. Networks warped with the displacement fluctuation for models $\widetilde{\mathscr{U}}_\mu^{\mathsf{L}}$ (red) and $\widetilde{\mathscr{U}}_\mu^{\mathsf{M}}$ (blue) at the last pseudo-time in the pure axial test.

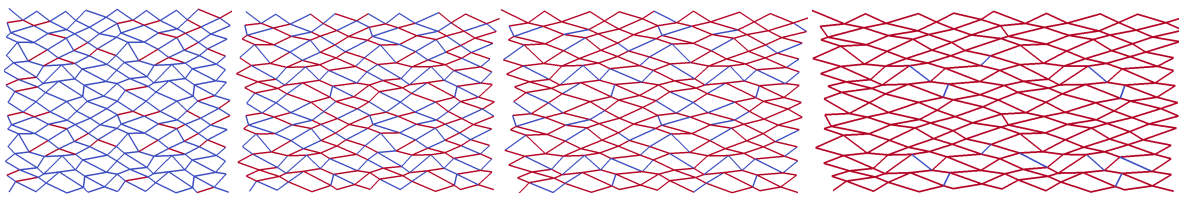

(a) $t = 0.2$

(b) $t = 0.4$

(c) $t = 0.6$

(d) $t = 1.0$

Figure 27 – Total deformed configuration of the RVE along the pseudo-time showing activated fibres (in red) for the $\widetilde{\mathscr{U}}_\mu^{\mathsf{M}}$ model, at the perturbation level l_2, and for the pure axial test.

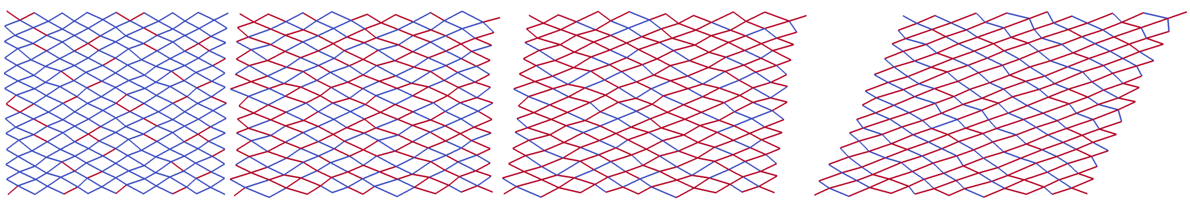

(a) $t = 0.2$

(b) $t = 0.4$

(c) $t = 0.6$

(d) $t = 1.0$

Figure 28 – Total deformed configuration of the RVE along the pseudo-time showing activated fibres (in red) for the $\widetilde{\mathscr{U}}_\mu^{\mathsf{M}}$ model, at the perturbation level l_1, and for the combined axial-shear test

.

In Fig. 29, the dependence of the homogenised PKST, $\mathbf{P} = \begin{pmatrix} P_{11} & P_{12} \\ P_{21} & P_{22} \end{pmatrix}$, on the RVE size is shown for the two perturbation levels l_1 and l_2, and for the two tests. Such plot was constructed considering $t = 1$ in the definition of the macroscale gradient. This figure provides a sense of convergence of the RVE constitutive response as the RVE size is enlarged, which makes the solution less sensitive to the choice of boundary conditions. We observe that in most of the situations the relative differences between the $\widetilde{\mathscr{U}}_\mu^{\mathsf{L}}$ and the $\widetilde{\mathscr{U}}_\mu^{\mathsf{M}}$ are rather small, hence yielding sharp bounds, at least under the hypotheses considered, for the constitutive response of these fibrous specimens.

Going into the details, for a more homogeneous RVE and pure axial test (see top row in Fig. 29a), the $\widetilde{\mathscr{U}}_\mu^{\mathsf{L}}$ model is less sensitive to the RVE size (see components P_{11}, P_{12} and P_{21}). In contrast, when the heterogeneities in the RVE are more pronounced (see bottom panels of Fig. 29b) the $\widetilde{\mathscr{U}}_\mu^{\mathsf{M}}$ model performs better, with the dominant stress components (see P_{11} and P_{22}) being less sensitive to the RVE size.

Similar features are seen for the combined axial-shear test in Fig. 29b. For the less perturbed state, the non-diagonal components, which are not negligible in this case, found with the $\widetilde{\mathscr{U}}_\mu^{\mathsf{M}}$ model are less sensitive to the RVE size. The opposite happens for the diagonal components. In the second perturbation level, P_{11} computed with the $\widetilde{\mathscr{U}}_\mu^{\mathsf{M}}$ model is much less sensitive to the RVE size, while for the other components the sensitivity of both models is comparable.

Note that a number of convergence patterns are found in Fig. 29 (see the behaviour of red and blue lines). For instance, at the bottom right plot of Fig. 29b we have the red curve decreasing, while the blue curve is increasing. In turn, in the top left plot of Fig. 29a, both curves are increasing, with the linear model being stiffer than the minimally constrained model. The explanation for the different patterns are twofold: i) some stress components have negligible order of magnitudes with respect to others, thus in general we should regard them according to their importance; and ii) the large levels of variability in the parameters, specially the activation stretch. It is important to keep in mind that for the dominant stress components, the linear model is always stiffer than the minimally constrained one for the same RVE size. Importantly, by increasing the RVE size, both models feature a convergent trend.

Using a different criterion to measure convergence with respect to the RVE size, figures 30a and 30c show the convergence study with respect to the total averaged strain energy in the RVE, i.e.,

$$\Psi := \frac{1}{|\Omega_\mu|} \sum_{\alpha \in \mathcal{F}_{\text{net}}} V_\alpha \Psi_\alpha^\mu(\lambda_\alpha), \tag{6.5}$$

evaluated at the equilibrium point when reaching the last loading step. In this case we have a very similar convergence pattern for all cases. Again, the linear model yields a stiffer behaviour than the minimally constrained model. Evidently, in cases where the mechanical problem can be understood as a minimisation problem (in the case of hyperelasticity), the total energy is necessarily smaller for the larger admissible space (i.e. the minimally constrained model).

Another interesting analysis consists in measuring the role played by the fluctuations

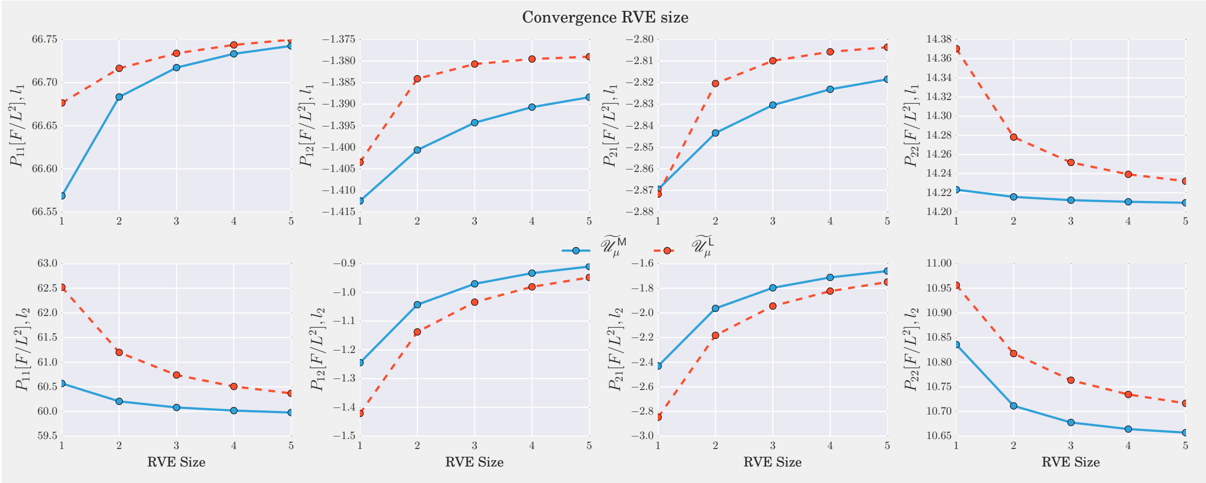

(a) Pure axial test for heterogeneity levels l_1 and l_2.

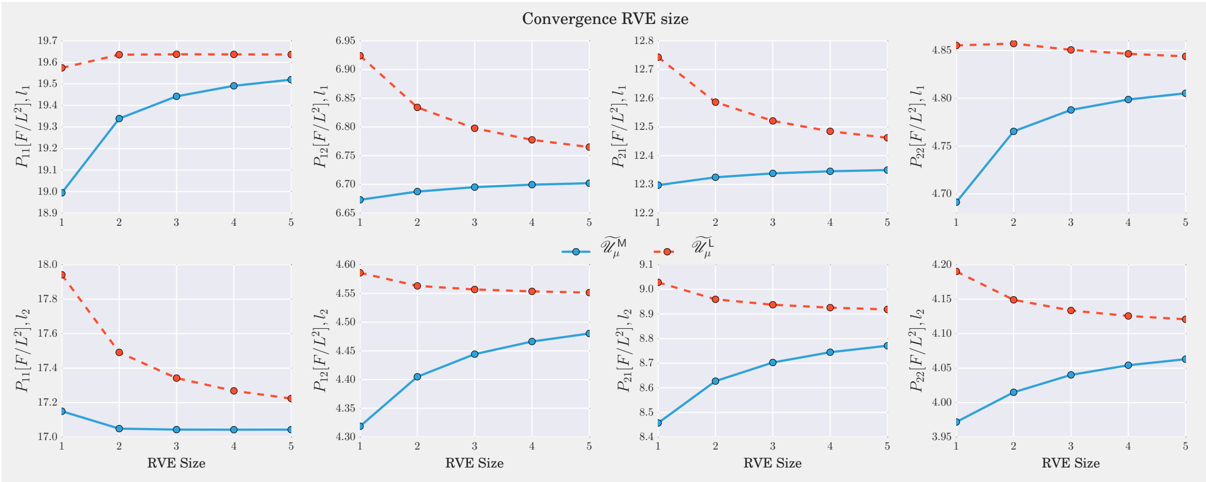

(b) Combined axial-shear test for heterogeneity levels l_1 and l_2.

Figure 29 – Convergence of the homogenised stress response with respect to the RVE size for the $\widetilde{\mathscr{U}}_\mu^{\mathsf{L}}$ (red dashed line) and $\widetilde{\mathscr{U}}_\mu^{\mathsf{M}}$ (blue solid line) models.

in terms of energy. To this end, we propose the fluctuation energy ratio, defined as

$$\tilde{\Psi}_{rel} := \frac{|\Psi - \overline{\Psi}|}{\Psi}, \tag{6.6}$$

where $\overline{\Psi} := \Psi|_{\tilde{\mathbb{U}}_\mu = \mathbb{O}}$ is the averaged energy due to the linear part of displacements, i.e., vanishing displacement fluctuation. We remark that $\Psi < \overline{\Psi}$ always holds since $\tilde{\mathbb{U}}_\mu = \mathbb{O}$ represents the Taylor model, which renders a higher level of energy. For the simulations reported in this section, the behaviour of this index is observed in figures 30b and 30d. As expected, the fluctuation energy ratio is always larger for the minimally constrained model. In addition, such contribution of energy becomes more important as the heterogeneities are higher as well as we move towards to a shear dominated regime.

Such results point out the importance of an adequate minimally constrained multiscale model, as proposed in this thesis, in order to provide consistent and sharp bounds for the constitutive response. Even if the differences observed are in some cases

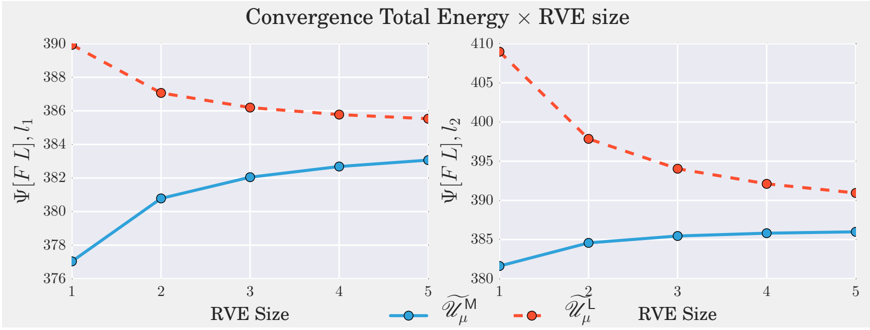

(a) Total strain energy for pure axial test.

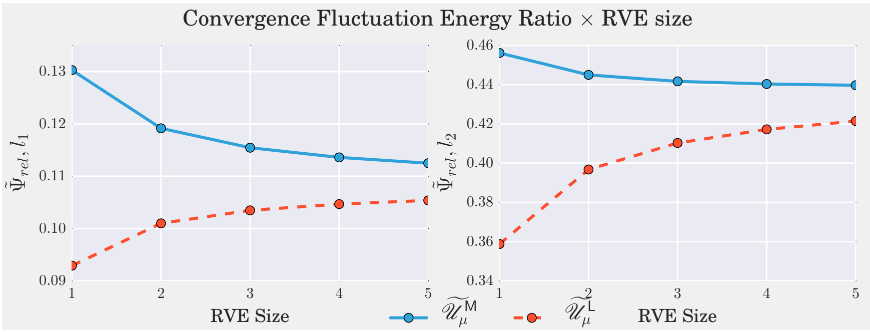

(b) Fluctuation energy ratio for pure axial test.

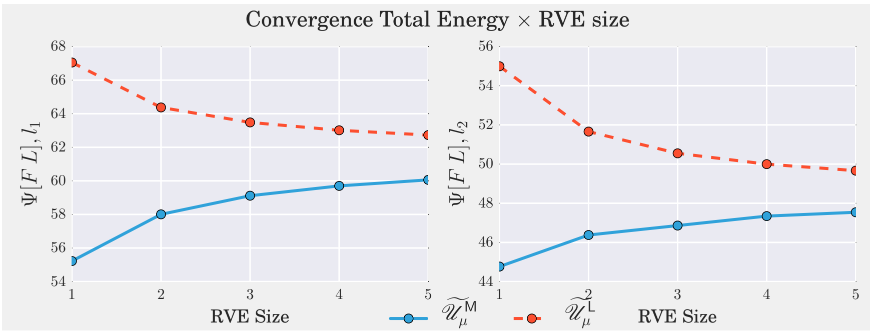

(c) Total strain energy for combined axial-shear test.

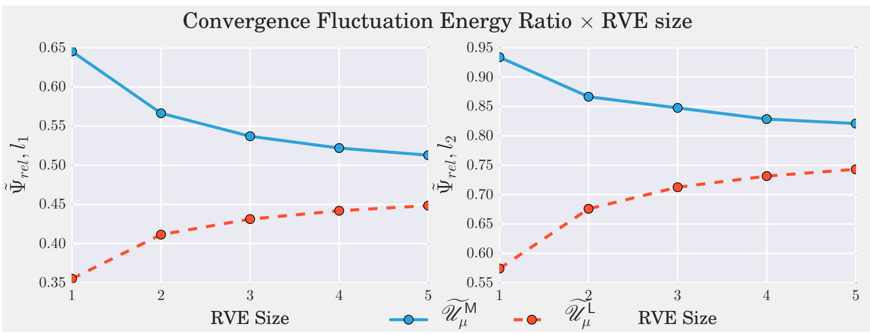

(d) Fluctuation energy ratio for combined axial-shear test.

Figure 30 – Convergence analyses with respect to the RVE size for the $\widetilde{\mathscr{U}}_\mu^{\mathsf{L}}$ (red dashed line) and $\widetilde{\mathscr{U}}_\mu^{\mathsf{M}}$ (blue solid line) models. Heterogeneity levels l_1 (left) and l_2 (right).

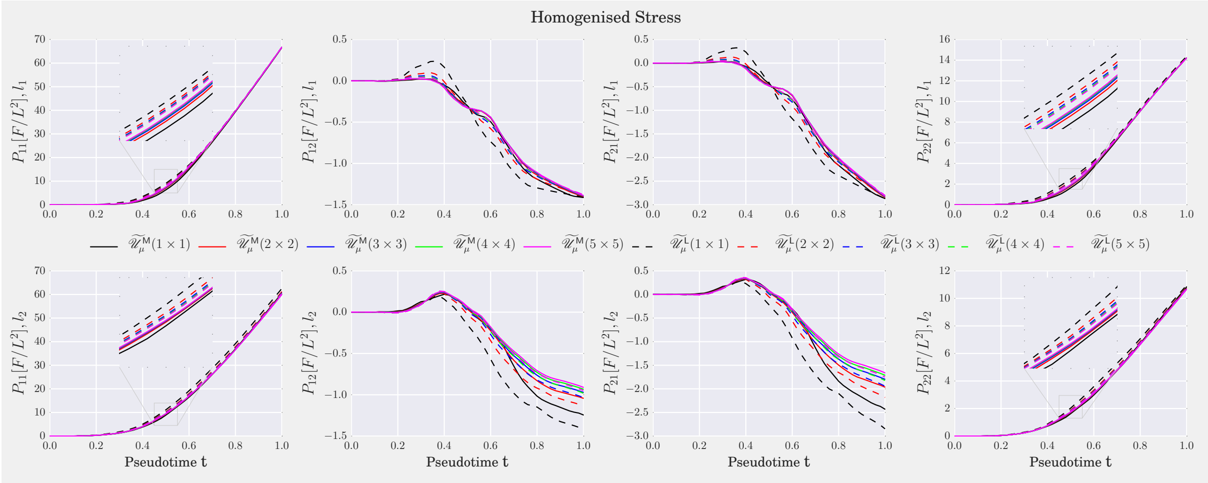

(a) Pure axial test for heterogeneity levels l_1 and l_2.

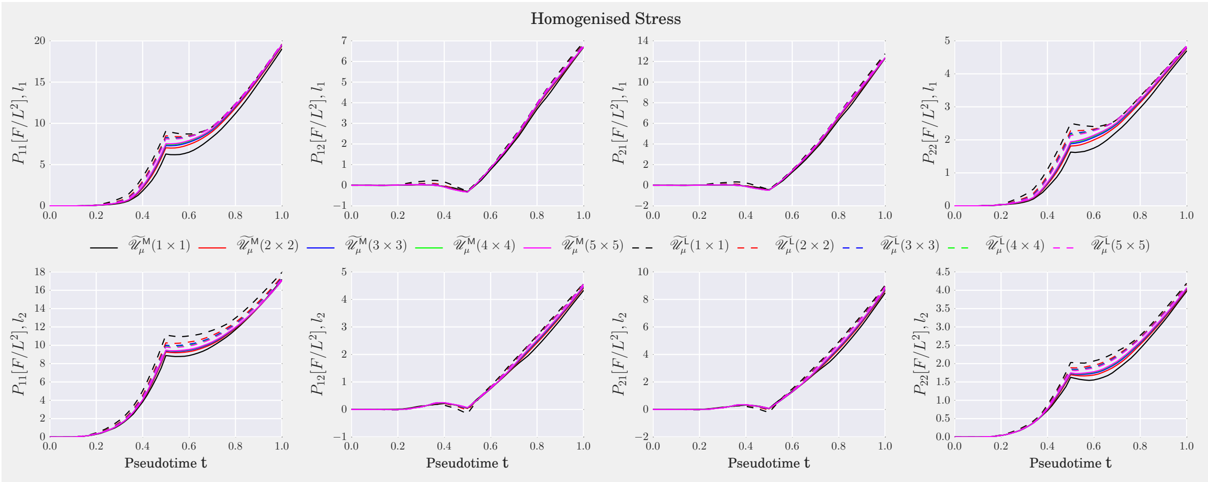

(b) Combined axial-shear test for heterogeneity levels l_1 and l_2.

Figure 31 – Homogenised stress for different boundary conditions. Stress components during pseudo-time for the $\widetilde{\mathscr{U}}_\mu^{\mathsf{L}}$ (dashed lines) and $\widetilde{\mathscr{U}}_\mu^{\mathsf{M}}$ (solid lines) models.

negligible (notice in some cases the stress scale in the plots is really small), the correct formulation of the $\widetilde{\mathscr{U}}_\mu^{\mathsf{M}}$ allowed us to quantify the impact of the choice of boundary conditions in the homogenised response in a wide variety of scenarios. Being more specific, the minimally constrained model is a lower bound for the homogenised stress, and the affine boundary model is an upper [5] bound of these curves. From Fig. 29, it is clear that this observation is always true, save for few cases where for relatively small values of the off-diagonal components these bounds are actually inverted.

To gain more insight into the complex behaviour the homogenised stress may render, Fig. 31 provides the stress components along the evolution of the pseudo-time for all the twenty cases ($\widetilde{\mathscr{U}}_\mu^{\mathsf{L}}$ and $\widetilde{\mathscr{U}}_\mu^{\mathsf{M}}$ with 5 RVE sizes each for pure axial and combined axial-shear tests). The convergence of the solution in the dominant stress components

[5] Naturally, the Taylor submodel provides a stiffer response than the affine boundary model. Thus, we restrict the term "upper bound" to boundary-like constraints, excluding the Taylor model from the analysis.

P_{11} and P_{22} always takes place as expected (see the insets in the corresponding panels), with the $\widetilde{\mathscr{U}}_\mu^{\mathsf{L}}$ model being an upper bound and the $\widetilde{\mathscr{U}}_\mu^{\mathsf{M}}$ model behaving as a lower bound. Remarkably, for the pure axial test and for components P_{12} and P_{21}, the response delivered by the $\widetilde{\mathscr{U}}_\mu^{\mathsf{L}}$ model is much more sensitive to the RVE size than the corresponding to the $\widetilde{\mathscr{U}}_\mu^{\mathsf{M}}$ model. This effect is reduced when off-diagonal stress components gain importance as in Fig. 31b. Observe that exactly at the point of axial phase becoming shear distortion the stress curves are less similar, but the trend remains similar to the cases discussed before.

6.1.2 Three-dimensional simulations

Network generation of the three-dimensional random fibre network was based on Voronoi tesselations. For this task, the open source library *Voro++* (RYCROFT, 2009) and its wrapper for Python *pyvoro* [6] have been employed. First, a certain number of points are chosen at random positions, and maintaining a certain distance among them. These points are used as barycentric of cells that form a partition of a rectangular parallelepiped whose dimensions are also inputs to the algorithm. Then, a fibre is considered over cell edges (transversal area and activation stretch are randomly assigned following a given distribution). Edges lying on the RVE boundary are removed. A preference direction is emulated by considering a preliminary network which is scaled differently in the different directions. An example of network resulting from this pipeline is shown in Fig. 32. The RVE is considered to be a representative piece of adventia layer (mainly composed by collagen) in a model of an arterial vessel. The initial network was generated in $0.5 \times 1.0 \times 1.0 L^3$ (sizes in the directions $\mathbf{e}_\theta$, $\mathbf{e}_z$ and $\mathbf{e}_r$, respectively) and then mapped to a size of $1.0 \times 1.0 \times 0.5 L^3$. The effect of this scaling procedure is translated in the, say, circumferential angle denoted by β (assumed positive but equally valid for negative value), as observed in Fig. 32. In this case $\beta < 45°$ as the initial block was scaled in $\mathbf{e}_\theta$ direction, whereas $\beta = 45°$ when no scaling is involved.

6.1.2.1 Effect of circumferential angle

In this example we study the sensitivity of the mechanical response with respect to differences in the circumferential angle β. To this end, we generated 6 networks, 3 for each of the 2 cases as the following procedure:

1. Map from $1/2 \times 1.0 \times 1.0$ to $1.0 \times 1.0 \times 0.5$: $\beta_1 = \arctan(1/2) = 26.57°$.
2. Map from $1/3 \times 1.0 \times 1.0$ to $1.0 \times 1.0 \times 0.5$: $\beta_2 = \arctan(1/3) = 18.43°$.

In all cases 200 random points (centres of the Voronoi cells) were uniformly picked inside the brick domain. This resulted in networks with approximately 750 fibres [7]. In addition,

[6] URL: https://pypi.org/project/pyvoro/1.3.1/.

[7] A certain number of Voronoi cells does not yield the same certain number of fibres.

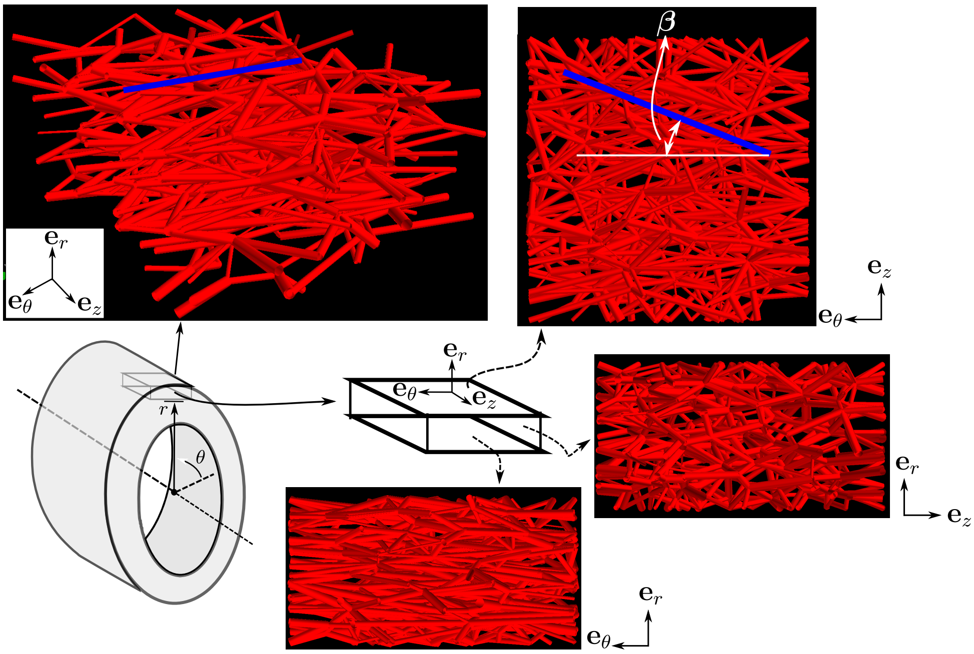

Figure 32 – Three-dimensional RVE from a piece of an adventitia layer and projections on the coordinate planes.

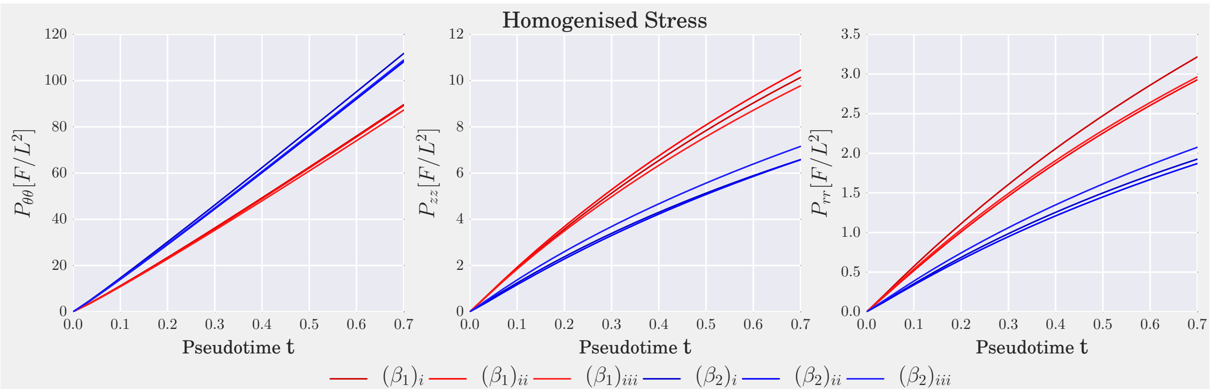

Figure 33 – Homogenised stress tensor components along the loading program for the different circumferential angles.

fibre areas were taken randomly from a normal distribution with mean $0.01L^2$ and standard deviation of $0.0005L^2$. Fibre constitutive model was assumed to be the same than for the examples from Section 6.1.1, with unitary uniform activation stretch for all fibres, and axial load applied along the circumferential direction. The macroscale applied strain program is characterised by the gradient $\mathbf{G}_t = t\mathbf{e}_\theta \otimes \mathbf{e}_\theta$, with $t \in [0.0, 0.7]$ divided into 20 equally spaced pseudo-time steps. The realisations are denoted $(\beta_a)_b$, $a \in \{1, 2\}, b \in \{i, ii, iii\}$ and some examples of undeformed meshes can be seen in Fig. 34a and Fig. 34b, the later displaying a smaller circumferential angle. To verify the preferred direction numerically we compute the structural tensors (see definition (4.65)) for the different cases

$$\mathbf{B}_{(\beta_1)_i} = \begin{bmatrix} \mathbf{0.69740} & -0.00513 & 0.00450 \\ -0.00513 & \mathbf{0.23118} & 0.00033 \\ 0.00450 & 0.00033 & \mathbf{0.07142} \end{bmatrix},$$

$$\mathbf{B}_{(\beta_2)_i} = \begin{bmatrix} \mathbf{0.82643} & -0.01320 & -0.00275 \\ -0.01320 & \mathbf{0.13334} & 0.00398 \\ -0.00275 & 0.00398 & \mathbf{0.04024} \end{bmatrix},$$

where the basis considered is $\{\mathbf{e}_\theta, \mathbf{e}_z, \mathbf{e}_r\}$ (in this order). Regarding the first value of the diagonal (related with the circumferential direction), we confirm the graphical suggestion, in general fibres are more aligned with $\mathbf{e}_\theta$ in the case $(\beta_2)_i$ than in case $(\beta_1)_i$.

Fig. 33 reports the components of the homogenised stress tensor for all three normal realisations and for both circumferential angles. As expected, the realisations with a smaller circumferential angle (group β_2) feature a stiffer response in the circumferential stress component, while for the axial and radial components RVEs in group β_1 are stiffer.

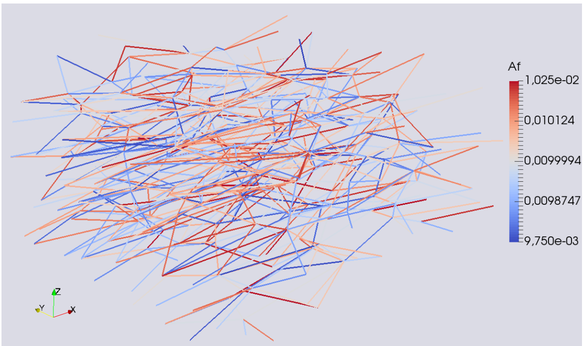

(a) Undeformed network for case $(\beta_1)_i$.

(b) Undeformed network for case $(\beta_2)_i$.

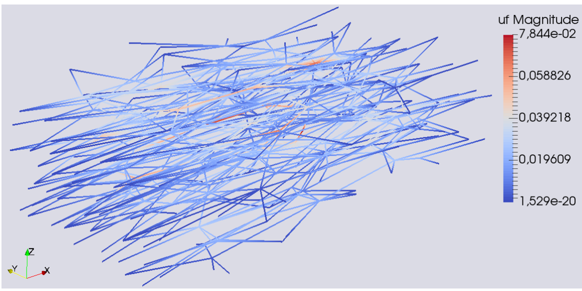

(c) Deformed network for case $(\beta_1)_i$.

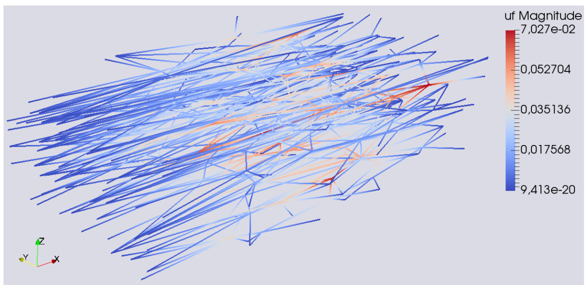

(d) Deformed network for case $(\beta_2)_i$.

Figure 34 – Reference and deformed configurations of 3D networks. Colours represent fibre area at the begining of the loading program (first row) and the fluctuation magnitude for the last loading step (second row).

6.1.3 Discussion

Based on the reported numerical experiments using the proposed novel multiscale model for fibrous materials, we can highlight the following features:

1. The mechanical response is sensitive to non-homogeneities in network parameters, such as fibre orientation, fibre area or activation stretches. In fact, different RVE realisations lead to different stress curves (see Fig. 21 left column).

2. The more structured and homogeneous the RVE, the stiffer the constitutive response (see also Fig. 21 left column). This goes along with a larger non-affinity in the network kinematics, as measures by the index I_{NA} (see Fig. 21 right column).

3. Concerning the dispersion of fibre orientations, it is observed that its variability and mechanical effect becomes less evident when RVE is stretched (see Fig. 20). Such fibre alignment reduces the rate of the non-affinity at late stretching stages (see Fig. 21 bottom right column panel).

4. Concerning the dependence upon the activation stretch distribution, it is observed that the homogenised mechanical response of an RVE, resulting from the intermingling of progressively activated fibres (as noticed in Fig. 24a), assumes a very distinct shape than the constitutive model adopted for a single fibre. In our particular case, an exponential-shaped stress curve (see Fig. 23) is retrieved by using simple linear (quadratic strain energy) constitutive laws for the microscale constituents, i.e., the fibres.

5. Finally, the comparison between two boundary conditions have resulted in two different scenarios. On the one hand, the more homogeneous, and then stiffer, the network, the more suitable results the Affine Boundary Model in terms of the solution delivered by small RVE sizes. On the other hand, for highly heterogeneous networks, the use of the Minimally Constrained Model (MCKMM) proposed in the present thesis yields better results in terms of the solution delivered by small RVE sizes. In any case, the two tested boundary conditions, which lead to two multiscale models, determine proper bounds (without considering Taylor submodel) for the constitutive response of fibrous microstructures. In this sense, we highlight that the proposed model constitutes an unprecedented lower bound for this kind of analyses.

Based on the results reported so far in this chapter, the relevance of a proper multiscale model for fibrous tissues is larger as the network heterogeneities are more pronounced, and this holds for any of the sources of heterogeneities studied in this work. Some recent phenomenological models even include specific parameters to account for the effect of dispersion in the fibre orientation (GASSER; OGDEN; HOLZAPFEL, 2006). However, as seen in this work, this is not enough to effectively predict the constitutive behaviour of fibrous networks with more accentuated heterogeneities. Moreover, up to the authors' knowledge, dispersion in fibre properties such as area and activation stretch have been overlooked in most of phenomenological, or even histologically-inspired constitutive models. It is worth mentioning that these data can also be extracted from images by using proper image processing techniques already available in the literature.

At last but not least, the proposed multiscale approach was straightforwardly extended from 2D to 3D RVEs, which makes it a versatile candidate to guide the construction of general constitutive laws capable of accounting for all the heterogeneities studied in this work.

6.2 Fibre networks featuring softening

The numerical tests in the following aim to show the descriptive capabilities of the multiscale theoretical framework presented here. Overall, four types of analyses are reported in different sections, ranging from simple test cases to more involved microstructural settings.

The constitutive behaviour considered for fibres is the one characterised by expressions (5.12) and (5.20), so the set of material parameters $\{\lambda_\alpha^a, E_\alpha, s_\alpha^u, G_\alpha^f\}$ needs to be specified for each fibre. As already commented, due to numerical issues, a fictitious viscosity parameter η_α, which is generally 2 orders of magnitude smaller than E_α is also employed. In principle, these parameters differ for each fibre, and this poses a major source of heterogeneity to the fibre network. Further sources of heterogeneity can be considered such as fibres featuring different cross-sectional areas A_α, different spatial orientations (denoted here ϕ_α) and different fibre agglomeration density throughout the microscale domain of analysis.

The network of fibres is computationally generated by providing a set of target properties. Initially, for a given average fibre orientation, say $\overline{\phi}_\alpha$, (measured with respect to the horizontal axis) and for a certain number of fibres n_{fib}, a homogeneous network is generated containing two families of fibres symmetrically oriented. Crossing-points are considered to be junctions, which are the extremes of computational segments composing the fibres. Then, the position of each node is individually perturbed in a random manner in terms of distance and direction, limited by a circle of radius δ_{max}. It turns out that the orientation of each fibre ϕ_α results from a combination of a given mean value $\overline{\phi}_\alpha$ and the perturbation. Once the network has been built, spatial distribution of material properties and fibre areas are selected. In the study cases presented below we consider either properties constant for all fibres, properties randomly sampled from a known probability density function (e.g. a normal distribution), or specifically modified in a specific region of the RVE, such as a band or ball. For the sake of simplicity, in the forthcoming examples the damage threshold stress s_α^u and the fibre area A_α are considered sources of heterogeneity.

The loading protocol is defined by the macroscale gradient, which progresses as a function of the pseudo-time parameter $t \in [t_{min}, t_{max}]$, discretised differently depending on the problem. Two strain paths are considered:

1. Axial stretch (pure axial test):

$$\mathbf{G}_t = \begin{bmatrix} t-1 & 0 \\ 0 & 0 \end{bmatrix}. \tag{6.7}$$

2. Early axial stretch and late shear-like distortion (combined axial-shear test):

$$\mathbf{G}_t = \begin{bmatrix} \min(t-1, t_0-1) & \max(0, t-t_0) \\ 0 & 0 \end{bmatrix}, \tag{6.8}$$

   where t_0 controls the size of the early axial stretch. The early pre-stretching stage is required in many cases to circumvent the lacking resistance state of the RVE where most of the fibres are compressively loaded.

Recalling the directions that emerge from the DBA, namely $\mathbf{n}$ and $\boldsymbol{\beta}$, we parametrise for in-plane case with two angles θ and β, respectively, as follows:

$$\mathbf{n} = \mathbf{n}(\theta) = \cos\theta \mathbf{e}_1 + \operatorname{sen}\theta \mathbf{e}_2, \tag{6.9}$$

$$\boldsymbol{\beta} = \boldsymbol{\beta}(\beta) = \cos\beta \mathbf{e}_1 + \operatorname{sen}\beta \mathbf{e}_2 \tag{6.10}$$

The search of the minimum determinant of the acoustic tensor $\mathbf{Q}$ (or $\overline{\mathbf{Q}}$) is then performed exhaustively by subdividing the range for θ (or β) (in the interval $[-90°, 90°]$) into 500 subintervals, sampled equally spaced.

For the sake of clarity, the dimensionless version of the acoustic tensor, defined as $\mathbf{Q}^* = \frac{1}{E_\alpha}\mathbf{Q}$ will be reported in the following examples. Note that we are using the elasticity parameter of the fibre E_α (constant for all fibres and in all examples) as the normalising factor. Moreover, as mentioned in 5.9, the determinant of tensor $\overline{\mathbf{Q}}$, effective to determine $\boldsymbol{\beta}$, changes its sign at the same instant than $\mathbf{Q}$ for all numerical examples reported in this paper. Therefore, $\det \overline{\mathbf{Q}}$ is not plotted in the analysis shown next.

6.2.1 Study 1: Detection of critical point, angle and direction of discontinuous bifurcation at macroscale

In this example we illustrate the detection of the critical point at which the problem requires the nucleation of a macroscale crack. To this aim, we consider an RVE made of a regular and homogeneous network of fibres. The only source of heterogeneity is the fibre damage threshold stress s^u_α, where a smaller value is assigned to a given location in the RVE, resulting in a weakened band of fibrous material. Particularly, we study the following three cases:

1. Vertical weakened fibre band, macroscale gradient as in (6.7), denoted Ex1-a.

<table>
<tr><th>Property</th><th>Ex1-a</th><th>Ex1-b</th><th>Ex1-c</th></tr>
<tr><td>λ_α^a</td><td colspan="3">1.0</td></tr>
<tr><td>$E_\alpha[F/L^2]$</td><td colspan="3">250.0</td></tr>
<tr><td>$\eta_\alpha[F/L^2]$</td><td>0.0</td><td>5.0</td><td>5.0</td></tr>
<tr><td>$s_\alpha^u[F/L^2]$</td><td>79.06
$\downarrow_{\text{max}}$= 50%
vertical band</td><td>79.06
$\downarrow_{\text{max}}$= 60%
21.8°-inclined band</td><td>79.06
$\downarrow_{\text{max}}$= 50%
vertical band</td></tr>
<tr><td>$G_\alpha^f[F/L]$</td><td colspan="3">500.0</td></tr>
<tr><td>$A_\alpha[L^2]$</td><td colspan="3">0.01</td></tr>
<tr><td>$\overline{\phi}_\alpha$</td><td>±29.05°</td><td>±36.87°</td><td>±33.69°</td></tr>
<tr><td>$|\mathcal{F}_{\text{net}}|/|\Omega_\mu|$</td><td>0.2069</td><td>0.2994</td><td>0.2884</td></tr>
<tr><td>δ_p</td><td colspan="3">0.0</td></tr>
<tr><td>n_{fib}</td><td>180</td><td>432</td><td>384</td></tr>
</table>

Table 4 – Material, geometrical and numerical parameters for the cases in Study 1. $\downarrow_{\text{max}}$: maximum reduction.

2. Inclined weakened fibre band, macroscale gradient as in (6.7), denoted Ex1-b.

3. Vertical weakened fibre band, macroscale gradient as in (6.8), with $t_0 = 1.2$, denoted Ex1-c.

In all cases, the MCS is employed, and we take $[t_{min}, t_{max}] = [1.0, 1.5]$, with 100 equally spaced pseudo-time steps. For the definition of all parameters see Table 4 [8].

In Fig. 35, we can see the results obtained for the first study case. From Fig. 35a, it can be seen that a vertical localisation band is obtained as a result of the applied load and the geometrical distribution of the weakened material. This phenomenon is captured by the DBA, as seen in Fig. 35b, where the vertical red line indicates the critical time instant t_N. In the bottom right panel we have that $\theta(t_N) = 0$ and $\beta(t_N) = 0$, implying that the RVE specimen begins to localise in a mode-I of fracture. Also, notice that, due to the simplicity of the test, the critical point coincides with the maximum value of the normal traction that in this case coincides with the stress component $(\mathbf{P})_{11}$. This may not be the case in more complex settings.

For the second study case the results are displayed in Fig. 36. Here, a mixed model of fracture is obtained as a consequence of the inclination of the weakened band and the loading program, see Fig. 36a. This phenomenon is predicted by the DBA, where two distinct values of β and θ are found at the critical point (precisely $t_N = 1.26$) , as seen in the bottom-right inset in Fig. 36b. We can observe that the value predicted for $\theta(t_N)$ (precisely $= 24.12°$) agrees well with the angle of the inclined band (precisely $= 21.8°$, see

[8] For cases Ex1-b and Ex1-c numerical viscosity was needed (taken $\eta = 5.0F/L^2$) and was removed after 5 pseudo-timesteps once the critical point was attained.

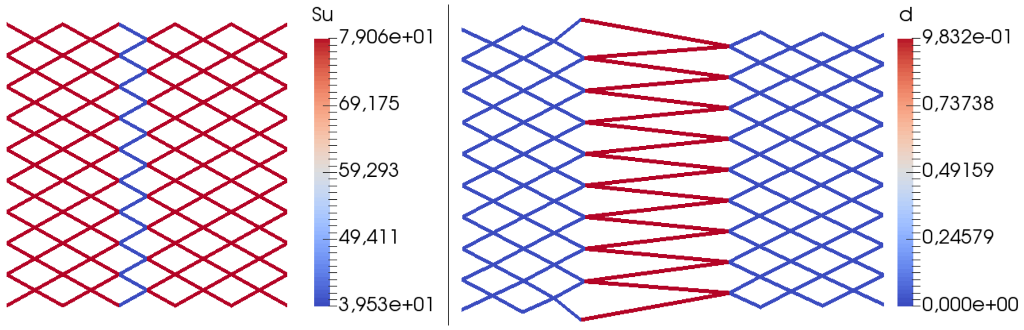

(a) Undeformed mesh displaying s_α^u distribution and deformed network showing the damage state d at $t = t_{max}$.

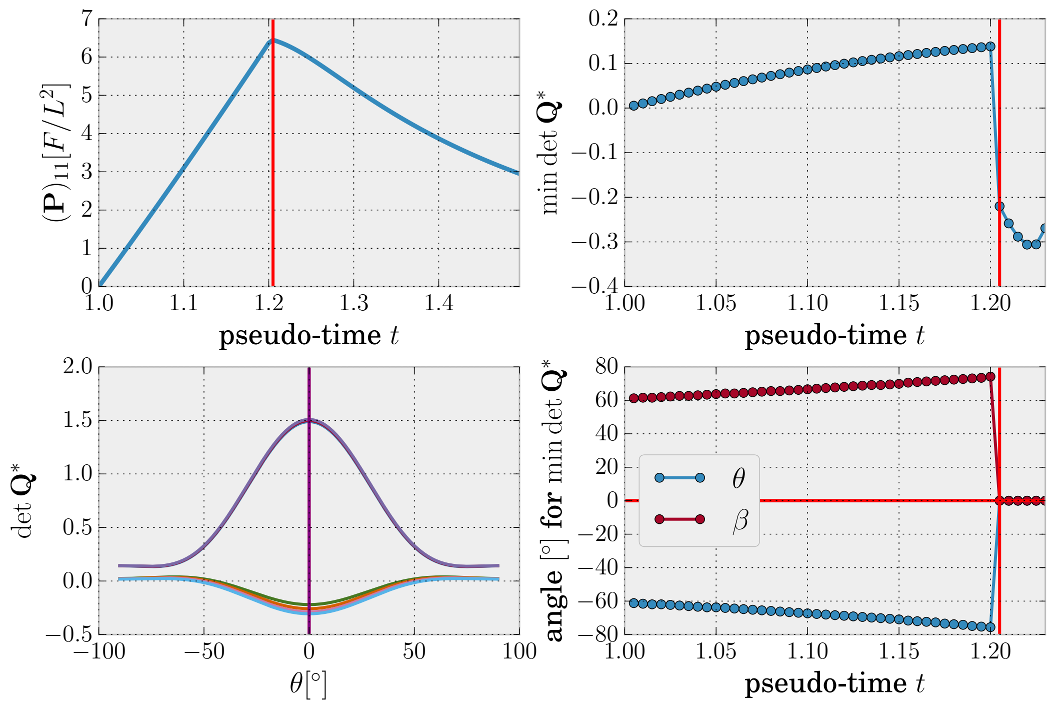

(b) DBA.

Figure 35 – Results of the study case Ex1-a.

Table 4). [9]. Regarding the prediction of $\beta(t_N)$ (precisely $= 13.32°$), this value is smaller than the inclination of the band but still larger than the direction established by the loading program. This confirms the expected result, since the direction of the crack-opening velocity is a consequence of these two factors combined. In addition, Fig. 36b presents the component $(\mathbf{P})_{11}$ of stress, which, because of the geometry, is presumably the most important in magnitude. Moreover, the softening behaviour greatly affects this component, whose peak almost coincides with the critical point detected by the DBA.

Finally, in the third study case, the situation is that illustrated in Fig. 37a, in which the localisation band appears as result of the applied shear loading. In the middle inset, it is shown the exact instant when the critical point is detected (precisely $t_N = 1.245$). Again,

[9] It is important to mention that the detected band inclination is comprised in the range of angles inside the finite band size induced by the domain with weakened properties.

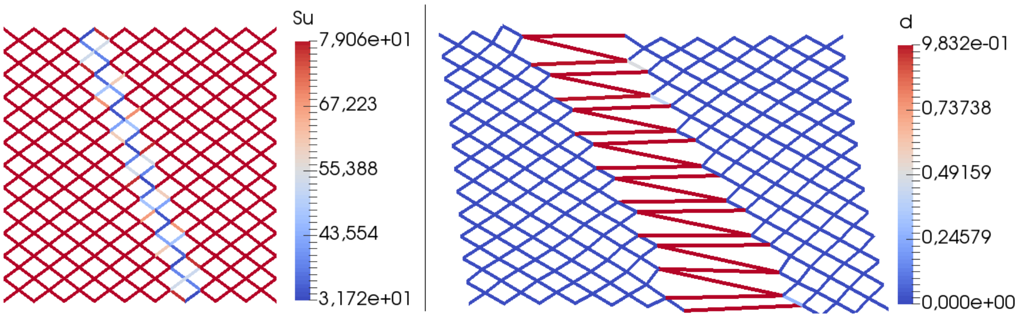

(a) Undeformed mesh displaying s^u_α distribution and deformed network showing the damage state at $t = t_{max}$.

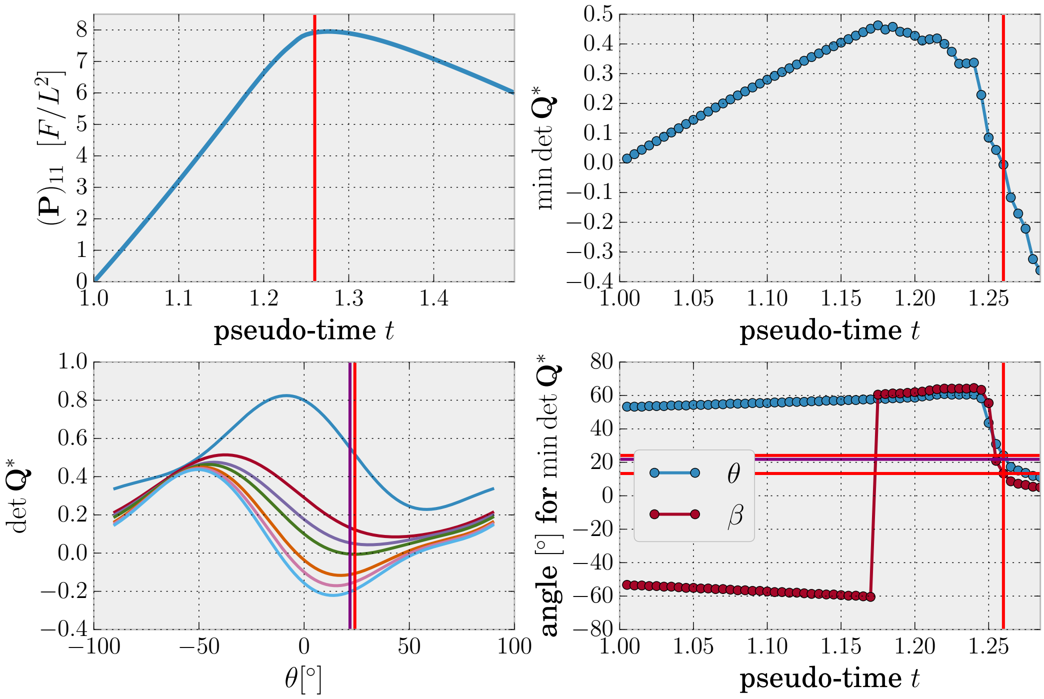

(b) DBA.

Figure 36 – Results of the study case Ex1-b.

the values detected for $\beta(t_N) = 30.6°$ and $\theta(t_N) = 55.44°$ at the critical point are distinct and not perpendicular (see middle-right panel in Fig. 37b), which characterises a mixed fracture mode. In the present situation, with two particular preferential directions of the fibre families, the localisation band is at an angle with respect to vertical. Interestingly, and although the normal of the band is not aligned with the horizontal direction, we observe that component $(\mathbf{P})_{11}$ still manifests the typical representation of the outcome of the DBA, therefore is the only component plotted.

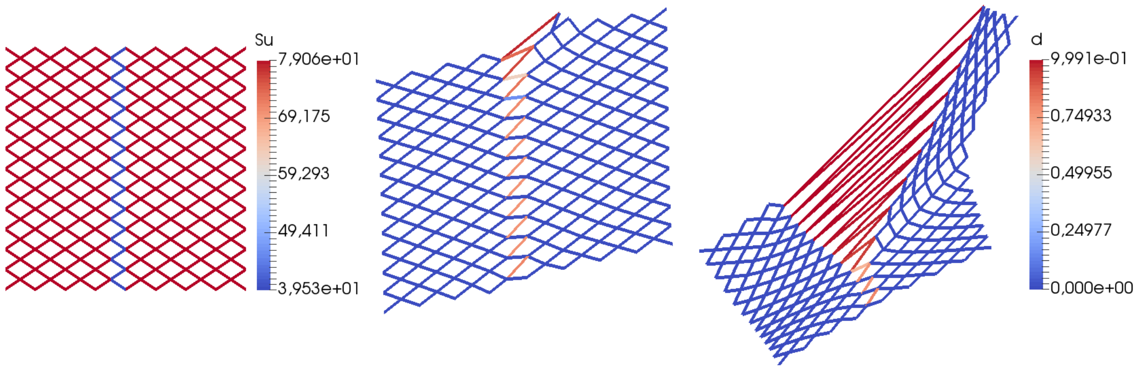

(a) From left to right: undeformed mesh displaying s_α^u distribution, deformed network showing the damage state d in the bifurcation instant, and in the last loading step.

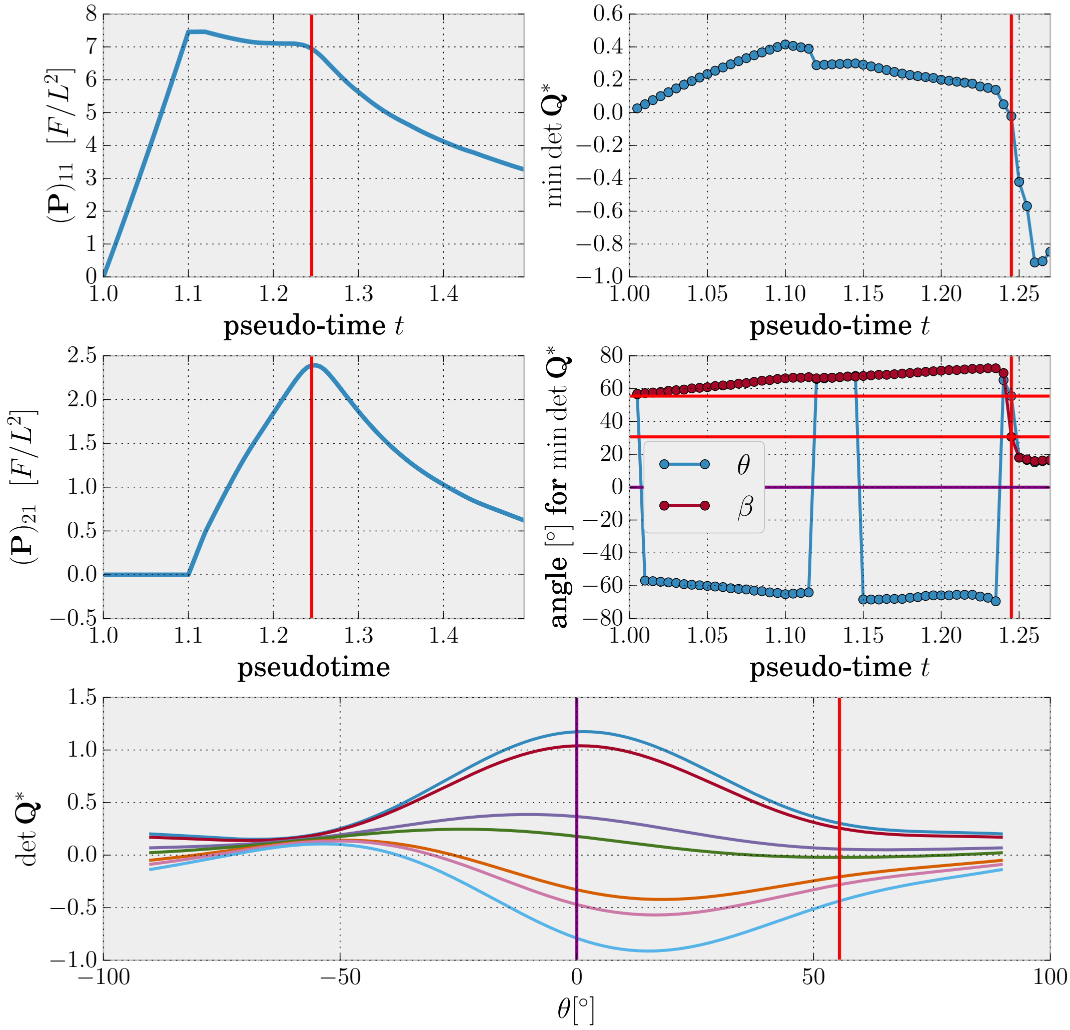

(b) DBA.

Figure 37 – Results of the study case Ex1-c.

6.2.2 Study 2: Sensitivity of critical point to boundary conditions

In this example we explore the influence of the choice of admissible fluctuations (i.e. the RVE boundary conditions) in the initiation of the localisation process. Specifically,

Property	Ex2-a	Ex2-b	Ex2-c
λ_α^a	1.0		
$E_\alpha[F/L^2]$	250.0		
$\eta_\alpha[F/L^2]$	20.0 (LBS) 0.1 (MCS)	20.0 (LBS) 5.0 (MCS)	20.0 (LBS) 10.0 (MCS)
$s_\alpha^u[F/L^2]$	79.06 $\downarrow_{\max}$= 40% inside the band	79.06 $\downarrow_{\max}$= 40% inside the band	79.06 $\downarrow_{\max}$= 40% inside the band
$G_\alpha^f[F/L]$	500.0		
$A_\alpha[L^2]$	$\mathcal{N}(\mu,\sigma) = \mathcal{N}(0.01, 0.0025)$		
$\overline{\phi}_\alpha$	$\pm 36.87°$	$\pm 36.87°$	$\pm 38.66°$
$\delta_p[L]$	0.04	0.02	0.0125
n_{fib}	192	432	768
$\lvert\mathcal{F}_{\text{net}}\rvert/\lvert\Omega_\mu\rvert$	0.2252		
Model	Both LBS and MCS		

Table 5 – Material, geometrical and numerical parameters for the cases in Study 2. $\downarrow_{\max}$: maximum reduction.

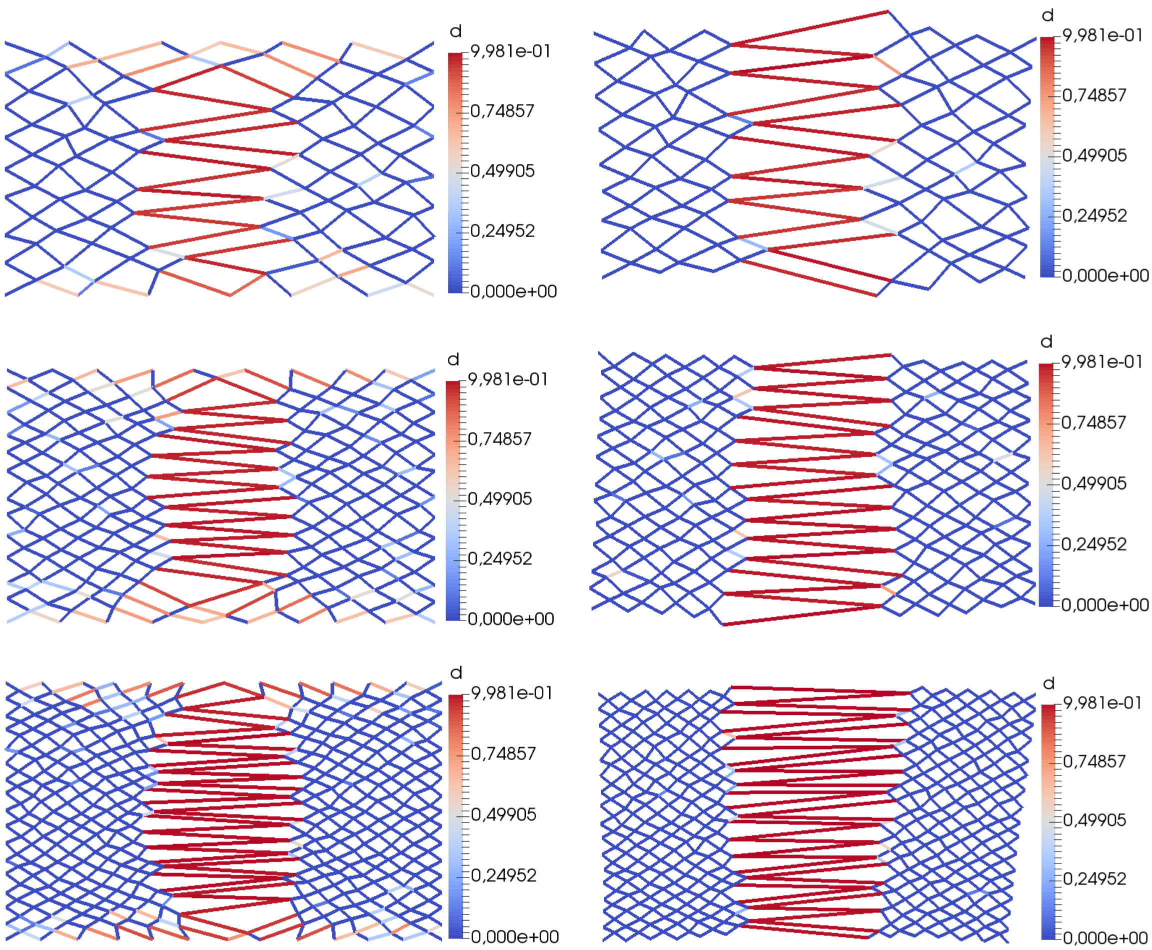

Figure 38 – Deformed state of fibre networks at the last step of the loading program. From top to bottom, cases Ex2-a to Ex2-c, with LBS (left) and MCS (right) being used.

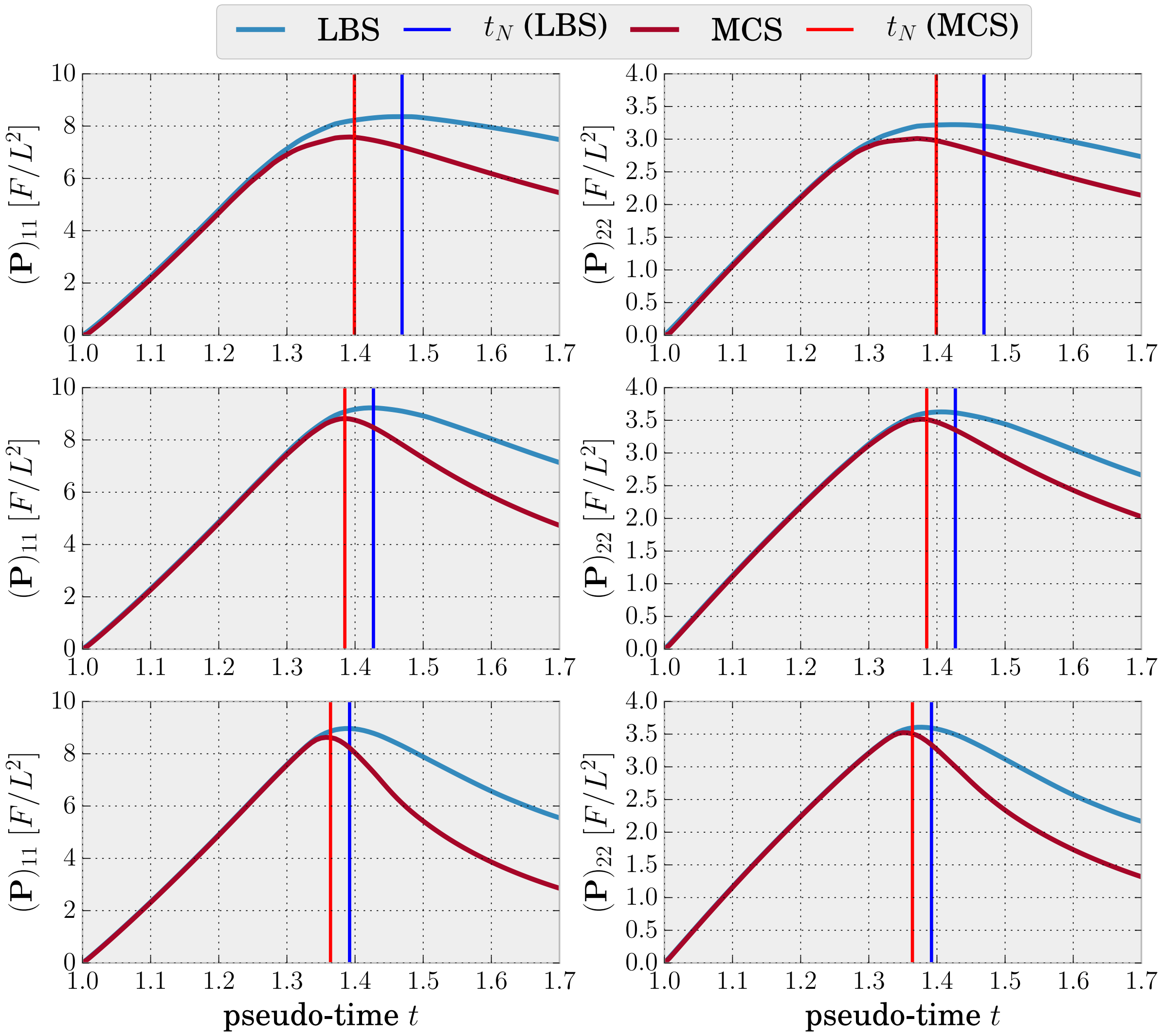

Figure 39 – Homogenised stress components throughout the loading program and critical points (vertical lines). From top to bottom: Ex2-a, Ex2-b and Ex2-c.

we analyse the MCS and LBS models. As we will see, the choice of boundary conditions severely affects the homogenised stress response, possibly delaying the appearance of the critical point.

We considered here three fibrous networks with a vertically weakened fibrous band in the middle of the RVE. Namely, we have the cases Ex2-a, Ex2-b and Ex2-c, with 192, 432 and 768 fibres each, respectively. The loading program is given by horizontal axial stretching, applied during $t \in [1.0, 1.7]$ in 100 equally spaced pseudo-time steps. Also, we have admitted some level of heterogeneity in the network parameters, namely: i) fibres areas follow a normal distribution $\mathcal{N}(\mu, \sigma)$, where μ stands for the mean value and σ for the standard deviation, and ii) the position of nodes in the network are randomly perturbed by a factor δ_p according to the number of fibres. Moreover, to circumvent the lack of convergence of the Newton-Raphson method, different values for the numerical viscosity ranging from 0.1 to 20.0 were employed as well as the SOR method with subrelaxation ranging from 0.7 to 0.8. The model parameters are reported in Table 5.

It is important to mention that the parameters of the normal distribution appearing in Table 5 are only used in the case Ex2-a. In cases Ex2-b and Ex2-c the same values were used just as an initial guess for fibre areas. Next, these areas were scaled accordingly in order to preserve the same volume fraction featured by case Ex2-a (note that the size of the RVE ($|\Omega_\mu|$) was kept unitary). This emulates the effect of increasing the size of the RVE. No matter the approach, this aims to render comparable results in terms of stresses, as shown in Fig. 39 and discussed in the following.

In Fig. 38 we report the deformed states for the three different cases of networks, each one being simulated with both the LBS and MCS multiscale models. For the LBS, the localisation band becomes more prominent as the number of fibres increases, and the bell-like shape can be considered an artifact caused by the overly constrained space of fluctuations over the RVE boundary. In contrast, the MCS features vertical localisation bands crossing entirely the RVE regardless the number of fibres.

Fig. 39 displays the components $(\mathbf{P})_{11}$ and $(\mathbf{P})_{22}$ of the homogenised stress tensor for the different models and for the different networks. The critical point is clearly delayed when considering LBS (blue curves), compared to the response delivered by model MCS (red curves). From top to bottom, as the number of fibres increases, the instant at which the critical point occurs is more sensitive when using the linear model. These results reveal another fundamental issue of multiscale models, the convergence of the mechanical response with respect to the size of the RVE [10]. Thus, we can assert that, in the present setting, model MCS delivers a more physically consistent solution than model LBS.

In the examples examined above, independently of the kind of boundary condition, we can appreciate from Fig. 39 that the shape of the post-critical mechanical response (curve after the vertical lines) strongly depends upon the RVE size. This is a manifestation of the well-known size-effect (BAZANT; PLANAS; BAZANT, 1998) and will be properly investigated and discussed in Section 6.2.4.

6.2.3 Study 3: Influence of heterogeneity

Heterogeneities (of all kinds) in the topological and material composition of fibre networks are the main sources of stress concentration, driving the damage processes and strain localisation phenomena. The study cases reported in this section aim to analise the effects of these factors. In the context of arterial tissues, heterogeneities can be originated by anomalous and non-uniform processes of growth and remodelling of collagen fibres, and so its study deserves special attention.

[10] As already commented, this is equivalent to increasing the number of fibres for the same size of the RVE, but scaling fibre areas in order to have comparable volume fractions.

Property	Ex3A-a	Ex3A-b
λ_α^a	1.0	
$E_\alpha[F/L^2]$	250.0	
$\eta_\alpha[F/L^2]$	0.0	10.0
$s_\alpha^u[F/L^2]$	79.06	
$G_\alpha^f[F/L]$	500.0	
$A_\alpha[L^2]$	0.01 $\downarrow_{\max}$= 40% band thickness 0.2	0.01 $\downarrow_{\max}$= 40% ($\times$2) ball radius 0.2
$\overline{\phi}_\alpha$	$\pm 33.69°$	
$\delta_p[L]$	0.02	
n_{fib}	600	

Table 6 – Material, geometrical and numerical parameters for all cases in Study 3 concerning fibre area reduction. $\downarrow_{\max}$: maximum reduction.

Particularly, we consider, heterogeneities of the following kinds:

1. Reduction of fibre areas in a certain region: In case Ex3A-a the perturbation in the fibre area is introduced in a vertical band whereas in case Ex3A-b such perturbation is introduced on two ball-shaped regions located in the upper-central part of the RVE. In both cases, damage threshold stress s_α^u is the same for all fibres. The model parameters data are found in Table 6.

2. Non-homogeneous spatial distribution of fibres: we induce a controlled and uneven spatial distribution by removing a percentage of fibres located in a region of the RVE. Particularly, we have considered vertical bands with width $0.3L$ (Ex3R-a) and $0.6L$ (Ex3R-b) centered with the RVE, in which, respectively, 10% and 5% of fibres were randomly selected to be removed. In each case, two realisations were simulated. Also, damage threshold stress s_α^u is the same for all fibres. Table 7 presents all model parameters.

As in the previous example, the RVE was stretched in the horizontal direction with $t \in [1.0, 1.6]$. Due to the larger sources of heterogeneities, numerical parameters for these simulations had to be carefully chosen in order to avoid poor or even lack of convergence of the Newton-Raphson method as well as to capture the more complex mechanical behaviour with more accuracy. In addition to fictitious viscosity and the SOR method, we have used an adaptive selection of the pseudo-time step, refining the time-discretisation near singular points (zero-derivative of stress) and at high gradient regions. In total, for all simulations of this study, 1000 pseudo-time steps have been used, with a maximum ratio between the largest and smallest steps of 20.0.

Property	Ex3R-a (k=1)	Ex3R-a (k=2)	Ex3R-b (k=1)	Ex3R-b (k=2)
λ_α^a	1.0			
$E_\alpha[F/L^2]$	250.0			
$\eta_\alpha[F/L^2]$	5.0	5.0	10.0	6.0
$s_\alpha^u[F/L^2]$	79.06			
$G_\alpha^f[F/L]$	500.0			
$A_\alpha[L^2]$	0.01			
$\bar{\phi}_\alpha$	$\pm 35.84°$			
$\delta_p[L]$	0.01			
n_{fib}	936			
Removal criterion	random 10% of fibres band thickness $0.3L$		random 5% of fibres band thickness $0.6L$	

Table 7 – Material, geometrical and numerical parameters for all cases in Study 3 concerning removal of fibres. Variable (k) is used to identify the realisation.

The obtained results are presented in Fig. 40 and Fig. 41. It is seen that the different cases of heterogeneous fibre areas yield similar homogenised mechanical responses in the pre-critical stage. In detail, since the region between the balls features fibres with larger area values, the total localisation in this case is slightly delayed (see the blue and red vertical lines in Fig. 41). This delay not only affects the critical point position but also the evolution of damage in the subsequent increments as depicted in the third row of Fig. 40. Notwithstanding this, both study cases provide a similar homogenised behaviour, quantitatively and qualitatively, in terms of the critical point and the constitutive response, for both stress components, $(\mathbf{P})_{11}$ and $(\mathbf{P})_{22}$.

Let us now analyse the cases Ex3R-a and Ex3R-b. From Fig. 42 and Fig. 44 we notice that the nucleation of localisation bands occurs by traversing the (randomly determined) regions in the RVE with reduced fibre density. This source of heterogeneity strongly affects the configuration of the deformed network for the different realisations. In addition, and as expected, the less concentrated is the remotion of fibres from the RVE (case Ex3R-b seen in Fig. 44 compared to Ex3R-a in Fig. 42) the more complex the localisation pattern that emerges in the RVE. These sources of heterogeneity affect differently the homogenised response. As seen in Fig. 45, the study cases denoted by Ex3R-b feature a more sensitive response along the whole loading program. Comparatively, the response obtained in the study cases Ex3R-a seen in Fig. 43 only features some differences during the post-critical stages. In either case, the directions of the nucleated macroscale crack obtained from the DBA remain the same.

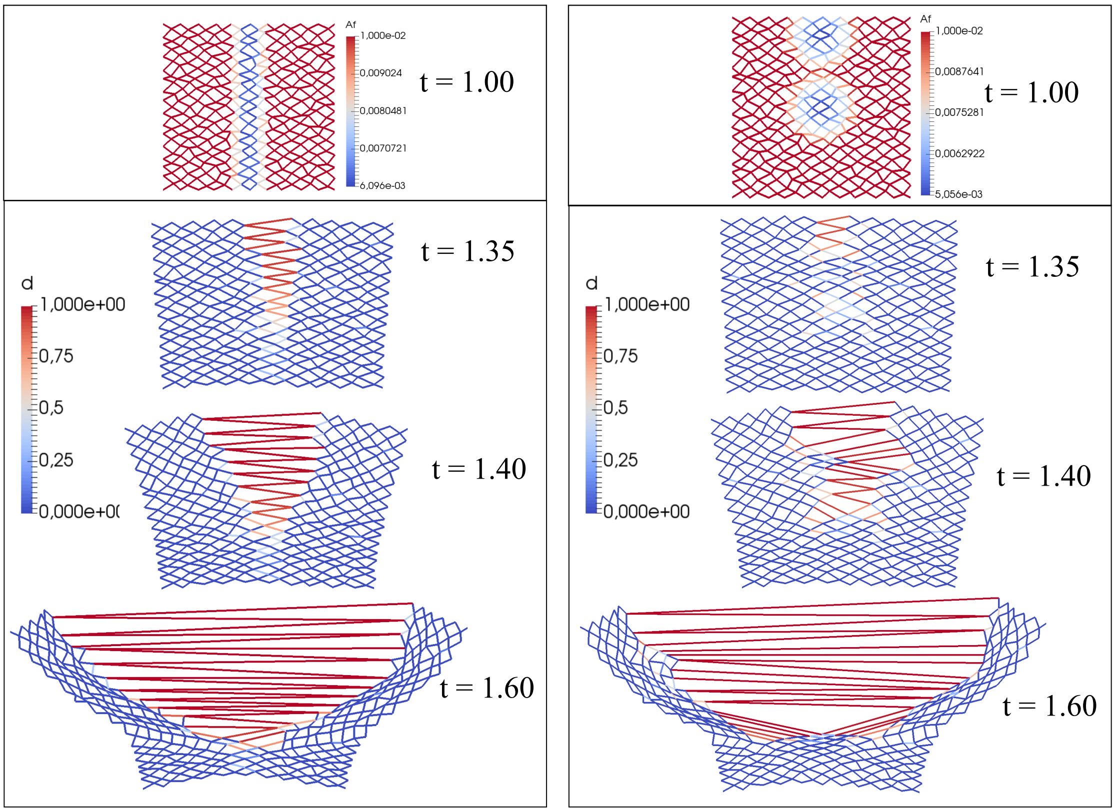

(a) Case Ex3A-a. (b) Case Ex3A-b.

Figure 40 – Different snapshots of the network of fibres for cases Ex3A-a and Ex3A-b displaying distribution of fibre area (upper frame) and deformed configuration for different states of material deterioration.

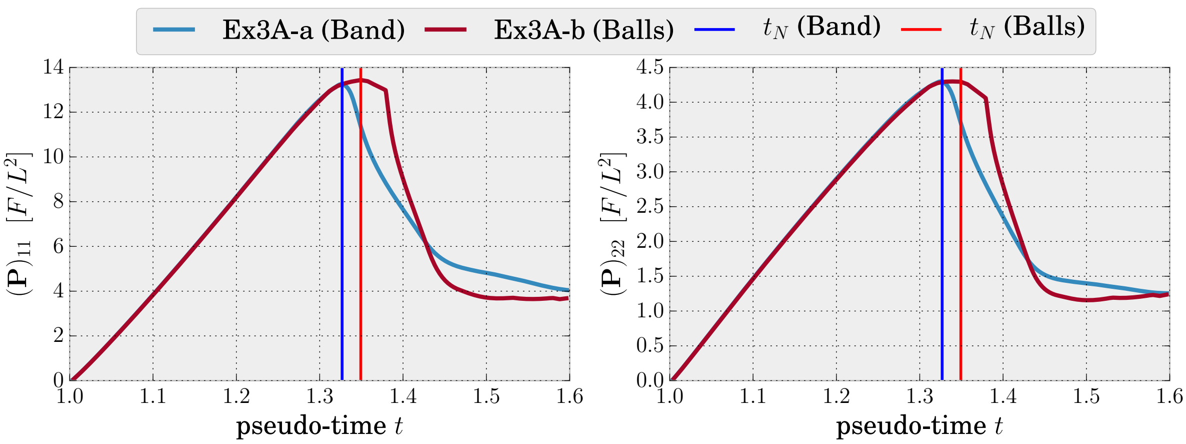

Figure 41 – Homogenised stress components throughout the loading program and critical points for Ex3A-a (band) and Ex3A-b (balls).

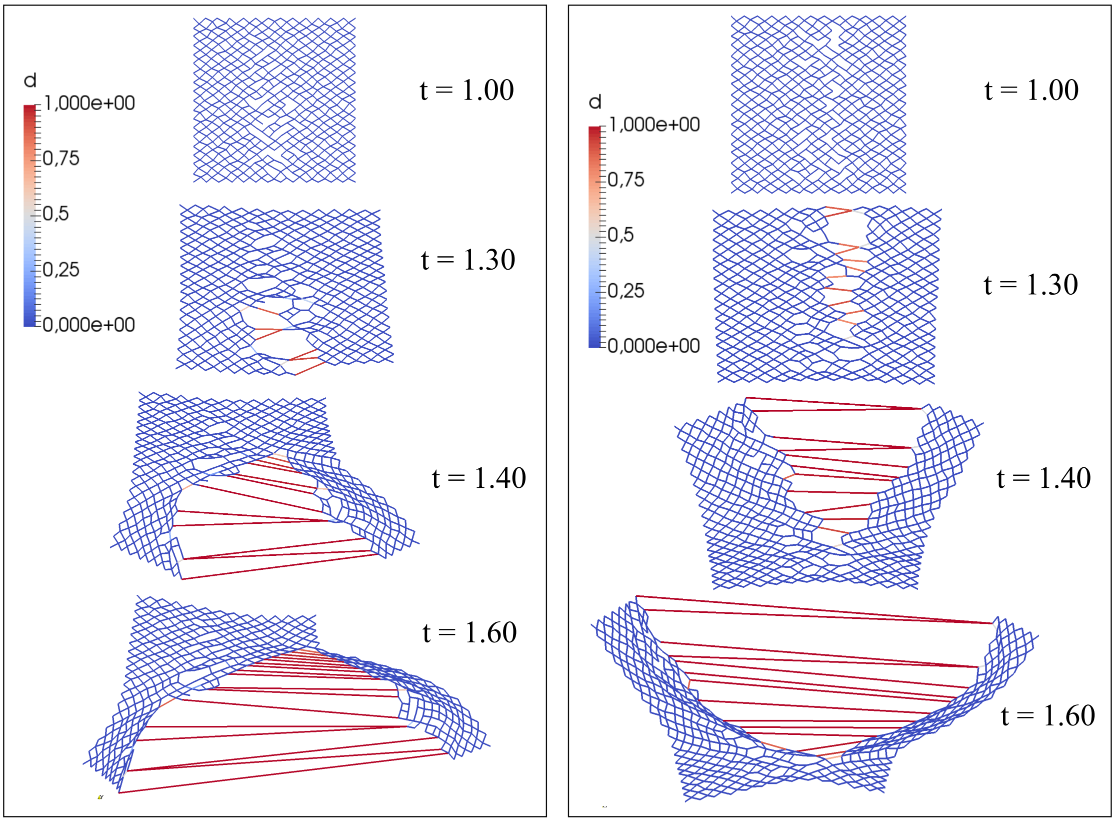

(a) Case Ex3R-a(k=1).

(b) Case Ex3R-a(k=2).

Figure 42 – Different snapshots of the network of fibres for different realisations in the case Ex3R-a.

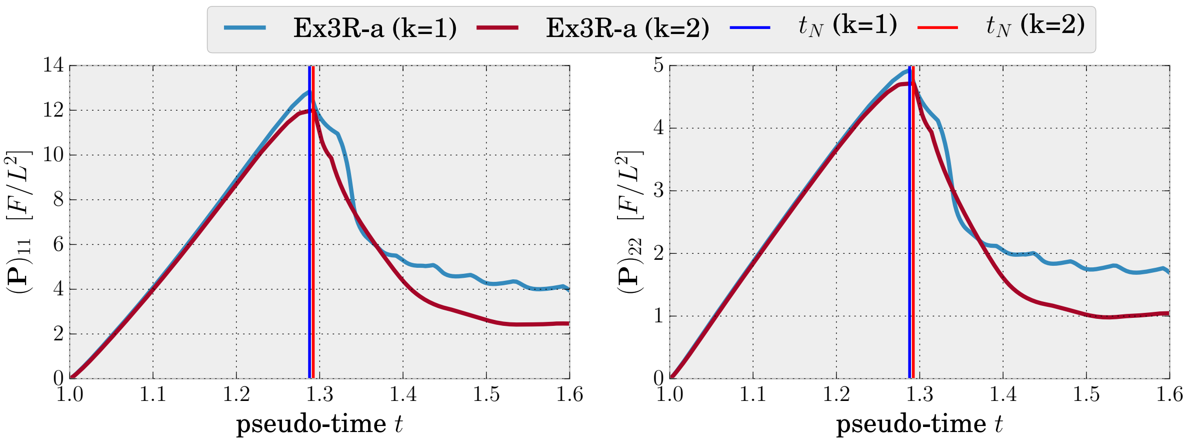

Figure 43 – Homogenised stress components throughout the loading program and critical points for different realisations of the case Ex3R-a.

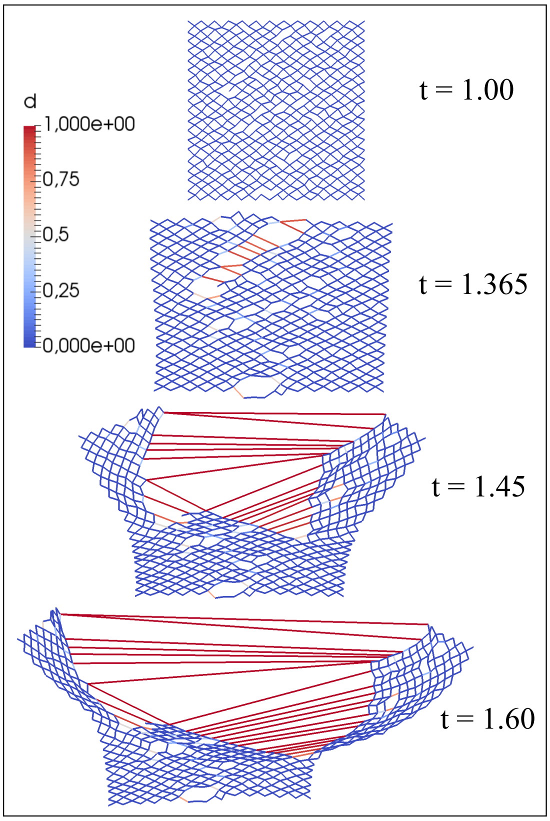

(a) Case Ex3R-b(k=1).

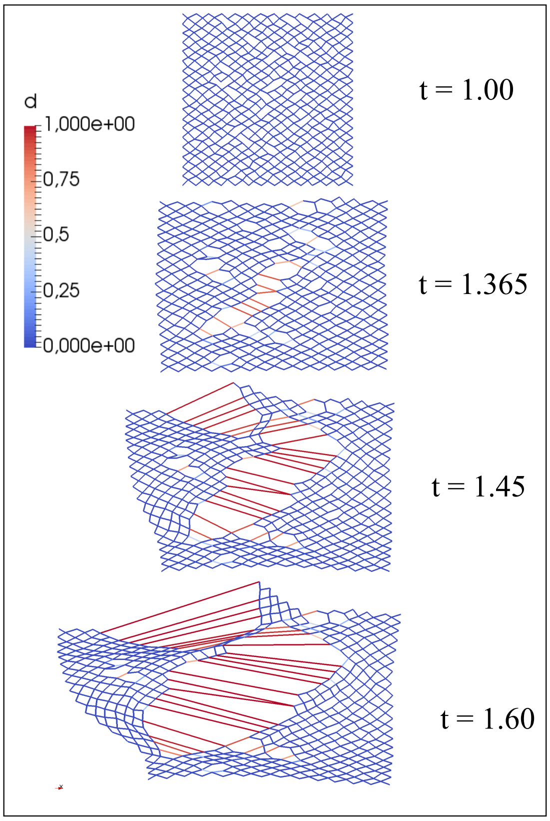

(b) Case Ex3R-b(k=2).

Figure 44 – Different snapshots of the network of fibres for different realisations in the case Ex3R-b.

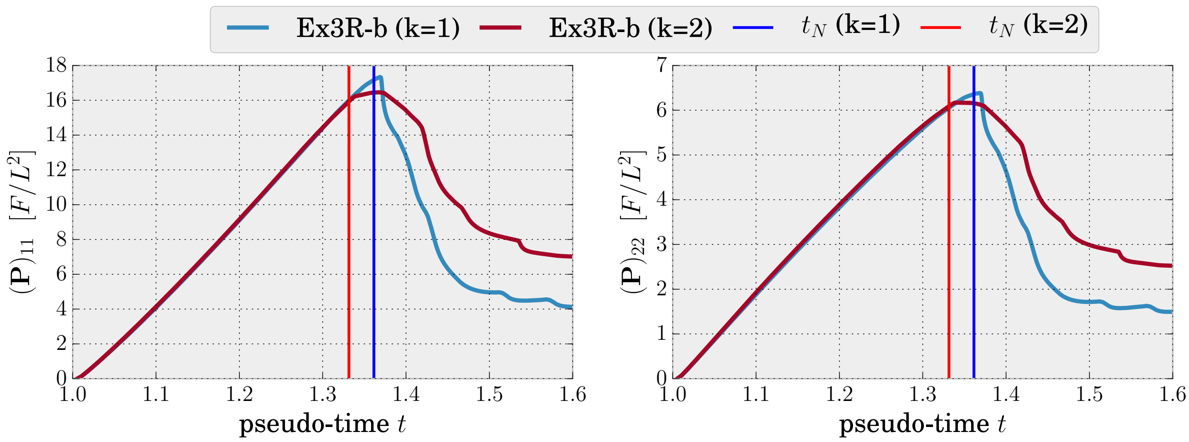

Figure 45 – Homogenised stress components throughout the loading program and critical points for different realisations in the case Ex3R-b.

6.2.4 Study 4: Size-effect during the post-critical regime

In this section, we study the size-effect observed in the homogenised RVE stress response during the post-critical regime, that is after the DBA points out the nucleation of a macroscale crack as a result of the microscale localisation bands.

Property	Ex4V-a	Ex4V-b
λ_α^a	1.0	
$E_\alpha[F/L^2]$	250.0	
$\eta_\alpha[F/L^2]$	10.0	5.0
$s_\alpha^u[F/L^2]$	79.06 $\downarrow_{\text{max}}$= 40% one vertical band	79.06 $\downarrow_{\text{max}}$= 40% two vertical bands
$G_\alpha^f[F/L]$	500.0	
$A_\alpha[L^2]$	$\mathcal{N}(\mu,\sigma) = \mathcal{N}(0.01, 0.0025)$	
$\overline{\phi}_\alpha$	$\pm 36.87°$	
$\delta_p[L]$	0.02	
n_{fib}	432	864
RVE size $[L^2]$	1×1	2×1
$\lvert\mathcal{F}_{\text{net}}\rvert/\lvert\Omega_\mu\rvert$	0.3359	0.3364

Table 8 – Material, geometrical and numerical parameters for all cases with a vertical band in Study 4. $\downarrow_{\text{max}}$: maximum reduction.

Property	Ex4I-a	Ex4I-b
λ_α^a	1.0	
$E_\alpha[F/L^2]$	250.0	
$\eta_\alpha[F/L^2]$	10.0	10.0
$s_\alpha^u[F/L^2]$	79.06 $\downarrow_{\text{max}}$= 40% one 21.8°-inclined band	79.06 $\downarrow_{\text{max}}$= 40% two 21.8°-inclined bands
$G_\alpha^f[F/L]$	500.0	
$A_\alpha[L^2]$	$\mathcal{N}(\mu,\sigma) = \mathcal{N}(0.01, 0.0025)$	
$\overline{\phi}_\alpha$	$\pm 36.87°$	
$\delta_p[L]$	0.02	
n_{fib}	432	864
RVE size $[L^2]$	1×1	2×1
$\lvert\mathcal{F}_{\text{net}}\rvert/\lvert\Omega_\mu\rvert$	0.3367	0.3364

Table 9 – Material, geometrical and numerical parameters for all cases with an inclined band in Study 4.

Hence, in this section we study the homogenised response of the RVE when its size is modified. Specifically, we double the RVE size in the horizontal direction by repeating its structure. The source of material heterogeneity is considered to be in the fibre damage threshold stress s_α^u, located in vertical (Ex4V-a and Ex4V-b, see Table 8) and inclined bands (ExI-a and ExI-b, see Table 9) inside the RVE. When the RVE is doubled, the band with altered properties is also repeated correspondingly. Regarding the imposed macroscale gradient, in all cases we consider progressive axial stretching, with $t \in [1.0, 2.0]$ discretised in 100 pseudo-time steps.

Fig. 46 shows, for a single realisation, the deformed state of the different RVEs. Clearly, after the bifurcation instant, the localisation occurs just in one of the bands, and, thus, the whole strain applied to the RVE is confined to the same region of space. In turn, the stress is homogenised using the whole size of the RVE. This implies that, during the post-critical regime, for the same level of the inserted macroscale strain, the larger RVE will have a larger crack opening, resulting in an apparently more brittle material, i.e., strain localisation is more severe. This behaviour can be noticed in Fig. 47. In such figure, the RVEs deliver the same response in the pre-critical stages regardless the RVE size. When the critical point is achieved, the localisation has become prominent, and the homogenised behaviours deviate from each other, highlighting the lack of objectivity of the stress response at post-critical instants. Although beyond the scope of this thesis, methodologies applied to circumvent this in continua are commented in Section 6.2.5.

6.2.5 Discussion

The multiscale model presented in this section is strictly valid for the pre-critical regime and up to the critical point signaled by the DBA. Moreover, the model provides a sound criterion (discontinuous bifurcation analysis) for the determination of the instant at which the material deterioration in the microscale has reached such a level that a macroscale crack must be nucleated to recover well-posedness of the macroscale mechanical problem. Once the critical point has been identified by the DBA, it is widely known that homogenisation strategies relying on the average of microscale stress-like entities throughout the entire RVE yields non-objective responses. More specifically, and as seen in the numerical experiments reported in this work, the post-critical effective response, obtained from traditional homogenisation procedures, in such cases depends on the size of the RVE (SÁNCHEZ et al., 2013). The development of a multiscale model capable of recovering an objective response in the post-critical regime is a matter of current research. This problem can be addressed by an appropriate generalisation of the insertion and kinematical homogenisation operators in the post-critical regime (BLANCO et al., 2014; BLANCO et al., 2016), resulting in different homogenisation procedures for the microscale stress as proposed in (SÁNCHEZ et al., 2013; TORO et al., 2016; BLANCO et al., 2014; BLANCO et al., 2016).

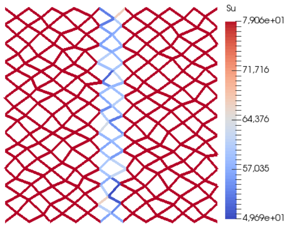

(a) RVE with vertical band.

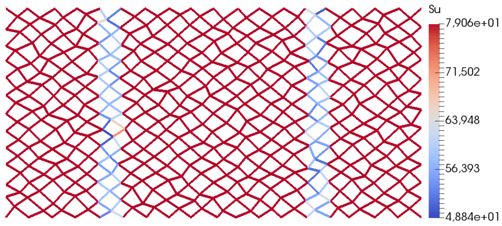

(b) Doubled RVE with vertical bands.

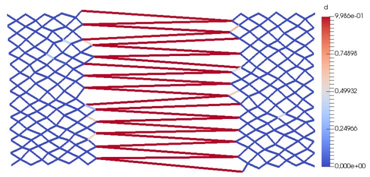

(c) RVE with vertical band after bifurcation.

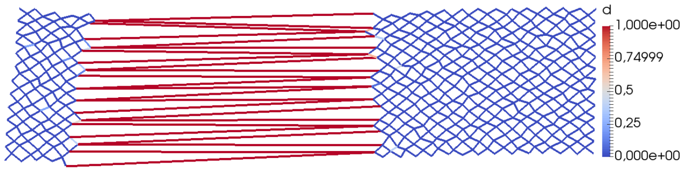

(d) Doubled RVE with vertical bands after bifurcation.

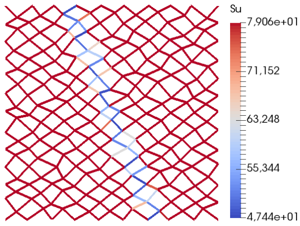

(e) RVE with inclined band.

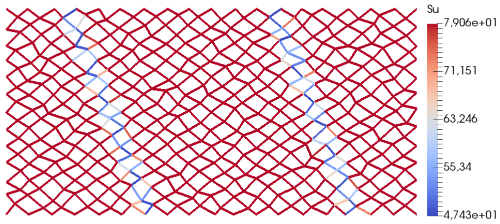

(f) Doubled RVE with inclined bands.

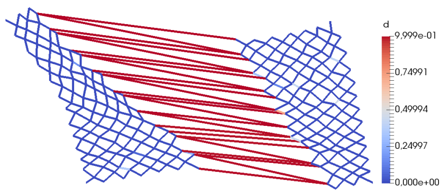

(g) RVE with inclined band after bifurcation.

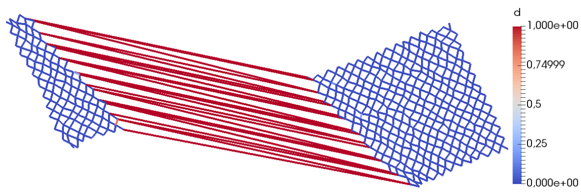

(h) Doubled RVE with inclined bands after bifurcation.

Figure 46 – Initial and final configurations for fibre networks of Study 4.

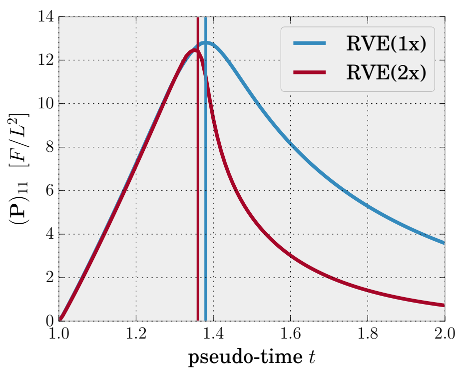

(a) Vertical band Ex4V.

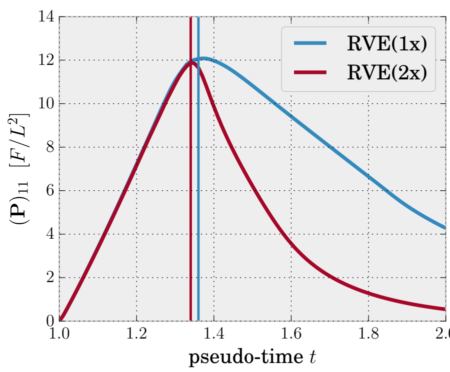

(b) Inclined band Ex4I.

Figure 47 – Homogenised stress responses showing the lack of objectivity in the mechanical response during the post-critical regime.

6.3 Closing Remarks

As already mentioned, this chapter was devoted to present the application of the framework developed in this thesis in some representative numerical experiments. Numerical simulations of Section 6.1 are related exclusively to Chapter 4 and can be found in the contribution (ROCHA et al., 2018). In turn, Section 6.2 demonstrated the theory developed in Chapter 5, subject of another contribution in (ROCHA et al., 2019).

Despite of the differences between the models MCS and LBS appreciated throughout the several computational experiments presented in this chapter, it is important to remark that both models are able to characterise the universe of possible solutions attainable through this kind of homogenisation procedures. Although no formal proof has been presented, MCS and LBS are respectively good candidates to be regarded as lower and upper bounds of the constitutive response (HILL, 1965) (we have discarded from this comparison the Taylor or rule of mixtures model).

In the context of the last part of this chapter, the use of the minimally constrained kinematical model enabled the localisation phenomena occurring at the microscale to reach the boundary and naturally give rise to visible localisation bands which, ultimately, are manifested at the macroscale through the prediction delivered by the discontinuous bifurcation analysis. More specifically, the proposed model allowed us to simulate the development of straight and inclined localisation bands, as well as the simulation of the effects of random heterogeneities in both the microscale mechanical state and the resulting homogenised response. Furthermore, it has been possible to evaluate the sensitivity of the material response to the presence of microscale regions with marked altered conditions.

7 Conclusion

Now this is not the end. It is not even the beginning of the end. But it is, perhaps, the end of the beginning.

Winston Churchill

This chapter is devoted to present some final remarks. Those addressing the contribution of the thesis are discussed in Section 7.1, those concerning the limitations of the work are presented in Section 7.2 followed by some comments about viability of multiscale simulations in Section 7.3. Finally, in Section 7.4 we briefly present some further branches of research that can be derived from this thesis.

7.1 On the contributions of the thesis

In this work, we presented the theoretical bases of a multiscale model to simulate material failure in fibrous materials. As well, we exhaustively analysed, through several numerical examples, the homogenised material response of networks of fibres targeting an improved representation of the mechanical environment unfolding at fine scales in rather general and complex mechanical settings, based on those found in arterial tissues. Models of the present type have the potential to analyse trends in mechanical behaviour of fibrous tissues in situations where fibre properties, including their spacial distribution, may be affected, for instance, by pathological conditions in the case of arterial tissue. Studies of this type may provide important clues as to the causes and potential consequences of pathologically-induced variations in fibre properties.

Looking at the specific contribution of Chapter 3, we have successfully extended the classical multiscale theory of solids to consistently address a more challenging scenario, i.e., for those RVEs featuring voids reaching the RVE boundary. In addition, we have also shown that the proposed minimally constraining boundary condition is equivalent to setting a uniform traction model. By using an analysis based on Lagrange Multipliers we have shown that in a purely constitutive model the reaction force originated by relaxing the constraint of zero-average fluctuation is zero, which demonstrates that the model is mechanically self-equilibrated, and thus consistent. Furthermore, the resulting candidate for the lower bound for the homogenised mechanical response is of great theoretical and practical interest, specially for the strain localisation problems as seen in Chapter 6.

With regards to the contribution of Chapter 4, it mainly consists in a rigorous and general derivation of the micromechanical equilibrium problem as well as of the homogenisation formula for the dual stress entity from a minimum set of basic kinematical hypotheses and through the use of the MMVP. Similarly to the model of porous RVEs, we have derived the minimally kinematically constrained model, which has been shown to be, through numerical examples of Chapter 6, a lower bound for the mechanical response. Moreover, the resulting homogenised response has shown to be sensitive to the presence of heterogeneities in the arrangement of fibres as well as to the choice of the multiscale model (i.e. choice of boundary conditions). It is worthwhile to mention that the proposed model can directly be implemented in 3D, as already demonstrated in Section 6.1.2.

Related to the contribution of Chapter 5, a new ingredient of this work is the analytical derivation of the fourth-order homogenised tangent, thus completing, together with the homogenised stress, a complete constitutive multiscale toolbox to be used in a fully-coupled multiscale scheme. An important subproduct obtained from the tangent tensor is the evaluation of the model loss of strong ellipticity via the acoustic tensor properties as described in Section 5.8. This method has been shown to be effective also in the present context in which we deal with a network of fibres, allowing the determination of the critical instant as well as the crack orientation and the instantaneous initial crack-opening velocity. Such characterisation is fundamental in the sense that these data are required for the simulation of the mechanical equilibrium at the macroscale continuum in the scenario of a strong discontinuous kinematics. Finally, simulations featuring strain localisation have been shown to yield a more realistic deformation pattern in the cases which the MCS was employed, in contrast to the artificial deformation patterns observed when the LBS was used.

7.2 Limitations

In the construction of the microscale kinematics, we have neglected phenomena related to some deformation modes the fibres may be subjected to. Bending and torsion are two examples as well as the interaction among fibres at junctions. Particularly, inter-fibre sliding, and torsional resistance of junctions as a consequence of fibre interactions are two examples which could provide an even more heterogeneous micro-mechanical phenomenology. Related to that, the so-called interlock effect among fibres is investigated by (DURVILLE et al., 2018), and references therein, where interactions caused by frictional contact are incorporated to address the problem. Particularly, inter-fibre sliding mechanisms have been modelled in (NADY; GANGHOFFER, 2016) by using auxiliary beams in the contact. Bending phenomena and torsional resistance of junctions have been partially addressed in (STYLIANOPOULOS; BAROCAS, 2007a). Even in the bending dominated range, it is possible to refine the fibre strain energy to indirectly model the crimp effect, as proposed in (GRYTZ; MESCHKE, 2009; SHEARER, 2015; MARINO; WRIGGERS, 2017). Nevertheless, in such work it has been shown that for physiological ranges of stretches, fibre stretching continued to play the most important role in the constitutive response. Based on this, the proposed model is suitable for biomedical application, and, moreover, it constitutes a general and consistent multiscale formalism which enables more kinematical complexities to be incorporated in order to test further hypotheses. In contrast, (BERKACHE et al., 2017) introduce a parameter representing the ratio between bending and axial stiffnesses to establish a transition where the response is dominated by bending or by axial tension.

Considering the theoretical suitability of the multiscale approach, we highlight that the present work focused on the coupling between a fibrous network and a standard continuum. When the hypothesis of scale separation is questionable, and size-effects are important, the model must be improved in order to capture a more complex phenomenology (FOREST; TRINH, 2011; TRINH et al., 2012). However, even in the context of higher-order continua, or fracture mechanics, the MMPV has proven to be a suitable tool for the development of effective multiscale models (BLANCO et al., 2016; SÁNCHEZ et al., 2013), by providing the characterisation of the minimally constrained kinematically admissible space in which the generalised Hill-Mandel principle has to be regarded. These issues have been addressed in fibrous materials by the works of (NADY; GANGHOFFER, 2016; BERKACHE et al., 2017).

7.3 Towards truly multiscale simulations

Truly multiscale simulations are those simulations in which the macroscale and microscale realms somehow interact to solve the macroscale equilibrium problem. From the numerical point of view, whenever the use coupled multiscale simulations (also called FE^2 (FEYEL; CHABOCHE, 2000b)) are to be conducted in the context of finite element procedures, the computational cost involved poses a challenge to be addressed. Within the context of a Newton scheme for the linearisation of the macroscale equilibrium problem, the application of the present multiscale approach requires, for each Newton iteration, and throughout the whole loading program, the determination of the stress and the tangent operator at each Gauss point. Besides, the assembly of the macroscale stiffness matrix and load vector through the solution of these microscale problems constitutes an inherently parallel process which requires an efficient management of the computational resources at hand. Currently, this is only possible if high performance computing facilities are available and several computationally efficient implementations have been proposed to mitigate costs (LOPES; PIRES; REIS, 2018; MATSUI; TERADA; YUGE, 2004; MOSBY; MATOUS, 2015; MOSBY; MATOUS, 2016).

One possible approach, appealing in the context of materials whose response is independent from the loading program, is the off-line construction of a database for the constitutive response, depending upon a number of parameters, which can be reduced by some technique as in (TEMIZER; ZOHDI, 2007; ZAGHI et al., 2018), or even relying on more sophisticated approaches of dimensionality reduction as in (YVONNET; HE, 2007; HERNÁNDEZ et al., 2014). This mapping could then be stored and accessed during on-line computations, drastically reducing the computational cost to practically the same burden than single-scale simulations. More specifically, for nonlinear inelastic constitutive laws (e.g. history-dependent materials), as the situation of the present work, few extensions of the database approach are available. For instance, (OLIVER et al., 2017) exploits the dimensionality reduction approach as in (HERNÁNDEZ et al., 2014) but applying it just to the elastic part of the domain, restricting the on-line simulations of the inelastic regime just to a small part of the domain. Approaches like this deserve further investigations to facilitate the use of multiscale models in more realistic applications. Finally, it is important to mention that in many cases there are reliable phenomenological constitutive laws which require the definition of model parameters. Then, it is possible to use homogenisation procedures in the form of an in-silico mechanical testing machinery to fit these material parameters, as carried out in (SPEIRS; NETO; PERIĆ, 2008).

7.4 Further perspectives

Based on what has been exposed above, we point out some topics that deserve a special attention in future:

- Implementation of a robust software infrastructure enabling fully coupled simulations (FE^2) taking advantage as much as possible of most modern distributed and parallel computer architectures. We do not expect that the pure application of this approach will ultimately, and massively, be used in practice, but it may guide the suitability evaluation of less computational demanding approaches, by comparison with this gold standard.

- Regularisation of multiscale model after the critical point is detected, by recovering the objectivity of the mechanical response by respect the RVE size. The work of (SÁNCHEZ et al., 2013), in continuum RVEs, may guide the extension of the multiscale model.

- Once a regularised model is available, it makes sense to use the multiscale modelling also for simulating the entire fracture process, i.e., finite element technologies that enable the modelling of strong discontinuous kinematics can be implemented. Examples of these methodologies are XFEM (MOËS; DOLBOW; BELYTSCHKO, 1999; BELYTSCHKO; BLACK, 1999) and the EFEM (OLIVER, 2004).

- Uncertainty quantification analysis to evaluate the impact of the uncertainties in the several model parameters, such as: morphology of the fibre networks, material parameters of the each fibre, initial state of degradation of each fibre, etc.

- Construction of truly biologically inspired RVEs for arterial wall and the experimental validation with the proposed methodology.
- Enrichment of the models concerning the individual fibre behaviour, e.g., bending consideration, and also at the level of the fibre network, e.g., inter-fibre sliding, fibre contact, torsional springs, etc.
- Modelling of mechanobiology phenomena applied to fibrous tissues, i.e., growth and remodelling of fibres. Note that such phenomena are in a different time scale, and thus an adequate treatment of this new scenario should developed.
- Exploit the concepts of dimensionality reduction and/or machine learning techniques applied to simulation of history-dependent materials, by using the simulations of microscale model to provide the necessary input and first principles for these approaches.
- Exploit high-order continuum theories, since the presence of the fibres leads to non-local effects, the hypothesis of scale separation is debatable.

Bibliography

BALAY, S. et al. *PETSc Web page*. 2018. <http://www.mcs.anl.gov/petsc>. Disponível em: <http://www.mcs.anl.gov/petsc>. Citado na página 126.

BALZANI, D.; BRINKHUES, S.; HOLZAPFEL, G. A. Constitutive framework for the modeling of damage in collagenous soft tissues with application to arterial walls. *Computer Methods in Applied Mechanics and Engineering*, Elsevier B.V., v. 213-216, p. 139–151, 2012. ISSN 0045-7825. Disponível em: <http://dx.doi.org/10.1016/j.cma.2011.11.015>. Citado 4 vezes nas páginas 24, 25, 105, and 111.

BAZANT, Z.; PLANAS, J.; BAZANT, Z. *Fracture and Size Effect in Concrete and Other Quasibrittle Materials*. [S.l.]: CRC Press, 1998. Citado na página 153.

BELYTSCHKO, T.; BLACK, T. Elastic crack growth in finite elements with minimal remeshing. *International Journal for Numerical Methods in Engineering*, John Wiley & Sons, Ltd., v. 45, n. 5, p. 601–620, 1999. ISSN 1097-0207. Disponível em: <http://dx.doi.org/10.1002/(SICI)1097-0207(19990620)45:5<601::AID-NME598>3.0.CO;2-S>. Citado na página 166.

BELYTSCHKO, T.; LOEHNERT, S.; SONG, J.-H. Multiscale aggregating discontinuities: A method for circumventing loss of material stability. *International Journal for Numerical Methods in Engineering*, v. 73, n. 6, p. 869–894, 2008. Disponível em: <https://onlinelibrary.wiley.com/doi/abs/10.1002/nme.2156>. Citado na página 29.

BELYTSCHKO, T.; MISH, K. Computability in nonlinear solid mechanics. *International Journal for Numerical Methods in Engineering*, v. 21, p. 1–24, 2001. ISSN 00295981. Disponível em: <http://onlinelibrary.wiley.com/doi/10.1002/nme.270/abstract>. Citado na página 118.

BELYTSCHKO, T.; SONG, J.-H. Coarse-graining of multiscale crack propagation. v. 81, p. 537–563, 2010. Citado na página 29.

BENSOUSSAN, A.; LIONS, J.; PAPANICOLAOU, G. *Asymptotic analysis for periodic structures*. North-Holland: Elsevier, 1978. Citado na página 29.

BERKACHE, K. et al. Construction of second gradient continuum models for random fibrous networks and analysis of size effects. *Composite Structures*, v. 181, p. 347–357, 2017. ISSN 02638223. Disponível em: <http://dx.doi.org/10.1016/j.compstruct.2017.08.078>. Citado 3 vezes nas páginas 31, 32, and 165.

BIGONI, D. *Nonlinear Solid Mechanics: Bifurcation Theory and Material Instability*. [S.l.]: Cambridge University Press, 2012. Citado na página 33.

BLANCO, P.; CLAUSSE, A.; FEIJÓO, R. Homogenization of the Navier–Stokes equations by means of the Multi-scale Virtual Power Principle. *Computer Methods in Applied Mechanics and Engineering*, v. 315, p. 760–779, 2017. ISSN 0045-7825. Disponível em: <http://www.sciencedirect.com/science/article/pii/S0045782516312385>. Citado 3 vezes nas páginas 29, 34, and 49.

BLANCO, P. et al. The method of multiscale virtual power for the derivation of a second order mechanical model. *Mechanics of Materials*, v. 99, p. 53–67, 2016. Disponível em: <https://www.scopus.com/inward/record.uri?eid=2-s2.0-84971492704&partnerID=40&md5=f24e024cdf8288b0f56c11558c9143a6>. Citado 3 vezes nas páginas 34, 49, and 165.

BLANCO, P. J.; GIUSTI, S. M. Thermomechanical multiscale constitutive modeling: Accounting for microstructural thermal effects. *Journal of Elasticity*, v. 115, n. 1, p. 27–46, 2014. ISSN 03743535. Citado 3 vezes nas páginas 29, 34, and 49.

BLANCO, P. J. et al. Variational foundations of RVE-based multiscale models. *LNCC Research and Development Internal Report*, 2014. Citado 11 vezes nas páginas 34, 37, 39, 42, 43, 59, 68, 69, 97, 105, and 160.

BLANCO, P. J. et al. Variational foundations and generalized unified theory of RVE-based multiscale models. *Archives of Computational Methods in Engineering*, Springer Netherlands, v. 23, p. 191–253, 2016. ISSN 1134-3060. Disponível em: <http://dx.doi.org/10.1007/s11831-014-9137-5>. Citado 11 vezes nas páginas 34, 37, 39, 42, 43, 59, 68, 69, 97, 105, and 160.

BLANCO, P. J. et al. A consistent multiscale mechanical formulation for media with randomly distributed voids (in submission process). *Computer Methods in Applied Mechanics and Engineering*, Elsevier B.V., 2019. Citado na página 75.

BLANCO, S.; POLINDARA, C. A.; GOICOLEA, J. M. A regularised continuum damage model based on the mesoscopic scale for soft tissue. *International Journal of Solids and Structures*, v. 58, p. 20 – 33, 2015. ISSN 0020-7683. Disponível em: <http://www.sciencedirect.com/science/article/pii/S0020768314004818>. Citado na página 31.

BOSCO, E. et al. On the role of moisture in triggering out-of-plane displacement in paper: From the network level to the macroscopic scale. *International Journal of Solids and Structures*, 2017. ISSN 0020-7683. Disponível em: <http://www.sciencedirect.com/science/article/pii/S0020768317301567>. Citado na página 33.

CAILLERIE, D.; MOURAD, A.; RAOULT, A. Cell-to-muscle homogenization. application to a constitutive law for the myocardium. *ESAIM: Mathematical Modelling and Numerical Analysis*, v. 37, n. 4, p. 681–698, 2003. Citado na página 32.

CARNIEL, T. A.; FANCELLO, E. A. A variational homogenization approach applied to the multiscale analysis of the viscoelastic behavior of tendon fascicles. *Continuum Mechanics and Thermodynamics*, Springer Berlin Heidelberg, 2018. ISSN 1432-0959. Disponível em: <https://doi.org/10.1007/s00161-018-0714-y>. Citado na página 33.

CARNIEL, T. A.; KLAHR, B.; FANCELLO, E. A. On multiscale boundary conditions in the computational homogenization of an RVE of tendon fascicles. *Journal of the Mechanical Behavior of Biomedical Materials*, Elsevier Ltd, v. 91, n. September 2018, p. 131–138, 2019. ISSN 18780180. Disponível em: <https://doi.org/10.1016/j.jmbbm.2018.12.003>. Citado na página 32.

CARO, C.; FITZ-GERALD, J. M.; SCHROTER, R. C. Atheroma and Arterial Wall Shear Observation, Correlation and Proposal of a Shear Dependent Mass Transfer Mechanism for Atherogenesis: Appendix. *Proceedings of the Royal Society B:*

Biological Sciences, v. 177, n. 1046, p. 133–159, 1971. ISSN 0962-8452. Disponível em: <http://rspb.royalsocietypublishing.org/cgi/doi/10.1098/rspb.1971.0020>. Citado na página 24.

CHANDRAN, P. L. Affine Versus Non-Affine Fibril Kinematics in Collagen Networks: Theoretical Studies of Network Behavior. *Journal of Biomechanical Engineering*, v. 128, n. 2, p. 259, 2005. ISSN 0148-0731. Disponível em: <http://biomechanical.asmedigitalcollection.asme.org/article.aspx?doi=10.1115/1.2165699>. Citado na página 78.

CHANDRAN, P. L.; BAROCAS, V. H. Deterministic material-based averaging theory model of collagen gel micromechanics. *Journal of biomechanical engineering*, v. 129, n. 2, p. 137–147, 2007. ISSN 01480731. Citado 3 vezes nas páginas 27, 32, and 113.

CHATZIZISIS, Y. S. et al. Role of Endothelial Shear Stress in the Natural History of Coronary Atherosclerosis and Vascular Remodeling. Molecular, Cellular, and Vascular Behavior. *Journal of the American College of Cardiology*, v. 49, n. 25, p. 2379–2393, 2007. ISSN 07351097. Citado na página 24.

CHENG, X.; HATAMI-MARBINI, H.; PINSKY, P. M. Modeling Collagen-Proteoglycan Structural Interactions in the Human Cornea. In: HOLZAPFEL, G. A.; KUHL, E. (Ed.). *Computer Models in Biomechanics*. Dordrecht: Springer Netherlands, 2013. p. 11–24. ISBN 978-94-007-5464-5. Citado na página 23.

COMELLAS, E.; BELLOMO, F.; OLLER, S. A generalized finite-strain damage model for quasi-incompressible hyperelasticity using hybrid formulation. *International journal for numerical methods in engineering*, 09 2015. Citado na página 116.

COMNINOU, M.; YANNAS, I. V. Dependence of stress-strain nonlinearity of connective tissues on the geometry of collagen fibres. *Journal of Biomechanics*, v. 9, n. 7, p. 427–433, 1976. ISSN 00219290. Citado na página 113.

CYRON, C. J. et al. Micromechanical simulations of biopolymer networks with finite elements. *Journal of Computational Physics*, Elsevier Inc., v. 244, p. 236–251, 2013. ISSN 00219991. Disponível em: <http://dx.doi.org/10.1016/j.jcp.2012.10.025>. Citado na página 78.

DAVIS, F. M.; VITA, R. D. A Nonlinear Constitutive Model for Stress Relaxation in Ligaments and Tendons. *Annals of Biomedical Engineering*, v. 40, n. 12, p. 2541–2550, 2012. ISSN 0090-6964. Disponível em: <http://link.springer.com/10.1007/s10439-012-0596-2>. Citado 2 vezes nas páginas 23 and 111.

DAVYDOV, D.; PELTERET, J. P.; STEINMANN, P. Comparison of several staggered atomistic-to-continuum concurrent coupling strategies. *Computer Methods in Applied Mechanics and Engineering*, Elsevier B.V., v. 277, p. 260–280, 2014. ISSN 00457825. Disponível em: <http://dx.doi.org/10.1016/j.cma.2014.04.013>. Citado na página 33.

DEGROOT, M.; SCHERVISH, M. *Probability and Statistics*. Addison-Wesley, 2012. ISBN 9780321500465. Disponível em: <https://books.google.com.br/books?id=4TlEPgAACAAJ>. Citado na página 128.

DEOGEKAR, S.; PICU, R. C. On the strength of random fiber networks. *Journal of the Mechanics and Physics of Solids*, Elsevier Ltd, v. 116, p. 1–16, 2018. ISSN 00225096. Disponível em: <https://doi.org/10.1016/j.jmps.2018.03.026>. Citado na página 33.

DIRRENBERGER, J.; FOREST, S.; JEULIN, D. Towards gigantic RVE sizes for 3D stochastic fibrous networks. *International Journal of Solids and Structures*, v. 51, p. 359–376, 2014. Citado na página 69.

DURVILLE, D. et al. International Journal of Solids and Structures Determining the initial configuration and characterizing the mechanical properties of 3D angle-interlock fabrics using finite element simulation. *International Journal of Solids and Structures*, Elsevier Ltd, v. 154, p. 97–103, 2018. ISSN 0020-7683. Disponível em: <https://doi.org/10.1016/j.ijsolstr.2017.06.026>. Citado na página 164.

FERRARA, a.; PANDOLFI, a. Numerical modelling of fracture in human arteries. *Computer methods in biomechanics and biomedical engineering*, v. 11, n. 5, p. 553–567, 2008. ISSN 1025-5842. Citado na página 25.

FERRARA, A.; PANDOLFI, A. A numerical study of arterial media dissection processes. *International Journal of Fracture*, v. 166, n. 1-2, p. 21–33, 2010. ISSN 03769429. Citado na página 25.

FEYEL, F.; CHABOCHE, J. FE^2 multiscale approach for modelling the elastoviscoplastic behaviour of long fibre SiC/Ti composite materials. v. 183, p. 309–330, 2000. Citado na página 29.

FEYEL, F.; CHABOCHE, J. L. FE2multiscale approach for modelling the elastoviscoplastic behaviour of long fibre SiC/Ti composite materials. *Computer Methods in Applied Mechanics and Engineering*, v. 183, n. 3-4, p. 309–330, 2000. ISSN 00457825. Citado na página 165.

FOREST, S.; TRINH, D. K. Generalized continua and non-homogeneous boundary conditions in homogenisation methods. *ZAMM Zeitschrift fur Angewandte Mathematik und Mechanik*, v. 91, n. 2, p. 90–109, 2011. ISSN 00442267. Citado na página 165.

GANGHOFFER, J. F. et al. Nonlinear viscous behavior of the tendon's fascicles from the homogenization of viscoelastic collagen fibers. *European Journal of Mechanics, A/Solids*, Elsevier Masson SAS, v. 59, p. 265–279, 2016. ISSN 09977538. Disponível em: <http://dx.doi.org/10.1016/j.euromechsol.2016.04.006>. Citado na página 23.

GASSER, T.; OGDEN, R.; HOLZAPFEL, G. Hyperelastic modelling of arterial layers with distributed collagen fibre orientations. *Journal of the Royal Society Interface*, v. 3, n. 6, p. 15–35, 2006. Disponível em: <http://www.scopus.com/inward/record.url?eid=2-s2.0-33745171176&partnerID=40&md5=120548119053f8311bfed4fafb69e277>. Citado 4 vezes nas páginas 23, 26, 94, and 144.

GASSER, T. C. An irreversible constitutive model for fibrous soft biological tissue : A 3-d microfiber approach with demonstrative application to abdominal aortic aneurysms. *Acta Biomaterialia*, Acta Materialia Inc., v. 7, n. 6, p. 2457–2466, 2011. ISSN 1742-7061. Disponível em: <http://dx.doi.org/10.1016/j.actbio.2011.02.015>. Citado na página 27.

GASSER, T. C.; HOLZAPFEL, G. A. Geometrically non-linear and consistently linearized embedded strong discontinuity models for 3d problems with an application to the dissection analysis of soft biological tissues. *Computer Methods in Applied Mechanics and Engineering*, v. 192, n. 47-48, p. 5059–5098, 2003. ISSN 00457825. Citado na página 25.

GASSER, T. C.; HOLZAPFEL, G. A. Modeling the propagation of arterial dissection. *European Journal of Mechanics, A/Solids*, v. 25, n. 4, p. 617–633, 2006. ISSN 09977538. Citado na página 25.

GASSER, T. C.; HOLZAPFEL, G. A. Modeling plaque fissuring and dissection during balloon angioplasty intervention. *Annals of Biomedical Engineering*, v. 35, n. 5, p. 711–723, 2007. ISSN 00906964. Citado na página 25.

GASSER, T. C. et al. Micromechanical characterization of intra-luminal thrombus tissue from abdominal aortic aneurysms. *Annals of Biomedical Engineering*, v. 38, n. 2, p. 371–379, 2010. ISSN 00906964. Citado na página 26.

GERMAIN, P. Sur l'application de la méthode des puissances virtuelles en mécanique des milieux continus. *C.R. Acad. Sci. Paris Sér. A*, v. 274, p. 1051–1055, 1972. Citado 2 vezes nas páginas 34 and 39.

GIDDENS, D. P.; ZARINS, C. K.; GLAGOV, S. The role of fluid mechanics in the localization and detection of atherosclerosis. *Journal of biomechanical engineering*, v. 115, n. 4B, p. 588–94, 1993. ISSN 0148-0731. Disponível em: <http://www.ncbi.nlm.nih.gov/pubmed/8302046>. Citado na página 24.

GRYTZ, R.; MESCHKE, G. Constitutive modeling of crimped collagen fibrils in soft tissues. *Journal of the Mechanical Behavior of Biomedical Materials*, Elsevier Ltd, v. 2, n. 5, p. 522–533, 2009. ISSN 17516161. Disponível em: <http://dx.doi.org/10.1016/j.jmbbm.2008.12.009>. Citado na página 164.

GURTIN, M. E. *An Introduction to Continuum Mechanics.* [S.l.]: New York: Academic Press, 1981. Citado na página 39.

HADI, M.; SANDER, E.; BAROCAS, V. Multiscale model predicts tissue-level failure from collagen fiber-level damage. *Journal of Biomechanical Engineering*, v. 134, n. 9, 2012. Disponível em: <http://www.scopus.com/inward/record.url?eid=2-s2.0-84865674799&partnerID=40&md5=2f233f3b8bb5f267d4f33037bc9b59a2>. Citado na página 33.

HADI, M. F.; BAROCAS, V. H. Microscale fiber network alignment affects macroscale failure behavior in simulated collagen tissue analogs. *Journal of biomechanical engineering*, v. 135, n. 2, p. 021026, 2013. ISSN 1528-8951. Disponível em: <http://0-biomechanical.asmedigitalcollection.asme.org.library.unl.edu/article.aspx?articleid=1666679>. Citado na página 78.

HATAMI-MARBINI, H.; PICU, R. C. Effect of fiber orientation on the non-affine deformation of random fiber networks. *Acta Mechanica*, v. 205, n. 1-4, p. 77–84, 2009. ISSN 00015970. Citado na página 27.

HAZANOV, S. Hill condition and overall properties of composites. *Archive of Applied Mechanics*, v. 68, p. 385–394, 1998. Citado na página 52.

HAZANOV, S.; HUET, C. Order relationships for boundary conditions effect in heterogeneous bodies smaller than the representative volume. *Journal of the Mechanics and Physics of Solids*, v. 42, p. 1995–2011, 1994. Citado 2 vezes nas páginas 52 and 69.

HERNÁNDEZ, J. A. et al. High-performance model reduction techniques in computational multiscale homogenization. *Computer Methods in Applied Mechanics and Engineering*, v. 276, p. 149–189, 2014. ISSN 00457825. Citado na página 166.

HEUSSINGER, C.; FREY, E. Stiff polymers, foams, and fiber networks. *Physical Review Letters*, v. 96, n. 1, p. 1–4, 2006. ISSN 10797114. Citado na página 78.

HILL, M. et al. A theoretical and non-destructive experimental approach for direct inclusion of measured collagen orientation and recruitment into mechanical models of the artery wall. *Journal of Biomechanics*, v. 45, n. 5, p. 762–771, 2012. Disponível em: <https://www.scopus.com/inward/record.uri?eid=2-s2.0-84857644518&doi=10.1016%2fj.jbiomech.2011.11.016&partnerID=40&md5=1284836f5f75a31ac8dd06f3a6060fbb>. Citado 2 vezes nas páginas 128 and 132.

HILL, R. A self-consistent mechanics of composite materials. *Journal of the Mechanics and Physics of Solids*, v. 13, n. 4, p. 213 – 222, 1965. ISSN 0022-5096. Disponível em: <http://www.sciencedirect.com/science/article/pii/0022509665900104>. Citado 5 vezes nas páginas 29, 31, 43, 47, and 162.

HOLZAPFEL, G.; GASSER, T.; OGDEN, R. A new constitutive framework for arterial wall mechanics and a comparative study of material models. *Journal of Elasticity*, v. 61, n. 1-3, p. 1–48, 2000. Disponível em: <http://www.scopus.com/inward/record.url?eid=2-s2.0-0034434740&partnerID=40&md5=8939d791d517facc6650c7ef3a1052a3>. Citado 5 vezes nas páginas 13, 23, 26, 27, and 113.

HOLZAPFEL, G.; OGDEN, R. Constitutive modelling of arteries. *Proceedings of the Royal Society A: Mathematical, Physical and Engineering Sciences*, v. 466, n. 2118, p. 1551–1597, 2010. Disponível em: <http://www.scopus.com/inward/record.url?eid=2-s2.0-77953418030&partnerID=40&md5=e2699a393b6c11e36d699cc3648862e2>. Citado 2 vezes nas páginas 23 and 112.

HOLZAPFEL, G. A. *Nonlinear Solid Mechanics. A continuum Approach for Engineering.* [S.l.]: London : John Wiley Sons, 2000. Citado na página 39.

JONES, E. et al. *SciPy: Open source scientific tools for Python*. 2001–. [Online; accessed <today>]. Disponível em: <http://www.scipy.org/>. Citado na página 126.

KABLA, A.; MAHADEVAN, L. Nonlinear mechanics of soft fibrous networks. *Journal of The Royal Society Interface*, v. 4, n. 12, p. 99–106, 2007. ISSN 1742-5689. Disponível em: <http://dx.doi.org/10.1098/rsif.2006.0151$\delimiter"026E30F$nhttp://rsif.royalsocietypublishing.org/cgi/doi/10.1098/rsif.2006.0151>. Citado na página 27.

KANIT, T. et al. Determination of the size of the representative volume element for random composites: statistical and numerical approach. *International Journal of Solids and Structures*, v. 40, n. 13, p. 3647–3679, 2003. ISSN 0020-7683. Disponível em: <http://www.sciencedirect.com/science/article/pii/S0020768303001434>. Citado na página 30.

KHISAEVA, Z. F.; OSTOJA-STARZEWSKI, M. On the Size of RVE in Finite Elasticity of Random Composites. p. 153–173, 2006. Citado na página 30.

KU, D. N. et al. Pulsatile flow and atherosclerosis in the human carotid bifurcation. Positive correlation between plaque location and low oscillating shear stress. *Arteriosclerosis, Thrombosis, and Vascular Biology*, v. 5, n. 3, p. 293–302, 1985. ISSN 1079-5642. Disponível em: <http://atvb.ahajournals.org/cgi/doi/10.1161/01.ATV.5.3.293>. Citado na página 24.

LEMAITRE, J.; CHABOCHE, J.-L. *Mechanics of Solid Materials*. [S.l.]: Cambridge University Press, 1990. Citado na página 107.

LI, D.; ROBERTSON, A. M. A structural multi-mechanism constitutive equation for cerebral arterial tissue. *International Journal of Solids and Structures*, Elsevier Ltd, v. 46, n. 14-15, p. 2920–2928, 2009. ISSN 00207683. Disponível em: <http://dx.doi.org/10.1016/j.ijsolstr.2009.03.017>. Citado na página 105.

LI, D. et al. Finite element modeling of cerebral angioplasty using a structural multi-mechanism anisotropic damage model. *International Journal for Numerical Methods in Engineering*, n. June, p. 457–474, 2012. Citado na página 25.

LI, K.; OGDEN, R. W.; HOLZAPFEL, G. A. Computational method for excluding fibers under compression in modeling soft fibrous solids. *European Journal of Mechanics, A/Solids*, v. 57, n. May, p. 178–193, 2016. ISSN 09977538. Citado na página 112.

LI, S.; URATA, S. An atomistic-to-continuum molecular dynamics: Theory, algorithm, and applications. *Computer Methods in Applied Mechanics and Engineering*, v. 306, p. 452–478, 2016. ISSN 00457825. Citado na página 33.

LI, W. Damage Models for Soft Tissues: A Survey. *Journal of Medical and Biological Engineering*, Springer Berlin Heidelberg, v. 36, n. 3, p. 285–307, 2016. ISSN 21994757. Citado na página 25.

LI, X.; E, W. Multiscale modeling of the dynamics of solids at finite temperature. *Journal of the Mechanics and Physics of Solids*, v. 53, n. 7, p. 1650–1685, jul. 2005. ISSN 00225096. Citado na página 33.

LOPES, I. A.; PIRES, F. M.; REIS, F. J. A mixed parallel strategy for the solution of coupled multi-scale problems at finite strains. *Computational Mechanics*, Springer Berlin Heidelberg, v. 61, n. 1-2, p. 157–180, 2018. ISSN 01787675. Citado na página 165.

MANDEL, J. *Plasticité classique et viscoplasticité*. [S.l.]: Springer-Verlag, 1972. Citado 4 vezes nas páginas 29, 31, 43, and 47.

MARINO, M.; WRIGGERS, P. Finite strain response of crimped fibers under uniaxial traction_ An analytical approach applied to collagen. *Journal of the Mechanics and Physics of Solids*, Elsevier, v. 98, n. April 2016, p. 429–453, 2017. ISSN 0022-5096. Disponível em: <http://dx.doi.org/10.1016/j.jmps.2016.05.010>. Citado na página 164.

MATSUI, K.; TERADA, K.; YUGE, K. Two-scale finite element analysis of heterogeneous solids with periodic microstructures. *Computers and Structures*, v. 82, n. 7-8, p. 593–606, 2004. ISSN 00457949. Citado na página 165.

MAUGIN, G. The method of virtual power in continuum mechanics: application to coupled fields. *Acta Mechanica*, v. 35, p. 1–70, 1980. Citado 2 vezes nas páginas 34 and 39.

MCDOWELL, D. A perspective on trends in multiscale plasticity. v. 26, p. 1280–1309, 2010. Citado na página 29.

MEIER, C. et al. Geometrically exact beam elements and smooth contact schemes for the modeling of fiber-based materials and structures. *International Journal of Solids and Structures*, Elsevier Ltd, v. 0, p. 1–23, 2017. ISSN 00207683. Disponível em: <http://dx.doi.org/10.1016/j.ijsolstr.2017.07.020>. Citado na página 78.

MICHEL, J.; MOULINEC, H.; SUQUET, P. Effective properties of composite materials with periodic microstructure: a computational approach. *Comput. Methods Appl. Mech. Engrg.*, v. 172, p. 109–143, 1999. Citado na página 29.

MIEHE, C.; DETTMAR, J. A framework for micro-macro transitions in periodic particle aggregates of granular materials. *Computer Methods in Applied Mechanics and Engineering*, v. 193, n. 3-5, p. 225–256, 2004. ISSN 00457825. Citado na página 33.

MIEHE, C.; DETTMAR, J.; ZAH, D. Homogenization and two-scale simulations of granular materials for different microstructural constraints. *International Journal for Numerical Methods in Engineering*, 2010. ISSN 0743-1619. Citado na página 33.

MIEHE, C.; SCHOTTE, J.; SCHROEDER, J. Computational micro-macro transitions and overall moduli in the analysis of polycrystals at large strains. *Computational Materials Science*, v. 6, p. 372–382, 1999. Citado na página 29.

MOËS, N.; DOLBOW, J.; BELYTSCHKO, T. A finite element method for crack growth without remeshing. *International Journal for Numerical Methods in Engineering*, v. 46, n. 1, p. 131–150, 1999. Disponível em: <http://www.scopus.com/inward/record.url?eid=2-s2.0-0033349534{&}partnerID=40{&}md5=458fb35c4f371a592f410e9b64>. Citado na página 166.

MOSBY, M.; MATOUS, K. Hierarchically parallel coupled finite strain multiscale solver for modeling heterogeneous layers. *International Journal for Numerical Methods in Engineering*, v. 102, n. 3-4, p. 748–765, 2015. ISSN 00295981. Disponível em: <http://doi.wiley.com/10.1002/nme.4755>. Citado na página 165.

MOSBY, M.; MATOUS, K. Computational homogenization at extreme scales. *Extreme Mechanics Letters*, Elsevier Ltd, v. 6, p. 68–74, 2016. ISSN 23524316. Citado na página 165.

NADY, K. E.; GANGHOFFER, J. F. Computation of the effective mechanical response of biological networks accounting for large configuration changes. *Journal of the Mechanical Behavior of Biomedical Materials*, Elsevier, v. 58, p. 28–44, 2016. ISSN 18780180. Disponível em: <http://dx.doi.org/10.1016/j.jmbbm.2015.09.009>. Citado 4 vezes nas páginas 31, 32, 164, and 165.

NADY, K. E.; GODA, I.; GANGHOFFER, J. F. Computation of the effective nonlinear mechanical response of lattice materials considering geometrical nonlinearities. *Computational Mechanics*, v. 58, n. 6, p. 957–979, 2016. ISSN 01787675. Citado 2 vezes nas páginas 31 and 32.

NEMAT-NASSER, S. Averaging theorems in finite deformation plasticity. *Mechanics of Materials*, v. 31, p. 493–523, 1999. Citado na página 29.

NETO, E. de S. et al. An RVE-based mutiscale theory of solids with micro-scale inertia and body force effects. *Mechanics of Materials*, v. 80, p. 136–144, 2015. ISSN 0167-6636. Disponível em: <http://www.sciencedirect.com/science/article/pii/S0167663614001872>. Citado 2 vezes nas páginas 34 and 49.

OGDEN, R. W. *Non-Linear Elastic Deformations.* [S.l.]: Ellis Horwood, 1984. Citado na página 39.

OLIVER, J. Theoretical and computational issues in modelling material failure in strong discontinuity scenarios. *Computer Methods in Applied Mechanics and Engineering*, v. 193, p. 2987–3014, 2004. Citado na página 166.

OLIVER, J. et al. Reduced order modeling strategies for computational multiscale fracture. *Computer Methods in Applied Mechanics and Engineering*, v. 313, p. 560–595, 2017. ISSN 00457825. Citado na página 166.

OLIVER, J.; HUESPE, A. E.; CANTE, J. C. An implicit/explicit integration scheme to increase computability of non-linear material and contact/friction problems. *Computer Methods in Applied Mechanics and Engineering*, v. 197, n. 21–24, p. 1865–1889, 2008. ISSN 0045-7825. Disponível em: <http://www.sciencedirect.com/science/article/pii/S0045782507004756>. Citado na página 118.

ÖZDEMIR, I.; BREKELMANS, W.; GEERS, M. Computational homogenization for heat conduction in heterogeneous solids. v. 73, n. 2, p. 185–204, 2008. Citado na página 29.

PAHR, D.; ZYSSET, P. Influence of boundary conditions on computed apparent elastic properties of cancellous bone. *Biomechanics and Modeling in Mechanobiology*, v. 7, p. 463–476, 2008. Citado 2 vezes nas páginas 29 and 52.

PEÑA, E. A rate dependent directional damage model for fibred materials: Application to soft biological tissues. *Computational Mechanics*, v. 48, n. 4, p. 407–420, 2011. ISSN 01787675. Citado na página 119.

PEÑA, E. Computational aspects of the numerical modelling of softening, damage and permanent set in soft biological tissues. *Computers and Structures*, v. 130, p. 57–72, 2014. ISSN 00457949. Citado na página 25.

PRITCHARD, R. H.; HUANG, Y. Y. S.; TERENTJEV, E. M. Mechanics of biological networks: from the cell cytoskeleton to connective tissue. *Soft matter*, v. 10, n. 12, p. 1864–84, 2014. ISSN 1744-6848. Disponível em: <http://www.ncbi.nlm.nih.gov/pubmed/24652375>. Citado na página 27.

RAINA, A.; MIEHE, C. A phase-field model for fracture in biological tissues. *Biomechanics and Modeling in Mechanobiology*, Springer Berlin Heidelberg, 2015. ISSN 1617-7959. Disponível em: <http://link.springer.com/10.1007/s10237-015-0702-0>. Citado na página 24.

RANGAMANI, P.; XIONG, G. Y.; IYENGAR, R. *Multiscale Modeling of Cell Shape from the Actin Cytoskeleton.* 1. ed. Elsevier Inc., 2014. v. 123. 143–167 p. ISSN 1877-1173. ISBN 9780123978974. Disponível em: <http://dx.doi.org/10.1016/B978-0-12-397897-4.00002-4>. Citado na página 23.

RICE, J. R. The localization of plastic deformation. In: *in: W.T. Koiter (Ed.), Theoretical and Applied Mechanics*. [S.l.]: North-Holland Publishing Company, 1976. p. 207–220. Citado 3 vezes nas páginas 33, 35, and 122.

ROBERTSON, A.; HILL, M.; LI, D. Structurally motivated damage models for arterial walls. theory and application. *D. Ambrosi, A. Quarteroni, G. Rozza (Eds.), Modelling of Physiological Flows, Simulation and Applications*, Springer, v. 5, p. 143–185, 2012. Disponível em: <http://www.scopus.com/inward/record.url?eid=2-s2.0-84874389120&partnerID=40&md5=bbfb558fa3dd47cd79a2386137c7876c>. Citado 2 vezes nas páginas 13 and 28.

ROBERTSON, A.; WATTON, P. *Mechanobiology of the Arterial Wall, In: Kuznetsov A, Becker S, editors. Transport in biological media*. [S.l.]: Elsevier, 2013. Citado 6 vezes nas páginas 13, 23, 24, 26, 28, and 30.

ROCHA, F. F. et al. Multi-scale modelling of arterial tissue: Linking networks of fibres to continua. *Computer Methods in Applied Mechanics and Engineering*, Elsevier B.V., v. 341, p. 740–787, 2018. ISSN 00457825. Disponível em: <https://linkinghub.elsevier.com/retrieve/pii/S0045782518303281>. Citado 5 vezes nas páginas 29, 75, 106, 110, and 162.

ROCHA, F. F. et al. Multi-scale modelling of damage-driven strain localisation in fibrous tissues (in revision process). *Journal of the Mechanics and Physics of Solids*, Elsevier B.V., 2019. Citado 3 vezes nas páginas 60, 125, and 162.

ROTH, G. A. et al. Demographic and Epidemiologic Drivers of Global Cardiovascular Mortality. *New England Journal of Medicine*, v. 372, n. 14, p. 1333–1341, 2015. ISSN 0028-4793. Disponível em: <http://www.nejm.org/doi/10.1056/NEJMoa1406656>. Citado na página 23.

RYCROFT, C. H. VORO++: A three-dimensional Voronoi cell library in C++. *Chaos*, v. 19, n. 4, p. 1–16, 2009. ISSN 10541500. Citado 2 vezes nas páginas 126 and 141.

SÁNCHEZ, P. et al. Failure-oriented multi-scale variational formulation: Micro-structures with nucleation and evolution of softening bands. *Computer Methods in Applied Mechanics and Engineering*, v. 257, n. 0, p. 221 – 247, 2013. ISSN 0045-7825. Disponível em: <http://www.sciencedirect.com/science/article/pii/S0045782512003659>. Citado 5 vezes nas páginas 29, 34, 160, 165, and 166.

SÁNCHEZ, P. J. et al. A macroscopic damage-plastic constitutive law for modeling quasi-brittle fracture and ductile behavior of concrete. *International Journal for Numerical and Analytical Methods in Geomechanics*, John Wiley & Sons, Ltd, v. 36, n. 5, p. 546–573, 2012. ISSN 1096-9853. Disponível em: <http://dx.doi.org/10.1002/nag.1013>. Citado na página 116.

SANCHEZ-PALENCIA, E. *Non-homogeneous media and vibration theory. Volume 127 on Lecture Notes in Physics*. Berlin: Springer-Verlag, 1980. Citado na página 29.

SANDSTRÖM, C.; LARSSON, F. Variationally consistent homogenization of Stokes flow in porous media. *Journal for Multiscale Computational Engineering*, v. 11, p. 117–138, 2013. Citado na página 29.

SANDSTRÖM, C.; LARSSON, F. On bounded approximations of periodicity for computational homogenization of Stokes flow in porous media. *International Journal for Numerical Methods in Engineering*, v. 109, p. 307–325, 2017. Citado na página 52.

SANDSTRÖM, C.; LARSSON, F.; RUNESSON, K. Weakly periodic boundary conditions for the homogenization of flow in porous media. *Advanced Modeling and Simulation in Engineering Sciences*, v. 2, p. 12, 2014. Citado na página 52.

SANG, C. et al. a Uniaxial Testing Approach for Consistent Failure in Vascular Tissues. *Journal of Biomechanical Engineering*, n. c, 2018. ISSN 0148-0731. Disponível em: <http://biomechanical.asmedigitalcollection.asme.org/article.aspx?doi=10.1115/1.4039577>. Citado 2 vezes nas páginas 25 and 33.

SHAHSAVARI, A. S.; PICU, R. C. Size effect on mechanical behavior of random fiber networks. *International Journal of Solids and Structures*, Elsevier Ltd, v. 50, n. 20-21, p. 3332–3338, 2013. ISSN 00207683. Disponível em: <http://dx.doi.org/10.1016/j.ijsolstr.2013.06.004>. Citado na página 32.

SHEARER, T. A new strain energy function for the hyperelastic modelling of ligaments and tendons based on fascicle microstructure. *Journal of Biomechanics*, Elsevier, v. 48, n. 2, p. 290–297, 2015. ISSN 18732380. Disponível em: <http://dx.doi.org/10.1016/j.jbiomech.2014.11.031>. Citado na página 164.

SIMO, J.; JU, J. Strain- and stress-based continuum damage models—i. formulation. *International Journal of Solids and Structures*, v. 23, n. 7, p. 821 – 840, 1987. ISSN 0020-7683. Disponível em: <http://www.sciencedirect.com/science/article/pii/0020768387900837>. Citado na página 114.

SIMO, J. C.; TAYLOR, R. L. Consistent tangent operators for rate-independent elastoplasticity. *Computer Methods in Applied Mechanics and Engineering*, v. 48, n. 1, p. 101–118, 1985. ISSN 00457825. Citado na página 110.

SOZUMERT, E. et al. Deformation and damage of random fibrous networks. *International Journal of Solids and Structures*, Elsevier Ltd, n. xxxx, 2018. ISSN 0020-7683. Disponível em: <https://doi.org/10.1016/j.ijsolstr.2018.12.012>. Citado na página 33.

SPEIRS, D. C. D.; NETO, E. A. de S.; PERIĆ, D. An approach to the mechanical constitutive modelling of arterial tissue based on homogenization and optimization. *Journal of Biomechanics*, v. 41, n. 12, p. 2673–80, 2008. ISSN 0021-9290. Disponível em: <http://www.biomedsearch.com/nih/approach-to-mechanical-constitutive-modelling/18674766.html>. Citado 4 vezes nas páginas 29, 31, 32, and 166.

STEIN, A. M. et al. An algorithm for extracting the network geometry of three-dimensional collagen gels. *Journal of Microcospy*, v. 232, n. May, p. 463–475, 2008. Citado 2 vezes nas páginas 31 and 78.

STEIN, A. M. et al. The micromechanics of three-dimensional collagen-I gels. *Complexity*, Wiley Subscription Services, Inc., A Wiley Company, v. 16, n. 4, p. 22–28, 2011. ISSN 1099-0526. Disponível em: <http://dx.doi.org/10.1002/cplx.20332>. Citado na página 27.

STEINMANN, P.; RICKER, S.; AIFANTIS, E. Unconstrained and Cauchy-Born-constrained atomistic systems: Deformational and configurational mechanics. *Archive of Applied Mechanics*, v. 81, n. 5, p. 669–684, 2011. ISSN 09391533. Citado na página 33.

STYLIANOPOULOS, T.; BAROCAS, V. H. Modeling for the Elastic Mechanical Behavior of Arterial. *Journal of Biomechanical Engineering*, v. 129, n. August, p. 611–618, 2007. ISSN 0148-0731. Citado 6 vezes nas páginas 31, 32, 77, 78, 113, and 164.

STYLIANOPOULOS, T.; BAROCAS, V. H. Volume-averaging theory for the study of the mechanics of collagen networks. *Computer Methods in Applied Mechanics and Engineering*, v. 196, n. 31-32, p. 2981–2990, 2007. ISSN 00457825. Citado 4 vezes nas páginas 31, 32, 77, and 78.

SVENNING, E.; FAGERSTRÖM, M.; LARSSON, F. On computational homogenization of microscale crack propagation. *International Journal for Numerical Methods in Engineering*, v. 108, p. 76–90, 2016. Citado na página 52.

TEMIZER, I.; WRIGGERS, P. Homogenization in finite thermoelasticity. v. 59, p. 344–372, 2011. Citado na página 29.

TEMIZER, I.; ZOHDI, T. I. A numerical method for homogenization in non-linear elasticity. *Computational Mechanics*, v. 40, n. 2, p. 281–298, 2007. ISSN 01787675. Citado na página 166.

THOMAS, T. *Plastic Flow and Fracture in Solids*. Acad. Press, 1961. (Mathematics in Science and Engineering). Disponível em: <https://books.google.com.br/books?id=Ph4IAQAAIAAJ>. Citado na página 122.

THUNES, J. R. et al. A structural finite element model for lamellar unit of aortic media indicates heterogeneous stress field after collagen recruitment. *Journal of Biomechanics*, v. 49, p. 1562–1569, 2016. Citado 3 vezes nas páginas 32, 112, and 115.

THUNES, J. R. et al. Structural Modeling Reveals Microstructure-Strength Relationship for Human Ascending Thoracic Aorta. *Journal of Biomechanics*, p. 1–10, 2018. ISSN 00219290. Disponível em: <http://linkinghub.elsevier.com/retrieve/pii/S0021929018300745>. Citado na página 32.

TORO, S. et al. Multiscale formulation for material failure accounting for cohesive cracks at the macro and micro scales. *International Journal of Plasticity*, v. 76, p. 75 – 110, 2016. Citado 2 vezes nas páginas 34 and 160.

TORO, S. et al. A two-scale failure model for heterogeneous materials : numerical implementation based on the finite element method. *International Journal for Numerical Methods in Engineering*, v. 97, p. 313–351, 2014. Citado 2 vezes nas páginas 29 and 34.

TORO, S. et al. Cohesive surface model for fracture based on a two-scale formulation: computational implementation aspects. *Computational Mechanics*, Springer Berlin Heidelberg, v. 58, n. 4, p. 549–585, 2016. ISSN 0178-7675. Disponível em: <http://link.springer.com/10.1007/s00466-016-1306-y>. Citado na página 34.

TRINH, D. K. et al. Evaluation of Generalized Continuum Substitution Models for Heterogeneous Materials. *International Journal for Multiscale Computational Engineering*, v. 10, n. 6, p. 527–549, 2012. ISSN 1543-1649. Disponível em: <http://www.dl.begellhouse.

com/journals/61fd1b191cf7e96f,3089bea11cd334bd,4e7afa9a21264ed3.html>. Citado na página 165.

URQUIZA, S.; VéNERE, M. An application framework architecture for fem and other related solvers. In: *I South American Congress on Computational Mechanics (MECOM)*. Santa Fé, Argentina: [s.n.], 2002. Citado na página 126.

VANDERHEIDEN, S. M.; HADI, M. F.; BAROCAS, V. H. Crack Propagation Versus Fiber Alignment in Collagen Gels: Experiments and Multiscale Simulation. *Journal of Biomechanical Engineering*, v. 137, n. 12, p. 121002, 2015. ISSN 0148-0731. Disponível em: <http://biomechanical.asmedigitalcollection.asme.org/article.aspx?doi=10.1115/1.4031570>. Citado na página 33.

VASSOLER, L. S. J. M.; FANCELLO; A., E. A variational framework for fiber-reinforced viscoelastic soft tissues including damage. *International journal for numerical methods in engineering*, v. 108, p. 865–884, 2016. ISSN 17359260. Citado na página 23.

VITA, R. D. *Structural Constitutive Models for Knee Ligaments*. 73 p. Tese (Doutorado) — University of Pittsburgh, 2005. Disponível em: <http://d-scholarship.pitt.edu/6982/1/DeVita{_}2005.> Citado 3 vezes nas páginas 111, 113, and 119.

WALT, S. van der; COLBERT, S. C.; VAROQUAUX, G. The numpy array: A structure for efficient numerical computation. *Computing in Science Engineering*, v. 13, n. 2, p. 22–30, March 2011. ISSN 1521-9615. Citado na página 126.

WARREN, W. E.; BYSKOV, E. Three-fold symmetry restrictions on two-dimensional micropolar materials. *European Journal of Mechanics, A/Solids*, v. 21, n. 5, p. 779–792, 2002. ISSN 09977538. Citado na página 32.

WEISBECKER, H. et al. Layer-specific damage experiments and modeling of human thoracic and abdominal aortas with non-atherosclerotic intimal thickening. *Journal of the Mechanical Behavior of Biomedical Materials*, v. 12, n. 0, p. 93 – 106, 2012. ISSN 1751-6161. Disponível em: <http://www.sciencedirect.com/science/article/pii/S1751616112000926>. Citado na página 25.

WEISBECKER, H.; UNTERBERGER, M. J.; HOLZAPFEL, G. A. Constitutive modelling of arteries considering fibre recruitment and three-dimensional fibre distribution. *Journal of the Royal Society, Interface / the Royal Society*, v. 12, n. 105, p. 20150111–, 2015. ISSN 1742-5662. Disponível em: <http://rsif.royalsocietypublishing.org/content/12/105/20150111>. Citado na página 23.

WITTHOFT, A. et al. A discrete mesoscopic particle model of the mechanics of a multi-constituent arterial wall. *Journal of the Royal Society Interface*, 2016. ISSN 1742-5662. Citado na página 32.

WRIGGERS, P. *Nonlinear Finite Element Methods*. [S.l.]: Berlin: Springer-Verlag, 2008. Citado na página 102.

YVONNET, J.; HE, Q. C. The reduced model multiscale method (R3M) for the non-linear homogenization of hyperelastic media at finite strains. *Journal of Computational Physics*, v. 223, n. 1, p. 341–368, 2007. ISSN 00219991. Citado na página 166.

ZAGHI, S. et al. Adaptive and off-line techniques for non-linear multiscale analysis. *Composite Structures*, v. 206, p. 215–233, 2018. ISSN 02638223. Citado na página 166.

ZHANG, L. et al. A Coupled Fiber-Matrix Model Demonstrates Highly Inhomogeneous Microstructural Interactions in Soft Tissues Under Tensile Load. *Journal of Biomechanical Engineering*, v. 135, n. 1, p. 011008, 2012. ISSN 0148-0731. Disponível em: <http://biomechanical.asmedigitalcollection.asme.org/article.aspx?doi=10.1115/1.4023136>. Citado 2 vezes nas páginas 78 and 94.

ZITNAY, J. L. et al. Molecular level detection and localization of mechanical damage in collagen enabled by collagen hybridizing peptides. *Nature Communications*, Nature Publishing Group, v. 8, p. 1–12, 2017. ISSN 20411723. Disponível em: <http://dx.doi.org/10.1038/ncomms14913>. Citado na página 31.